The Dynamics and Evolution of Supermassive Black Holes in Merging Galaxies

Dissertation Advisor: Professor Abraham Loeb Laura Elizabeth Blecha

The Dynamics and Evolution of Supermassive Black Holes in Merging Galaxies

Abstract

This thesis is a theoretical study of supermassive black holes (SMBHs) in merging galaxies. We consider the dynamics that govern inspiralling SMBH pairs and gravitational-wave (GW) recoiling SMBHs, as well as the fueling of active galactic nuclei (AGN) during galaxy mergers. In particular, we focus on the observable signatures that could distinguish dual or recoiling AGN from those in isolated galaxies, and we explore the implications of these events for the coordinated evolution of SMBHs and galaxies.

In the second and third chapters, semi-analytical models for GW-recoiling SMBHs are developed. The second chapter illustrates that bound recoiling SMBHs may have long wandering timescales and that recoil events can self-regulate SMBH growth. In the third chapter, we study the evolution of recoiling SMBHs in evolving, gaseous merger remnants. We find that the presence of gas greatly influences recoiling SMBH trajectories and may partially suppress even large recoil kicks in some cases. We also show that kinematically- and spatially-offset AGN can have substantial lifetimes for a wide range in kick speeds. Finally, this chapter illustrates that GW recoil influences the observed SMBH-galaxy relations as well as central star formation in the merger remnant.

In the fourth chapter we turn our attention to inspiralling SMBH pairs with kiloparsec-scale separations. We use a novel approach to model the narrow-line emission from these SMBH pairs, in order to understand their relationship to observations of

double-peaked narrow-line AGN. Our results indicate that double-peaked narrow-line AGN often arise from gas kinematics rather than from dual SMBH motion, but that the latter are a generic, short-lived phase of SMBH inspiral in gaseous mergers. We identify several diagnostics that could aid in distinguishing the true AGN pairs in the double-peaked sample.

Finally, the fifth chapter examines a particular galaxy that exhibits signatures of both a recoiling AGN and an AGN pair. Applying methods developed throughout this thesis, we design models for both scenarios that are well-matched to the available data. Currently, neither possibility can be excluded for this object, but our models constrain the most relevant parameters for determining its nature and for the design of future observations.

Contents

Acknowledgments

I would like to begin by thanking my family for their love and unwavering support over the years. My parents deserve credit as my first scientific mentors for their time spent seeking out public lectures, space camps, and meteor showers to foster my early interests in astronomy. I also want to thank my wonderful boyfriend Diego for supporting and understanding me, and for always being by my side to keep me sane and make me laugh.

I am very grateful to have had Avi Loeb as my advisor. He has been a great source of inspiration and guidance, and I have very much enjoyed our scientific conversations. Avi has provided countless insightful suggestions for problems I found intractable. He kept track of my progress and responded quickly to my questions, but he also allowed me freedom to develop as an independent researcher. Avi has been conscientious about my career development as well, sending me to conferences early and often throughout my graduate career and providing me with valuable advice.

I also feel quite fortunate to have had the opportunity to work closely with Lars Hernquist while at Harvard. Lars welcomed me to his group when I started working with him on simulations. I've learned a lot from him and have benefitted greatly from his ability to identify the relevant physics underlying often-messy numerical results. In addition to his scientific guidance, Lars has in many ways has been my unofficial co-advisor, often offering career advice and travel funding throughout my graduate studies. I greatly appreciate his willingness to take on this role.

My other collaborators have also been indispensable in the completion of this thesis.

T. J. Cox taught me to use GADGET and shared with me his ample library of analysis scripts; these tools made possible the large majority of my thesis. Most of all I am eternally grateful for his endless patience with my questions and for helping me make sense out of my simulations. I also want to thank Ramesh Narayan for encouraging me to tackle the problem of kiloparsec-scale black hole pairs, and for working with me and Avi to design the necessary theoretical model. I thank Martin Elvis and Francesca Civano for allowing me to be part of a very interesting project with them; they've also taught me a lot about X-ray astronomy and observations in general.

I wouldn't be where I am today without the early guidance of my excellent undergraduate advisor, Vicky Kalogera. She invested many hours in helping me to complete interesting and relevant projects as an undergrad, and her enthusiasm inspired me to continue doing theoretical research. I thank her for always encouraging and supporting me throughout my undergraduate years.

In addition to those I have collaborated with directly, many others have shared valuable knowledge, technical expertise, advice, and opinions with me along the way. I would like to thank Dušan Kereš, Patrik Jonsson, Chris Hayward, Debora Šijački, Mark Vogelsberger, Bence Kocsis, Yue Shen, Xin Liu, Julie Comerford, and Greg Shields. I would especially like to thank Volker Springel for valuable scientific discussions as well as for sharing his code with the community.

I am very thankful for the tireless efforts of Jean Collins, Peg Herlihy, Donna Adams, Uma Mirani, Nina Zonnevylle, and Peg Hedstrom to keep the department and the ITC running seamlessly. In addition to making sure the day-to-day details are attended to, they genuinely care about the well-being of the graduate students, and their presence

helps to make the CfA a great place to work.

Finally, I would like to thank my fellow graduate students for making my time at Harvard a thoroughly enjoyable experience. I especially want to thank Gurtina Besla, my former roommate, and Sarah Ballard, my officemate, for their steadfast friendship and support. I also want to thank Chris Hayward, Jack Steiner, Robert Harris, Joey Neilsen, Ryan O'Leary, Nick Stone, Greg Snyder, Sarah Rugheimer, Zach Berta, Paul Torrey, Andy Friedman, and Cesar Fuentes for keeping life interesting and fun amidst our studies.

In Loving Memory of Brian

Chapter 1

Introduction

1.1 Co-evolution of Supermassive Black Holes and Galaxies

It has been close to half a century since the existence of supermassive black holes (SMBHs, $M_{\rm BH} \sim 10^6 - 10^9$ $M_\odot$) was first proposed as a possible mechanism for fueling luminous quasars (Lynden-Bell 1969). In the intervening decades, the study of SMBHs has grown to be among the most active areas of astronomical research. Among the most remarkable discoveries was the finding that virtually all local galaxies host central SMBHs (e.g., Kormendy & Richstone 1995; Richstone et al. 1998; Ferrarese & Ford 2005), supporting the notion that quasars are simply short-lived phases of accretion onto SMBHs that are otherwise quiescent (Soltan 1982). More surprisingly, strong correlations were found between SMBH masses and properties of their host galaxies, such as the bulge mass (Kormendy & Richstone 1995; Magorrian et al. 1998; Marconi

& Hunt 2003; Merritt & Ferrarese 2001) and velocity dispersion (Gebhardt et al. 2000; Ferrarese & Merritt 2000; Tremaine et al. 2002a). This suggests that the processes that regulate SMBH accretion on scales of a few Schwarzschild radii are somehow connected to galaxy evolution on vastly larger scales.

Feedback processes from active galactic nuclei (AGN) are likely responsible, at least in part, for driving these SMBH–galaxy correlations. By injecting large amounts of energy and momentum into the surrounding gas during periods of active accretion, the SMBH may heat up and expel much of its fuel supply of cold gas, thereby self-regulating its growth and quenching star formation (e.g., Wyithe & Loeb 2003; Begelman & Nath 2005; Di Matteo et al. 2005; Springel 2005; Hopkins et al. 2006a; Debuhr et al. 2010). Indeed, AGN feedback energy may regulate the energy balance of baryons on even larger scales. For example, AGN jets and outflows are thought to be crucial for the prevention of catastrophic cooling flows in galaxy clusters (e.g., Tabor & Binney 1993; Sijacki & Springel 2006; Croton et al. 2006; McNamara & Nulsen 2007). Observations of hot bubbles in the intracluster medium originating from active central radio galaxies provide strong evidence of this process at work (e.g., McNamara et al. 2000; Fabian et al. 2003; Wise et al. 2007).

Crucial to this picture of AGN fueling and feedback is understanding what triggers these phases of active SMBH growth. The dominant AGN triggering mechanism is still a subject of active debate and almost certainly depends on factors such as AGN luminosity and redshift (e.g., Koss et al. 2010; Cisternas et al. 2011; Ellison et al. 2011). However, major mergers between galaxies, which are a relatively common occurrence in hierarchical structure formation, can efficiently drive gas to the central galactic regions and fuel luminous quasars (e.g., Sanders & Mirabel 1996; Mihos & Hernquist

1996; Di Matteo et al. 2005; Hopkins et al. 2008d). As such, galaxy mergers have been the focus of much effort to understand the coordinated growth of SMBHs and galaxies. Merger models for triggering quasars and starbursts, based on both numerical simulations and semi-analytic methods, have shown success in reproducing numerous observations, including the quasar luminosity function, the SMBH mass-host galaxy bulge relations, and the transformation from blue star-forming galaxies to red-and-dead ellipticals (e.g., Robertson et al. 2006a; Hopkins et al. 2006b, 2008b; Somerville et al. 2008). Additionally, quasar pairs with separations $\lesssim 0.1$ to 1 Mpc are significantly more common than expected from cosmological clustering, supporting the notion that galaxy interactions fuel quasars (Hennawi et al. 2006, 2010; Myers et al. 2008).

1.2 Supermassive Black Hole Mergers and Gravitational-Wave Recoil: Theory

Because almost all galaxies harbor central SMBHs, mergers between galaxies have another important consequence as well – they lead to the formation of SMBH binaries and possible SMBH mergers. This process can be divided into dynamically distinct phases. During the early stages of a galaxy merger, the SMBHs simply follow the motion of their host galaxies and may be observed as quasar pairs on scales of tens to hundreds of kiloparsec (Liu et al. 2011; da Silva et al. 2011). Later on, the galaxies combine to form a single, disturbed remnant. The SMBHs begin to spiral in toward the center of the merger remnant via dynamical friction, each retaining a cusp of stars and gas. At this stage they are best described as an SMBH pair or as dual SMBHs (rather than an

SMBH binary), because for their motion is governed by the galactic potential rather than their mutual gravity. Only when the pair separation falls below their radii of influence do the SMBHs form a truly bound *binary*. The BH radius of influence is usually defined as the radius within which the its mass dominates the mass of surrounding material ($M_{\rm gal}(< r_{\rm infl}) = 2M_{\rm BH}$, or $r_{\rm infl} = GM_{\rm BH}/\sigma^2$ for an isothermal sphere); typically, $r_{\rm infl}$ is a few parsec to a few tens of parsec.

Early studies that modeled SMBH binaries as massive bodies orbiting in a spherical, collisionless system of stars demonstrated that the binary would eject all stars on low-angular-momentum orbits (the "loss cone" of stars) via three-body interactions in a fairly short time, long before the SMBHs were close enough ($\lesssim 0.01$ pc) for gravitational wave (GW) emission to be a significant source of energy loss. Left with no further means of removing energy from the system, the binary evolution would stall at a radius of ~ 1 parsec for up to a Hubble time, leading this effect to be dubbed the "final parsec problem" (e.g., Begelman et al. 1980; Milosavljević & Merritt 2001; Yu 2002).

More realistic models have demonstrated that numerous mechanisms can drive the binary evolution well past parsec-scale separations (see Dotti et al. 2012, for a review). For example, in non-axisymmetric or rotating stellar systems the loss cone refilling timescale is much shorter than in spherical systems (e.g., Gerhard & Binney 1985; Berczik et al. 2006; Berentzen et al. 2009; Preto et al. 2011), such that even SMBH pairs with mass ratios $q = 0.1$ may merge within a Hubble time (Khan et al. 2012). And of course, most galaxies are not collisionless; gas in the galactic center may form a circumbinary disk, in which case gravitational torques from the disk may remove sufficient angular momentum from the binary to allow efficient merging in as little as $10^6 - 10^7$ yr (e.g., Escala et al. 2005; Mayer et al. 2007; Dotti et al. 2007; Callegari et al. 2009; Roedig et al.

2012). As the binary evolution proceeds, these torques between the binary and disk clear most of the gas from the central disk region, creating a circumbinary gap. Further binary evolution is driven by the outward transfer of angular momentum to the disk as well as by SMBH accretion from streams of gas flowing through the inner disk edge.

SMBH mergers are among the most energetic events in the Universe. An amount of energy equivalent to up to 10% of the progenitor BH mass can be released in gravitational waves during the merger event (e.g., Lousto et al. 2010a). These events could be detected at arbitrarily high redshifts with future space-based GW observatories (e.g., Amaro-Seoane et al. 2012). Pulsar timing arrays (PTAs, Hobbs et al. 2010) could detect SMBH mergers out to $z \sim 1.5$ (e.g., Sesana et al. 2007; Tanaka et al. 2011). Detections of SMBH mergers would serve as direct probes of gravity in the strong-field regime, and if electromagnetic (EM) counterparts to the GW events could be identified, the combination would provide an exquisitely precise measurement of cosmological parameters. Moreover, if the GW emission from the merger is asymmetric, as is expected for astrophysical mergers with unequal mass ratios or spins, the remnant SMBH will receive a recoil kick in the opposite direction (Peres 1962; Bekenstein 1973; Fitchett 1983).

Numerous attempts were made to calculate the gravitational waveforms and recoil kick velocities from BH mergers by extrapolating from the inspiral or post-merger "ringdown" phases (e.g., Favata et al. 2004; Blanchet et al. 2005; Damour & Gopakumar 2006). However, the strongest GW emission and the dominant contribution to the recoil kick occur during the final plunge and merger – a highly nonlinear regime. Attempts to simulate BH mergers using full general relativity were for many years characterized by when, not if, the codes would crash during the inspiral (see Centrella et al. 2010, for a

review).

This changed in 2005, when a series of breakthroughs in numerical techniques finally allowed for full numerical relativity (NR) simulations of BH inspiral, merger, and recoil (Pretorius 2005; Baker et al. 2006; Campanelli et al. 2006). Soon thereafter, it was discovered that recoil velocities could be up to thousands of km s^{-1}, with a maximum velocity of ~ 5000 km s^{-1} (Campanelli et al. 2007a,b; González et al. 2007b; Lousto & Zlochower 2011a). This means that GW recoils may actually eject SMBHs from their host galaxies altogether in some cases. While only a small portion of the parameter space of SMBH mergers has been explored thus far, fitting formulae for the probability distributions of remnant kick velocities, masses, and spins based on these empirical results have reached good convergence (Baker et al. 2008; van Meter et al. 2010; Lousto & Zlochower 2009; Lousto et al. 2012).

Still quite uncertain, however, are the distributions of progenitor BH masses, spins, and spin orientations. SMBH pairs with small mass ratios ($q \ll 0.1$) are unlikely to result in SMBH mergers, as the dynamical friction timescale for inspiral should exceed the Hubble time. Numerous studies have modeled SMBH binary mass ratio and spin evolution in a cosmological framework, though such models necessarily depend on a number of assumptions about SMBH evolution and merger timescales (e.g., Volonteri et al. 2003, 2005; Berti & Volonteri 2008; Barausse 2012). The progenitor BH spin orientations are still more uncertain. Bogdanović et al. (2007) suggested that if the SMBHs are embedded in a circumbinary gas disk prior to merger, gas torques may align or partially align their spins. In the case of perfectly aligned spins, the maximum recoil velocity is < 200 km s^{-1}. BH binaries in stable, non-star-forming disks can align efficiently to within $\sim 10^\circ$ (Perego et al. 2009; Dotti et al. 2010). King et al.

(2008) suggest that rapid star formation may occur in circumnuclear disks, resulting in a clumpy, turbulent medium rather than a coherent gas flow that would efficiently align the SMBH spins. However, recent simulations by Maio et al. (2012) indicate that spin alignment in gaseous disks may be efficient even in the presence of ongoing star formation. Additionally, GR precession effects can preferentially align BH spins, though the same mechanism can preferentially *anti*-align the spins, yielding larger recoil velocities (Kesden et al. 2010; Berti et al. 2012). Interestingly, recent results by Lousto & Zlochower (2011a) indicate that the maximum kick velocity is not only higher than previously thought, it also occurs for partially-aligned spins (within $\sim 50^\circ$).

One can therefore estimate the likelihood of large recoil kicks, modulo some assumptions about the pre-merger environment of the SMBHs. In the most optimistic scenario – likely most relevant to nearly-collisionless or "dry" galaxy mergers – the progenitor SMBH spins are randomly oriented. If one additionally assumes that the SMBH spins are large ($a = 0.9$) and consider mass ratios of $0.1 < q < 1$, then more than 2/3 of BH mergers will result in a kick > 500 km s^{-1}, and more than 1/3 of kicks will be > 1000 km s^{-1} (e.g., van Meter et al. 2010). Lousto et al. (2012) find that if spin alignment is efficient to within 10° and a cosmologically-motivated distribution of mass ratios between 0 and 1 is assumed, these fractions become $\sim 6\%$ and $< 1\%$, respectively.

1.3 Observable Signatures of Gravitational-Wave Recoil

The possibility of large GW recoil kicks implies that some SMBHs may spend substantial time in motion and off-center from their host galaxies. Much effort in the last few years has been devoted to exploring the observable signatures of recoiling SMBHs and searching for possible candidates.

If a SMBH is actively accreting at the time of the recoil kick, it will carry along a portion of its accretion disk and may appear as an offset AGN (Madau & Quataert 2004). In essence, the gas with orbital speed $v_{\rm orb} > v_{\rm k}$ will remain bound to the recoiling SMBH (Loeb 2007). Thus, the SMBH can retain its inner accretion disk and broad line region (BLR), while leaving behind gas at larger radii, including the narrow-line region (NLR). This could produce shifted broad lines with respect to stellar absorption lines or narrow emission lines at the redshift of the host galaxy. If the AGN travels far enough from the galactic center before exhausting its fuel supply, it could also be observed as a spatially offset AGN.

Other possible signatures of recoiling SMBHs have been proposed as well. A small cusp of stars should remain bound to the SMBH after it is kicked, which could be observed as a dense globular cluster with unusually large velocity dispersion (O'Leary & Loeb 2009, 2011; Merritt et al. 2009). A recoil kick can also increase the rate of stellar tidal disruptions (Komossa & Merritt 2008b; Stone & Loeb 2011a), particularly if the SMBH remains bound to the galaxy and makes multiple orbits through the galactic center (Stone & Loeb 2011b). Both of these signatures have the advantage that they

do not require the presence of gas, and thus they could be the only means of detecting recoiling SMBHs that have exhausted their bound accretion disk, or those that occur in dry mergers. Additionally, Boylan-Kolchin et al. (2004) and Gualandris & Merritt (2008) find that in collisionless systems, repeated central passages by recoiling SMBHs may scour out a large stellar core (i.e., a central region with a shallow density profile), indicating that ellipticals containing unusually large cores could provide indirect evidence for a past history of GW recoil.

Prompt EM counterparts to GW recoil events—i.e., those that occur on timescales of months or years after the SMBH merger—may also be detectable (see Schnittman 2011, for a review). An X-ray afterglow may be produced as the circumbinary gap around the merged SMBH evolves inward on a viscous timescale (Milosavljević & Phinney 2005; Tanaka & Menou 2010). Also, the recoil kick perturbs the accretion disk that is ejected with the SMBH, causing shocks that may produce observable EM flares (Megevand et al. 2009; Anderson et al. 2010). Shocks may also be created when the gas that is marginally bound to the SMBH is perturbed and falls back onto the galactic disk, which could produce infrared or X-ray flares (Lippai et al. 2008; Shields & Bonning 2008; Schnittman & Krolik 2008). Furthermore, recent numerical relativity simulations of BH mergers in the presence of EM fields, test particles, or an ideal fluid indicate that the BH merger event itself may induce EM flares or even jets in the surrounding medium (Palenzuela et al. 2010; Farris et al. 2011; Moesta et al. 2011; Bode et al. 2012).

Prior to the advent of a GW observatory capable of detecting SMBH mergers, searches for GW recoil candidates will be focused on long-lived rather than prompt signatures of recoil. In particular, recent studies have searched for kinematically- or spatially-offset AGN. Bonning et al. (2007) conducted a systematic search for offset BLs

in SDSS quasars, finding a null result for offsets > 800 km s^{-1}. However, Komossa et al. (2008) identified an SDSS quasar with a BL offset of 2650 km s^{-1} and proposed it as a candidate recoiling AGN. Others suggested that it might be a close binary SMBH (Dotti et al. 2009; Bogdanović et al. 2009) or a superposition of two AGN (Heckman et al. 2009; Shields et al. 2009a), though to date none of these theories have been confirmed (Decarli et al. 2009; Vivek et al. 2009; Komossa 2012). In the meantime, a handful of other recoiling AGN candidates have been identified via either spatial offsets (Batcheldor et al. 2010; Jonker et al. 2010), spectral offsets (Shields et al. 2009b; Robinson et al. 2010), or both (Civano et al. 2010, 2012). Alternative explanations exist for all of these candidates, so dedicated follow-up studies will be required to confirm their nature.

A major goal of this thesis is to provide a sound theoretical basis for the observable signatures of recoiling SMBHs. In Chapter 2, we use semi-analytic models to study the dynamics of recoiling SMBHs in a galactic potential, demonstrating that even bound recoiling SMBHs may wander through their host galaxies for $\sim 10^9$ yr before settling back to the center. We also follow the accretion histories of these kicked SMBHs and their active lifetimes as offset AGN. We show that although recoil can disrupt "traditional" AGN feedback processes. the limited fuel supply of a recoiling AGN acts as an alternate means of self-regulating its growth.

In Chapter 3, we build upon these results substantially by using smoothed particle hydrodynamics (SPH) simulations with GADGET-3 (Springel et al. 2005b) to model recoiling SMBHs in realistic, evolving merger remnants. Specifically, we simulate galaxy mergers from first infall through final coalescence and impart a recoil velocity to the resultant SMBH at the time of SMBH merger. We conduct a large parameter study in which we vary the merger model parameters and the recoil velocities, allowing us to

study systematic trends in the evolution of recoiling SMBHs. Our results demonstrate the crucial role of gas dynamics in determining recoil trajectories. We also show that kinematically- and spatially-offset AGN may be observable for tens of Myr, for a fairly wide range of kick speeds, and that recoil events can either decrease *or increase* the total AGN lifetime.

Chapter 3 also explores another important question regarding GW recoil: what effects do recoil events have on the host galaxies, and on the local BH-bulge relations? Several studies have examined the implications of GW recoil for the retention of SMBHs in high-redshift galaxies, where escape speeds are generally lower than in the local Universe. The discovery of massive quasars at $z \sim 6$, less than 10^9 years after the Big Bang, places stringent constraints on the formation efficiency of SMBHs (e.g., Fan et al. 2001, 2003), and this situation is exacerbated by the possibility that SMBH might be ejected form their hosts during mergers. Specifically, the formation of quasars at $z = 6$ implies that SMBH growth at high redshift occurs in only highly-biased halos (Volonteri & Rees 2006), or that SMBH seeds are relatively massive (Sijacki et al. 2009).

By modeling individual galaxy mergers rather than following hierarchical growth in a cosmological framework, our approach allows us to follow in detail the trajectories and AGN light curves of both bound and ejected recoiling SMBHs, at the expense of statistical power. We demonstrate in Chapter 3 that recoiling SMBHs may be up to ~ 5 times less massive than their stationary counterparts, and that individual recoil events contribute to scatter in the $M_{\rm BH} - \sigma_*$ relation, even when they are not ejected entirely from the galaxy. In addition, the removal of AGN feedback from the central galactic region delays the quenching of star formation, particularly in gas-rich mergers, resulting in a higher stellar mass and a denser cusp in the remnant.

The observable signatures of GW recoil are discussed further in Chapter 5, where we focus on the special case of CID-42, the only GW recoil candidate with evidence for both spatial *and* spectroscopic offsets (Civano et al. 2010). We use similar hydrodynamic methods to model CID-42 as a late-stage merger remnant and to constrain the possible parameters of the GW recoil scenario.

1.4 Observable Signatures of Supermassive Black Hole Pairs

In addition to the recent focus on GW recoil candidates, there has been renewed interest in identifying SMBH pairs. It has long been hypothesized that binary SMBHs could exhibit observable signatures distinguishing them from their solo counterparts (Begelman et al. 1980). However, promising binary SMBH candidates have proved to be quite elusive. The blazar OJ287 has a quasi-periodic light curve that has been proposed to arise from the orbital motion of a sub-parsec binary SMBH (e.g., Sillanpaa et al. 1988; Lehto & Valtonen 1996; Valtonen et al. 2008), though this interpretation relies on a detailed model of the jet and accretion physics. Another SMBH binary candidate, SDSS J153636.22+044127, exhibits two broad emission line systems, which could indicate orbital motion on sub-parsec scales (Boroson & Lauer 2009). Recently, Tsalmantza et al. (2011) have identified nine binary SMBH candidates in SDSS data based on spectral models of unusual BL profiles. Similarly, Eracleous et al. (2011) identified a population of 88 quasars with offset BLs in SDSS, and found 14 candidates for which significant motion of the line centroid was detected over several years, as would be expected for

sub-parsec binaries with orbital periods of this order. However, hydrodynamic processes such as outflows could also produce acceleration of BL gas, so at a minimum, a strong candidate binary SMBH requires that such motion be demonstrably periodic. In general, because SMBH binary candidates with separations $\ll 1$ pc are not spatially resolvable, their interpretations rely on accurate modeling quasar fueling and binary motion in an evolving galaxy merger remnant – a highly nontrivial task.

Exactly one confirmed binary SMBH is known; the radio galaxy 0402+379 has a separation of 7.3 parsec and thus falls in the hard binary regime. It was identified by Rodriguez et al. (2006) via VLBA imaging of a pair of compact nuclei, with one apparently emitting jets. In an effort to find more such objects, Burke-Spolaor (2011) analyzed over 3000 archival VLBI images but found no additional candidate binary SMBHs. This is a strong indication that binary radio-loud AGN are quite rare.

At kpc-scale separations, SMBH pairs are not gravitationally bound, but they are generally spatially resolvable, which has led to the serendipitous discovery of several dual AGN (Komossa et al. 2003; Bianchi et al. 2008; Green et al. 2010; Koss et al. 2011b). One candidate was recently discovered with a separation of only ~ 150 *parsec* (Fabbiano et al. 2011). However, this handful of candidates represents only a small fraction of the dual SMBHs that should exist within a hierarchical growth model for structure formation. One idea that has gained recent attention is that double-peaked narrow lines with velocity separations of a few hundred km s^{-1} could indicate SMBH orbital motion on kiloparsec scales, assuming each SMBH has a distinct, active NLR (e.g., Heckman et al. 1981; Zhou et al. 2004; Gerke et al. 2007). Comerford et al. (2009b) conducted a search for such signatures in the DEEP2 survey of AGN, which benefitted from the high spectral resolution of the DEIMOS spectrograph. They found two double-peaked NL

(dNL) AGN in a sample of 91 objects. Interestingly, they also found that nearly 50% of the AGN had *offset* NLs that they argue cannot easily be explained by outflows; some of these could indicate kpc-scale SMBH pairs in which only one SMBH is active.

Soon thereafter, two groups conducted similar surveys of Type I (Smith et al. 2010) and Type II (Liu et al. 2010b) AGN in SDSS. Despite their different selection criteria, both surveys found that $\sim 1\%$ of AGN have dNLs, which is also consistent with the results of Comerford et al. (2009b). These surveys, and subsequent follow-up observations, have focused solely on dNLs, rather than offset NLs, as the latter population are likely more contaminated with AGN outflows or other NLR kinematics. Even within the population of dNL AGN, only a fraction are expected to contain dual SMBHs. Still, this sample of over 300 dNL AGN has vastly increased the number of candidates.

Thus far, the results from follow-up observations are quite promising. Numerous strong candidates have been identified by combining long-slit or integral field unit (IFU) spectra with high-resolution imaging (Liu et al. 2010a; Shen et al. 2011; Fu et al. 2011b; McGurk et al. 2011). Specifically, strong dual AGN candidates are those in which a spatial offset detected in the 2D or IFU spectrum coincides with spatially-resolved dual brightness peaks in the image. At least 10% of dNL AGN fall into this category (Shen et al. 2011). Other follow-up studies have identified dNL AGN with disturbed host galaxy morphology indicative of recent merger activity (Fu et al. 2011a; Rosario et al. 2011). (Comerford et al. 2011b) find that *all* of the slit spectra analyzed for a large sample of dNL AGN have spatially-separated emission components, though 42% of objects have extended emission indicating that their double-peaked spectra are more likely due to outflows. Finally, the detection of dual compact X-ray sources in one object (Comerford et al. 2011a) and dual compact radio sources in another (Fu et al. 2011c)

provide much more concrete evidence for the presence of two AGN in these systems than is possible with optical and near-infrared observations alone.

While it is already is clear that the spectroscopic technique of selecting dNL AGN is an effective means of identifying dual AGN candidates, much work remains to be done to confirm or rule out the presence of dual SMBHs in these objects. In particular, the idea that double-peaked signatures are produced by two NL AGN orbiting on kiloparsec scales was heretofore untested by theoretical models. In Chapter 4, we address this issue directly by bridging the gap between photoionization models for NL AGN, which are generally applied to static environments, and galaxy merger models, which have not considered photoionization or kinematics of NL gas. We develop the first semi-analytic model for the NLR in hydrodynamic simulations of galaxy mergers, with the aim of understanding the origin of dNL AGN and their relationship to SMBH pairs.

Using our model, we show that dNL AGN induced by dual SMBH motion naturally result from the late stages of gas-rich galaxy mergers, though they are short-lived. The majority of dNL AGN arise from gas kinematics such as rotation, even within the kiloparsec-scale phase of evolution. However, many of these dNL profiles may be *influenced* by SMBH motion via altered peak ratios or overall velocity offsets. We discuss the dependence of dNL AGN lifetimes on factors such as viewing angle and the host galaxy properties. Finally, we identify several characteristics of dNL AGN induced by dual SMBH motion, such as large dNL velocity splittings, overall velocity shifts, and spatial alignment with the apparent ellipticity of the host galaxy, which may aid in identifying the true dual SMBHs in the dNL AGN sample. Because we find that dNL AGN arise from a heterogeneous population with no single definitive signature for SMBH pairs, we conclude that multiple diagnostics and multi-wavelength follow-up observations

are critical for confirming dual AGN candidates.

Iin Chapter 5 we examine a single unique source: the galaxy COSMOS J100043.15+020637.2, or CID-42. Initially discovered serendipitously by Comerford et al. (2009a) in the *HST*-COSMOS survey, this object has an unusual morphology including a prominent tidal tail and two well-resolved optical brightness peaks in its center, separated by ~ 2.5 kpc. Initial spectral analysis indicates the presence of double-peaked NLs, leading Comerford et al. (2009a) to propose this source as a candidate kpc-scale dual AGN. However, Civano et al. (2010) presented additional spectra in which a *broad-line* offset was detected, with $\Delta v \sim 1300$ km s^{-1}. This is too large to be explained by SMBH orbital motion on kiloparsec scales, but BL/NL offsets are a signature expected from recoiling AGN. Thus, Civano et al. (2010) suggested that CID-42 might contain one brightness peak corresponding to a recoiling AGN and the other to the empty stellar cusp left behind. More intriguingly, high-resolution *Chandra* imaging demonstrates that only one of these optical brightness peaks (the purported recoiling AGN) is an X-ray source (Civano et al. 2012).

We apply the hydrodynamic simulation methods of Chapters 3 & 4 to develop models for both the recoiling and dual AGN scenarios for CID-42. We additionally use the three-dimensional, polychromatic dust radiative transfer code SUNRISE to estimate the attenuation and emergent SEDs for each model. Our models are consistent with the observed morphology as well as the inferred stellar mass, star formation rate, and SMBH luminosity of this object. While the current data do not allow us to rule out either scenario, we are able to constrain the required parameters for a GW recoil event or SMBH pair in CID-42. For example, an important diagnostic for the recoil scenario will be to determine the origin of the observed NL emission, which seems to require either

a very rapidly-recoiling AGN observed just after the kick or an unusual star forming region. Similarly, the dual SMBH scenario requires the combination of a Compton-thick AGN with an unobscured AGN that additionally has an atypically large BL velocity shift, so spatially-resolved spectroscopy will be key to determining the likelihood of this scenario as well.

Chapter 2

Effects of Gravitational-Wave Recoil on the Dynamics and Growth of Supermassive Black Holes

L. Blecha & A. Loeb *The Monthly Notices of the Royal Astronomical Society*, Vol. 390, pp. 1311-1325, 2008

Abstract

Simulations of binary black hole mergers indicate that asymmetrical gravitational wave (GW) emission can cause black holes to recoil at speeds up to thousands of km s^{-1}. These GW recoil events can dramatically affect the coevolution of recoiling supermassive black holes (SMBHs) and their host galaxies. However, theoretical studies of SMBH-galaxy evolution almost always assume a stationary central black hole. In

light of the numerical results on GW recoil velocities, we relax that assumption here and consider the consequences of recoil for SMBH evolution. We follow the trajectories of SMBHs ejected in a smooth background potential that includes both a stellar bulge and a multi-component gaseous disk. In addition, we calculate the accretion rate onto the SMBH as a function of time using a hybrid prescription of viscous (α-disk) and Bondi accretion. We find that recoil kicks between 100 km s^{-1} and the escape speed cause SMBHs to wander through the galaxy and halo for $\sim 10^6 - 10^9$ yr before settling back to the galactic center. However, the mass accreted during this time is roughly constant at $\sim 10\%$ of the initial mass, independent of the recoil velocity. This indicates that while large recoils may disrupt active galactic nuclei feedback processes, recoil itself is an effective means of regulating SMBH growth. Recoiling SMBHs may be observable as spatially or kinematically offset quasars, but finding such systems could be challenging, because the largest offsets correspond to the shortest quasar lifetimes.

2.1 Introduction

Supermassive black holes (SMBHs, $\gtrsim 10^6$ M$_\odot$) have long been considered the probable central engines for quasars (Lynden-Bell 1969). Observations now indicate that they are ubiquitous in the centers of both active and quiescent galaxies (e.g. Kormendy & Richstone (1995); Richstone et al. (1998); Ferrarese & Ford (2005)). Considerable evidence links SMBHs closely to dynamical properties of their host galaxies, indicating that SMBHs and galaxies may have evolved concurrently. Measured SMBH masses are closely correlated with the luminosity, and hence the mass, of their host galactic bulges (Kormendy & Richstone 1995; Magorrian et al. 1998; Marconi & Hunt 2003; Merritt &

Ferrarese 2001). Also, a strong correlation has been observed between SMBH mass and stellar velocity dispersion in the bulge: $M_{\rm BH} \propto \sigma_*^4$ (Gebhardt et al. 2000; Ferrarese & Merritt 2000; Tremaine et al. 2002a).

These findings indicate that SMBHs offer a wealth of information about the formation and evolution of structure in our universe. In this context, much theoretical work has been devoted to studying the details of SMBH accretion and how it relates to galaxy evolution (e.g., Silk & Rees 1998; Wyithe & Loeb 2003; Di Matteo et al. 2005; Hopkins et al. 2006a). However, virtually all such studies have one common assumption: that the black hole (BH) remains stationary at the center of the galaxy. This is a reasonable assumption in light of the observed ubiquity of central compact objects in galaxies, although the observed sample contains only local galaxies, so in principle few constraints exist on the dynamics of SMBHs over the lifetimes of galaxies. However, if two SMBHs coalesce after a major galaxy merger, gravitational-wave (GW) recoil can impart a large kick to the resultant merged BH (Peres 1962; Bekenstein 1973; Fitchett & Detweiler 1984). When the merging BHs have unequal masses or spins, asymmetrical emission of gravitational waves creates a net linear momentum flux at merger, causing the merged BH to recoil in the opposite direction. This effect has long been known as an interesting relativistic phenomenon, but its importance as an astrophysical phenomenon remained very uncertain until recently; the best estimates from approximate methods indicated that kick velocities were most likely to be small, $v_{\rm k} \lesssim$ few $\times$ 100 km s^{-1} (Blanchet et al. 2005; Damour & Gopakumar 2006). Results from simulations using full numerical relativity have demonstrated that if high BH spins are included, kicks up to 4000 km s^{-1} are possible with certain mass and spin configurations (Campanelli et al. 2007a,b). These velocities easily exceed the escape speed of any known galaxy, so the

ramifications of large recoil kicks would clearly be dramatic. Not only will the position of the BH in the galaxy vary, but also the rate of fueling and the amount and type of active galactic nucleus (AGN) feedback generated. For example, according to the Bondi accretion model, which is commonly used in simulations, the accretion rate is inversely proportional to the velocity of the accretor cubed (Bondi & Hoyle 1944).

The velocity of recoil kicks depends strongly on the spin parameters, spin alignment, and mass ratio of the merging BHs. The distributions of these quantities in the population of merging galaxies are highly uncertain. Bogdanović et al. (2007) have suggested that torques in a circumbinary gas disk may align the BH spins with the disk orbital plane, causing the recoil distribution to be skewed toward in-plane kicks (and consequently low kick velocities). Schnittman & Buonanno (2007), Campanelli et al. (2007a), & Baker et al. (2008) have each calculated probability distributions of recoil kick velocities assuming randomly distributed BH mass ratios and spin orientations. We allow for both aligned and random spins by considering a variety of kick inclinations. Observing signatures of GW recoil in the future would be one way to constrain these distributions.

A common result of early SMBH merger simulations was the so-called "final parsec problem", whereby inspiralling SMBHs "stall" at a characteristic radius of about a parsec after hollowing out the host galaxy's core and before gravitational wave (GW) emission becomes dominant (e.g., Milosavljević & Merritt 2001; Yu 2002). This has been referred to as a "problem" because until very recently (see Rodriguez et al. 2006), no direct evidence for any such unmerged binary SMBHs existed, let alone a large population of them. Numerous viable solutions to this problem have been introduced, for example by adding a slightly triaxial potential or a nonnegligible gas fraction (e.g., Gerhard &

Binney 1985; Yu 2002; Berczik et al. 2006; Escala et al. 2004; Gould & Miralda-Escude 1997). It is certainly possible, however, that in "dry" mergers of galaxies containing small gas fractions, the SMBH inspiral time would exceed the time for another major merger to occur. This could result in formation of a triple SMBH system, which may impart a significant kick to one of the BHs (e.g., Hut & Rees 1992; Xu & Ostriker 1994). Recently, the first fully relativistic simulations of close triple-BH encounters demonstrated that substantial kicks can indeed occur (Campanelli et al. 2008). Using non-relativistic simulations, Hoffman & Loeb (2007) conducted a statistical analysis of the triple-SMBH problem; they found that most three-body encounters cause the binary BH to merge without ejecting the third BH, and that ejection of the third BH (which may also be followed by the merger of the other two) occurs in less than half of all encounters. It should be noted that if triple-SMBH systems do form in galaxies and if the most likely outcome is an SMBH merger, then GW recoil kicks could be at least as likely to result from this configuration as dynamical kicks to the third BH.

Madau & Quataert (2004) and Loeb (2007) have considered some of the observational signatures we might expect from these sources, such as spatially and kinematically offset quasars. These could be either SMBHs that are ejected from their host galaxies and carry an accretion disk along, or wandering SMBHs on bound trajectories that may significantly disrupt galactic structure. Because no known quasars have been conclusively identified as such, we can assume the fraction of offset quasars is relatively small. Similarly, Volonteri (2007) considered the limits placed on ejected BHs by the $M_{\rm BH} - \sigma_*$ relation. She concluded that ejection of SMBHs could not have been a very common occurrence throughout most of the history of the universe, or we would observe considerably more scatter in BH-galaxy relations. However, Volonteri points out that

in large halos at high redshift, mergers were more frequent and recoil kicks, which are independent of absolute mass, could more easily have ejected BHs from the relatively small host galaxies.

Gualandris & Merritt (2008) studied GW recoil with a set of N-body simulations following the motion of a kicked SMBH in a stellar potential. They find that BHs on bound orbits have long oscillation timescales, up to ~ 1 Gyr, including a phase of low-amplitude oscillations in the stellar core. A large stellar core is scoured out by these oscillations, in some cases larger than the cores that binary SMBHs are expected to produce. Gualandris & Merritt (2008) also discuss the possible observational signatures of such oscillating BHs, such as displaced AGN and offset jets.

In a recent paper, Kornreich & Lovelace (2008) have focused on a different aspect of GW recoil, namely its effect on galaxy morphology. Using GADGET-2, they also find that BHs on bound orbits have long oscillation timescales and conclude that recoil events can produce significant asymmetry in galactic disks. We note, however, that by definition, any galaxy containing a recoiling SMBH will have recently undergone a merger, which will also produce asymmetric morphology.

Magain et al. (2005) discovered a quasar with no apparent host galaxy located near an Ultra-Luminous Infrared Galaxy (ULIRG), which had likely undergone a recent merger. A number of papers discussed whether this might be an ejected SMBH (Haehnelt et al. 2006; Merritt et al. 2006; Hoffman & Loeb 2006). This does not appear to be the case for this system, however. Among other factors, the quasar has a significant narrow-line region indicating the presence of more gas than could be ejected with the SMBH, and recently, direct evidence for a host galaxy has been observed (Feain et al.

2007).

While this paper was undergoing revision, Komossa et al. (2008) announced that the quasar SDSSJ0927+2943 is a candidate recoiling SMBH with a velocity of 2650 km s^{-1}. They have observed an offset between the broad emission lines and some of the narrow emission lines in this unusual quasar's spectrum, which they suggest can be explained if the broad line region is gravitationally bound to a recoiling BH and the narrow line region is left behind in the galactic disk. 2650 km s^{-1} is close to the maximum possible recoil kick velocity, and the actual velocity may be even higher if there is a velocity component perpendicular to the line of sight. Thus, this proposed recoil event is certainly not a typical event.

Bonning et al. (2007) conducted a targeted search for GW recoil events. They examined a quasar population for Doppler shifts in spectral lines that would indicate a moving source and found a null result. However, this method applies only to high-velocity BHs that are active quasar sources. Additionally, because a BH on a bound trajectory spends a large fraction of its time at turnaround, such objects are statistically more likely to be observed with low velocities.

In this paper, we focus on the dynamical aspect of SMBH accretion in the context of large kicks from GW recoil. We emphasize that the details of BH accretion occur on scales below the current resolution of state-of-the-art simulations of galaxy mergers, and that the physics of turbulent viscosity driving this accretion cannot be simulated easily. Thus, a semi-analytic approach is an appropriate first step toward understanding accretion onto recoiling BHs. We use a set of semi-analytical models to follow the trajectories of SMBHs ejected with varying kick velocities in the potential of a galaxy

containing both gas and stellar components; we also estimate the accretion rate for the moving SMBHs. Our model and choice of parameters are outlined in § 2.2. The results of these calculations for our fiducial model are given in § 2.3.1, while § 2.3.2 & 2.3.3 detail the results of varying the SMBH mass and galaxy gas fraction. In § 2.3.4, we consider the implications of our results for observational signatures of GW recoil. § 2.3.5 contains comments on the sensitivity of our results to our choice of parameters. Finally, in § 2.4 we summarize and discuss these results in the broader context of SMBH-galaxy coevolution.

2.2 Model

We construct a galaxy model consisting of two distinct components: a spherical stellar bulge and a gaseous disk. Note that in reality, the stellar and gas distributions may be highly asymmetric following a major merger. Choosing symmetric distributions is therefore a simplification necessary for our semi-analytical approach, although if the SMBH merger timescale is long, the galaxy may in fact be significantly relaxed when the recoil occurs. The dark matter (DM) halo is ignored for the purpose of following SMBH orbits, because the halo profile will be fairly flat on the scale of the baryonic galaxy. Also, on large scales the halo is expected to be significantly triaxial (Jing & Suto 2002; Bullock et al. 2001), so even though the DM halo would decrease the SMBH orbital decay time, it would also increase the chance of scattering the BH onto a less-centrophilic orbit, such that the BH would wander in the halo instead of returning to the galaxy center. The details of this scattering are highly dependent on the shape of the triaxial potential, so we ignore this effect and consider it a source of uncertainty in our high-velocity recoil

runs.

2.2.1 Stellar bulge

The stellar bulge is assumed to follow an η-model density profile (Tremaine et al. 2002b) with $\eta = 2.5$. We choose this profile that is slightly flatter than a Hernquist (1990) profile ($\eta = 2$) under the assumption that a galaxy merger remnant will have a flattened core due to stellar ejections during SMBH binary inspiral. The total stellar bulge mass is estimated from the SMBH mass using the relation of Marconi & Hunt (2003),

$$M_* = 4.06 \times 10^{10} \mathrm{M}_\odot \left(\frac{M_{\mathrm{BH}}}{10^8 \mathrm{M}_\odot} \right)^{1.04}. \tag{2.1}$$

The scale radius, a, for the η-model profile is related to the SMBH mass in terms of the half-mass radius, $r_{1/2}$,

$$a = r_{1/2}(2^{1/\eta} - 1). \tag{2.2}$$

An approximate relation for the ratio of effective (half-light) radius to half-mass radius is given by Dehnen (1993, Eq. (17))

$$\frac{R_{\mathrm{e}}}{r_{1/2}} \approx 0.7549 - 0.00439(3-\eta) + 0.00322(3-\eta)^2 - 0.00182(3-\eta)^3 \pm 0.0007. \tag{2.3}$$

The effective radius is $R_{\mathrm{e}} = GM_*/3\sigma_*^2$, and the one-dimensional velocity dispersion, σ_*, is calculated from the $M_{\mathrm{BH}} - \sigma_*$ relation (Tremaine et al. 2002a),

$$\sigma_* = 220\,\mathrm{km\,s^{-1}} \left(\frac{M_{\mathrm{BH}}}{2 \times 10^8 \mathrm{M}_\odot} \right)^{0.249}. \tag{2.4}$$

Thus, the scaling of the stellar model radii with BH mass is (R_{e}, $r_{1/2}$, a) $\propto M_{\mathrm{BH}}^{1/2}$.

Stellar dynamical friction on the ejected SMBH is modeled using the Chandrasekhar (1943) formula. Assuming a Maxwellian velocity distribution, the drag force on a BH

moving with velocity $v_{\rm BH}$ through a background density ρ_* is:

$$\mathbf{f}_{\rm df} = -I(\mathcal{M}) \times \frac{4\pi\rho_*(GM_{\rm BH})^2}{\sigma_*^2}\frac{\mathbf{v}_{\rm BH}}{v_{\rm BH}}, \tag{2.5}$$

where

$$I(\mathcal{M}) = \frac{\ln(\Lambda)}{\mathcal{M}^2}\left(\mathrm{erf}\left(\frac{\mathcal{M}}{\sqrt{2}}\right) - \sqrt{\frac{2}{\pi}}\mathcal{M}e^{-\mathcal{M}^2/2}\right), \tag{2.6}$$

and the Mach number $\mathcal{M} \equiv v_{\rm BH}/\sigma_*$. We use 3.1 for the Coulomb logarithm $\ln(\Lambda)$ (Escala et al. 2004; Gualandris & Merritt 2008).

2.2.2 Gaseous disk component

In addition to a stellar bulge, most galaxies will contain a significant gaseous component. This is especially true of merger remnants, as mergers are more frequent between galaxies at high redshift, where gas fractions are generally higher. We assume that by the time a SMBH binary has merged in the galaxy center, the gas has cooled into a disk. For our fiducial model, we assume the disk mass is determined by the gas fraction $f_{\rm gas} \equiv M_{\rm disk}/M_* = 0.5$, such that the galaxy is relatively gas-rich.

Disk structure

Analytical models of disk structure generally fall into two distinct categories: SMBH-dominated, viscosity-driven accretion disks (i.e., α-disks) with $M_{\rm disk} \ll M_{\rm BH}$, and self-gravitating, star-forming galactic disks with $M_{\rm disk} \gg M_{\rm BH}$. The intermediate regime, $M_{\rm disk} \sim M_{\rm BH}$, is less straightforward to model analytically and is seldom resolved by hydrodynamical simulations. This regime also defines the SMBH radius of influence, $r_{\rm infl}$, through the relation $M_{\rm disk}(< r_{\rm infl}) = 2M_{\rm BH}$. Goodman (2003) & Goodman & Tan (2004)

discuss the issue of self-gravitating accretion disks, though they focus on scales of $\lesssim$ pc where the disk is still nearly Keplerian (as in our Zone II, defined below). Thompson et al. (2005) conduct a more detailed analysis of this problem all the way to the BH radius of influence using a semi-analytical model of the disk structure that includes dust; this is a more involved approach than is necessary for the scope of our paper.

In addition to seeking a simpler disk model, we address the more general question of whether a purely analytic disk solution can be constructed for the entire region between the self-gravity radius and the BH radius of influence. Solutions have been derived by other authors for various limits, but to our knowledge this is the first attempt to extrapolate these limits to model the entire disk. Our approach is to construct an analytic model of the disk structure at all radii, from the innermost stable circular orbit around the BH to the outer reaches of the galaxy. Because this range incorporates vastly different physical environments that cannot be modeled by a single set of simple equations, we define several regimes separated by critical radii. Fig. 2.1 shows the four concentric "zones" we have defined in this "onion-skin" model. Extending the disk continuously from galactic scales down to the innermost radii is important for calculating the accretion rate and ejected mass for a wide range of recoil velocities. However, we note that BHs kicked out of the disk plane spend a small fraction of their wandering time in the inner disk regions, such that the *dynamics* of these BHs will generally be dominated by the outermost disk region (Zone IV) and the stellar distribution. Thus, our dynamical results are largely independent of the details of the inner disk model described here.

The innermost zone, Zone I, is a standard α-disk (Shakura & Sunyaev 1973). The outer edge of this region, $r_{\rm Q1}$, is defined as the radius at which the disk becomes unstable

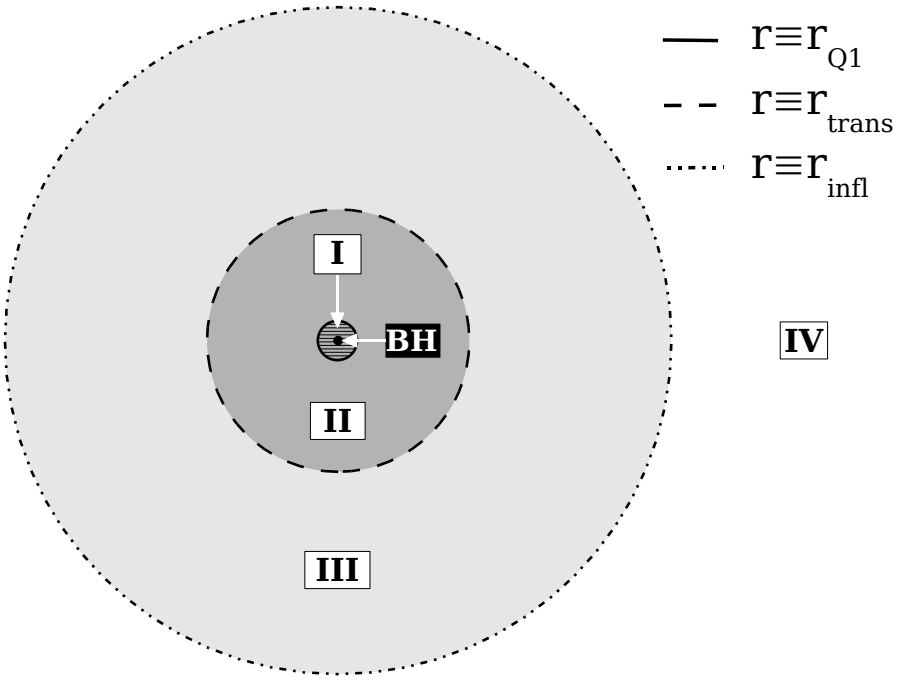

Figure 2.1.—: Schematic face-on diagram of our model for the gaseous galactic disk (not to scale). Zone I is the standard Shakura & Sunyaev (1973) α-disk, marked with horizontal hash-marks. The solid circle denotes the radius $r_{\rm Q1}$. Zone II (shown in dark gray) is the inner (BH-dominated) portion of the self-gravitating accretion disk, while Zone III (shown in light gray) is the outer (disk-dominated) portion of the accretion disk. The transition between the two, $r_{\rm trans}$, is marked with the long-dashed circle. The BH radius of influence, $r_{\rm infl}$, is marked with the dot-dashed circle. Beyond this radius is the exponential disk (Zone IV), which has no defined outer boundary.

according to the Toomre (1964) parameter,

$$Q = \frac{c_{\rm s}\kappa_\Omega}{\pi G\Sigma}, \tag{2.7}$$

where $c_{\rm s}$ is the gas sound speed, $\kappa_\Omega^2 = 4\Omega^2 + r(\partial\Omega^2/\partial r)$ is the epicyclic frequency defined in terms of the rotation angular frequency, Ω, and Σ is the disk surface density. $Q < 1$ corresponds an unstable (i.e., self-gravitating) disk. Following Goodman & Tan (2004), we assume radiation pressure dominates gas pressure at $r \lesssim r_{\rm Q1}$, such that the sound speed is simply given by $c_{\rm s}^2 = 4\sigma_B T^4/3c\rho$, where σ_B is the Stefan-Boltzmann constant. Although radiation pressure dominates in this region, we assume the viscosity scales only with the gas pressure; otherwise the disk may be unstable. From these assumptions one can derive the radius $r_{\rm Q1}$ (Goodman 2003; Goodman & Tan 2004):

$$r_{\rm Q1} \approx 1.5\times10^{-2}\,{\rm pc}\left(\frac{\alpha/0.3}{\mu}\right)^{1/3}\left(\frac{f_{\rm Edd}}{\epsilon_{\rm rad}/0.1}\right)^{1/6}\left(\frac{\kappa}{\kappa_{\rm es}}\right)^{1/2}\times\left(\frac{M_{\rm BH}}{10^8{\rm M}_\odot}\right)^{1/2}. \tag{2.8}$$

Here μ is the mean molecular weight of the gas, $f_{\rm Edd} = \dot{M}_\alpha/\dot{M}_{\rm Edd}$ is the ratio of the α-disk accretion rate to the Eddington rate, $\epsilon_{\rm rad}$ is the radiative efficiency, and the opacity κ is scaled to the electron-scattering value, $\kappa_{\rm es} = 0.4$. We use $\kappa = \kappa_{\rm es}$ in our calculations. For our fiducial parameters, the radius at which the radiation and gas pressures are equal is $r_{\rm peq} \approx r_{\rm Q1}$, and the dependence of $r_{\rm Q1}$ on BH mass is weak; thus, it is reasonable to calculate $r_{\rm Q1}$ assuming that Zone I of the disk is radiation-pressure dominated in general (see Table 2.1). Likewise, for $r > r_{\rm Q1}$ the disk is assumed to be gas-pressure dominated.

The self-gravitating region beyond $r_{\rm Q1}$ will cool and undergo star formation, which will heat the disk via feedback processes. Gas compression and shocks may also form due to gravitational instabilities created when $Q < 1$. It has frequently been argued that these feedback and cooling processes will balance, leaving the disk in a marginally stable

state with $Q \sim 1$ (e.g., Hohl 1971; Paczynski 1978; Bertin 1997). This is supported by results from various simulations (e.g., Gammie 2001; Lodato & Rice 2004). Accordingly, we constrain the disk beyond $r_{\rm Q1}$ to have $Q = 1$, which is effectively an equation balancing heating and cooling processes in the gas. We derive our set of equations using this constraint in place of the equation for balance between radiation and viscous dissipation of orbital energy (see, e.g., Bertin 1997; Bertin & Lodato 1999; Goodman 2003). We retain the assumption of a steady accretion rate via viscous dissipation of angular momentum,

$$\dot{M}_\alpha = 3\pi\nu\Sigma = 3\pi\alpha c_{\rm s} h\Sigma = \text{const}, \tag{2.9}$$

where the viscosity $\nu = \alpha c_{\rm s} h$ is defined according to the α-disk prescription, h is the disk scale height, and the dimensionless constant α is a free parameter, usually assumed to be in the range $\sim 0.01 - 0.1$. Goodman (2003) suggests that for self-gravitating, $Q = 1$ disks, this value may be as high as 0.3. This is the fiducial value we use in our disk calculations. Consumption of gas via star formation in the disk is neglected, such that $\dot{M}$ remains constant, although the energy input from star formation is included indirectly by setting $Q = 1$. We also use the thin-disk approximation, as well the relation $\rho_{\rm g} \equiv \Sigma/2h$ for the gas density.

We construct the intermediate disk regime as follows. Just beyond $r_{\rm Q1}$, the BH still overwhelmingly dominates the gravitational potential. Likewise, at the BH radius of influence, $r_{\rm infl}$, the disk becomes dominated by its own gravitational potential. We use these two limits to define two zones (Zones II & III) in the region $r_{\rm Q1} < r < r_{\rm infl}$: in Zone II the disk contribution to the potential is neglected, and in Zone III the BH term is neglected. The transition radius, $r_{\rm trans}$, is defined where the two density profiles intersect ($\Sigma_{\rm II} = \Sigma_{\rm III}$), thus creating a smooth transition between the two regimes. In the thin-disk,

BH-dominated regime (Zone II), $c_{\rm s} = h\Omega_{\rm BH}$, where $\Omega_{\rm BH}^2 = GM_{\rm BH}/r^3$. The relation for $c_{\rm s}$, along with Eqs. (2.7) & (2.9), can be solved to give expressions for $\Sigma, c_{\rm s}$ and h:

$$\Sigma_{\rm II} = \frac{\Omega_{\rm BH}}{\pi}\left(\frac{\dot{M}_\alpha}{3\alpha G^2 Q^2}\right)^{1/3} \tag{2.10}$$

$$c_{\rm s,II} = \left(\frac{GQ\dot{M}_\alpha}{3\alpha}\right)^{1/3} \tag{2.11}$$

$$h_{\rm II} = \Omega_{\rm BH}^{-1}\left(\frac{GQ\dot{M}_\alpha}{3\alpha}\right)^{1/3}. \tag{2.12}$$

For Zone III, $c_{\rm s}$ is approximated by using only the disk potential term to solve for vertical hydrostatic equilibrium and the radial Poisson equation, giving $c_{\rm s}^2 = 2\pi G\Sigma h$. $\Omega(r)$ similarly is taken to depend only on the disk mass, $M_{\rm disk}$: $\Omega(r)^2 = GM_{\rm disk}(< r)/r^3$. This is the form of $\Omega(r)^2$ for a spherical distribution; using this expression for a disk is initially a simplifying assumption. However, we find a self-consistent solution for a disk with a $1/r$ surface density profile – i.e., a Mestel disk (Mestel 1963). In this special case, the disk's rotation curve exactly equals that of an equivalent spherical distribution, so $\Omega(r)$ is not an approximation. The general equation for the viscous mass accretion rate in a non-Keplerian disk is:

$$\dot{M}_\alpha = 2\pi\nu\Sigma\left|\frac{{\rm d}\ln\Omega}{{\rm d}\ln r}\right| = {\rm const.} \tag{2.13}$$

Eqs. (2.7) & (2.13), along with the sound speed equation, yield the disk quantities for Zone III:

$$\Sigma_{\rm III} = \left(\frac{4}{\pi Q^2}\right)\left(\frac{\dot{M}_\alpha^2}{\alpha^2 G}\right)^{1/3} r^{-1} \tag{2.14}$$

$$c_{\rm s,III} = \left(\frac{G\dot{M}_\alpha}{\alpha}\right)^{1/3} \tag{2.15}$$

$$h_{\rm III} = \frac{Q^2}{8}r. \tag{2.16}$$

This results in an angular velocity $\Omega(r)^2 = (c_{\rm s,III}/h_{\rm III})^2\,(h_{\rm III}/r)$. In a recent review, Lodato (2008) also derives the set of equations for what we call Zone III and defines the radius of transition to a Keplerian disk. Note that his numerical factors differ slightly from ours due to a different definition of the disk scale height.

We model the region beyond $r_{\rm infl}$ (Zone IV) with an exponential profile, $\Sigma_{\rm IV} = \Sigma_0 {\rm e}^{-r/r_{\rm disk}}$, where the scale radius $r_{\rm disk}$ is set by matching $\Sigma_{\rm III}(r_{\rm infl}) = \Sigma_{\rm IV}(r_{\rm infl})$. Σ_0 is obtained by integrating Σ(r) from $r_{\rm infl}$ and equating this to the gas mass beyond $r_{\rm infl}$:

$$\Sigma_0 = \frac{M_{\rm disk}(> r_{\rm infl})}{2\pi r_{\rm disk}^2 \left(\frac{r_{\rm infl}}{r_{\rm disk}} + 1\right) e^{-r_{\rm infl}/r_{\rm disk}}}. \tag{2.17}$$

To calculate the disk gravitational potential at points outside the disk plane, we again use the approximation of spherical symmetry for the gravitational potential, namely, $\partial\Phi/\partial R = GM(< R)/R^2$. However, a perfectly spherically symmetric potential is clearly unphysical given the asphericity of the gas disk. To break this symmetry, we introduce a small elliptical perturbation to the potential by writing the radial coordinate as $\tilde{R} = \sqrt{r^2 + (z/q)^2}$, where $q < 1$ is the axial ratio of an equipotential ellipsoid. This parameter is not intended to accurately reproduce the ellipticity profile of the galactic potential at all radii – in fact, in this approximation the ellipticity is constant at all radii. Instead, it merely allows some precession of the orbits in the $r - z$ plane, as one expects due to torques introduced by the aspherical mass distribution. As a fiducial value in our runs, we choose $q = 0.99$ (i.e, a 1% distortion of the axial ratio). We find that the largest effects due to this perturbation occur for near-escape orbits with $v_{\rm k} \approx v_{\rm esc}$, where the BH reaches the largest radii. This further validates the choice of small q, since in reality the galactic potential will tend toward sphericity at large radii. See § 2.3.5 for further

discussion on the sensitivity of our results to this parameter.

When the SMBH is ejected from the center of the galaxy, it carries with it a portion of the gaseous disk out to a radius $r_{\rm ej}$. This radius can be estimated simply as $r_{\rm ej} = GM_{\rm BH}/(v_{\rm k}^2 + c_{\rm s}^2)$; namely, the gas orbiting the BH with $v_{\rm orb} > v_{\rm k}$ remains bound to the BH as it leaves the galaxy center (Loeb 2007). We thus assume the total mass ejected is $M_{\rm ej} = M_{\rm BH} + M_{\rm disk,ej}$. Another consideration is that numerous studies have found that in hydrodynamical simulations a binary BH with moderate mass ratio (such as would produce large recoils) creates torques on the surrounding gas disk that carve out a circumbinary gap about twice the size of the semimajor axis (Liu et al. 2003; Escala et al. 2005; Milosavljević & Phinney 2005; MacFadyen & Milosavljevic 2006; Hayasaki et al. 2007). As the binary approaches merger, the gravitational-wave merger timescale, $t_{\rm gw}$, decreases rapidly, and the BH orbit decays faster than the hole's viscous timescale to refill, $t_{\rm visc}$. The final gap size at merger is determined by the point at which $t_{\rm gw} << t_{\rm visc}$, which for our models is $\sim 100\, r_{\rm S}$ (Milosavljević & Phinney 2005, $r_{\rm S}$ is the Schwarzschild radius). The disk mass within this radius is negligible, so we can ignore the circumbinary gap in our simulations.

We also assume that the ejected disk leaves a hole in the galactic gas disk of radius $r_{\rm ej}$ in our model. The hole will eventually refill; we assume refilling will take place on the viscous timescale $t_{\rm visc} \sim r^2/\nu = r^2/\alpha c_{\rm s} h$, though we note that Milosavljević & Phinney (2005) have suggested that the hole should refill faster than the viscous timescale. We calculate this timescale in each of our runs, based on the environment at the hole radius $r_{\rm ej}$. For BHs kicked into the disk plane with low velocity, this timescale will be $\gtrsim 10^8$ yr, which in this case is generally longer than $t_{\rm fin}$, the time for the BH to settle back to the center. For out-of-plane kicks, $t_{\rm visc} > t_{\rm fin}$ for low $v_{\rm k}$, when $r_{\rm ej}$ is large. The velocity $v_{\rm k}$

where $t_{\rm visc} = t_{\rm fin}$ depends on the galaxy model and kick inclination, and is $\sim 300 - 400$ km s^{-1} for our fiducial model. We neglect the refilling of the central hole in these cases. However, for larger kick velocities, the hole is very small ($r_{\rm ej} \propto 1/v^2$) and makes little difference to the overall dynamics and accretion of the moving BH.

Gas dynamical friction

When the BH + ejected disk are moving through the galactic disk, gas dynamical friction acts on them in addition to stellar dynamical friction. Ostriker (1999) derived an analytical formula for a body moving through a gaseous medium that has the same form as Chandrasehkar's formula, but with a different function I($\mathcal{M}$) and with $\mathcal{M} \equiv v_{\rm BH}/c_{\rm s}$. This formula provides a fairly accurate estimate of gas drag forces and has been used by many other authors (e.g., Narayan 2000; Karas & Šubr 2001; Kim et al. 2005). However, Escala et al. (2004), as well as Sánchez-Salcedo & Brandenburg (2001), have found that Ostriker's formula overestimates the dynamical friction somewhat for slightly supersonic velocities, $\mathcal{M} \sim 1$. To get around this problem, we adopt the approach of Escala et al. (2004) and choose a simple parametric form for I($\mathcal{M}$) that approximates Ostriker's formula for a given value of $\ln(\Lambda)$ but lowers the drag force in the region $\mathcal{M} \sim 1 - 2$. Assuming $\ln(\Lambda) = 3.1$ as a reasonable nominal value (cf. Lin & Tremaine 1983; Cora et al. 1997), we use Chandrasekhar's formula (Eq. 2.5) for the gas dynamical friction, but with $\ln(\Lambda) = 4.7$ for $\mathcal{M} \geq 0.8$ and $\ln(\Lambda) = 1.5$ for $\mathcal{M} < 0.8$.

We must also consider that the kinetic energy removed from the SMBH by dynamical friction is added to the gas disk; this energy input is not negligible. Detailed treatment of this process would require a full hydrodynamical approach, but ignoring it completely

yields unphysical results. We therefore modify our prescription for gas dynamical friction to account for the heating of the disk as follows. We assume the disk is "puffed up" to a modified scale height $h' \sim r$, such that the gas density is reduced by a factor h/r and the sound speed $c_{\rm s}$ is increased by a factor $(h/r)^{-1}$, where h is the initial scale height. We furthermore assume, due to the large initial energy input as the BH moves through the cold disk, that this heating occurs effectively instantaneously, and we always use the modified quantities in the dynamical friction calculation.

SMBH mass accretion rate

In addition to tracking the trajectory of the SMBH, we also make an estimate of the accretion rate at each timestep. Nominally, the accretion rate is set to $\dot{M}_\alpha$, a free parameter for $r < r_{\rm infl}$ (disk zones I - III). We define $\dot{M}_\alpha = f_{\rm Edd} \times \dot{M}_{\rm Edd}$, where

$$\dot{M}_{\rm Edd} = \frac{4\pi G M_{\rm BH}}{\kappa_{\rm es}\, c\, \epsilon_{\rm rad}}, \tag{2.18}$$

and we adopt a value of $\epsilon_{\rm rad} = 0.1$ for the radiative efficiency. We set $f_{\rm Edd} = 1$ for the gas-rich ($f_{\rm gas} = 0.5$) models, such that the accretion is Eddington-limited. For consistency we keep the same ratio $f_{\rm Edd} = 2 f_{\rm gas}$ for the $f_{\rm gas} = 0.1$ model (such that $f_{\rm Edd} = 0.2$ in this case). If the SMBH is out of the plane of the disk, its accretion rate is $\dot{M}_\alpha$ for $0 < t < t_{\rm accr}$, where $t_{\rm accr}$ is the accretion timescale $M_{\rm disk,ej}/\dot{M}_\alpha$. After this time, we assume the ejected disk has been consumed, and the accretion rate is set to zero. When the SMBH is in the gas disk, either as it leaves the center or on subsequent passages through the disk ("disk crossings"), the accretion rate may change. Again, at $t < t_{\rm accr}$, we can nominally assume that the BH carries with it a disk of its own that feeds the BH at a rate $\dot{M}_\alpha$. However, the BH may pass through regions of the galactic

gas disk with a much larger scale height than in its own disk, meaning that the BH may accrete mass from all directions, not just its disk plane – i.e., mass in the galactic disk may be swept up by the BH. The accretion from above and below is more accurately modeled by Bondi-Hoyle accretion (Bondi & Hoyle 1944):

$$\dot{M}_{\rm B} = \frac{4\pi (GM)^2 \rho_{\rm g,\infty}}{(v_{\rm rel}^2 + c_{\rm s,\infty}^2)^{3/2}}, \tag{2.19}$$

where $\mathbf{v}_{\rm rel}(\mathbf{r}) = [\, v_{\rm BH,r}(r)\hat{\mathbf{r}}, (v_{\rm BH,\phi}(r) - v_{\rm circ})\,\hat{\phi}, v_{\rm BH,z}(r)\hat{\mathbf{z}}\,]$, $v_{\rm circ} = v_{\rm circ}(r + r_{\rm ej})$ is the circular velocity at the outer edge of the BH disk, and $\rho_{\rm g,\infty}, c_{\rm s,\infty}$ are also evaluated at this radius. This can be rewritten in terms of the Bondi radius $r_{\rm B} = 2GM_{\rm ej}/(v_{\rm rel}^2 + c_{\rm s}^2)$ as

$$\dot{M}_{\rm B} = \pi \rho_{\rm g,\infty} \sqrt{v_{\rm rel}^2 + c_{\rm s,\infty}^2}\, r_{\rm B}^2 f_{\rm geom}, \tag{2.20}$$

where we have added the geometric factor $f_{\rm geom} \equiv \min(1, h/r_{\rm B})$ to account for the reduced cross-sectional area of accretion if the Bondi radius is larger than the physical height of the disk. Because the BH also carries with it a disk from which it is accreting at a rate $\dot{M}_\alpha$, the accretion cannot be modeled by either the Bondi-Hoyle or α prescriptions alone; we therefore introduce a hybrid prescription. We first assume that as long as $t < t_{\rm accr}$, the BH accretion rate will not fall below $\dot{M}_\alpha$ while passing through the galactic disk, because it accretes at this rate from its bound disk. Bondi-Hoyle accretion alone decreases with BH velocity as $1/v_{\rm BH}^3$, but it also varies with environment, which depends on radius. It is unclear *a priori* whether the accretion rate will increase or decrease in this case. We therefore calculate the accretion rate as follows. $\dot{M}_{\rm B}(\mathbf{r},\mathbf{v})$ for a moving object is related to $\dot{M}_{\rm B}(0)$, the Bondi rate for a stationary, central object by

$$\dot{M}_{\rm B}(\mathbf{r},\mathbf{v}) = f \times \dot{M}_{\rm B}(0),$$
$$f = \left(\frac{c_{\rm s,\infty}(0)}{\sqrt{c_{\rm s,\infty}^2 + v_{\rm rel}^2}}\right)^3 \times \left(\frac{\rho_{\rm g,\infty}}{\rho_{\rm g,\infty}(0)}\right) \times \left(\frac{M_{\rm ej}}{M_{\rm BH}}\right)^2 \times \left(\frac{f_{\rm geom}}{f_{\rm geom}(0)}\right). \tag{2.21}$$

For a cold disk rather than an idealized infinite, homogeneous background, the low gaseous sound speed in the disk gives a Bondi radius much larger than the BH radius of influence when the BH is stationary, while in reality the two should be about equal. To avoid calculating unphysical accretion rates much greater than $\dot{M}_{\rm Edd}$, we define a fiducial sound speed $c_{\rm s,\infty} \equiv (2GM/r_{\rm infl})^{1/2}$, where $M = M_{\rm BH}$ for $c_{\rm s,\infty}(0)$ and $M = M_{\rm ej}$ for $c_{\rm s,\infty}$. These are the sound speeds used in the equation above. Because we know that the BH will nominally accrete at the α-model rate instead of the Bondi rate, we adopt the factor f defined in Eq. (2.21), which depends on $c_{\rm s,\infty}$, $v_{\rm rel}$, $\rho_{\rm g,\infty}$, $M_{\rm ej}$, and $f_{\rm geom}$, and normalize it to $\dot{M}_\alpha$. We then have the accretion rate $\dot{M} = f_{\rm amp} \times \dot{M}_\alpha$, where $f_{\rm amp} \equiv \max(f, 1)$ prevents $\dot{M}$ from falling below $\dot{M}_\alpha$. As mentioned above, this applies only when $t < t_{\rm accr}$; otherwise, the BH is naked when it passes through the galactic disk and its accretion rate is just $\dot{M}_{\rm B}(\mathbf{r}, \mathbf{v})$ as given in Eq. (2.21).

From this approach, and also adding the requirement that the accretion rate be Eddington-limited, we can define five distinct accretion regimes for the BH:

- $|z_{\rm BH}| > h, t \leq t_{\rm accr} : \dot{M} = \dot{M}_\alpha$
- $|z_{\rm BH}| > h, t > t_{\rm accr} : \dot{M} = 0$
- $|z_{\rm BH}| \leq h, t \leq t_{\rm accr}, f_{\rm amp} = 1 : \dot{M} = \dot{M}_\alpha$
- $|z_{\rm BH}| \leq h, t \leq t_{\rm accr}, f_{\rm amp} > 1 : \dot{M} = \min(f_{\rm amp}\dot{M}_\alpha, \dot{M}_{\rm Edd})$
- $|z_{\rm BH}| \leq h, t > t_{\rm accr} : \dot{M} = \min(\dot{M}_{\rm B}(\mathbf{r}, \mathbf{v}), \dot{M}_{\rm Edd})$

In practice, we find that the amplification factor $f_{\rm amp}$ is almost never greater than unity; slight amplification occurs in our dry-merger model for the (low-velocity) in-plane

kicks. In all other cases the v^{-3} dependence in the Bondi-Hoyle formula dominates the dependence on the changing gaseous environment, such that any contributions to the mass accretion from above and below the BH-disk plane are negligible. In other words, a negligible amount of mass is swept up by the BH. We can therefore choose $f_{\rm Edd} = 1$ for our fiducial model, such that $\dot{M}_\alpha = \dot{M}_{\rm Edd}$, and disregard the amplification factor. When $t > t_{\rm accr}$, however, $\dot{M}$ is determined solely by the Bondi-Hoyle formula and can have more interesting behavior as seen in Figs. 2.3, 2.4, & 2.7.

2.2.3 Calculation of SMBH trajectories

We integrate the trajectories of SMBHs under the influence of gravity and dynamical friction for a range of kick velocities and angles. The integration is stopped when one of four criteria is met:

- The BH escapes from the galaxy. The actual escape velocity is slightly higher than that calculated from the gravitational potential alone, due to the drag from dynamical friction. We consider the BH "escaped" when it exceeds the nominal escape velocity, $\sqrt{-2\Phi}$, and is still moving away from the galaxy at a distance of 5 $r_{\rm disk}$.

- The BH settles back in the center of the galaxy, with velocity $v_{\rm BH} < 0.01\sigma_*$, where $\sigma_* = \sigma_*(R_{\rm e})$ is the stellar velocity dispersion calculated from the $M_{\rm BH} - \sigma_*$ relation.

- Sufficient energy is injected into the gas via dynamical friction to effectively unbind the disk. The binding energy of the gas disk is estimated to be $\sim 0.5\, G\, M_{\rm disk}/(5\, r_{\rm disk})$. The cumulative energy injected by dynamical friction is the

sum of the energy at each timestep $\mathrm{d}t$, $\sim M_{\rm ej}\, \mathrm{f}_{\rm df}\, v_{\rm BH}\, \mathrm{d}t$. (This limit is not reached in any of our simulations.)

- The integration time reaches a Hubble time. (This limit is not reached in any of our simulations.)

2.2.4 Fiducial model parameters

In our fiducial model (Model A), we use a BH mass of 10^8 $\mathrm{M}_\odot$ and a gas fraction of $f_{\rm gas} = 0.5$. Other galactic parameters are scaled to these two input parameters as outlined in § 2.2.1 & 2.2.2, and Table 2.1 summarizes these quantities. We test kick inclinations of $i = 0^{\rm o}$, $45^{\rm o}$, and $90^{\rm o}$ relative to the disk plane[1]. Two merging BHs that have no spin or aligned spins oriented along the binary orbital rotation axis produce a recoil kick in the binary orbital plane. This very specific configuration would be important only if the BH spins are preferentially aligned by some mechanism, such as torques from the gas disk (Bogdanović et al. 2007). In this case we can assume that the orbital plane and resultant recoil kick would both be aligned with the disk plane. Simulations using full numerical relativity have shown that the maximum recoil kick velocity in this case is ~ 200 km s^{-1} (González et al. 2007b), so we include only data with $v_{\rm k} \leq 200$ km s^{-1} for in-plane ($i = 0^{\rm o}$) runs.

In the absence of empirical evidence for preferentially aligned spins, we must also consider that the distribution of merging BH spins may be closer to random, producing a random distribution of kick inclinations (cf. Schnittman & Buonanno 2007; Campanelli

[1]All kicks velocities are oriented along the positive x-axis; thus, inclined kicks are initially in the x-z plane and in-plane kicks are initially purely on the x-axis.

et al. 2007a; Baker et al. 2008). Thus, we also consider kicks with $i = 45^{\rm o}$ & $i = 90^{\rm o}$. For these out-of-plane kicks, recoil velocities could be very large (Campanelli et al. 2007a; González et al. 2007a) – up to 4000 km s^{-1} (Campanelli et al. 2007b). However, trajectories are uninteresting for $v_{\rm k} > v_{\rm esc}$, so we calculate trajectories for kick velocities ranging from 100 km s^{-1} up to the escape velocity, in increments of 20 km s^{-1}.

2.2.5 Additional models

We also test three models in addition to our fiducial model (see Table 2.1). We calculate the same set of trajectories with BH masses of 10^6 and 10^9 M$_\odot$ (Models B & C, respectively), representing the lower and higher ends of the observed SMBH mass function. 10^6 M$_\odot$ BHs are of particular interest because the mergers of these BHs would be observable with the LISA gravitational wave detector[2]. In addition, because models A, B, & C are "gas-rich" models, we also test a model with $M_{\rm BH} = 10^9$ M$_\odot$ and a gas fraction of $f_{\rm gas} = 0.1$ (Model D), corresponding to a massive, low-z galaxy that has undergone a nearly "dry" merger.

2.3 Results

2.3.1 Fiducial model

All the results in this subsection pertain to our fiducial model (Model A). As explained in § 2.2, only low velocities ($\lesssim 200$ km s^{-1}) are important for in-plane ($i = 0^{\rm o}$) kicks.

[2]Website: http://lisa.nasa.gov/

Very little happens in these runs; the kick is effectively a small perturbation that is quickly damped out in $\lesssim 10^{6.5}$ yr. We do not expect these low-velocity, in-plane kicks to be easily observable.

Inclined kicks with low kick velocity are also mostly uninteresting; an example is shown in Fig. 2.2. Here, the trajectory and mass accretion rate are plotted for the $i = 45^{\rm o}$, $v_{\rm k} = 100$ km s^{-1} run. The BH (and its accompanying disk) wander about 20 pc away from the galactic center in the x and z directions, settling back to the center in < 4 Myr after just one orbital period. The timescale for the BH to accrete the ejected disk, $t_{\rm accr}$, exceeds the wandering time; hence, the accretion rate $\dot{M} = \dot{M}_\alpha$ is constant throughout the simulation.

We have plotted an example of a BH with a moderate kick velocity ($v_{\rm k} = 440 {\rm km\,s^{-1}}$) in Fig. 2.3. Compared to the low-velocity example in Fig. 2.2, the wandering time of the BH is much longer, ~ 15 Myr, and and the BH travels much further from the galactic center. Note also that the size of the ejected disk, and hence $t_{\rm accr}$, are smaller for higher kick velocities. In this case, $t_{\rm accr} \approx 9$ Myr is marked with a red dot in Fig. 2.3b, and corresponds to the point at which $\dot{M}$ first drops to zero. The subsequent spikes correspond to passages through the disk, or disk crossings, where the BH is again fed by the gas via Bondi-Hoyle accretion.

The effective escape speed for $i = 45^{\rm o}$ kicks is between 740-760 km s^{-1}. At $v_{\rm k} = 740$ km s^{-1} (Fig. 2.4), the behavior is a qualitatively similar but greatly amplified version of the moderate-velocity example in Fig. 2.3. The orbital precession induced by the ellipticity of the galactic potential is quite apparent in this case. The BH consumes its small ejected disk almost immediately and reaches a maximum distance of ~ 14 kpc from

Model		**A**	**B**	**C**	**D**
$M_{\rm BH}$	$[\mathbf{M}_\odot]$	$\mathbf{10^8}$	$\mathbf{10^6}$	$\mathbf{10^9}$	$\mathbf{10^9}$
$f_{\rm gas}$		**0.5**	**0.5**	**0.5**	**0.1**
M_*	$[10^{10}\mathrm{M}_\odot]$	4.1	0.034	45	45
$r_{\rm peq}$	$[10^{-2}$ pc]	4.0	0.026	50	15
$r_{\rm Q1}$	$[10^{-2}$ pc]	1.5	0.15	4.7	3.6
$r_{\rm trans}$	[pc]	13	2.8	28	82
$r_{\rm infl}$	[pc]	60	6.9	160	250
$r_{\rm disk}$	$[10^2$ pc]	7.8	1.1	20	18
a	$[10^2$ pc]	7.2	0.60	25	25
$\dot{M}_{\rm Edd}$	$[\mathrm{M}_\odot$ yr$^{-1}]$	2.2	0.022	22	22
$\dot{M}_\alpha$	$[\mathrm{M}_\odot$ yr$^{-1}]$	2.2	0.022	22	4.4

Table 2.1:: Parameters used in different galaxy models. The free parameters, $M_{\rm BH}$ and $f_{\rm gas}$, are shown in bold. The other parameters are derived from these as defined in the text.

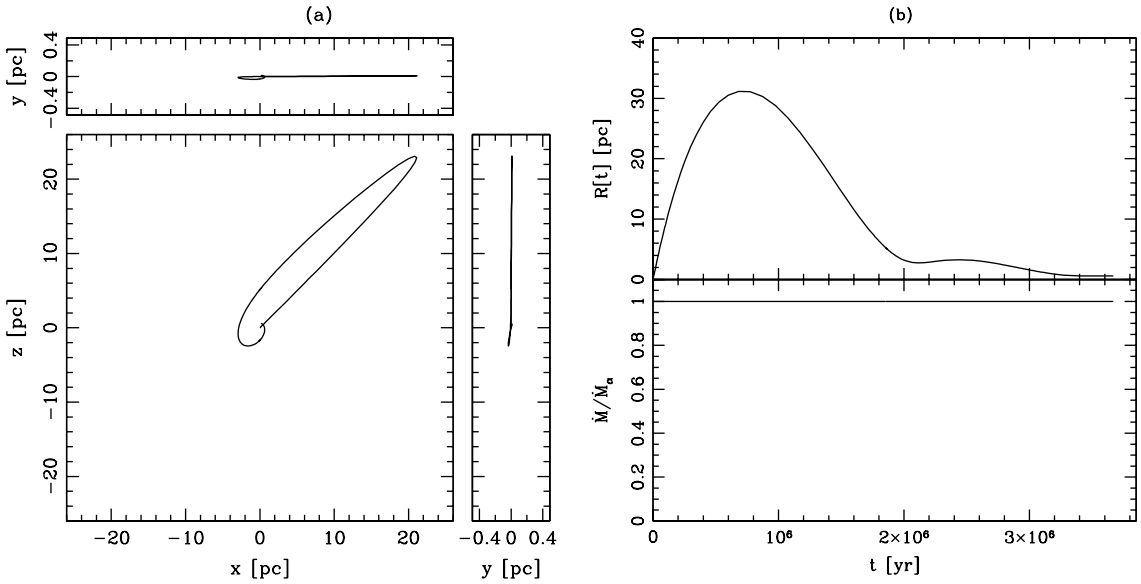

Figure 2.2.—: *(a)* SMBH trajectory for Model A run with $i = 45^{\rm o}, v_{\rm k} = 100$ km s^{-1}, seen from three orthogonal orientations. Turnaround points are numbered in sequence to show the BH trajectory. The y-axis (top & side panels) has been expanded by a factor of 10 to show greater detail. *(b) top panel:* radial distance of SMBH from center vs. time. Maxima are numbered to correspond with turnaround points in *(a). Bottom panel:* Calculated mass accretion rate vs. time, normalized to the α-model accretion rate. Note that in this low-$v_{\rm k}$ example, the accretion rate is constant ($\dot{M} = \dot{M}_{\alpha}$) for the entire run.

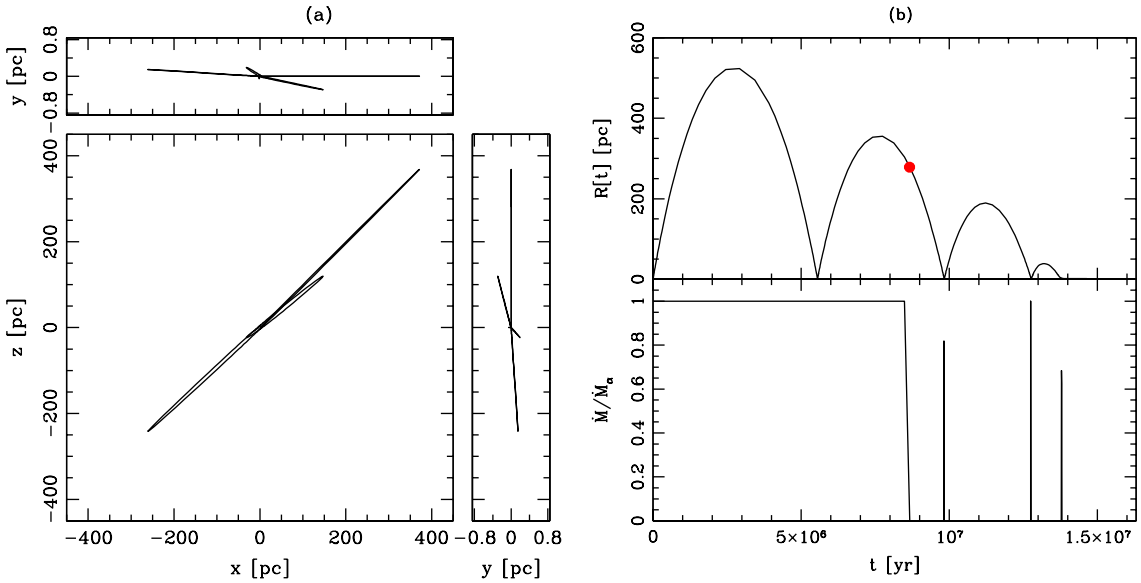

Figure 2.3.—: Same data as Fig. 2.2, but with $v_{\rm k} = 440$ km s^{-1}. In Fig. 2.3a, the y-axis (top & side panels) has been expanded by a factor of 100 to show greater detail. Turnaround points are numbered in sequence to show the BH trajectory; only the first 3 are numbered. The red dot in the top panel of Fig. 2.3b indicates the time $t_{\rm accr} = M_{\rm disk,ej}/\dot{M}_\alpha$ when the ejected disk has been consumed by the SMBH. Correspondingly, the accretion rate (bottom panel) drops to zero here, and is nonzero again only when the SMBH crosses the galactic disk.

the center. During the ~ 1.2 Gyr it takes to settle back to the center, it crosses the disk 28 times, producing multiple short bursts of accretion (Fig. 2.4b). This is an idealized scenario, however, because on scales $\gtrsim$ kpc, the DM halo potential will start to dominate that of the baryonic galaxy component. Because the DM distribution is likely to be significantly triaxial on these scales, the BH may be scattered onto an orbit that takes significantly longer to return to the center of the galaxy, or it may wander indefinitely in the halo. (See Vicari et al. 2007, for a more detailed analysis of this regime.) This means that the number of disk crossings and total mass accretion are upper limits, and the BH

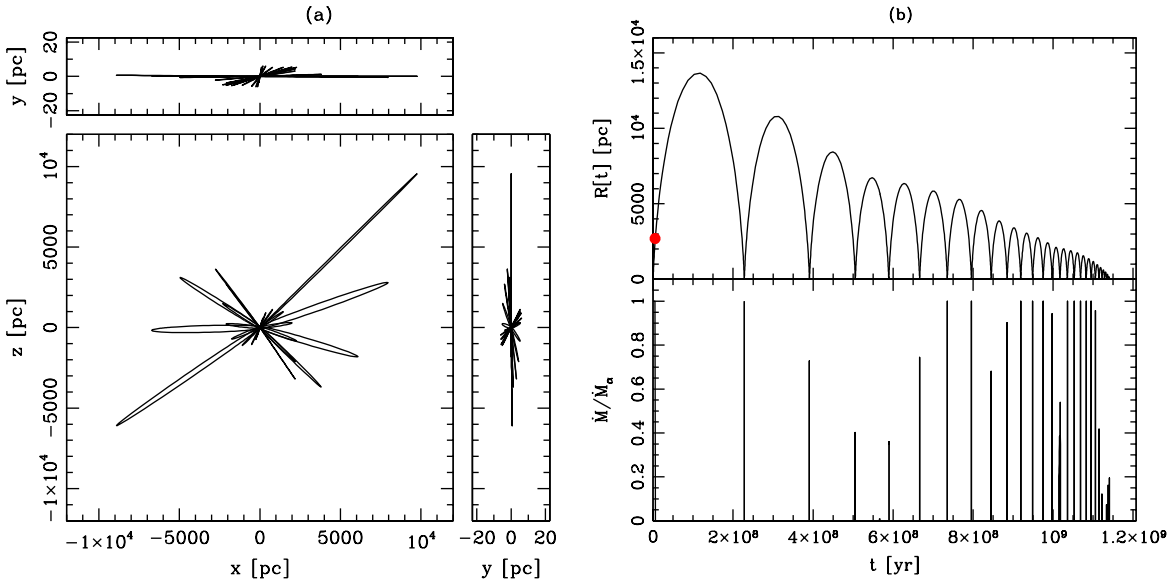

Figure 2.4.—: Same data as Fig. 2.2, but with $v_{\rm k} = 740$ km s^{-1} (i.e., just below the escape speed for this inclination from this galaxy model). In Fig. 2.4a, the y-axis (top & side panels) has been expanded by a factor of 100 to show greater detail. Turnaround points are numbered in sequence to show the BH trajectory; only the first 9 are numbered. The red dot indicates the timescale $t_{\rm accr}$, as described in Fig. 2.3.

wandering time is a lower limit. The amount of accretion will in reality be reduced even further; 1.2 Gyr is well in excess of typical starburst timescales ($\sim$ 100 Myr, cf. e.g., Springel et al. 2005b; Marcillac et al. 2006), after which less gas will be left to accrete. Additionally, this wandering time is roughly comparable to typical timescales between major galaxy mergers, so this may be another complicating factor. We note, however, that the upper limit of $\sim$ 1 Gyr for the wandering timescale in massive galaxies is a similar result to that of Gualandris & Merritt (2008), despite the substantially different physics and parameters that were included in our respective models.

When the BH is kicked directly out of the plane ($i = 90^{\rm o}$), the effective escape

velocity is slightly lower than in the $i = 45^{\rm o}$ case (~ 660 km s^{-1} for Model A). The main difference in this case, however, is that very little accretion occurs after $t_{\rm accr}$. This is because the BH precesses very little about the galaxy center when it is ejected directly along the vertical axis; all of its disk crossings occur very close to the center where the disk height is small, so the disk crossing time is typically too short for any measurable accretion to occur.

To understand how GW recoil may affect the mass accretion history of SMBHs, we calculate the total mass accreted by the SMBH during each simulation (ΔM). We are also interested in how this compares with the mass that would have been accreted by a stationary BH of the same mass over the same time ($\Delta M_0 \equiv t_{\rm fin}/\dot{M}_\alpha$). Fig. 2.5 shows the SMBH growth as a function of kick velocity. ΔM_0, and correspondingly $t_{\rm fin}$, increase monotonically with kick velocity until $v_{\rm esc}$ is reached. In the middle panel where ΔM is shown, one can see the remarkable result that *the mass accreted by wandering SMBHs is fairly constant at* $\sim 10\%$ *for all kick velocities* $\lesssim v_{\rm esc}$. This appears to be a coincidental balance between the competing factors of the wandering time, which increases with $v_{\rm k}$, and the time to accrete the ejected disk, which decreases with higher $v_{\rm k}$. § 2.3.4 gives further details about this result.

2.3.2 SMBH mass models

In Model B with a 10^6 M$_\odot$ BH, kick velocities as low as ~ 200 km s^{-1} result in escape of the BH from the galaxy (Fig. 2.6a). Since the magnitude of GW recoil depends on the mass ratio of the progenitor BHs but not on their absolute masses, the probability of large recoil kicks is the same for smaller SMBHs as it is for the most massive ones. Note

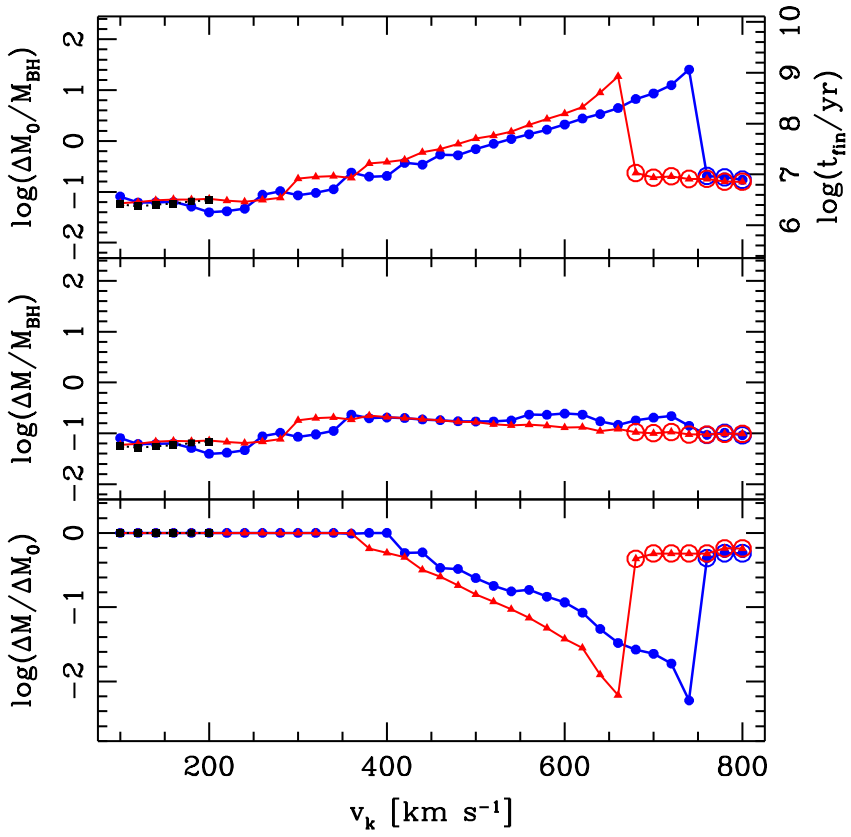

Figure 2.5.—: SMBH mass increment for Model A, as a function of kick velocity. In all panels, black filled squares with dotted line denote $i = 0^{\rm o}$ kicks (low $\rm v_k$ only), blue filled circles with thick line denote $i = 45^{\rm o}$ kicks, and red filled triangles with thin line denote kicks with $i = 90^{\rm o}$. Open circles around a point indicate that the BH escaped from the galaxy's baryonic component. *Top panel:* The estimated BH growth, normalized to the initial BH mass, if the BH were to remain in the galactic center for the simulation time ($\Delta M_0 = \dot{M}_\alpha \times t_{\rm fin}$). Because ΔM_0 scales linearly with $t_{\rm fin}$, the latter is shown on the right vertical axis. *Middle panel:* The estimated BH growth, normalized to the inital BH mass, calculated based on the moving BH's trajectory. *Bottom panel:* The ratio of these two quantities.

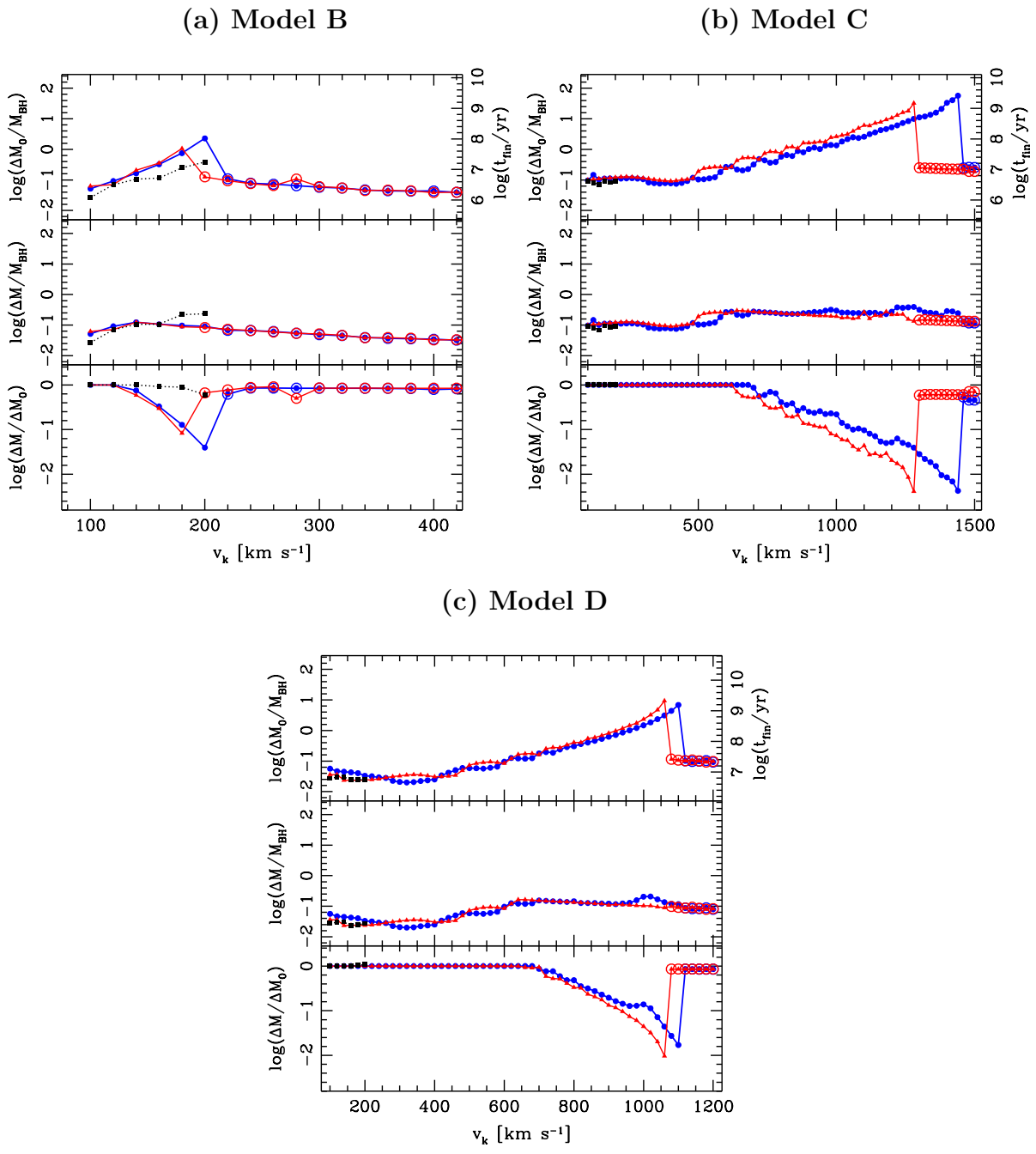

Figure 2.6.—: SMBH growth for Models B, C, & D as a function of kick velocity. Notation is the same as in Fig. 2.5.

that $\Delta M/M_{\rm BH} \sim 10\%$ for $v \lesssim v_{\rm esc}$ in this model as well. For $v > v_{\rm esc}$, however, one can see that $\Delta M/M_{\rm BH}$ gradually declines, because $t_{\rm accr}$ is also decreasing (see Fig. 2.9).

Fig. 2.6b shows that the growth for a 10^9 $M_\odot$ BH is qualitatively similar to that of a 10^8 $M_\odot$ BH, but here the trends are even more apparent. AGN feedback or gas depletion via star formation should reduce the accretion onto stationary BHs over the long timescales shown in the top panel; the projected growth factor of almost 100 is clearly unphysical. However, the middle panel demonstrates that recoil kicks are effective at suppressing the BH growth; the growth factor is again remarkably constant at $\sim$ few $\times$ 10% regardless of kick velocity.

2.3.3 Dry merger model

Model D (a "dry merger") has the same parameters as the 10^9 $M_\odot$ model above, but with a gas fraction of 0.1. Fig. 2.6c shows the BH growth for this model, which is again qualitatively similar to Fig. 2.6b. As would be expected, the escape velocity is lower for the galaxy containing less gas (note that we have defined $f_{\rm gas}$ such that this model, with lower $f_{\rm gas}$, is less massive overall than the others). Aside from this, the growth factor for the wandering BH is still $\sim 10\%$, suggesting again that dynamics, not the details of the gas physics, dominate the determination of the final BH mass when the BH is not stationary.

Fig. 2.7 shows an example of the BH accretion in Model D, with $\dot{M}_\alpha < \dot{M}_{\rm Edd}$. The kick velocity $v_{\rm k} = 1100$ km s^{-1} is just below the effective escape velocity for this model, so $t_{\rm accr}$ is very short and $\dot{M}$ quickly drops from $\dot{M}_\alpha$ to zero. The accretion rate on all subsequent passages through the disk is set by the Bondi rate $\dot{M}_{\rm B}$, which

varies depending on the velocity and position of the disk crossing. Near the end of the simulation, as the BH slows down, its accretion becomes Eddington-limited.

2.3.4 Observational signatures

Because GW recoil has not been unambiguously observed in any astrophysical system, an important application of this work is to consider the observational signatures that recoiling BHs could produce such that their existence could be directly confirmed. An observable recoiling BH, i.e. one with significant accretion luminosity, could be distinguished from a stationary central BH via offsets in either physical space or velocity space. A BH with a resolvable spatial offset from its host galaxy is statistically more likely to have a relatively low velocity, since a large fraction of orbital time is spent at turnaround. Likewise, the largest velocity offsets will occur either soon after the recoil event or on subsequent passages of the BH through the galactic disk, where the spatial offset from the galactic center is small. The duty cycle for the former type of event depends on the size of the accretion disk that the recoiling BH carries with it; higher recoil speeds result in smaller ejected disks and shorter duty cycles. After this disk is exhausted, the most plausible way for the wandering BH to become observable again is by accreting matter as it makes subsequent passages through the galactic disk, possibly generating a quasi-periodic signature such as knotted or twisted jets.

Accordingly, we distinguish between two types of "recoiling quasars:" the former, primarily spatially-offset active BHs are identified as "off-center quasars," and the latter, primarily velocity-offset sources are identified as "disk-crossing quasars." Note, however, that there is not a one-to-one correspondence between quasar velocity offsets

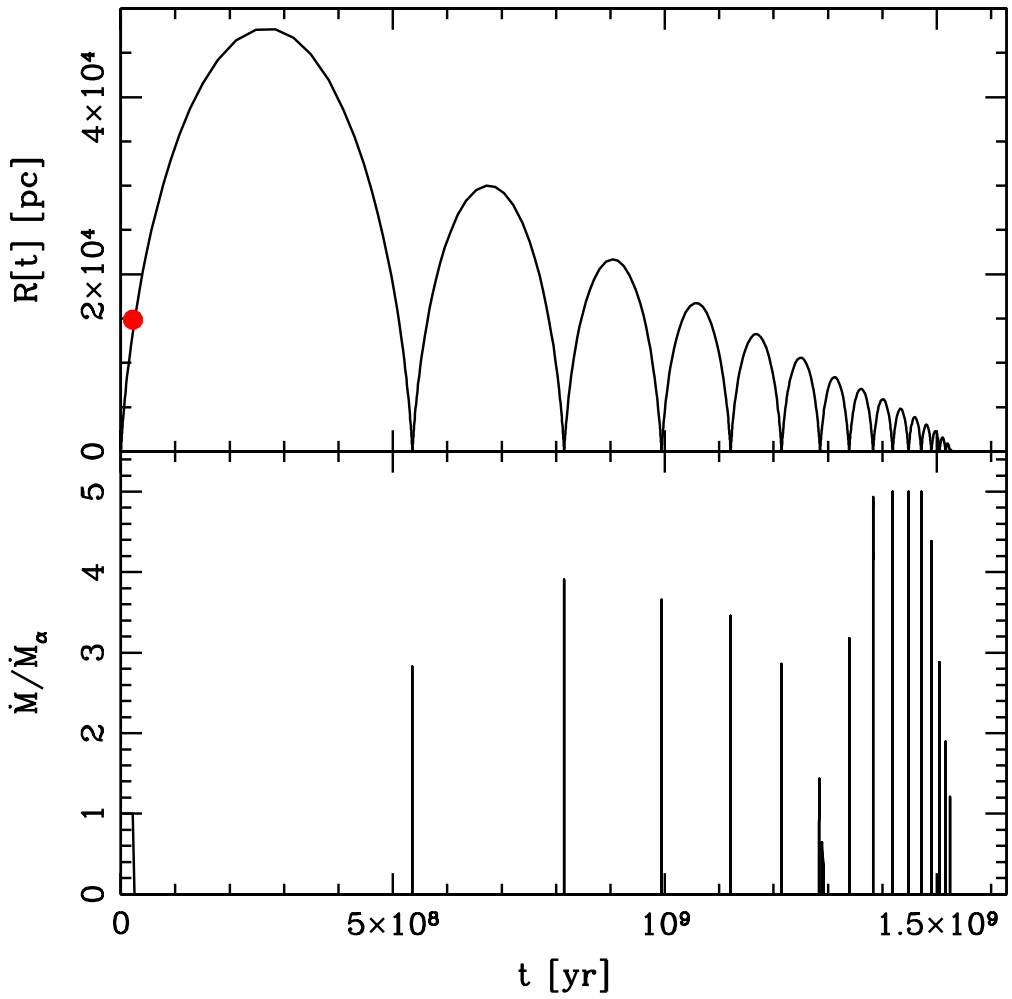

Figure 2.7.—: Same notation as Fig. 2.2b, here showing data from Model D for a trajectory with $v_{\rm k} = 1100$ km s^{-1}, $i = 45^{\rm o}$. In this case, Bondi-Hoyle accretion amplifies $\dot{M}$ above $\dot{M}_\alpha = 0.2\dot{M}_{\rm Edd}$ up to the Eddington limit.

and disk-crossings, nor between spatial offsets and "off-center" quasars. In particular, ejected quasars will often only be visible for a short time after ejection, while they still carry an accretion disk, so that off-center quasars will often have a significant velocity offset as well. Similarly, many "disk-crossing" events occur when the BH is settling back to the center of the galaxy and slowing down, so their velocity offsets will be small. Note also that the term "quasar" is used loosely here to refer to a source with observable accretion activity; recall that in our runs all BHs except those in Model D radiate at their Eddington luminosities.

To quantify the duty cycles for off-center quasars, we plot both the simulation time $t_{\rm fin}$ (the time for the BH to settle back to the galactic center) and the calculated accretion time for the ejected BH disk, $t_{\rm accr}$, as functions of $v_{\rm k}$ (Fig. 2.8). The bold lines show the actual time for which the BH might be visible as an off-center quasar. At low kick velocities, the BH settles back to the center before consuming its bound disk, and at high kick velocities, the BH accretes its disk and then continues to wander as a naked BH. The effective time for off-center quasar activity, $\sim 10^{6.2} - 10^{7}$ yr, varies relatively little with $v_{\rm k}$. This balance helps explain why the growth of the wandering BHs is also roughly constant with varying kick velocity (Figs. 2.5, & 2.6). However, Fig. 2.9 shows that $t_{\rm accr}$ continues to decrease, albeit slowly, for $v_{\rm k} > 800$ km s^{-1}. Thus, we expect a lower $\Delta M/M_{\rm BH}$ for $v_{\rm k} \gg v_{\rm esc}$.

The simple picture shown in Fig. 2.8 provides a plausible explanation for the accretion behavior seen in our simulations based on off-center quasar activity alone, suggesting that accretion during disk crossings is relatively unimportant. Also, for $v_{\rm k} \approx v_{\rm esc}$, $\Delta M/M_{\rm BH} \sim 10\%$ regardless of whether the BH escapes or returns for subsequent disk passages, further indicating that disk crossings contribute negligibly to

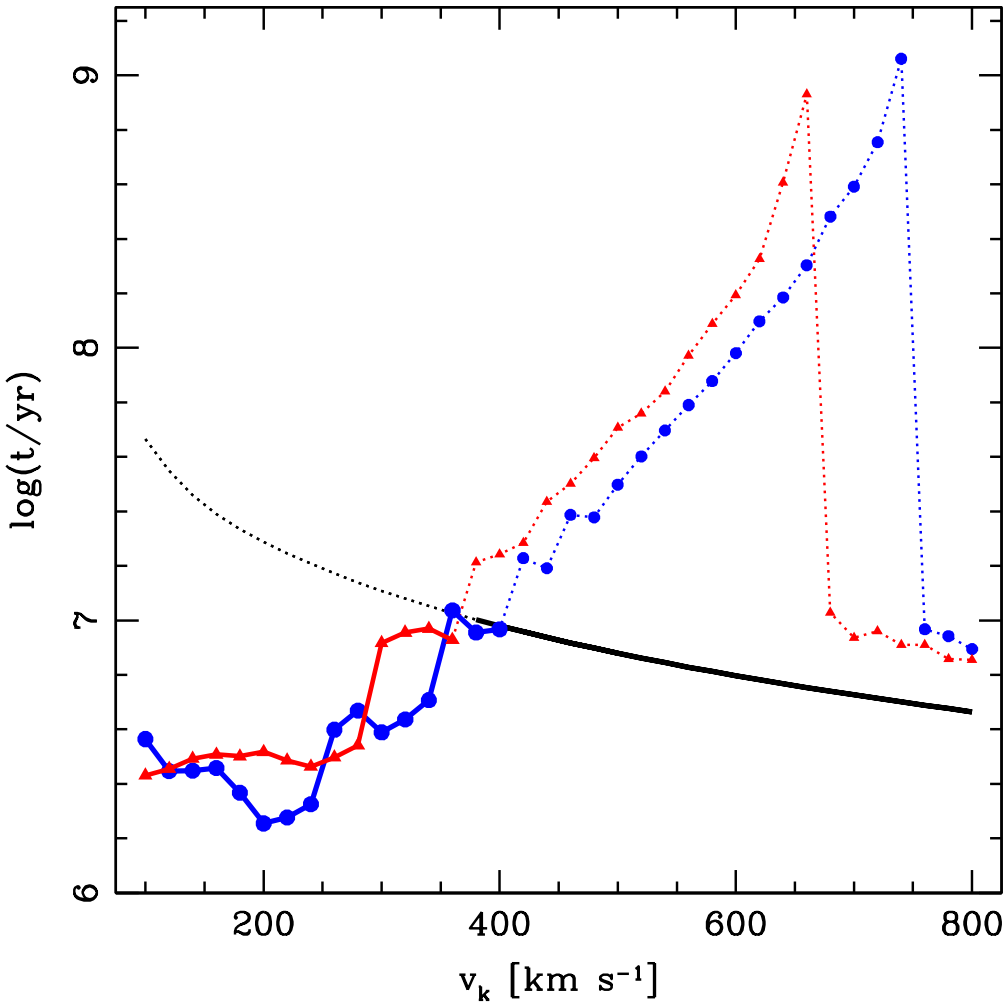

Figure 2.8.—: Relevant timescales for off-center quasars. *Black line:* lifetime $t_{\rm accr} = M_{\rm disk,ej}/\dot{M}_{\alpha}$ of the accretion disk ejected with the BH. *Blue line with filled circles:* simulation time $t_{\rm fin}$ for runs with $i = 45^{\rm o}$. *Red line with filled triangles:* $t_{\rm fin}$ for runs with $i = 90^{\rm o}$. In all cases, the bold portions of the line indicate the minimum of ($t_{\rm accr}$, $t_{\rm fin}$) at each $v_{\rm k}$; remaining portions are shown with a dotted line.

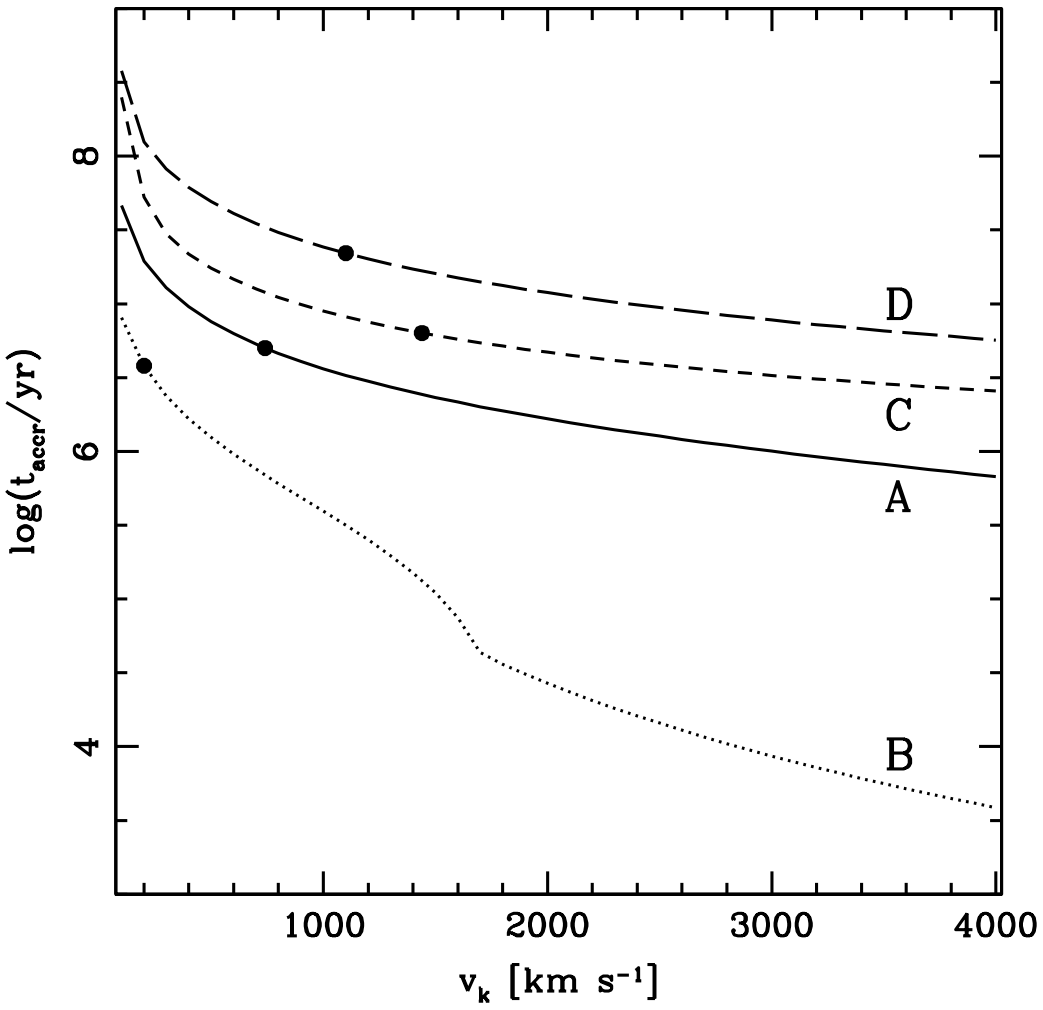

Figure 2.9.—: $t_{\rm accr} = M_{\rm disk,ej}/\dot{M}_{\alpha}$ is plotted for $100 \leq v_{\rm k} \leq 4000$ km s^{-1}, for models A, B, C, & D. The solid dot on each curve denotes the escape velocity for that model. The bump in curve B occurs when $r_{\rm ej} < r_{\rm Q1}$ and the disk profile changes.

the growth of recoiling BHs. However, a more quantitative analysis demonstrates that this is not the complete picture.

As one would expect, the number of disk crossings ($N_{\rm cross}$) generally increases with increasing kick velocity (Fig. 2.10). In each model, even Model B with the least massive BH, $N_{\rm cross} > 10$ for the highest kick velocities. The kick inclination has little effect on the number of disk crossings. However, as mentioned in § 2.3.1, the amount of quasar activity during these crossings *is* inclination-dependent; virtually no accretion occurs when $i = 90^{\rm o}$, due to the small disk height in the inner regions. Additionally, very low kick inclinations will produce few disk crossings; we therefore expect recoil kicks with moderate inclinations to be the most likely candidates for producing observable disk-crossing quasar activity. We accordingly restrict our discussion of disk-crossing quasars to our runs with $i = 45^{\rm o}$.

Figs. 2.11a & b compare the contributions of both quasar types to the total quasar activity. Fig. 2.11a shows the total mass accreted for the fiducial model, as well as the mass accreted via off-center quasars only and via disk crossings only. We see that as expected, the off-center quasar phase dominates the overall growth, although at kick velocities $550\,{\rm km\,s^{-1}} \lesssim v_{\rm k} < v_{\rm esc}$, the two contributions are comparable. Note that in this same velocity range, the simulation time is generally greater than the expected timescale for a merger-induced starburst, $\sim 10^8$ yr. Because accretion during disk crossings does not dominate the BH growth, however, a paucity of fuel in the post-starburst phase would reduce the total mass accretion by only a moderate amount. Furthermore, if triggering of the starburst happens late in the merger process, the fuel supply may last longer.

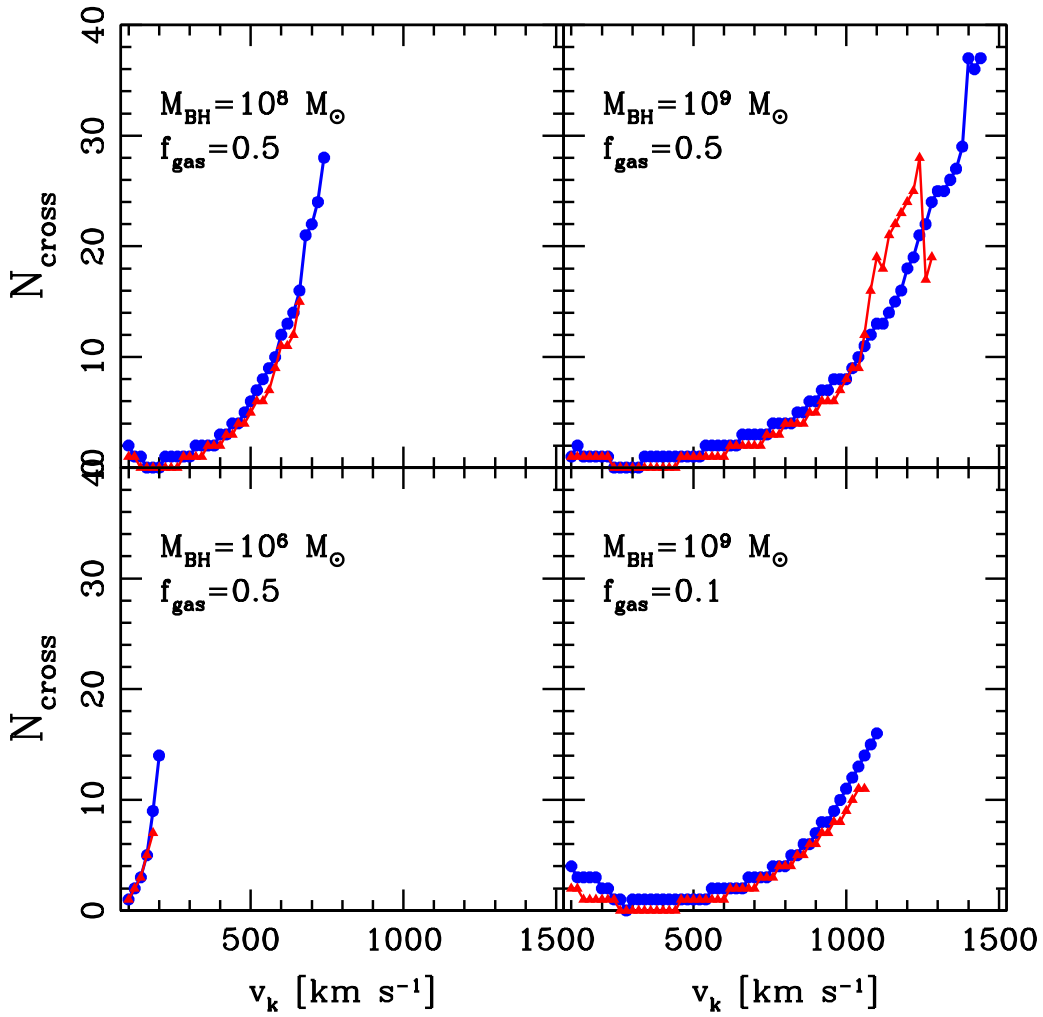

Figure 2.10.—: Number of disk crossings versus $v_{\rm k}$ for each model. Blue with filled circles indicates kicks with $i = 45^{\rm o}$, and red with filled triangles indicates $i = 90^{\rm o}$. *Upper left:* Model A. *Lower Left:* Model B. *Upper right:* Model C. *Lower right:* Model D. Only bound trajectories are shown, because the escaping BHs do not cross the disk.

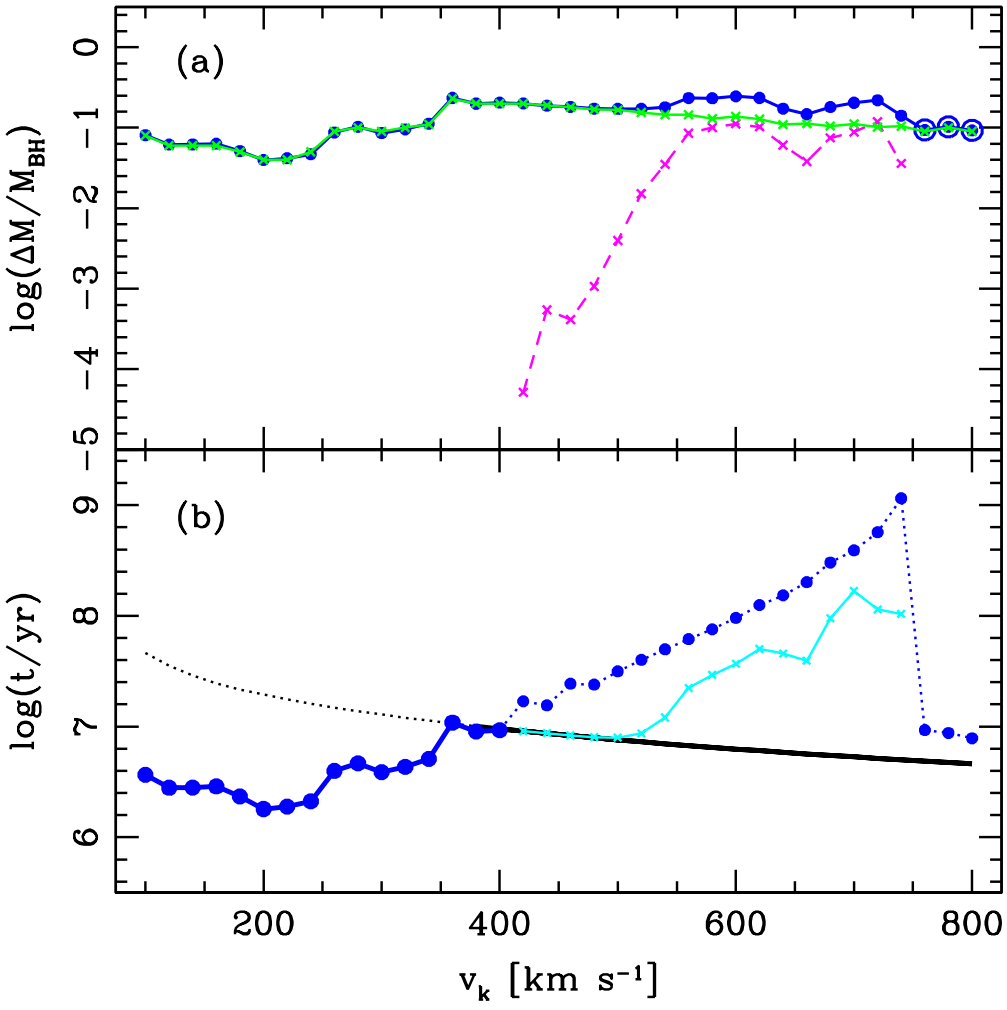

Figure 2.11.—: *(a)* $\Delta M/M_{\rm BH}$ for Model A, $i = 45°$. *Blue thick line with filled circles:* total mass accreted during simulation (same as in Fig. 2.5). Open circles denote simulations in which BH escaped from the galaxy. *Green thin line with crosses:* mass accreted from the ejected accretion disk, as an off-center quasar. *Magenta dashed line with crosses:* mass accreted during disk crossings. *(b)* Same plot as Fig. 2.8, but with $i = 90°$ runs omitted and a (*cyan*) line with crosses added denoting the total quasar duty cycle for each simulation, i.e, $t_{\rm accr} + t_{\rm cross}$, where $t_{\rm cross}$ is the sum of duty cycles for all disk crossings in each run.

Fig. 2.11b is the same as Fig. 2.8 except that the $i = 90^{\rm o}$ runs are excluded, and an extra line is added to denote the total active quasar time for each simulation, $t_{\rm accr} + t_{\rm cross}$. Interestingly, the total time spent in disk-crossing quasar phases is quite large at high velocities, up to ~ 100 Myr in a few cases. This result has two important caveats, however. First, the accretion rate is clearly not Eddington-limited for the entirety of these long duty cycles, since the mass contribution from this type of accretion is at most comparable to that of off-center quasars. Evidence for this sub-Eddington accretion can be seen in Fig. 2.4b. Correspondingly, the luminosities of disk-crossing quasar events may often be relatively low and thus harder to detect than off-center quasar activity. The second caveat is that the longest duty cycles for disk crossings are those in which the BH has the lowest velocity, i.e., the final passages before the BH settles back to the galaxy center. This is a tradeoff in observability: the disk-crossing quasars that would be most easily distinguished observationally from stationary quasars are those with the highest-velocity disk passages and, by definition, the shortest duty cycles.

Fig. 2.12 demonstrates this point more quantitatively; the distributions of velocity and spatial offsets are shown for three selected runs, with green and magenta lines denoting the time spent in off-center and disk-crossing quasar phases, respectively. The top panels show the Model A run with $v_{\rm k} = 440$ km s^{-1}, in which the BH retains an accretion disk for about half of its wandering time. The off-center quasar spends most of its lifetime at low velocities (near turnaround) and at spatial offsets of a few hundred parsec. The BH crosses the disk only four times, however, so the time fraction it spends in disk-crossing quasar phases is very small. The runs shown in the middle and bottom panels of Fig. 2.12, which have $v \lesssim v_{\rm esc}$ for their respective models, have shorter off-center quasar duty cycles and longer wandering times, so the time fractions of the

Figure 2.12.—: Probability distributions of velocity (*left panels*) and spatial (*right panels*) offsets for selected runs. In all cases, *black lines* denote the distribution for the entire simulation, *green lines* denote the distribution of time spent in off-center quasar phases only (i.e., $t < t_{\rm accr}$), and *magenta lines* denote the distribution of time spent in disk crossing phases only. *Top panels:* Model A run with $i = 45^{\rm o}$ and $v_{\rm k} = 440$ km s^{-1} (trajectory shown in Fig. 2.3). *Middle panels:* Model A run with $i = 45^{\rm o}$ and $v_{\rm k} = 740$ km s^{-1} (trajectory shown in Fig. 2.4). *Bottom panels:* Model C run with $i = 45^{\rm o}$ and $v_{\rm k} = 1440$ km s^{-1} (trajectory not shown). Note that the probability distributions of off-center quasar phases in the higher-velocity runs are plotted, but are so low that they are almost invisible.

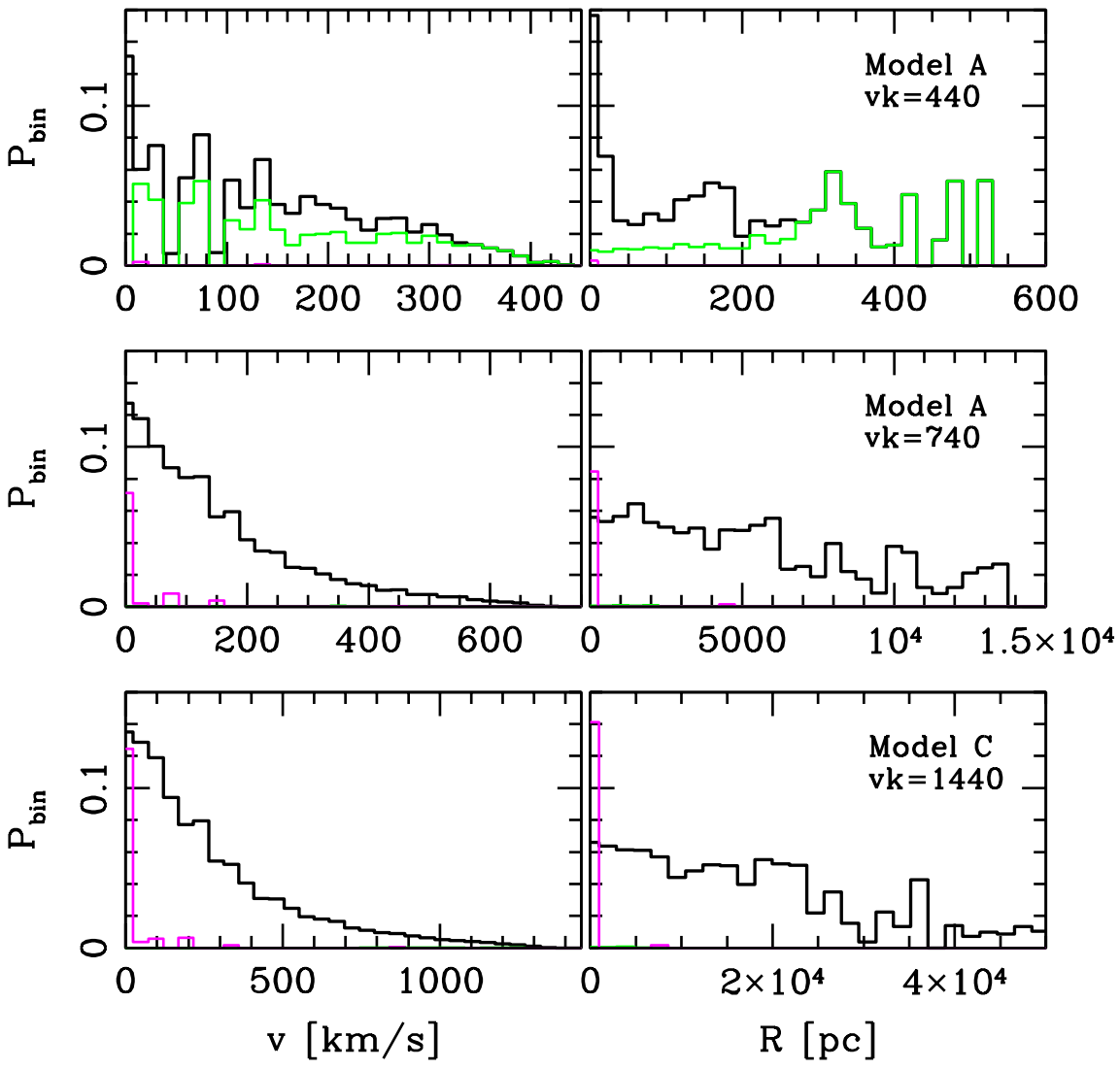

Figure 2.12.—: (Continued)

off-center quasar phases are very low – virtually indiscernible. The time fraction spent in disk-crossing quasar phases is more substantial, but because many disk crossings occur late in the simulation as the BH is settling back to the center, these are primarily constrained to the lowest velocity bin (and as expected, the smallest distance bin as well). Therefore, while it is certainly possible in principle for GW recoil to produce a quasar with a measurable offset, it may prove challenging to observe one directly, especially one with a very high kick velocity.

As mentioned in § 2.1, Komossa et al. (2008) have proposed that SDSSJ0927+2943 is a recoiling quasar with a velocity offset of 2650 km s^{-1}. We do not plot any recoil trajectories with kick velocities this high, because this is well above galactic escape velocities. Were we to reproduce the distributions in Fig. 2.12 for a run with $v_{\rm k} = 2650$ km s^{-1}, we would find a delta function at $v_{\rm k}$, because the BH would be ejected from the galaxy with little deceleration. The quasar lifetime, however, would be short. Taking the mass and luminosity values estimated by Komossa et al. (2008), $M_{\rm BH} \sim 6 \times 10^8$ $M_\odot$ and $L \sim 0.1 L_{\rm Edd}$, we find that the BH will only retain a gas disk of mass $\sim 2\% M_{\rm BH}$ and radius ~ 0.37 pc, which it will accrete within $\sim 10^7$ yr. This is much shorter than the upper limit of $\sim 10^9$ yr that Komossa et al. (2008) estimate using $M_{\rm disk,ej} \approx M_{\rm BH}$. If the conclusion of Komossa et al. (2008) is accurate, then their discovery is extremely serendipitous, because it combines two low-probability events. The first is the merger of two BHs with spins, mass ratio, and spin alignment configured in an unlikely manner to give a kick near the maximum possible GW recoil velocity, and the second is the observation of the recoiling BH during its relatively short quasar phase. This combined probability is difficult to calculate due to its dependence on unknown distributions of BH binary parameters, and it is unclear *a priori* whether this rare recoil event is in

fact more or less likely to occur than a superposition of somewhat unusual quasars. The possible role of gaseous outflows is also unclear. Although outflows cannot easily explain all the unusual spectral lines, neither can the recoil scenario explain all of the narrow lines without outflows or similar phenomena being invoked at any rate. Follow-up observations of this intriguing source would help to clarify the situation.

Our finding that high-velocity GW recoil events are unlikely to be observed is consistent with the null result of Bonning et al. (2007), who conducted a search for velocity offsets > 800 km s^{-1} in quasar spectra. In Fig. 2.9, we have plotted $t_{\rm accr}$ in all of our models, for the range $100 \leq v_{\rm k} \leq 4000$ km s^{-1}. The decline in quasar duty cycle for high velocities can easily be seen, and at the highest velocities, all models have $t_{\rm accr} \lesssim 10^7$ yr. The duty cycle for an off-center quasar with $v_{\rm k} = 800$ km s^{-1} is $6 \times 10^5 - 5 \times 10^6$ yr for our models in which $v_{\rm esc} < 800$ km s^{-1} (Models A & B), although the BH decelerates over this time. The most massive BHs (Models C & D) retain more mass after they are ejected and thus have longer duty cycles, but decelerate more quickly since they are on bound orbits at this $v_{\rm k}$. Duty cycles are somewhat longer for these off-center quasars if the accretion luminosity is lower, although of course they then will be dimmer. The duty cycles for disk-crossing quasars with $v \sim 800$ km s^{-1} are shorter, however, $\sim 10^5$ yr. In all cases, duty cycles are shorter still if one considers higher $v_{\rm k}$. Clearly, the probability of observing a recoiling quasar is low, although future searches sensitive to smaller velocity offsets will increase these probabilities. Finally, as a corollary to the arguments on the detectability of disk-crossing quasars, we note that King & Dehnen (2005) and Libeskind et al. (2006) have argued that some of the brightest ultraluminous X-ray sources (ULXs) might be explained as wandering intermediate-mass BHs ($M_{\rm BH} \sim 10^2 - 10^5 {\rm M}_\odot$) that were ejected from their host galaxies in previous merger events and that begin accreting

again upon returning to a dense gaseous region.

There is another possibility for detecting recoil events in addition to observing quasar offsets. Lippai et al. (2008), Shields & Bonning (2008), and Schnittman & Krolik (2008) have recently pointed out that strong flares may occur following a GW recoil as the surrounding gas is disrupted and gas marginally bound to the BH falls back onto the galactic disk. Lippai et al. (2008) argue that strong shocks are a natural consequence of perturbations to highly supersonic gas, as is the case with thin accretion disks. If the shock propagates at $v_{\rm shock} \lesssim v_{\rm k}$, it will produce a flare with an emission spectrum peaking at $k\,T_{\rm shock} = (3/16)\mu\,m_{\rm H}\,v_{\rm shock}^2 \approx 19\,{\rm eV}\,(v_{\rm shock}/100\,{\rm km\,s^{-1}})^2$. Such flares would be observable in soft X-rays for recoil kicks $\gtrsim 200 - 300$ km s^{-1}; below these energies, most of the emission would be absorbed by interstellar hydrogen. The highest kick velocities ($\gtrsim 1000$ km s^{-1}) could produce hard X-ray flares, though these would be short-lived. These photon energy ranges would change if the shock propagates at only a small fraction of the kick velocity, as Lippai et al. (2008) have estimated; in this case some flares might be observable at UV energies. Shields & Bonning (2008) estimate a typical flare timescale $t_{\rm flare} \sim 10^4$ yr and an observable flare rate of ~ 1 in 10^4 quasars. Schnittman & Krolik (2008) suggest that because the disk is optically thick, recoil flares may produce long-lived infrared afterglows, of which up to $\sim 10^5$ might be visible today. These numbers are uncertain, however, and detailed hydrodynamical simulations of recoiling disks will be needed to more accurately determine the frequency and duration of these flares, as well as whether their spectra and luminosities can be distinguished easily from concurrent AGN activity. The important point to note, however, is that a recoiling BH making numerous passages through the disk may create a succession of flares, rather than just an initial flare during the recoil event. This could substantially

increase the rate at which recoil flares occur.

2.3.5 Sensitivity of results to q parameter

As mentioned above, we have accounted for the ellipticity of the gas disk potential Φ(R) by introducing a small perturbation, q, in the radial coordinate such that $\tilde{R} = \sqrt{r^2 + (z/q)^2}$ and $\Phi = \Phi(\tilde{R})$. We use $q = 0.99$ as a fiducial value for our runs, and here we investigate the sensitivity of our results to this choice of q. *A priori*, one can expect the largest perturbation to the BH orbit to occur near turnaround, where the velocity is low and the BH is most sensitive to acceleration from the (perturbed) gravitational potential. Therefore, the largest cumulative perturbation should occur for orbits with the most turnarounds, i.e. those with large $v_{\rm k}$. Orbits with large $v_{\rm k}$ also have longer turnaround times, since turnaround can be defined as a fixed fraction of the orbital period, which increases for higher kick velocities. Fig. 2.13 shows the total mass accretion, $\Delta M/M_{\rm BH}$, as a function of q for low, moderate, and high values of $v_{\rm k}$. Indeed, we see that very little variation with q occurs except in the highest velocity case, $v_{\rm k} \lesssim v_{\rm esc}$. We can thus conclude that the value of q does not matter for simulations with low-to-moderate $v_{\rm k}$. For the largest kicks, we can assume that choosing q fairly close to unity is appropriate, since turnarounds will occur mostly at large radii where the degree of ellipticity of equipotential contours should be small. Furthermore, BH trajectories for $v_{\rm k} \lesssim v_{\rm esc}$ are already the most susceptible to other inaccuracies due to physical effects that were not included here. For example, at the largest radii probed by orbits bound to the baryonic galactic component (generally tens of kpc), BHs are likely to encounter perturbations due to the triaxiality of the DM halo. The host galaxy is also likely to

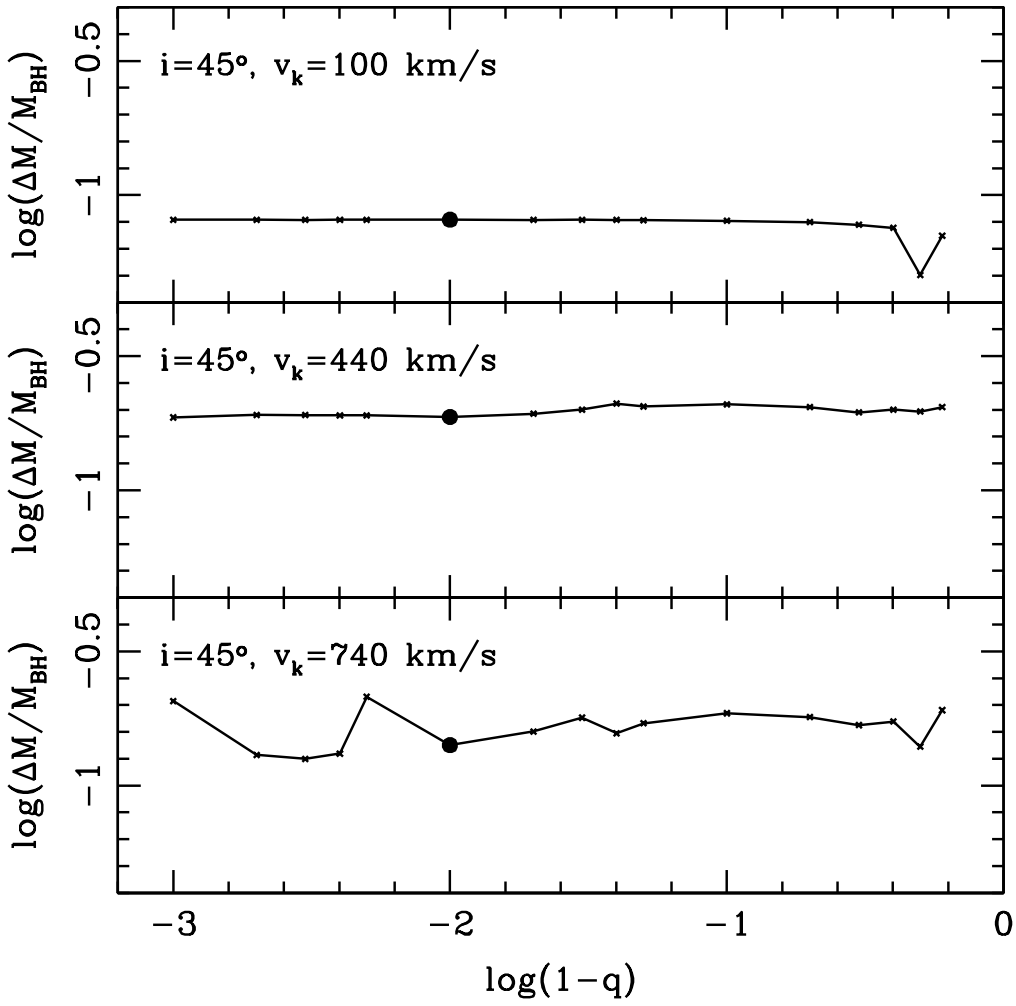

Figure 2.13.—: $\Delta M/M_{\rm BH}$ as a function of the ellipticity parameter q, using Model A and $i = 45^{\rm o}$. The low ($v_{\rm k} = 100$ km s^{-1}, *top panel*), moderate ($v_{\rm k} = 440$ km s^{-1}, *middle panel*), and high-velocity ($v_{\rm k} = 740$ km s^{-1}, *bottom panel*) kicks shown in § 2.3.1 are chosen again here to demonstrate variation with q. For clarity, the value $\log(1 - q)$ is plotted on the x-axis. The solid dot denotes our chosen fiducial value $q = 0.99$.

evolve and undergo star formation during the the long ($\gtrsim$ Gyr) wandering time of the BH in these cases.

2.4 Discussion

We have considered SMBH accretion without requiring that the SMBH remains stationary at the center of its host galaxy. Instead, the SMBH was assumed to be "kicked" from the center at 100s - 1000s of km s^{-1}, which can occur due to GW recoil following a BH merger. To calculate the trajectories of recoiling SMBHs in a galactic potential, we have developed an analytical model that includes a stellar bulge and a multi-component gaseous disk. The SMBH mass and gas fraction are free parameters that we varied in four different cases (Models A-D). For bound trajectories, we examined the dynamics and the wandering timescales of the SMBHs, as well as the effect of this wandering on SMBH growth.

Surprisingly, the kick velocity, $v_{\rm k}$, has little effect on the amount of mass accreted onto the SMBH while it wanders through the galaxy. For all cases, the fractional SMBH growth, $\Delta M/M_{\rm BH}$, is roughly 10% over the time from the recoil kick to when the BH settles back to the galactic center. This is primarily the combined result of two different effects: the total wandering time is short for low $v_{\rm k}$, where the BH quickly settles back to the center, and the accretion time is short for high $v_{\rm k}$, where the accretion disk bound to the BH is small. Due to these competing factors, the timescale for off-center accretion, and hence the amount of growth in this time, remains almost constant for all $v_{\rm k}$. Additionally, bursts of accretion during subsequent disk crossings contribute little to the total BH mass. The consistency of $\Delta M/M_{\rm BH}$ implies that GW recoil is an effective

means of self-regulation for SMBH growth. If the SMBH remained stationary at the galactic center, substantial growth could occur. This growth could be regulated via more conventional processes such as energy or momentum feedback, but these depend on the details of the gas physics and may vary greatly in different galactic environments. In contrast, GW recoil depends only on the parameters of the merging SMBH progenitors. It is also interesting to note that because other feedback processes will be halted when the recoiling SMBH has depleted its reservoir of bound gas, these two methods of growth regulation are complementary. The possibility that both wandering and stationary SMBHs self-regulate their masses indicates how recoiling BHs could be consistent with the observed $M_{\rm BH} - \sigma_*$ relation, even if large recoils $\lesssim v_{\rm esc}$ are not rare occurrences. The latter conclusion assumes, of course, that the escape fraction of recoiling SMBHs is still small; otherwise we would expect to see more scatter in the $M_{\rm BH} - \sigma_*$ relation (Libeskind et al. 2006; Volonteri 2007) or galaxies without a central SMBH in the local universe, which are not observed (e.g., Kormendy & Richstone 1995; Richstone et al. 1998; Ferrarese & Ford 2005).

Even small recoil kicks can have a significant impact on accretion and feedback processes. For the lowest kick we consider, $v_{\rm k} = 100$ km s^{-1}, the BH wanders in the galaxy core for a few Myr before settling back to the center and carries along a large accretion disk. Thus, feedback from moving sources will be distributed over much larger volumes than the emitting regions of stationary AGN. For example, in our fiducial model, a BH kicked at 100 km s^{-1} reaches ~ 30 pc before turning around. Assuming most of the AGN emission originates from a region $\sim 10^2 - 10^3\ r_{\rm S}$ across, the initial volume in which energy is released by the BH increases by about 8 orders of magnitude in this case. Most of the energy will be deposited at the largest radii, since turnaround takes

the largest fraction of the orbital time. This implies an even greater disparity between the impact of moving and stationary BHs on their surrounding environments.

The importance of GW recoil in the evolution of SMBHs clearly depends on how often significant recoil kicks occur. This is difficult to estimate, because the recoil kick distribution depends on the spin and mass ratio distributions of the progenitor BH binaries, which are not well known. Schnittman & Buonanno (2007), Campanelli et al. (2007a), & Baker et al. (2008) have calculated kick distributions; Schnittman & Buonanno (2007) use an approximate method, and the latter two derive empirical formulae from numerical relativity simulations. The differences in the results of the latter two stem from different assumptions of how the kick velocity scales with BH progenitor mass ratio. Assuming BH spins of $a = 0.9$, mass ratios in the range $1/10 \leq q \leq 1$, and random spin orientations, the three groups respectively estimate that $(12, 36, \& 23\%)$ of recoiling BHs will have $v_{\rm k} > 500$ km s^{-1} and $(3, 13, \& 9\%) > 1000$ km s^{-1}. Note that these fractions are not insignificant, although they might be much smaller if BH spins are on average lower or are preferentially aligned (cf. Bogdanović et al. 2007). To constrain the actual recoil kick distribution, better observational constraints on merging BHs or observations of individual recoiling BHs will be required.

Our results indicate that the latter method for constraining GW recoil, i.e. direct observations of recoiling BHs, will be challenging, because several factors make recoiling BHs difficult to observe. First, the BH must be actively accreting to appear as an observable source. The recoil could be observed either via spatial offsets from the galactic nucleus or via velocity offsets in the quasar spectrum. In both cases, larger offsets resulting from large recoil kicks are more easily observable, but large kicks imply a small disk bound to the BH and thus a short off-center quasar duty cycle. After it

exhausts its supply of bound gas, the moving BH could again become an active source on subsequent passages through the galactic gas disk, an effect which could be observed as a velocity offset in its spectrum. This could also be a source of periodic quasar or disk flare activity. However, the greater the velocity offset, the shorter the duty cycle for these "disk crossing" quasars, since they pass rapidly through the relatively thin galactic disk. It is worth emphasizing that because our results indicate that GW recoil may be difficult to observe directly and that the growth of wandering BHs may be consistent with observed galaxy-BH relations, neither of these observational methods may be able to rule out a significant population of recoiling BHs.

If, indeed, GW recoil is a relatively common phenomenon in SMBH mergers, this represents a fundamental change in our understanding of SMBH-galaxy coevolution, because we cannot gain a complete picture by considering only stationary SMBHs. In reality, GW recoil and AGN feedback are likely to work together to produce the observed SMBH-galaxy relations.

Chapter 3

Recoiling Black Holes in Merging Galaxies: Relationship to AGN Lifetimes, Starbursts, and the $M_{BH} - \sigma_*$ Relation

L. Blecha, T. J. Cox, A. Loeb, & L. Hernquist *The Monthly Notices of the Royal Astronomical Society*, Vol. 412, pp. 2154-2182, 2011

Abstract

Gravitational-wave (GW) recoil of merging supermassive black holes (SMBHs) may influence the co-evolution of SMBHs and their host galaxies. We examine this possibility

using SPH/N-body simulations of gaseous galaxy mergers, including SMBH accretion, in which the merged BH receives a recoil kick. This enables us to follow the trajectories and accretion of recoiling BHs in self-consistent, evolving merger remnants. In contrast to recent studies on similar topics, we conduct a large parameter study, generating a suite of over 200 simulations with more than 60 merger models and a range of recoil velocities ($v_{\rm k}$). With this, we can identify systematic trends in the behavior of recoiling BHs. Our main results are as follows. (1) BHs kicked at nearly the central escape speed ($v_{\rm esc}$) may oscillate on large orbits for up to a Hubble time, but in gas-rich mergers, BHs kicked with up to $\sim 0.7\ v_{\rm esc}$ may be confined to the central few kpc of the galaxy, owing to gas drag and steep central potentials. (2) $v_{\rm esc}$ in gas-rich mergers may increase rapidly during final coalescence, in which case recoil trajectories may depend sensitively on the *timing* of the BH merger relative to the formation of the central potential well. Delays of even a few $\times 10^7$ yr in the BH merger time may substantially suppress recoiling BH motion for a fixed kick speed. (3) Recoil events generally reduce the lifetimes of bright active galactic nuclei (AGN), but short-period recoil oscillations may actually *extend* AGN lifetimes at lower luminosities. (4) Bondi-Hoyle accretion dominates recoiling BH growth for $v_{\rm k}/v_{\rm esc} \lesssim 0.6-0.8$; for higher $v_{\rm k}$, the BH accretes primarily from its ejected gas disk, which we model as a time-dependent accretion disk. (5) Kinematically-offset AGN may be observable either immediately after a high-velocity recoil or during pericentric passages through a gas-rich remnant. In either case, AGN lifetimes may be up to ~ 10 Myr (for $\Delta v > 800$ km s^{-1}), though the latter generally have higher luminosities. (6) Spatially-offset AGN can occur for $v_{\rm k} \gtrsim 0.5 - 0.7\ v_{\rm esc}$ (for $\Delta R > 1$ kpc); these generally have low luminosities and lifetimes of $\sim 1 - 100$ Myr. (7) Rapidly-recoiling BHs may be up to ~ 5 times less massive than their stationary counterparts. These mass deficits

lower the normalization of the $M_{\rm BH} - \sigma_*$ relation and contribute to both intrinsic and overall scatter. (8) Finally, the displacement of AGN feedback after a recoil event enhances central star formation rates in the merger remnant, thereby extending the starburst phase of the merger and creating a denser, more massive stellar cusp.

3.1 Introduction

Within the hierarchical structure formation paradigm, a significant fraction of galaxy growth occurs via successive mergers. Given the ample evidence that most, if not all, local galaxies host central supermassive black holes (SMBHs; e.g., Kormendy & Richstone 1995; Richstone et al. 1998; Ferrarese & Ford 2005), major galaxy mergers (those with mass ratios $q \gtrsim 0.25$) should inevitably result in the formation of SMBH binaries. The fate of these binaries is somewhat uncertain and likely depends on the conditions within their host galaxies. In highly spheroidal, gas-poor galaxies, these binaries may "stall" at separations of about a parsec for up to a Hubble time (e.g., Begelman et al. 1980; Milosavljević & Merritt 2001; Yu 2002). In gas-rich galaxy mergers, however, gas is driven to the central region of the merging galaxies simultaneously with the formation of the SMBH binary. Numerical simulations indicate that BH merger timescales may be much shorter than galaxy merger timescales in this case ($\sim 10^6 - 10^7$ yr from the hard binary stage; e.g., Escala et al. 2005; Dotti et al. 2007). This implies that the SMBH binaries most able to accrete gas and produce electromagnetic signatures are likely to be short-lived.

To date, observations seem to confirm this scenario. Several quasar *pairs* with kpc-scale separations have been found in merging galaxies (Komossa et al. 2003; Bianchi

et al. 2008; Comerford et al. 2009a; Green et al. 2010). Recently, spectroscopic and photometric observations have found that between $10^{-3} - 10^{-2}$ of active galactic nuclei (AGN) at $z \lesssim 0.7$ may in fact contain dual BHs with separations of $\sim$ kpc (Comerford et al. 2009b; Smith et al. 2010; Liu et al. 2010b,a; Smith et al. 2010; Fu et al. 2010). However, only one unambiguous case of a SMBH *binary* has been found, with a separation of ~ 7 pc (Rodriguez et al. 2006). Several additional objects have been identified as candidate SMBH binaries but are still unconfirmed (Sillanpaa et al. 1988; Komossa et al. 2008; Dotti et al. 2009; Bogdanović et al. 2009; Boroson & Lauer 2009). Thus, it is clear that the large majority of AGN do not contain binary SMBHs, which suggests that any substantial population of long-lived SMBH binaries must exist in gas-poor environments where they are quiescent.

If most binaries are therefore assumed to merge on reasonably short timescales, then gravitational-wave (GW) recoil must be a common phenomenon throughout the merger history of galaxies. GW recoil is a natural consequence of gravitational radiation from BH binary mergers (Peres 1962; Bekenstein 1973; Fitchett & Detweiler 1984). If the binary system has any asymmetry – unequal masses, spins or spin orientations – then gravitational waves are radiated asymmetrically, resulting in a net linear momentum flux from the final BH at the time of merger. This causes the BH to recoil in the opposite direction. Whether these recoil kicks were large enough to be astrophysically interesting was uncertain until a few years ago, because accurate calculations of the recoil velocity require BH merger simulations using full general relativity. These simulations have revealed that GW recoils may be quite large. Recoil velocities up to 4000 km s^{-1} are possible for special configurations, which is far greater than galactic escape speeds (Campanelli et al. 2007a,b). The implication that SMBHs may spend substantial time in

motion and off-center has opened a new line of inquiry into the ramifications for SMBHs and their host galaxies.

A useful starting point for such inquiries would be the distribution of recoil kick velocities, but this is quite difficult to ascertain in practice. The final velocity depends sensitively on not just the mass ratio of the progenitor BHs, but on their spin magnitudes and orientations as well. The distributions of SMBH binary mass ratios and spins at various redshifts have been estimated using halo merger trees and semi-analytical models of SMBH growth (e.g., Volonteri et al. 2003, 2005; King et al. 2008; Berti & Volonteri 2008). These distributions depend on a number of model assumptions, however, and the BH spin *orientations* prior to merger are far more uncertain still. Thus, based on recent results from BH merger simulations using full numerical relativity (NR), several groups have calculated kick probability distributions as a function of BH mass ratio for either fixed or random values of BH spin, with the assumption that the spins are randomly oriented (Schnittman & Buonanno 2007; Campanelli et al. 2007a; Baker et al. 2008; Lousto et al. 2010a,b; van Meter et al. 2010). Their results are in good agreement with each other and imply that the fraction of high-velocity GW recoils is substantial. This underscores the potential for recoil events to be an important component of galaxy mergers.

It is quite possible, of course, that the spins of SMBH binaries are not randomly oriented, but are preferentially aligned in some way. Bogdanović et al. (2007) have suggested that torques in a circumbinary gas disk may align the BH spins with the orbital axis of the disk. In this case, the resulting in-plane kicks would hsave a maximum recoil velocity of < 200 km s^{-1}, although spins that became anti-aligned by the same mechanism could result in recoil velocities up to 500 km s^{-1} (e.g., González et al. 2007b;

Campanelli et al. 2007a; Baker et al. 2008). Additionally, simulations by Dotti et al. (2010) demonstrate efficient spin alignment of merging BHs in the presence of a highly coherent accretion flow, although it is unclear how efficient this process might be in a gaseous environment that includes, e.g., star formation. Kesden et al. (2010) have recently demonstrated that BH spin alignment may instead occur via relativistic spin precession, regardless of whether a gas disk is present. The aforementioned recoil kick probability distributions are therefore upper limits on the actual distributions.

Numerous possible consequences of GW recoil events have been discussed in the literature. GW recoils may have a large effect at high redshifts, where escape velocities of galaxies are smaller (e.g., Merritt et al. 2004; Madau & Quataert 2004; Volonteri 2007). This is a concern for attempts to understand, for example, the origin of the $z = 6$ SDSS quasars (e.g., Fan et al. 2001, 2003). Volonteri & Rees (2006) suggest that growth of SMBHs at high z must occur only in highly-biased halos. Using cosmological hydrodynamic simulations, Sijacki et al. (2009) investigate BH growth in massive high-z halos, including the ejection of BHs with recoil velocities above $v_{\rm esc}$. Their findings are consistent with the observed populations of bright quasars at $z = 6$, despite the effects of GW recoil.

At lower redshifts, recoiling BHs may produce electromagnetic signatures. The main signatures we will focus on here are recoiling AGN that are either spatially or kinematically offset from their host galaxies (Madau & Quataert 2004; Loeb 2007; Blecha & Loeb 2008; Komossa & Merritt 2008a; Guedes et al. 2009). Other possible signatures include flares from shocks induced by fallback of gas marginally bound to the ejected BH (Lippai et al. 2008; Shields & Bonning 2008; Schnittman & Krolik 2008), enhanced rates of stellar tidal disruptions (Komossa & Merritt 2008b; Stone & Loeb 2010), and compact

stellar clusters around ejected BHs (O'Leary & Loeb 2009; Merritt et al. 2009).

Thus far, no confirmed GW recoil events have been observed. An inherent challenge in observing offset quasars is that larger spatial or kinematic offsets are easier to resolve, but less gas will be bound to the recoiling BH at higher recoil velocities, so its AGN lifetime will be shorter. Bonning et al. (2007) conducted a search for kinematic offsets in SDSS quasar spectra and found a null result at a limit of 800 km s^{-1}. Several recoil candidates have been proposed, but their extreme inferred velocities should be exceedingly rare. Indeed, the recoil candidate with a 2600 km s^{-1} offset, proposed by Komossa et al. (2008), may in fact be a superposition of two galaxies (Heckman et al. 2009; Shields et al. 2009a) or a binary SMBH system (Dotti et al. 2009; Bogdanović et al. 2009). Another candidate with an even higher (3500 km s^{-1}) offset is most likely a double-peaked emitter (Shields et al. 2009b). Recently, Civano et al. (2010) have suggested that an unusual galaxy discovered in the COSMOS survey by Comerford et al. (2009a), which those authors proposed to be a dual SMBH system, may in fact be a recoiling BH, as new spectra indicate a kinematic offset of 1200 km s^{-1}. This candidate has a less extreme velocity than the others, but further observations are needed to confirm the nature of this object.

In addition to producing direct observational signatures, GW recoil may play a role in the co-evolution of SMBHs and their host galaxies. Strong empirical correlations exist between SMBH mass and properties of the host galaxy bulge, including the bulge luminosity, mass, and stellar velocity dispersion (e.g., Kormendy & Richstone 1995; Magorrian et al. 1998; Gebhardt et al. 2000; Ferrarese & Merritt 2000; Merritt & Ferrarese 2001; Tremaine et al. 2002a; Marconi & Hunt 2003). These correlations are well-reproduced by galaxy formation models in which much of BH and galaxy

bulge growth occurs via successive mergers, and in which merger-triggered BH fueling is self-regulated via AGN feedback (e.g., Silk & Rees 1998; Wyithe & Loeb 2003; Di Matteo et al. 2005; Hopkins et al. 2006a). However, because GW recoil events may occur simultaneously with this rapid BH accretion phase, recoils could significantly disrupt the coordinated growth of BHs and galaxy bulges. In particular, GW recoil may contribute to scatter in the $M_{\rm BH} - \sigma_*$ relation caused by ejected (Volonteri 2007) or bound recoiling (Blecha & Loeb 2008; Sijacki et al. 2010) BHs; we will examine the latter possibility in greater detail. It is also unclear *a priori* what effects, if any, GW recoil may have on the host galaxies themselves. In purely collisionless galaxies, Boylan-Kolchin et al. (2004) and Gualandris & Merritt (2008) have shown that bound recoiling BHs may scour out a stellar core. In gas-rich galaxy mergers, copious of amounts of cold gas are driven to the central galactic region during coalescence, triggering a luminous starburst such that the galaxy may appear as a ULIRG (Sanders et al. 1988a; Sanders & Mirabel 1996). Feedback from a central AGN may terminate this the starburst phase by expelling gas and dust from the central region (e.g., Hopkins et al. 2006a, 2008b; Somerville et al. 2008). We will investigate whether observable starburst properties or gas and stellar dynamics may be affected by the sudden displacement of this central AGN via recoils (see also recent work by Sijacki et al. 2010).

Our current work was initiated as a follow-up of Blecha & Loeb (2008), hereafter BL08. BL08 explored the trajectories and accretion of BHs on bound orbits in a static potential with stellar bulge and gaseous disk components. They found that recoil kicks $\lesssim v_{\rm esc}$ could produce long-lived ($\gtrsim$ Gyr) oscillations of the BH; similar results were found by Gualandris & Merritt (2008), Kornreich & Lovelace (2008) & Guedes et al. (2009). BL08 also demonstrated that GW recoil can affect SMBH growth even when the

BH is not ejected entirely from the host galaxy. By removing accreting BHs from the central dense region and thereby limiting the BH's fuel supply, BHs receiving recoil kicks $\gtrsim 0.5\ v_{\rm esc}$ may be less massive than stationary BHs.

In the present study, we use hydrodynamic simulations to self-consistently calculate the dynamics and accretion of recoiling BHs in realistic merger remnant potentials. We simulate galaxy mergers using GADGET-3 (Springel 2005), an SPH/N-body code, and apply a recoil kick to the BH at the time of BH merger. Due to the detailed initial conditions and many free parameters involved in such merger simulations, we conduct a large parameter study with dozens of galaxy merger models and a wide range of kick velocities. Each merger model is simulated with at least one kick velocity and also with no recoil kick, for comparison. With this suite of recoil simulations, we are able to observe trends in the behavior of recoiling BHs in different environments. When paired with our time-dependent, sub-resolution models for recoiling BH accretion, this approach allows us to, for example, determine velocity-dependent recoiling AGN lifetimes and estimate the effect of GW recoil on scatter in the $M_{\rm BH} - \sigma_*$ relation.

As this paper was in the final stages of preparation, two papers appeared that also involve hydrodynamic simulations of recoiling BHs in galaxy merger remnants (Guedes et al. 2010; Sijacki et al. 2010). However, each study used only a few simulations, probing only a small part of parameter space. Guedes et al. (2010) used results of three merger simulations as initial conditions, and ran hydrodynamic simulations of recoiling BHs in these merger remnants for a short time. These initial trajectories were used to calibrate semi-analytic calculations of the recoil trajectory in the remnant potential. A range of kick velocities was tested in each of the three merger models used. Sijacki et al. (2010) simulate recoils in an isolated, stable disk galaxy; they also use this galaxy model as the

initial condition for a full merger simulation with GW recoils. Both studies also include prescriptions for accretion onto recoiling BHs. We provide a comparison of our results to the findings of these papers in § 3.6.

Our simulation methods, GW recoil treatment, and galaxy merger models are outlined in § 3.2. § 3.3 - 3.5 contain our results, organized as follows. In § 3.3, the general characteristics of our galaxy merger simulations with stationary central BHs (i.e., no recoil kicks). We discuss the variation in merger dynamics and remnant morphologies between models. In § 3.4, the dynamics of recoiling BHs are discussed. We describe the general characteristics of recoil trajectories and trends between models in § 3.4.1. In § 3.4.2, we analyze the sensitivity of recoil trajectories to the BH merger time, and in § 3.4.3 we investigate the dependence of recoil trajectories on the direction of the kick. § 3.5 contains our results for the accretion and feedback of recoiling BHs. In § 3.5.1, we examine accretion and feedback of recoiling BHs, compare to the fueling of stationary BHs, and calculate AGN lifetimes from Bondi-Hoyle accretion. In § 3.5.2, we describe our time-dependent analytic model for calculating accretion onto a recoiling BH from a disk of gas ejected with the BH. Using this accretion model, along with accretion from ambient gas, we present in § 3.5.3 the velocity-dependent AGN luminosities and active lifetimes for recoiling BHs. In particular, we calculate lifetimes for spatially-offset and kinematically-offset recoiling AGN. In § 3.5.4, we compare the $M_{\rm BH} - \sigma_*$ relations derived from our set of no-recoil simulations and our set of high-velocity recoil simulations, and discuss implications for the observed $M_{\rm BH} - \sigma_*$ relation. Finally, in § 3.5.5, we explore the effects of GW recoil on star formation rates and the host galaxy structure. We summarize and discuss our results in § 3.6.

3.2 Simulations

For our simulations of galaxy mergers, we employ the smoothed particle dynamics (SPH) code GADGET-3 (Springel 2005), which conserves both energy and entropy (Springel & Hernquist 2002). The code includes radiative cooling as well as a subresolution model for a multiphase interstellar medium (ISM) (Springel & Hernquist 2003) that accounts for star formation and supernova feedback. In addition, the code models BHs as gravitational "sink" particles that contain a BH seed and a gas reservoir. The reservoir is replenished by stochastic accretion of neighboring gas particles, but the actual accretion rate onto the BH is calculated smoothly using the Bondi-Hoyle-Lyttleton formula with locally-averaged values for the density and sound speed. Angular momentum is conserved during accretion of gas particles, but because this is a stochastic process owing to the finite mass resolution, we also introduce an analytic accretion drag force ($\propto \dot{M}\, v$) calculated from the Bondi accretion rate at each timestep. These prescriptions are described in more detail in Springel et al. (2005b).

Because we are presently interested in GW recoil, we allow for an arbitrary velocity to be added to the remnant BH at the time of the BH merger, $t_{\rm mrg}$. To more easily compare recoil events in different merger models, we scale this velocity to the central escape speed at the time of merger, $v_{\rm esc}(t_{\rm mrg})$. We define $v_{\rm esc} = \sqrt{-2\Phi(\mathbf{x}_{\rm BH})}$ at each timestep, i.e., the escape speed at the position of the BH, which is close to the position of the potential minimum in the absence of a recoil kick. Campanelli et al. (2007a), Baker et al. (2008), & van Meter et al. (2010) have all fit distributions to the data from full NR simulations of BH mergers, with results in good agreement. For major mergers ($0.25 < q < 1$, the range we consider in our simulations), high spins ($a_1 = a_2 = 0.9$),

and randomly-distributed spin orientations, van Meter et al. (2010) find that 69.8% of recoil kicks will be above 500 km s^{-1} and 35.3% will be above 1000 km s^{-1}. If the BH spin magnitudes are also randomly distributed ($0 \leq a_1, a_2 \leq 1$), the these fractions are 41.6% and 13.5%. Our fiducial-mass merger simulations (described below) have $v_{\rm esc} = 689 - 1248$ km s^{-1}, and we also use low-mass simulations with $v_{\rm esc}$ as low as 338 km s^{-1}. The NR results indicate that there is a substantial probability of BHs in these models receiving kicks up to $\sim v_{\rm esc}$. In our high-mass simulations, however, $v_{\rm esc} = 1737 - 2555$ km s^{-1}, so the probability of recoil events with $v_{\rm k} \sim v_{\rm esc}$ is much lower in these models.

We also slightly modify the treatment of BH mergers in the code. In the standard GADGET prescription, the BHs merge when they are separated by less than a gravitational softening length ($a_{\rm sep} < R_{\rm soft}$) and have a relative velocity $v_{\rm rel} < 0.5\, c_{\rm s}$, where $c_{\rm s}$ is the local sound speed. If, as can happen in gas-rich mergers, the central escape velocity is increasing rapidly when the BHs merge, small variations in $t_{\rm mrg}$ can result in very different BH trajectories (see Fig. 3.8). In order to reliably compare results from different simulations, we therefore force the BHs to merge at a given time that is predetermined as follows. We define the "coalescence time" $t_{\rm coal}$ as the earliest time after which the BH binary is tight enough that it could plausibly merge. Given the numerical uncertainties near the spatial resolution limit, we generously choose $t_{\rm coal}$ to be the time when the BH separation falls below $a_{\rm sep} = 10\, R_{\rm soft}$ (and $v_{\rm rel} < 0.5\, c_{\rm s}$, as before). For reference, $R_{\rm soft} = 80$ pc in our fiducial-mass simulations (see below). Then, restarting the simulation slightly before $t_{\rm coal}$, we force the BHs to merge at a predetermined time $t_{\rm mrg} \geq t_{\rm coal}$. $t_{\rm mrg}$ can then be varied as a free parameter, allowing us to systematically probe the range of possible BH merger times. In practice, this is

only necessary for nearly equal-mass, gas-rich mergers in which $v_{\rm esc}$ varies significantly throughout the merger. In other cases the results are insensitive to the choice of merger time, so $t_{\rm mrg}$ is simply chosen to be $t_{\rm coal}$.

For the majority of our simulations, we use the same total mass, 1.36×10^{12} $M_\odot$, for the primary galaxy, and scale the secondary to yield the desired mass ratio. The exception is a small subset of simulations with lower and higher total mass, described below. For all of our "fiducial mass" simulations, we use a gravitational softening length of $R_{\rm soft} = 80$ pc for baryons and $R_{\rm soft,DM} = 240$ pc for the dark matter (DM). In each galaxy, 4.1% of the total mass is in a baryonic disk component. The primary galaxy has $N_{\rm halo} = 4.8 \times 10^5$ DM halo particles, and for $f_{\rm gas} = 0.4$ it has $N_{\rm disk} = 3.2 \times 10^5$ disk particles, with equal numbers of gas and star particles. In all other models, $N_{\rm halo}$ and $N_{\rm disk}$ are set such that the same particle mass resolution is maintained for each component ($m_{\rm star} = 4.2 \times 10^5$ $M_\odot$, $m_{\rm gas} = 2.8 \times 10^5$ $M_\odot$, & $m_{\rm halo} = 5.4 \times 10^6$ $M_\odot$).

Each galaxy is given a single BH particle, which as previously stated, consists of a "seed" BH along with a gas reservoir from which an accretion rate is calculated smoothly. We use a small initial seed mass for the BH, 1.43^5 $M_\odot$, in accordance with the $M_{\rm BH}$ - $M_{\rm bulge}$ (Magorrian et al. 1998) relation, because our initial galaxies are pure disks with no bulge component. We find that our results are insensitive to the choice of seed mass. The total mass of this hybrid particle is the "dynamical" mass of the BH; this is the mass that is used for gravitational force calculations. This dynamical BH mass is set to 10^{-5} of the total galaxy mass initially. This value is chosen such that the seed mass and dynamical mass have similar values by the time of the recoil kick, to avoid a disparity between the mass used for gravitational forces and that used for accretion physics of the recoiling BH. To help ensure that the BH remains in the center of the galaxy prior

to the BH merger and recoil kick, we set the accretion drag force equal to its value for Eddington-limited accretion prior to the BH merger (though the actual accretion rate is still calculated self-consistently based on the Bondi-Hoyle formula). Once the BHs merge, the accretion drag force is calculated using the actual Bondi-Hoyle accretion rate for the remainder of the simulation.

Our set of fiducial-mass simulations covers a wide range of galaxy mass ratios and gas fractions, but in order to probe the effects of GW recoil on black hole - host galaxy relationships, as we do in § 3.5.4, we require a larger range in total galaxy mass. We have run a sample of seven high and low mass simulations with a primary galaxy mass ranging from 0.05 - 20 times the fiducial primary mass, which we refer to as M_0. For the lower-mass runs, we maintain the same number of particles as in the fiducial simulations, such that higher mass resolution is achieved. Accordingly, we reduce the softening lengths in these simulations by $(M/M_0)^{1/3}$. For the higher-mass runs ($M_0 \times 10$ & $M_0 \times 20$), an increase in particle number by this factor would be prohibitively computationally expensive, so we instead increase the particle number by a factor of 5 in each case, compromising a factor of 2 and 4 in mass resolution, respectively. In the latter case, we maintain a reasonable $M_{\rm BH}/M_{\rm particle}$ ratio by increasing the initial dynamical mass by a factor of 10.

In order to evaluate the sensitivity of our results to numerical artifacts such as the choice of mass resolution, softening length, and integration accuracy, we have run a number of additional simulations in which we systematically vary these parameters. In addition to these tests, two of the models included in our results have higher mass resolution (and correspondingly higher spatial resolution) than our fiducial runs: our low-mass merger models have the same number of particles as our fiducial-mass models

and thus have 10 and 20× higher mass resolution. Higher mass and spatial resolution reduce the noisiness of the potential, and varying the resolution changes the detailed structure of the gas, especially in the highest density regions. Higher integration accuracy also reduces numerical noise. Consequently, the exact trajectory, and hence the settling time, of a given recoil event will be affected to some extent by these numerical factors. However, the variation in recoil trajectories for different choices of resolution and integration accuracy are small compared to the differences for varying kick speed and merger remnant properties. We also define the settling radius of the BH to be $4\,R_{\rm soft}$ to avoid sensitivity of our conclusions to the BH motion in the innermost galaxy region where the softened potential may dominate. Most importantly, for all choices of mass resolution, spatial resolution, and integration accuracy parameters tested, the qualitative behavior of the recoiling BHs and the relative differences between simulations are robust. Therefore our main results do not depend on these numerical factors.

Table 3.1 lists the parameters for the galaxy merger models we have constructed. We have tested a total of 62 different galaxy merger models in which we vary the galaxy mass ratio (q), the gas fraction ($f_{\rm gas}$), the orbital configuration. 55 of these models use the "fiducial" primary galaxy mass, and for easier reference we assign each of these a name given by q[*value*]fg[*value*][*orb*], where "q" denotes the galaxy mass ratio, "fg" denotes the initial gas fraction, and each letter *orb* is identified with a specific orbital configuration. The remaining seven models have higher or lower total mass and are referred to by q[*value*]fg[*value*]M[*factor*][*orb*], where "M" denotes the total galaxy mass relative to the equivalent fiducial-mass galaxy.

In all cases, the orbital configuration is specified by six parameters, and the galaxies are initially set on parabolic orbits. The choice of impact parameter for the first

pericentric passage, $R_{\rm peri}$, and initial galaxy separation, $a_{\rm i}$, determine the initial orbital energy and angular momentum. In our fiducial-mass models, we set $a_{\rm i} = 143$ kpc and $R_{\rm peri} = 7.1$ kpc, except for orbit "b", which has $R_{\rm peri} = 14.3$ kpc. In our high- and low-mass models, $a_{\rm i}$ and $R_{\rm peri}$ are scaled such that $a_{\rm i}$ is the same fraction (0.625) of the virial radius, R_{200}, and $a_{\rm i}/R_{\rm peri} = 20$. We denote these orbits with letters w - z to differentiate them from the orbits a - k of our fiducial-mass mergers. Note that the orbital parameters do not remain constant as the merger progresses, owing to energy losses via dynamical friction. The angles (θ_1, ϕ_1) and (θ_2, ϕ_2) determine the initial orbital phase and inclination, respectively, of each galaxy. These angles, as well as $R_{\rm peri}$ for each galaxy model are given in Table 3.1. Our fiducial merger orbit (orbit "a") is a "generic" orbit, in that no symmetries exist in the initial orientation angles of the disks. Note that many of these orbits are identical to those used in Cox et al. (2006) and Robertson et al. (2006a).

For each model, we run a merger simulation in which the BHs are not allowed to merge. From this we can determine $t_{\rm coal}$, which is used to set $t_{\rm mrg}$. Then, restarting slightly before $t_{\rm mrg}$, we simulate both a merger with no recoil kick and a merger with $v_{\rm k}/v_{\rm esc} = 0.9$. For the models shown in boldface in Table 3.1, we also simulate recoil kicks with $v_{\rm k}/v_{\rm esc} = 0.4, 0.5, 0.6, 0.7, 0.8, 1.0, 1.1$, and 1.2. Each simulation is run for 2.9 Gyr after $t_{\rm mrg}$. Finally, using the q0.5fg0.3a model, we simulate a small sample of recoil kicks with varying kick orientation $(\theta_{\rm k}, \phi_{\rm k})$, the results of which are discussed in § 3.4.3.

Table 3.1

	Initial model parameters									Resulting merger quantities			
Model	q	$M_{\rm tot}$	$M_{\rm disk}$	$f_{\rm gas}$	$R_{\rm peri}$	θ_1	ϕ_1	θ_2	ϕ_2	$t_{\rm mrg}$	$v_{\rm esc}(t_{\rm mrg})$	$v_{\rm esc,max}$	% diff.
		[10^{10} M$_\odot$]	[10^{10} M$_\odot$]		[kpc]	[deg]	[deg]	[deg]	[deg]	[Gyr]	[km s^{-1}]	[km s^{-1}]	
q1fg0.6a	**1.0**	**272.1**	**11.16**	**0.6**	**7.1**	**30**	**60**	**-30**	**45**	**1.55**	**1258**	**1494**	**18.7**
q1fg0.5a	1.0	272.1	11.16	0.5	7.1	30	60	-30	45	1.58	1157	1568	35.6
q1fg0.4a	1.0	272.1	11.16	0.4	7.1	30	60	-30	45	1.60	1102	1472	33.6
q1fg0.3a	**1.0**	**272.1**	**11.16**	**0.3**	**7.1**	**30**	**60**	**-30**	**45**	**1.63**	**1118**	**1337**	**19.6**
q1fg0.3b	1.0	272.1	11.16	0.3	14.3	30	60	-30	45	2.01	1165	1256	7.8
q1fg0.3c	1.0	272.1	11.16	0.3	7.1	150	60	-30	45	1.70	1113	1264	13.6
q1fg0.3d	1.0	272.1	11.16	0.3	7.1	150	0	-30	45	1.69	1152	1271	10.4
q1fg0.3e	1.0	272.1	11.16	0.3	7.1	90	60	-30	45	1.76	970	1194	23.1
q1fg0.3M20w	1.0	5442	223.1	0.3	19.4	30	60	-30	45	1.54	2555	2727	6.7
q1fg0.3M10x	1.0	2721	111.6	0.3	15.4	30	60	-30	45	1.69	2067	2290	10.8
q1fg0.3M0.1y	1.0	27.21	1.116	0.3	3.3	30	60	-30	45	1.60	457	641	40.3
q1fg0.3M0.05z	1.0	13.61	0.5578	0.3	2.7	30	60	-30	45	2.00	338	497	47.0
q1fg0.2a	1.0	272.1	11.16	0.2	7.1	30	60	-30	45	1.67	1049	1182	12.6
q1fg0.1a	**1.0**	**272.1**	**11.16**	**0.1**	**7.1**	**30**	**60**	**-30**	**45**	**1.72**	**876**	**931**	**6.3**
q1fg0.1b	1.0	272.1	11.16	0.1	14.3	30	60	-30	45	2.09	921	923	0.2
q1fg0.1c	1.0	272.1	11.16	0.1	7.1	150	60	-30	45	1.80	891	956	7.3

Continued on Next Page...

Table 3.1 – Continued

	Initial model parameters									Resulting merger quantities			
Model	q	$M_{\rm tot}$	$M_{\rm disk}$	$f_{\rm gas}$	$R_{\rm peri}$	θ_1	ϕ_1	θ_2	ϕ_2	$t_{\rm mrg}$	$v_{\rm esc}(t_{\rm mrg})$	$v_{\rm esc,max}$	% diff.
		[10^{10} M$_\odot$]	[10^{10} M$_\odot$]		[kpc]	[deg]	[deg]	[deg]	[deg]	[Gyr]	[km s^{-1}]	[km s^{-1}]	
q1fg0.1d	1.0	272.1	11.16	0.1	7.1	150	0	-30	45	1.82	863	906	5.0
q1fg0.1e	1.0	272.1	11.16	0.1	7.1	90	60	-30	45	1.84	860	918	6.7
q1fg0.1M10x	1.0	2721	111.6	0.1	15.4	30	60	-30	45	1.74	1924	2033	5.7
q1fg0.04a	1.0	272.1	11.16	0.04	7.1	30	60	-30	45	1.76	823	848	3.1
q1fg0a	**1.0**	**272.1**	**11.16**	**0.0**	**7.1**	**30**	**60**	**-30**	**45**	**1.84**	**772**	**790**	**2.3**
q0.9fg0.4a	0.9	258.5	10.60	0.4	7.1	30	60	-30	45	1.61	1104	1455	31.8
q0.9fg0.3a	0.9	258.5	10.60	0.3	7.1	30	60	-30	45	1.65	1154	1337	15.9
q0.9fg0.1a	0.9	258.5	10.60	0.1	7.1	30	60	-30	45	1.74	866	918	6.1
q0.75fg0.4a	0.75	238.1	9.762	0.4	7.1	30	60	-30	45	1.69	1113	1302	17.1
q0.75fg0.3a	0.75	238.1	9.762	0.3	7.1	30	60	-30	45	1.73	1090	1225	12.3
q0.75fg0.1a	0.75	238.1	9.762	0.1	7.1	30	60	-30	45	1.83	810	867	7.1
q0.667fg0.4a	0.667	226.8	9.297	0.4	7.1	30	60	-30	45	1.68	1086	1219	12.3
q0.667fg0.3a	0.667	226.8	9.297	0.3	7.1	30	60	-30	45	1.73	883	1166	32.1
q0.667fg0.1a	0.667	226.8	9.297	0.1	7.1	30	60	-30	45	1.85	846	847	0.1
q0.5fg0.6a	**0.5**	**204.1**	**8.368**	**0.6**	**7.1**	**30**	**60**	**-30**	**45**	**1.88**	**914**	**1116**	**22.1**
q0.5fg0.5a	0.5	204.1	8.368	0.5	7.1	30	60	-30	45	1.89	963	1076	11.7

Continued on Next Page...

Table 3.1 – Continued

	Initial model parameters									Resulting merger quantities			
Model	q	$M_{\rm tot}$	$M_{\rm disk}$	$f_{\rm gas}$	$R_{\rm peri}$	θ_1	ϕ_1	θ_2	ϕ_2	$t_{\rm mrg}$	$v_{\rm esc}(t_{\rm mrg})$	$v_{\rm esc,max}$	% diff.
		[10^{10} M$_\odot$]	[10^{10} M$_\odot$]		[kpc]	[deg]	[deg]	[deg]	[deg]	[Gyr]	[km s^{-1}]	[km s^{-1}]	
q0.5fg0.4a	0.5	204.1	8.368	0.4	7.1	30	60	-30	45	1.95	893	983	10.1
q0.5fg0.4b	0.5	204.1	8.368	0.4	14.3	30	60	-30	45	2.46	965	1060	9.8
q0.5fg0.4c	0.5	204.1	8.368	0.4	7.1	150	60	-30	45	1.90	1024	1112	8.6
q0.5fg0.4d	0.5	204.1	8.368	0.4	7.1	150	0	-30	45	1.90	1061	1117	5.2
q0.5fg0.3a	**0.5**	**204.1**	**8.368**	**0.3**	**7.1**	**30**	**60**	**-30**	**45**	**1.97**	**993**	**994**	**0.1**
q0.5fg0.3b	0.5	204.1	8.368	0.3	14.3	30	60	-30	45	2.45	920	1003	9.0
q0.5fg0.3c	0.5	204.1	8.368	0.3	7.1	150	60	-30	45	1.97	1012	1017	0.5
q0.5fg0.3d	0.5	204.1	8.368	0.3	7.1	150	0	-30	45	1.92	1014	1069	5.4
q0.5fg0.3e	0.5	204.1	8.368	0.3	7.1	90	60	-30	45	2.05	915	1126	23.1
q0.5fg0.3f	0.5	204.1	8.368	0.3	7.1	90	0	0	0	1.94	978	1029	5.2
q0.5fg0.3g	0.5	204.1	8.368	0.3	7.1	60	60	150	0	2.23	805	820	1.9
q0.5fg0.3h	0.5	204.1	8.368	0.3	7.1	0	0	0	0	1.84	927	1111	19.8
q0.5fg0.3i	0.5	204.1	8.368	0.3	7.1	180	0	0	0	1.84	1028	1146	11.4
q0.5fg0.3j	0.5	204.1	8.368	0.3	7.1	180	0	180	0	2.09	823	930	13.0
q0.5fg0.3k	0.5	204.1	8.368	0.3	7.1	10	0	-10	0	1.84	1046	1087	4.0
q0.5fg0.3M10x	0.5	2041	83.68	0.3	15.4	30	60	-30	45	2.02	2081	2070	-0.5

Continued on Next Page...

Table 3.1 – Continued

	Initial model parameters									Resulting merger quantities			
Model	q	$M_{\rm tot}$	$M_{\rm disk}$	$f_{\rm gas}$	$R_{\rm peri}$	θ_1	ϕ_1	θ_2	ϕ_2	$t_{\rm mrg}$	$v_{\rm esc}(t_{\rm mrg})$	$v_{\rm esc,max}$	% diff.
		[10^{10} M$_\odot$]	[10^{10} M$_\odot$]		[kpc]	[deg]	[deg]	[deg]	[deg]	[Gyr]	[km s^{-1}]	[km s^{-1}]	
q0.5fg0.2a	0.5	204.1	8.368	0.2	7.1	30	60	-30	45	2.02	830	862	3.8
q0.5fg0.1a	**0.5**	**204.1**	**8.368**	**0.1**	**7.1**	**30**	**60**	**-30**	**45**	**2.12**	**777**	**798**	**2.7**
q0.5fg0.1b	0.5	204.1	8.368	0.1	14.3	30	60	-30	45	2.56	812	813	0.1
q0.5fg0.1c	0.5	204.1	8.368	0.1	7.1	150	60	-30	45	2.12	811	813	0.2
q0.5fg0.1d	0.5	204.1	8.368	0.1	7.1	150	0	-30	45	2.12	814	810	-0.5
q0.5fg0.1M10x	0.5	2041	83.68	0.1	15.4	30	60	-30	45	2.07	1737	1737	0.0
q0.5fg0.04a	0.5	204.1	8.368	0.04	7.1	30	60	-30	45	2.18	740	748	1.0
q0.5fg0a	**0.5**	**204.1**	**8.368**	**0**	**7.1**	**30**	**60**	**-30**	**45**	**2.30**	**689**	**706**	**2.4**
q0.333fg0.4a	0.333	181.4	7.438	0.4	7.1	30	60	-30	45	2.28	810	816	0.7
q0.333fg0.3a	0.333	181.4	7.438	0.3	7.1	30	60	-30	45	2.38	856	858	0.3
q0.333fg0.1a	0.333	181.4	7.438	0.1	7.1	30	60	-30	45	2.57	741	744	0.3
q0.25fg0.4a	0.25	170.1	6.974	0.4	7.1	30	60	-30	45	2.94	829	830	0.1
q0.25fg0.3a	0.25	170.1	6.974	0.3	7.1	30	60	-30	45	2.90	852	852	-0.1
q0.25fg0.1a	0.25	170.1	6.974	0.1	7.1	30	60	-30	45	3.18	722	725	0.3

Continued on Next Page...

Table 3.1 – Continued

	Initial model parameters									Resulting merger quantities			
Model	q	$M_{\rm tot}$	$M_{\rm disk}$	$f_{\rm gas}$	$R_{\rm peri}$	θ_1	ϕ_1	θ_2	ϕ_2	$t_{\rm mrg}$	$v_{\rm esc}(t_{\rm mrg})$	$v_{\rm esc,max}$	% diff.
		[10^{10} M$_\odot$]	[10^{10} M$_\odot$]		[kpc]	[deg]	[deg]	[deg]	[deg]	[Gyr]	[km s^{-1}]	[km s^{-1}]	

Table 3.1:: Galaxy merger models. Boldface entries denote those for which we have varied $v_{\rm k}$. Fiducial-mass merger models are labeled as q[*value*]fg[*value*][*orb*], where "q" is the galaxy mass ratio, "fg" is the initial gas fraction, and each letter *orb* corresponds to a specific orbit ("a" being our "fiducial" configuration). High- and low-mass models are denoted by q[*value*]fg[*value*]M[*factor*][*orb*], where "M" is the ratio of the primary galaxy mass to the fiducial mass.

3.3 Mergers Without GW Recoil

We begin by examining galaxy merger simulations with no GW recoil kick given to the BHs. Some basic characteristics of a galaxy merger simulation with $q = 0.5$ and $f_{\rm gas} = 0.3$ (our "fiducial" merger, model q0.5fg0.3a) are illustrated in Figs. 3.1 & 3.2. Fig. 3.1 shows the gas distribution at the time of BH merger, as well as the paths of the two BHs prior to merger. The gas distribution is very irregular, with distinct tidal streams. The inner region of the merger remnant is also lumpy and irregular. In other words, the initial disk structure of the progenitors has been destroyed by the merger, and the remnant is still highly disturbed at the time of BH coalescence. Fig. 3.2 shows the BH accretion and star formation throughout the simulation as well as the evolution of the BH separation prior to merger. This example illustrates some characteristics that are generic to our galaxy merger simulations. Simultaneous bursts of star formation and BH accretion occur after the first close pericentric passage and at final coalescence (Mihos & Hernquist 1994b, 1996) as the result of gas inflows caused by gravitational torques (Barnes & Hernquist 1991, 1996). As we shall demonstrate, these gas inflows can greatly influence the dynamics of ejected black holes by deepening the central potential and by providing additional drag force. Note that because our simulations include star formation throughout, the gas fraction at the time of BH merger is significantly lower than its initial value; in the example shown, 60% of the initial gas has been consumed by $t_{\rm mrg}$. By the end of the simulation, 2.9 Gyr after the merger, almost 80% of the gas has been depleted by star formation, and the BH accretion rate is very low. In our other merger models, 47-80% of the initial gas is depleted by the time of BH merger, and 62-88% is depleted by the end of the simulation. The final black hole mass in this

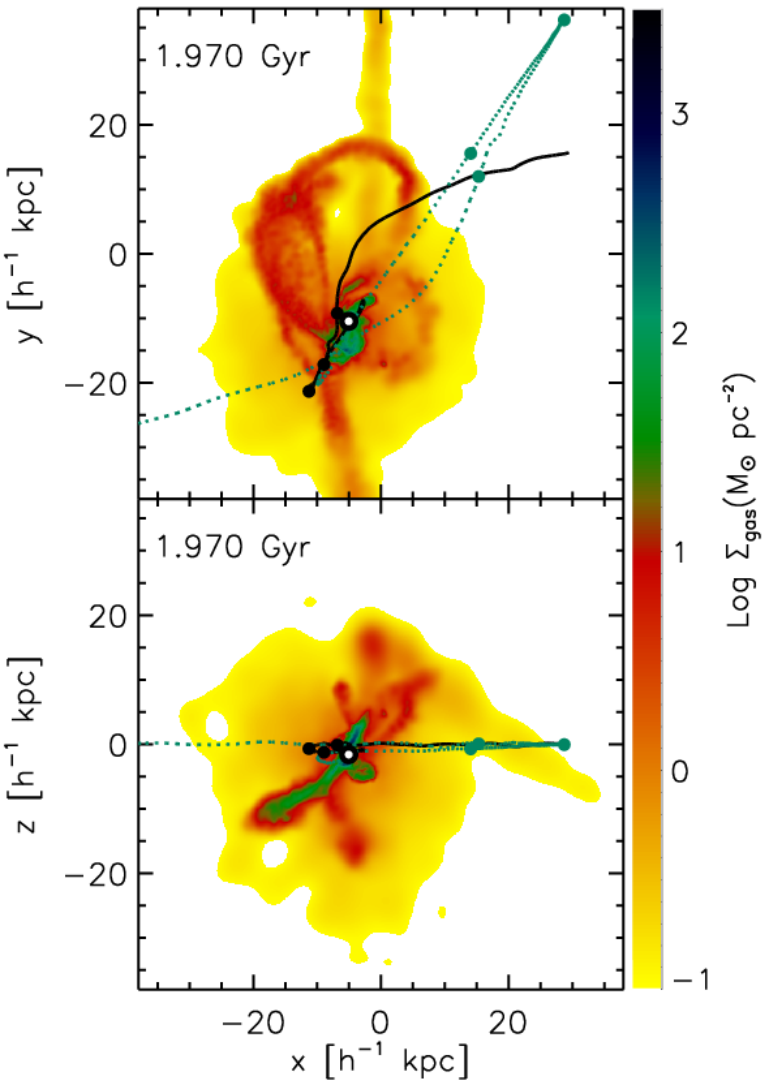

Figure 3.1.—: Fiducial example of a galaxy merger with BHs but no recoil kick (model q0.5fg0.3a). The gas distribution at time of BH merger (1.97 Gyr) is shown in both the x-y (*top*) and x-z (*bottom*) projections, with the density scale shown on the right-hand side. The black solid and green dotted lines show the pre-merger path of the BHs corresponding to the larger and smaller galaxies, respectively. The filled dots denote the BH positions at 500 Myr intervals. The black-and-white dot indicates the position of the merged BH at the moment of merger.

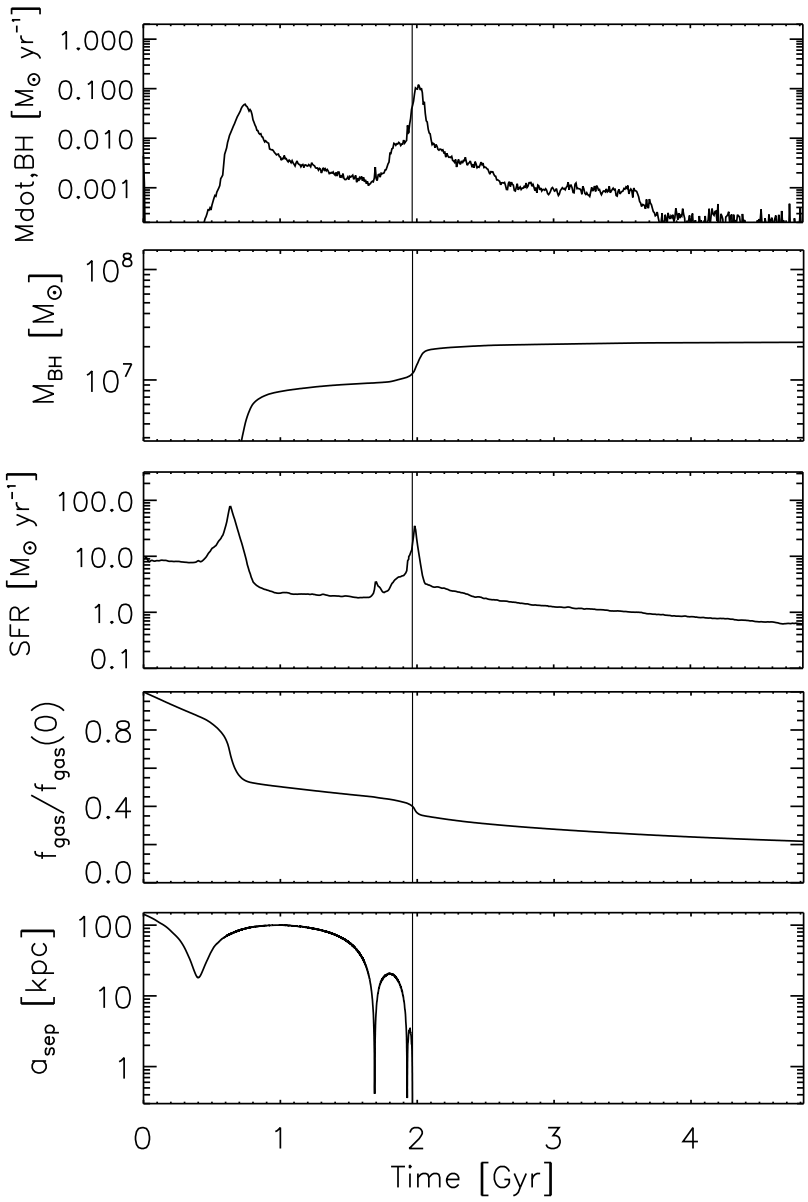

Figure 3.2.—: For the same simulation shown in Fig. 3.1 (model q0.5fg0.3a), the evolution of following quantities throughout the simulation is shown, from top to bottom: BH accretion rate ($\dot{M}_{\rm BH}$), global star formation rate, normalized galaxy gas fraction ($f_{\rm gas}/f_{\rm gas,0}$), BH mass ($M_{\rm BH}$), and BH separation prior to merger. Vertical lines indicate the time of BH merger.

example (2.2×10^7 $M_\odot$) is also typical of our fiducial-mass mergers.

Fig. 3.3 shows gas and stellar density distributions of this fiducial (q0.5fg0.3a) model and five other merger models. Each plot shows gas and stellar density from three different projections. These examples are chosen to illustrate the generic nature of the morphological features mentioned above. In all cases, the merger remnants are visibly disturbed and lumpy. Tidal tails are ubiquitous, though their size and density varies. Higher-$f_{\rm gas}$ mergers have more compact remnants (Hopkins et al. 2008a; Hopkins & Hernquist 2010a). Lower-q mergers are less strongly disrupted; a disk-like structure can be seen in the $x-z$ orientation of model q0.25fg0.3a. A special case is shown in the lower-right corner of Fig. 3.3. Model q0.5fg0.3h has a coplanar orbit with both galaxies rotating prograde to the orbital motion. Due to the highly aligned orbit, the disk structure of the progenitor galaxies is preserved in this merger remnant; tidal features are visible only from the face-on ($x-y$) projection. Our other "highly aligned" orbits (i, j, & k) result in similar remnant morphologies; they are included in our suite of merger models mainly for comparison, as mergers generally will not have such careful alignment.

As mentioned in § 3.2, in nearly equal-mass, gas rich mergers, the potential well in which the BH sits may deepen rapidly during final coalescence. Once the merger is complete, the remnant central potential will become shallower as the central stellar region begins to relax. The phase of rapid $v_{\rm esc}$ fluctuation coincides with the time of BH coalescence and may therefore affect recoiling BH dynamics. Fig. 3.4 shows the evolution of the BH escape speed ($v_{\rm esc}$) for four merger simulations without recoil kicks. The solid lines denote $t_{\rm mrg}$ and $v_{\rm esc}(t_{\rm mrg})$, while the dotted lines denote the maximum (post-merger) value of $v_{\rm esc}$ and the time at which it occurs. The difference between $v_{\rm esc}(t_{\rm mrg})$ and $v_{\rm esc,max}$ is small in all except the top left panel, which shows the q1fg0.4a merger. It is

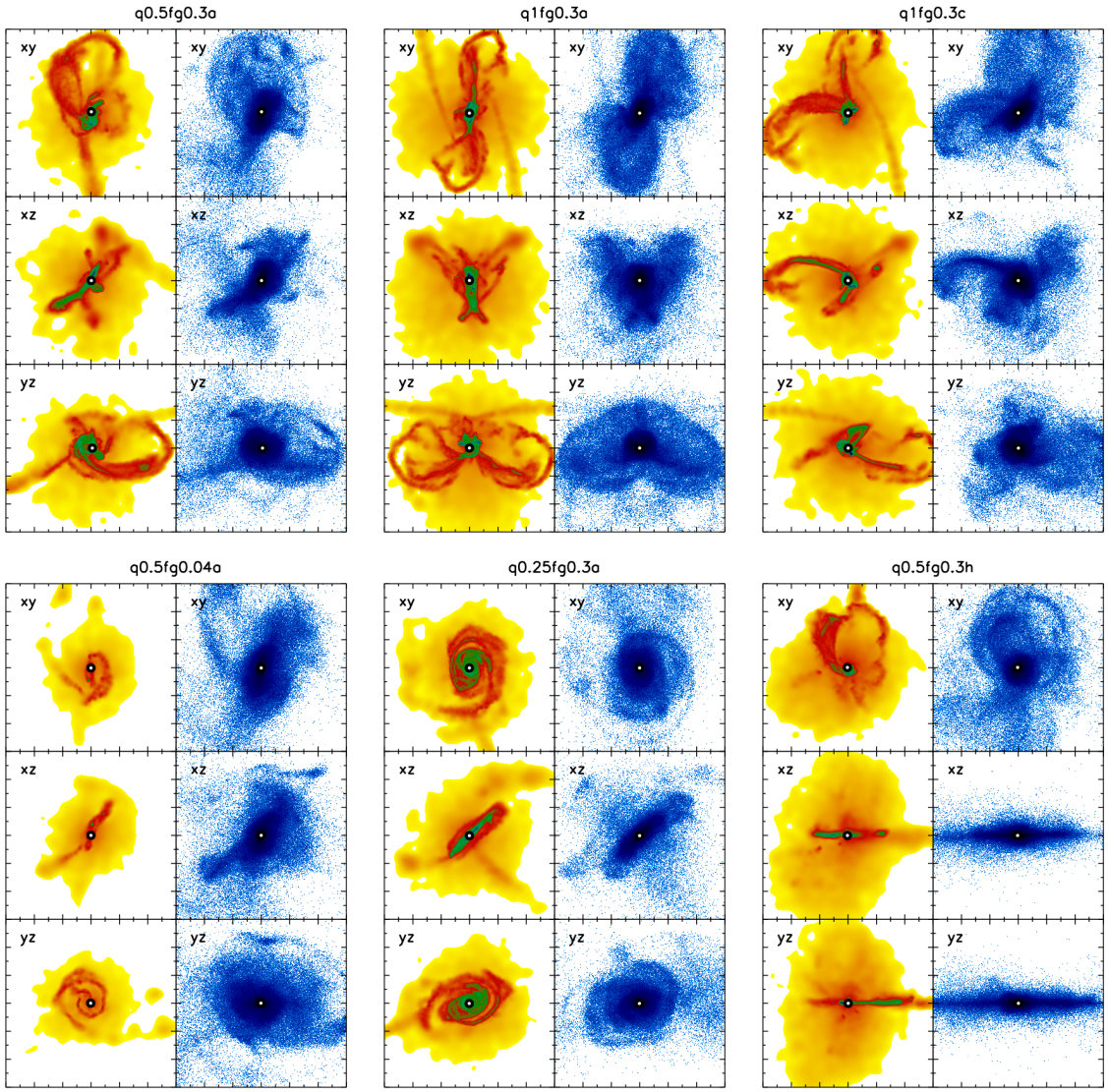

Figure 3.3.—: Projected gas (yellow/red) and stellar (blue) density distributions for six different merger models, shown at the time of BH merger in each case. The black-and-white dot indicates the position of the BH in each panel. The spatial scale of all panels is 86 kpc, and the projection (x-y, x-z, or y-z) is labeled on each panel. The models shown are (clockwise from top left, also labeled on each plot) q0.5fg0.3a, q1fg0.3a, q1fg0.3c, q0.5fg0.04a, q0.25fg0.3a, & q0.5fg0.3h.

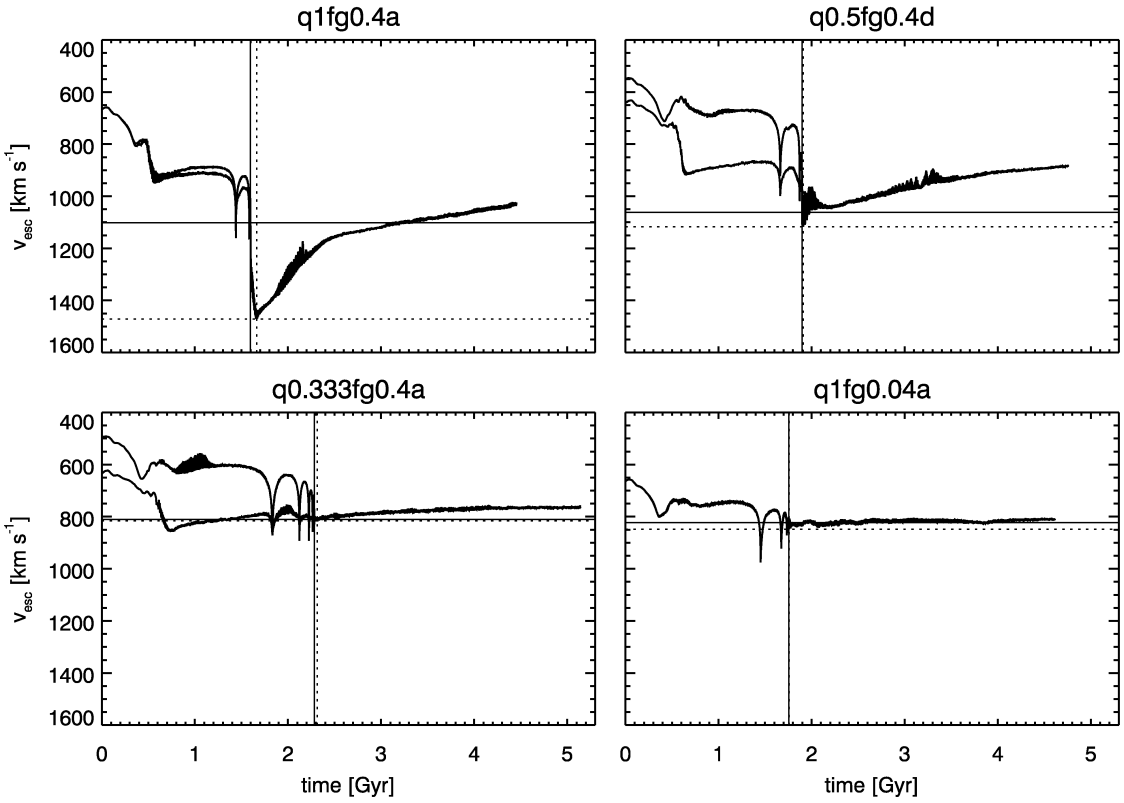

Figure 3.4.—: BH $v_{\rm esc}$ vs. time for a sample of four galaxy merger simulations with no recoil kick imparted to the BH. ($v_{\rm esc} \equiv \sqrt{-2\Phi(\mathbf{x}_{\rm BH})}$.) In each panel, the two curves represent $v_{\rm esc}$ of each BH prior to merger. After the merger, the escape speed of the remnant BH is shown. The solid vertical and horizontal lines mark the time of BH merger, $t_{\rm mrg}$, and the BH escape speed at that time, $v_{\rm esc}(t_{\rm mrg})$. The dotted vertical and horizontal lines denote the (post-merger) time of the maximum escape speed and its value. *Top left panel:* q1fg0.4a; *top right panel:* q0.5fg0.4d; *lower left panel:* q0.333fg0.4a; *lower right panel:* q1fg0.04a.

clear that the escape speed, and hence the trajectory, of a kicked BH in this model will depend on whether the kick occurs at $t_{\rm coal}$ or at some slightly later time. However, the sharp increase of $v_{\rm esc}$ occurs *only* in gas-rich, nearly-equal-mass mergers. The other three panels in Fig. 3.4 show $v_{\rm esc}$ vs. t for a sample of simulations with lower q and $f_{\rm gas}$; in these models, $v_{\rm esc}$ is much less volatile during and after the BH merger. Moreover, the example shown in Fig. 3.4 is not the most gas-rich of our merger models but is chosen because of the large difference between $v_{\rm esc}(t_{\rm coal})$ and $v_{\rm esc,max}$, 34%. Larger differences between these quantities yield larger uncertainty in our results for BH dynamics when the recoil kick is assigned at $t_{\rm mrg} = t_{\rm coal}$. The final four columns in Table 3.1 give $t_{\rm mrg}$, $v_{\rm esc}(t_{\rm mrg})$, $v_{\rm esc,max}$, and the fractional difference between $v_{\rm esc}(t_{\rm mrg})$ and $v_{\rm esc,max}$ for each merger model. All mergers with $f_{\rm gas} < 0.3$ have $\lesssim 10\%$ difference between $v_{\rm esc}(t_{\rm mrg})$ and $v_{\rm esc,max}$, and mergers with $q < 0.5$ have $< 1\%$ difference. Therefore, while our results for nearly equal-mass, gas-rich mergers are subject to the assumption that the BH merger occurs on a short timescale, the results for our other models are insensitive to the merger time. We explore further the case of gas-rich, $q \sim 1$ mergers in § 3.4.2.

3.4 Recoiling Black Hole Dynamics

3.4.1 Characterization of Recoil Trajectories

A universal feature of our recoil trajectories is that they have low-angular-momentum orbits, which occurs because the centrally-concentrated baryonic component of the galaxy dominates the BH trajectories even when they extend far into the halo. Consequently, we refer throughout the paper to the trajectories as "oscillations" of the BH about the

galactic center. We see this clearly in Fig. 3.5, which shows the trajectories of BHs kicked with $v_{\rm k}/v_{\rm esc} = 0.4 - 1.0$ for eight different merger models. Also readily apparent in these plots is the variation in BH oscillation amplitude and duration between models. For a fixed value of $v_{\rm k}/v_{\rm esc}$, BHs travel further from the galactic center in mergers with lower q and $f_{\rm gas}$. In the q1fg0.6a model, BHs kicked with $v_{\rm k} = 0.7\ v_{\rm esc}$ ($= 878$ km s^{-1}) travel < 2 kpc from the galactic center, while in the collisionless q1fg0a model, the same $v_{\rm k}/v_{\rm esc}$ allows the BH to travel ten times further. Note that scaling the kick speeds to $v_{\rm esc}$ is important for determining the trends between galaxy models; $v_{\rm esc}(t_{\rm mrg})$ for all of our models ranges from $338 - 2555$ km s^{-1} ($689 - 1258$ km s^{-1} for the fiducial-mass models).

The trend toward smaller recoil oscillation amplitude for higher $f_{\rm gas}$ occurs because higher gas fractions result in more compact remnants that have higher central densities, and these remnants also have larger available supplies of gas. Both factors contribute to steeper central potentials and increased gas drag and dynamical friction. We can also see from Fig. 3.5 that recoil oscillations are slightly larger for lower q, though the trend is more evident in higher-$f_{\rm gas}$ remnants. Higher mass ratio mergers create stronger perturbations that drive gas more efficiently to the galaxies' central regions, further contributing to the steep potentials and high densities.

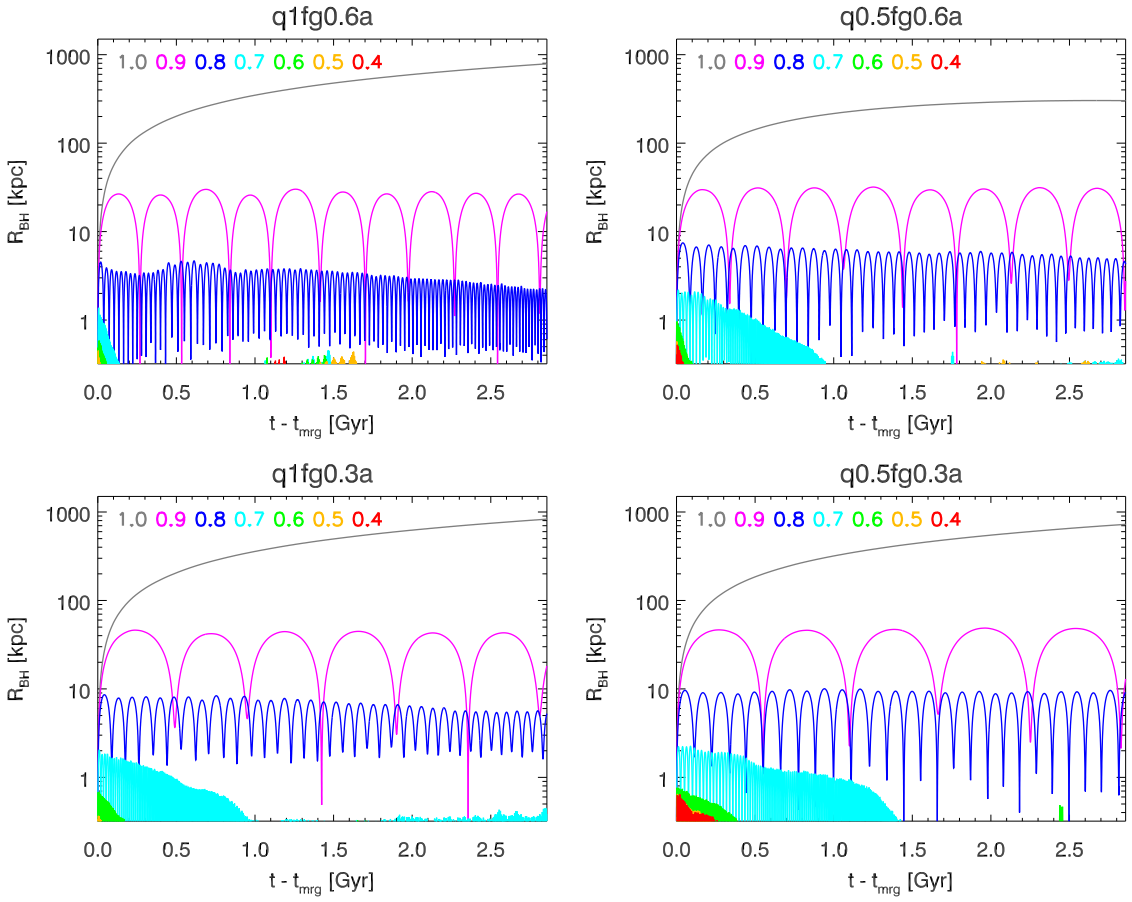

Figure 3.5.—: (Continued on next page.) In each plot, BH recoil oscillation amplitudes are shown for varying kick velocities within a single model. The x-axis is the time after the BH merger, $t - t_{\rm mrg}$. The color-coded numbers on each plot indicate $v_{\rm k}/v_{\rm esc}$ for each curve. Galaxy models shown are, from left to right and top to bottom: q1fg0.6a, q0.5fg0.6a, q1fg0.3a, q0.5fg0.3a, q1fg0.1a, q0.5fg0.1a, q1fg0a, q0.5fg0a.

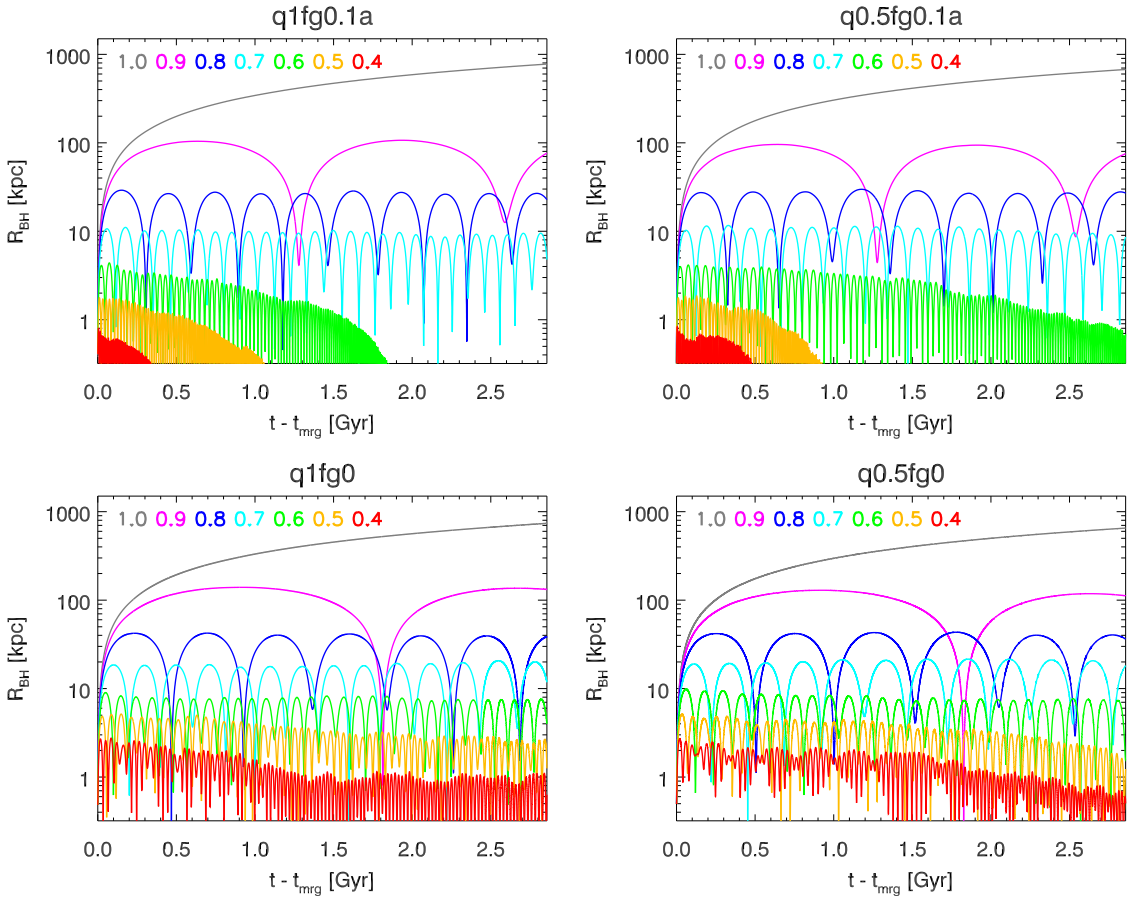

Figure 3.5.—: (Continued)

These trends are more clearly shown in Fig. 3.6. The top plot shows the maximum galactocentric distance of each orbit in Fig. 3.5, normalized to the half-mass effective radius of the galaxy ($R_{\rm max}/R_{\rm eff}$). The bottom plot shows the settling time, $t_{\rm settle}$, defined as the time when the apocentric distance of the BH oscillations, relative to the stellar center of mass, falls below $4\,R_{\rm soft}$. This definition is chosen to avoid following BH trajectories below a scale where their oscillations may be dominated by numerical noise or gravitational softening. We find that our conclusions are not sensitive to the exact definition of $t_{\rm settle}$. Note that for some high-velocity recoils (for all recoils in the collisionless simulations), we have only lower limits on $t_{\rm settle}$, because in these cases the BH did not settle by the end of the simulation.

In the top panel of Fig. 3.6, the curves for a given $f_{\rm gas}$ lie nearly on top of each other. This supports our assertion that the initial gas fraction is more important than the mass ratio in determining $R_{\rm max}/R_{\rm eff}$ for a given $v_{\rm k}/v_{\rm esc}$. By normalizing these quantities. we essentially isolate the effects of gas drag or potential shape from variation in galaxy size or central potential depth. One can easily see from Fig. 3.6 that, especially for lower $v_{\rm k}/v_{\rm esc}$, a gas fraction $\geq 30\%$ can reduce the amplitude of BH oscillations by up to an order of magnitude with respect to a purely collisionless system.

Note that $R_{\rm max}/R_{\rm eff}$ is at least as large for $f_{\rm gas} = 0.6$ as it is for $f_{\rm gas} = 0.3$, opposite the trend we expect if gas drag dominates the BH trajectories. However, galaxies with higher $f_{\rm gas}$ generally have higher star formation rates, so systems with initial gas fractions of $0.3 - 0.6$ will have similar amounts of gas by the time of the BH merger. Furthermore, as previously stated, higher gas fractions yield more concentrated merger remnants (smaller $R_{\rm eff}$). Combined, these effects result in similar $R_{\rm max}/R_{\rm e}$ for recoils in mergers with initial $f_{\rm gas} = 0.3 - 0.6$.

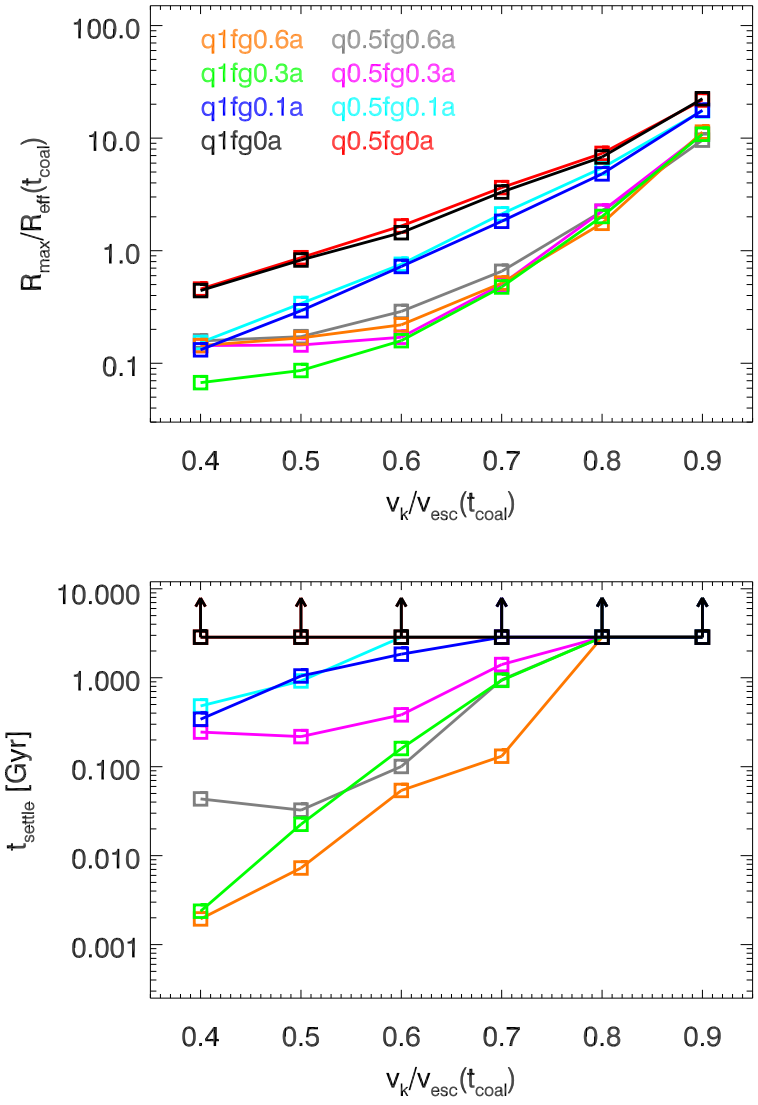

Figure 3.6.—: $R_{\rm max}/R_{\rm eff}$ (*top window*) and $t_{\rm settle}$ (*bottom window*) are plotted versus $v_{\rm k}/v_{\rm esc}$ for the eight models whose trajectories are shown in Fig. 3.5. $t_{\rm settle}$ is defined as the time after the BH merger at which the apocentric distance of the BH orbits drops below $4\,R_{\rm soft}$. Arrows denote lower limits on $t_{\rm settle}$ in cases when the BH has not settled by the end of the simulation (defined as $t_{\rm mrg} + 2.9$ Gyr).

As discussed in § 3.2, the recoil trajectories may be sensitive to numerical parameters such as resolution or integration accuracy. In particular, because $R_{\rm eff}$ is of the order of a few kpc, recoiling BHs with $R_{\rm max}/R_{\rm eff} \lesssim 0.1$ spend substantial time at or below the spatial resolution limit. $R_{\rm max}$ and $t_{\rm settle}$ are therefore approximate in these cases. The BH settling times are also susceptible to possible inaccuracies in dynamical friction forces due to our finite mass resolution, which is likely to result in underprediction of the true amount of dynamical friction. However, we can predict that the effect of this uncertainty on our results is likely to be small; in our lower-mass galaxy mergers, which have 10× and 20× better mass resolution, BHs kicked near the escape speed still experience very little dynamical friction and have very long wandering times. Even if dynamical friction is still underestimated in these higher-resolution runs, it is clear that in general, recoils near the escape speed will result in wandering times of at least a few Gyr, and that in gaseous mergers, recoiling BHs with $v_{\rm k} \lesssim 0.5\ v_{\rm esc}$ remain within the central kpc of the galaxy. Finally, because we use the same mass resolution in all of our simulations (excepting the low/high mass runs), the relative trends that we find between different galaxy models are robust.

We expect some variation in $R_{\rm max}$ for different merger orbits as well. In the set of eleven different orbital configurations we simulated with $q = 0.5$ & $f_{\rm gas} = 0.3$, the central escape speeds at $t_{\rm mrg}$ vary from $805 - 1046$ km s^{-1}. Since the total mass in all of these simulations is constant, the variation in $v_{\rm esc}$ reflects differences in the central concentration, and hence the steepness of the potential well. We simulate recoil trajectories in each of these with $v_{\rm k}/v_{\rm esc} = 0.9$, and find that $R_{\rm max}/R_{\rm eff} = 4 - 20$. Based on this example, we see that the merger orbit alone can influence the remnant central potential well enough to change the amplitude of recoil trajectories by a factor of ~ 5.

Fig. 3.7 shows two examples of recoil trajectories in three different projections as well as $R(t)$. The top plot shows a recoil event with $v_{\rm k}/v_{\rm esc} = 0.6$, which in this model (q0.5fg0.3a) corresponds to $v_{\rm k} \approx 600$ km s^{-1}. Note that the orbit is highly non-planar; it looks similar in all three projections. The orbit is also centrophilic, which as we have noted is common to all of our recoil simulations. The average orbital period is short, $\sim 7 \times 10^5$ yr, and $t_{\rm settle} \sim 400$ Myr, such that the BH settles to the center well before the end of the simulation.

Recoil events with velocities near $v_{\rm esc}$ produce long-lived ($>$ Gyr), large-amplitude BH oscillations. Many of these oscillations still have large amplitudes at the end of the simulation, 2.9 Gyr after the BH merger, so we have only lower limits on $t_{\rm settle}$. The bottom plot in Fig. 3.7 illustrates this type of recoil event, again for the q0.5fg0.3a model. The trajectory shown has a kick speed of $v_{\rm k}/v_{\rm esc} = 0.9$, so $v_{\rm k} \approx 900$ km s^{-1}. The amplitude of these oscillations is ~ 50 kpc, almost two orders of magnitude greater than in the lower-$v_{\rm k}$ example. Although the BH only completes five orbits before the end of the simulation, we can see that again there is no evidence for a preferred orbital plane; the orbit is three-dimensional. Because the oscillation amplitude is so large and shows no sign of damping out by the end of the simulation, it is likely that such an orbit will not return to the galaxy center within a Hubble time, and certainly not within the mean time between major galaxy mergers. Such BHs essentially can be considered "lost" to the galaxy. If in other cases the BHs do return to the galactic center after several Gyr and another galaxy merger has taken place in the meantime, the returning and new BHs could form another binary.

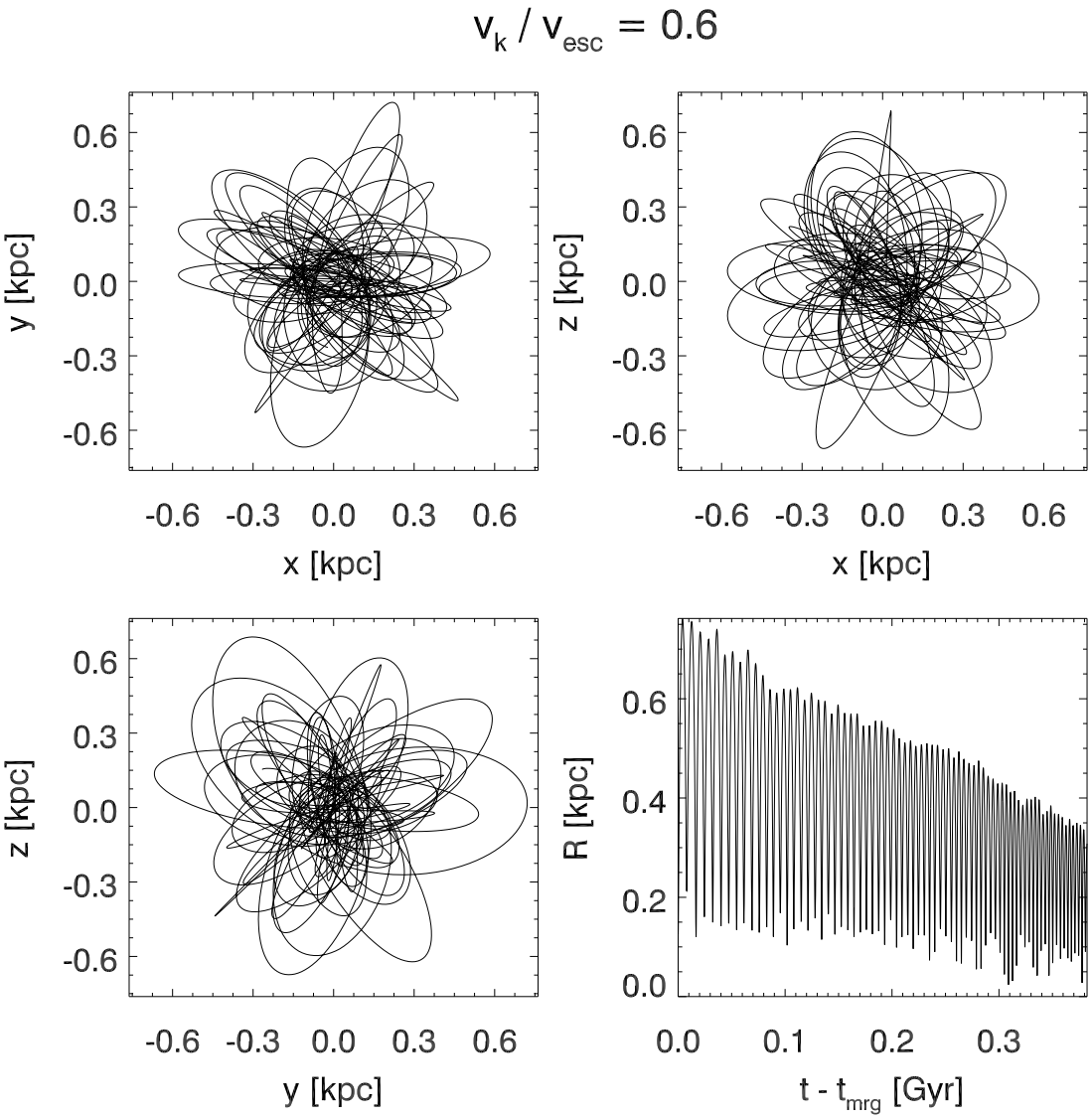

Figure 3.7.—: (Continued on next page.) Panels on this page: trajectory for the $v_{\rm k}/v_{\rm esc} = 0.6$ recoil simulation with the q0.5fg0.3a model. Panels on next page: trajectory for the $v_{\rm k}/v_{\rm esc} = 0.9$ recoil simulation with the q0.5fg0.3a model. In each case, the four windows show the trajectories in the $x-y$, $x-z$, and $y-z$ projections, as well as the BH's galactocentric distance versus time. Note the greatly different spatial scales of the two simulations.

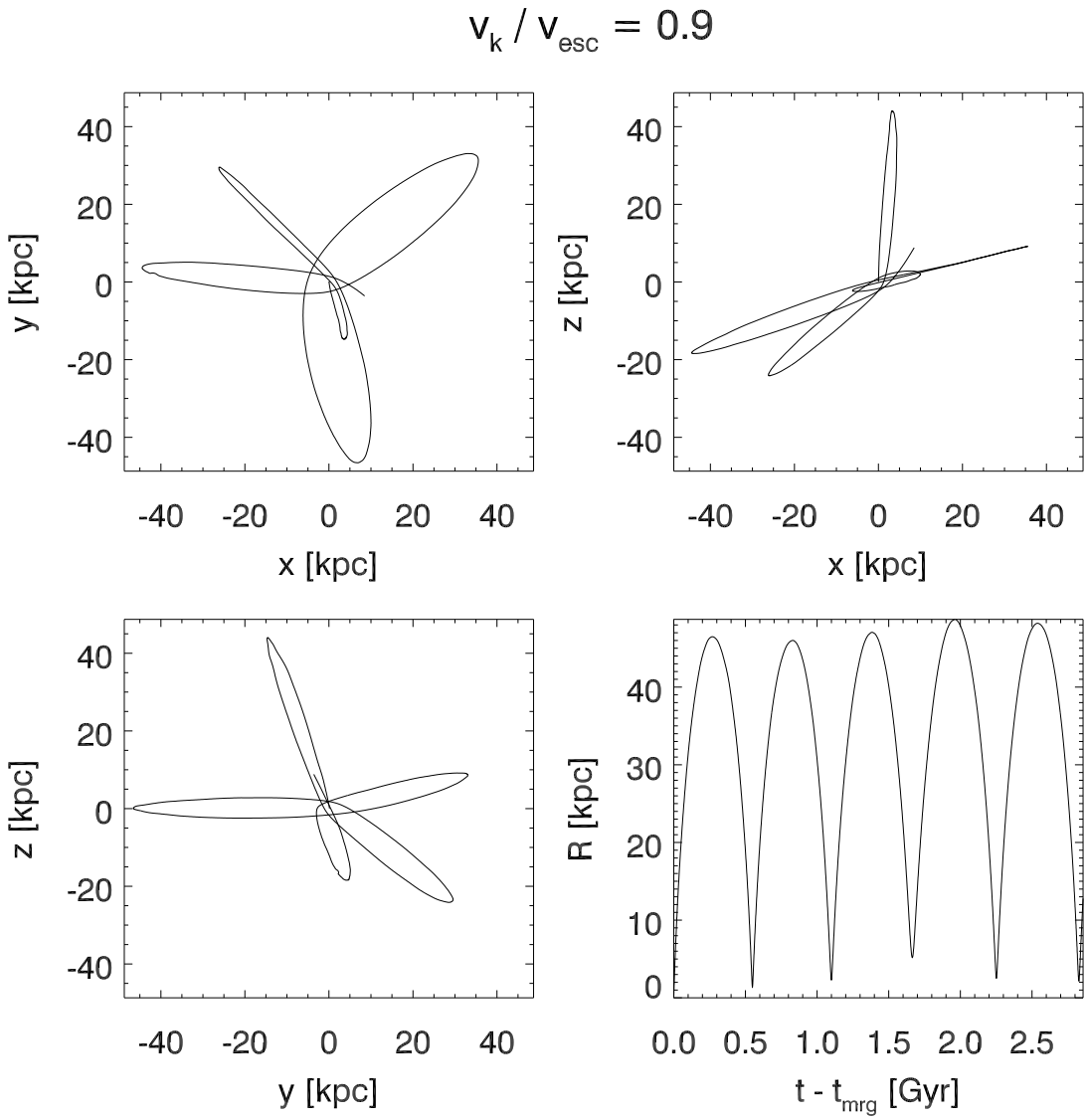

Figure 3.7.—: (Continued)

In recoil events with $v > v_{\rm esc}$, the rapidly recoiling BH can only take a small amount of gas with it; only gas that is orbiting the BH with $v_{\rm orb} \gtrsim v_{\rm k}$ stays bound to the BH when it is ejected. The accretion timescale and luminosity of these ejected disks is discussed in § 3.5.2. Once this supply is exhausted, the naked BH is unlikely to become active again, as this would require a serendipitous passage through a dense gas cloud, as well as a sufficiently low relative velocity that substantial accretion could occur. (Recall that Bondi-Hoyle accretion scales as $v_{\rm BH}^{-3}$.) These escaping BHs are therefore likely to wander indefinitely, undetected, through intergalactic space.

3.4.2 BH Merger Time

As illustrated in Fig. 3.4, $v_{\rm esc}$ can increase significantly during coalescence in equal-mass, gas-rich mergers. To better understand how this may affect BH trajectories, we have run a series of simulations with the BH merger (and recoil kick) occurring at sequentially later times using model q1fg0.4a. The $v_{\rm esc}$ evolution of model q1fg0.4a is replotted in the top window of Fig. 3.8, with the fiducial merger time, $t_{\rm mrg} = t_{\rm coal}$, marked by the solid black line and the subsequent merger times tested marked by black dashed lines. We have tested simulations with each of these merger times twice, once with $v_{\rm k} = 1000$ km s^{-1} and once with $v_{\rm k}/v_{\rm esc}(t_{\rm mrg}) = 0.9$. By conducting the second experiment we are normalizing to the evolving depth of the central potential well, which helps us to separate the gravitational and drag effects on the trajectories.

Fig. 3.8 shows $R_{\rm max}$ for the BH orbits in each of these varying-$t_{\rm mrg}$ simulations, with the $v_{\rm k} = 1000$ km s^{-1} simulations in the middle panel and the $v_{\rm k}/v_{\rm esc}(t_{\rm mrg}) = 0.9$ simulations in the bottom panel. As $v_{\rm esc}$ increases from 1100 km s^{-1} at $t_{\rm coal}$ to almost

1500 km s^{-1} at its maximum, the amplitudes of BH trajectories from constant-v_k recoil events decrease by more than two orders of magnitude. However, the bottom panel of Fig. 3.8 shows that when v_k is set to a constant *fraction* of the escape speed, the BHs kicked from deeper potential wells (larger v_{esc}) still have smaller-amplitude trajectories, but the variation is much less severe than when v_k = constant. The variation that persists even for fixed v_k/v_{esc} can be attributed to the enhanced gas drag and dynamical friction, as well as the steeper central potential well, that result from the rapid formation of the central dense cusp. At very late merger times, $100 - 500$ Myr after t_{coal}, the opposite trend is seen. The amplitude of constant-v_k trajectories increases by almost an order of magnitude from the minimum at $t_{coal}+70$ Myr to the value at $t_{coal}+500$ Myr. This is partly because the central potential becomes shallower as the merger remnant begins to relax. The same trend occurs at late times in the constant-v_k/v_{esc} simulations, because the potential well also becomes less steep, and gas drag becomes less efficient as more of the gas is consumed in star formation. We note that merger times up to $t_{coal} + 500$ Myr are included here only for illustrative purposes; in reality, such delayed mergers are probably unrealistic in gas-rich systems.

If the BHs are able to merge rapidly, before the central potential reaches its maximum depth, another interesting effect can occur. During the period of rapid central potential evolution, the timescale on which v_{esc} increases is typically much shorter than the timescale for a recoiling BH orbit to decay via gas drag or dynamical friction. Consequently, on its first several pericentric passages through the central region, the BH encounters an increasingly deep potential well, and its velocity is actually boosted by a small amount, such that the ratio v_{BH}/v_{esc} is roughly constant on subsequent pericentric passages. Because only v_{BH} increases, not v_{BH}/v_{esc}, the BH's galactocentric distance is

not boosted beyond its initial maximum, $R_{\rm max}$, and once the rapid potential evolution ceases, drag forces become dominant and the velocity begins to decay. This effect is by design short-lived, and it is strongest when the BH orbital timescale is short, such that the BH orbit is dominated by the dynamics of the inner galaxy region. These velocity boosts are therefore mostly an interesting illustration of the sensitivity of recoil dynamics to the BH merger time, although we will see some implications of this effect for the recoiling AGN lifetimes calculated in § 3.5.3.

The primary implication of our BH merger time analysis is that in nearly equal-mass, gas-rich mergers such as the example shown in Fig. 3.8, a delay of even a few $\times 10^7$ yr in the BH merger may significantly reduce the amplitude and duration of recoiling BH oscillations. Based on results from numerous hydrodynamic simulations of binary BH inspiral (e.g., Escala et al. 2005; Dotti et al. 2007), we have good reason to believe that BHs in gas-rich systems merge efficiently in general, but the merger time of a given BH binary is impossible to predict with this precision. By assuming $t_{\rm mrg} = t_{\rm coal}$ in our simulations, we exclude the possibility of delayed mergers, but we also take steps to ensure that this has a minimal effect on our results. First, only a small number of our simulations have large variation in $v_{\rm esc}$. In these cases, we see by comparing Figs. 3.6 & 3.8 that the variation in oscillation amplitudes for a given $v_{\rm k}/v_{\rm esc}$ due to evolving central density (less than a factor of 10) is generally much less than the variation for different values of $v_{\rm k}/v_{\rm esc}$ (up to three orders of magnitude). All of the analysis in this study is presented in terms of $v_{\rm k}/v_{\rm esc}$. Therefore, the dramatic suppression of recoil trajectories with fixed $v_{\rm k}$, while an important result in itself, does not affect our other conclusions.

Figure 3.8.—: (Following page.) *Top window:* $v_{\rm esc}$ is plotted as a function of $t - t_{\rm coal}$ for the q1fg0.4a merger simulation. The portion shown here is a zoom-in of the top-left window in Fig. 3.4. The solid vertical line denotes $t_{\rm coal}$, and the dashed vertical lines denote the subsequent merger times used to test variation in $t_{\rm mrg}$. *Middle window:* $R_{\rm max}/R_{\rm eff}$ is plotted versus BH merger time for the set of delayed-merger simulations done using model q1fg0.4a. Each BH in these simulations is assigned a recoil kick of 1000 km s^{-1}. *Bottom window:* Same as middle window, but for a set of simulations in which the kick speed in km s^{-1} varies, but is held to a constant value of $v_{\rm k}/v_{\rm esc}$; in every case $v_{\rm k}/v_{\rm esc} = 0.9$. The x-axis ranges from $t_{\rm mrg} = t_{\rm coal}$ to $t_{\rm mrg} = t_{\rm coal} + 500$ Myr.

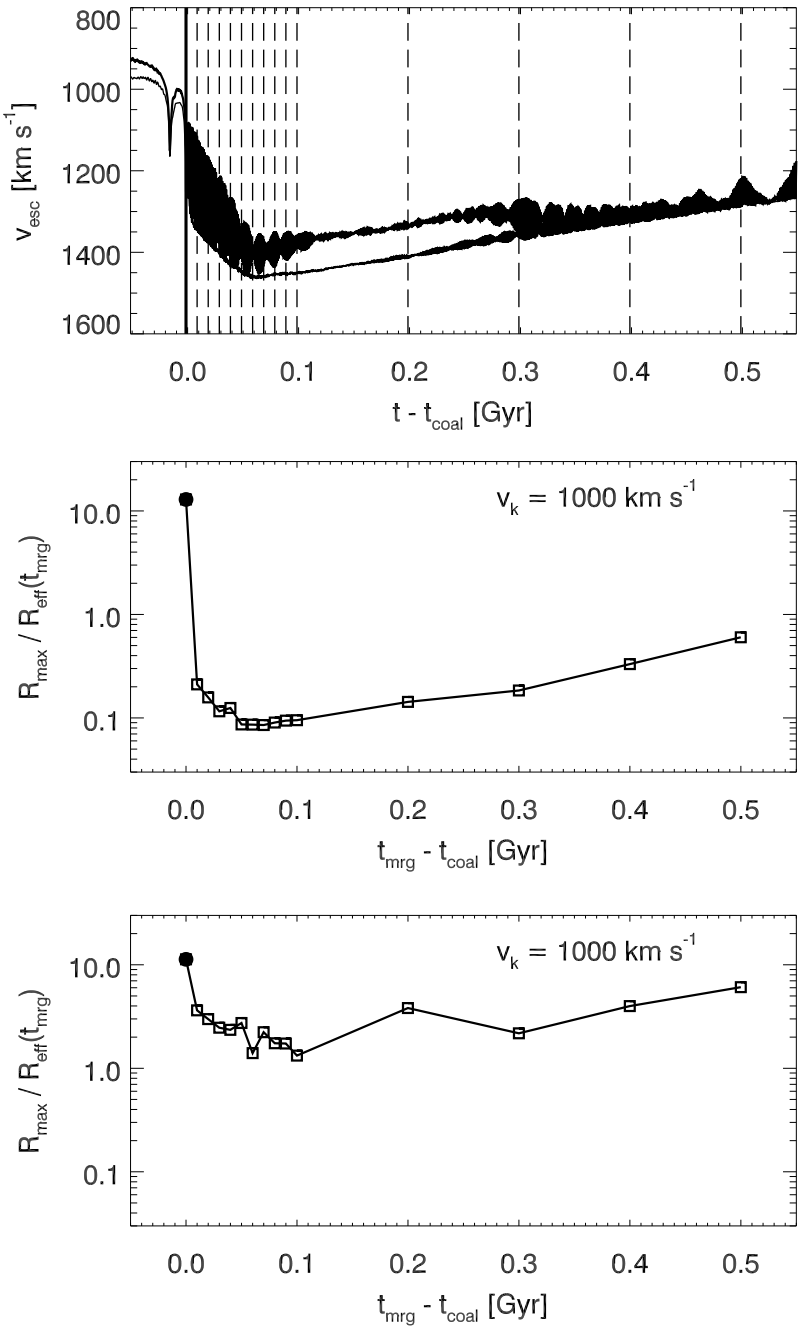

Figure 3.8.—: (Continued)

3.4.3 Recoil Kick Direction

Most of our recoiling BHs have $v_{\rm k} \gtrsim 500$ km s^{-1}, in which case their kicks will be oriented out of the orbital plane of the binary (Campanelli et al. 2007a,b; Lousto & Zlochower 2009). However, because the BH binary inspiral occurs on sub-resolution scales in our simulations, the binary orbital angular momentum vector cannot be predicted. Furthermore, the galactic disk structure of the merger progenitors is disrupted by major mergers (see Fig. 3.3), except when the galaxies have nearly coplanar orbits. In generic mergers, there is no obvious reference direction in which to orient the recoil kick with respect to the progenitors' initial structure. Clearly, on certain recoil trajectories (i.e., along tidal tails or central clumps) a BH will encounter denser gaseous regions than on others. However, it is unclear *a priori* whether these density variations are sufficient to cause significant variation in BH recoil trajectories. In most of our simulations, we simply orient the recoil kick along the z-axis of the simulation, $(\theta_{\rm k}, \phi_{\rm k}) = (0, 0)$, in the coordinate system with respect to which the initial galaxy orbits are assigned. Here, we examine a subset of simulations with varying kick orientation to determine the sensitivity of our results to this choice.

We test a sample of different kick orientations with three different values of $v_{\rm k}/v_{\rm esc}$ (0.6, 0.8, & 0.9) in our q1fg0.3a and q0.5fg0.3a merger models. As a gauge of how the BH trajectories differ among this sample, we calculate the maximum galactocentric distance ($R_{\rm max}$) and average orbital period ($\langle P_{\rm orb} \rangle$) of the BH in each simulation. Fig 3.9 shows the distributions of these quantities, normalized to $R_{\rm max}$ and $\langle P_{\rm orb} \rangle$ of the $(\theta_{\rm k}, \phi_{\rm k}) = (0, 0)$ simulations for each corresponding $v_{\rm k}/v_{\rm esc}$ value. The q0.5fg0.3a distributions peak slightly below 1.0 and the q1fg0.3a distributions peak

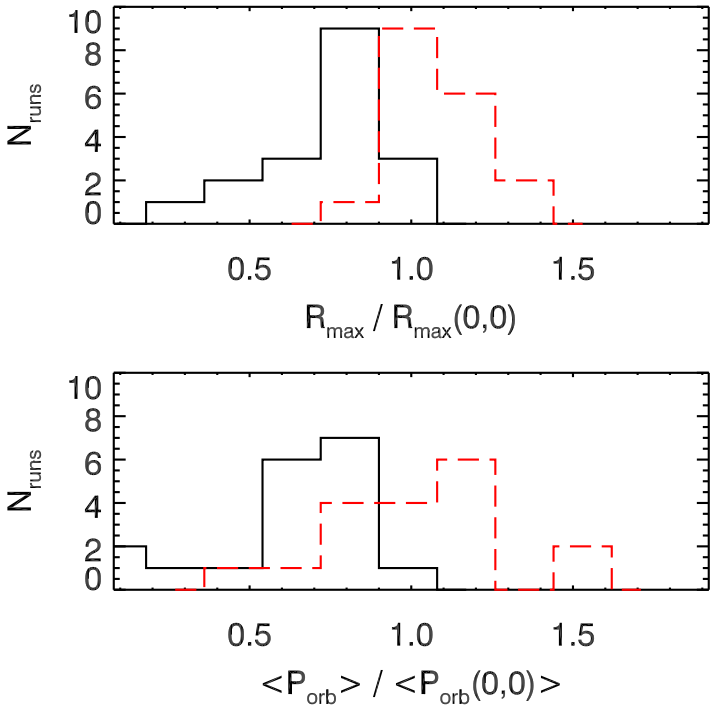

Figure 3.9.—: Top window: distribution of $R_{\rm max}$ for our set of $(\theta, \phi) \neq (0,0)$ simulations, normalized to $R_{\rm max}(0,\ 0)$ for each corresponding $v_{\rm k}/v_{\rm esc}$ value. The set of simulations includes runs with $v_{\rm k}/v_{\rm esc} = 0.6,\ 0.8,\ \&\ 0.9$. The black solid line is the distribution of simulations with the q0.5fg0.3a model, and the red dashed line corresponds to the q1fg0.3a model. Bottom window: the distributions of the average orbital period are shown for the same simulations as in the top window, normalized to $\langle P_{\rm orb}(0,0)\rangle$.

slightly above 1.0, but the combined histogram is distributed fairly evenly around unity. In other words, the $(\theta_{\rm k}, \phi_{\rm k}) = (0,\, 0)$ kick orientation is not a "special" direction. The overall variation in $R_{\rm max}/R_{\rm max}(0,\, 0)$ for each model is less than a factor of 4. In contrast, Fig. 3.5 shows that $R_{\rm max}$ is almost two orders of magnitude higher for $v_{\rm k}/v_{\rm esc} = 0.9$ than for 0.6. Clearly, the amplitude and duration of BH oscillations depends much more strongly on the kick *magnitude* than its direction, and we need not concern ourselves too much with our choice of kick orientation.

3.5 Black Hole Accretion and Feedback

3.5.1 Bondi Accretion and AGN Lifetimes

Fig. 3.10 compares the BH accretion and star formation histories for simulations of the q0.5fg0.3a merger model with $v_{\rm k} = 0$ and $v_{\rm k}/v_{\rm esc} = 0.5 - 0.8$. The top windows in Fig. 3.10 show that even kicks with $v_{\rm k}/v_{\rm esc} = 0.5 - 0.6$ produce qualitatively different AGN lightcurves (as inferred from $\dot{M}_{\rm BH}$) than in the zero-kick case, although the final BH masses are similar. In these cases, the peaks in accretion rate at coalescence ($t \approx 2$ Gyr) are slightly lower due to the sudden removal of the BHs from the highest-density region. However, the BHs remain within 1 kpc of the galactic center, and accretion continues through the end of the simulation at higher rates than in the zero-kick case. Thus, although the total mass accreted is about the same for $v_{\rm k}/v_{\rm esc} = 0 - 0.6$, the active lifetime is longer when a recoil kick occurs.

In the $v_{\rm k}/v_{\rm esc} = 0.7$ simulation, the BH accretion cuts off more sharply at $t_{\rm mrg}$ and is subsequently highly variable, due to the larger-amplitude, longer-lived BH oscillations.

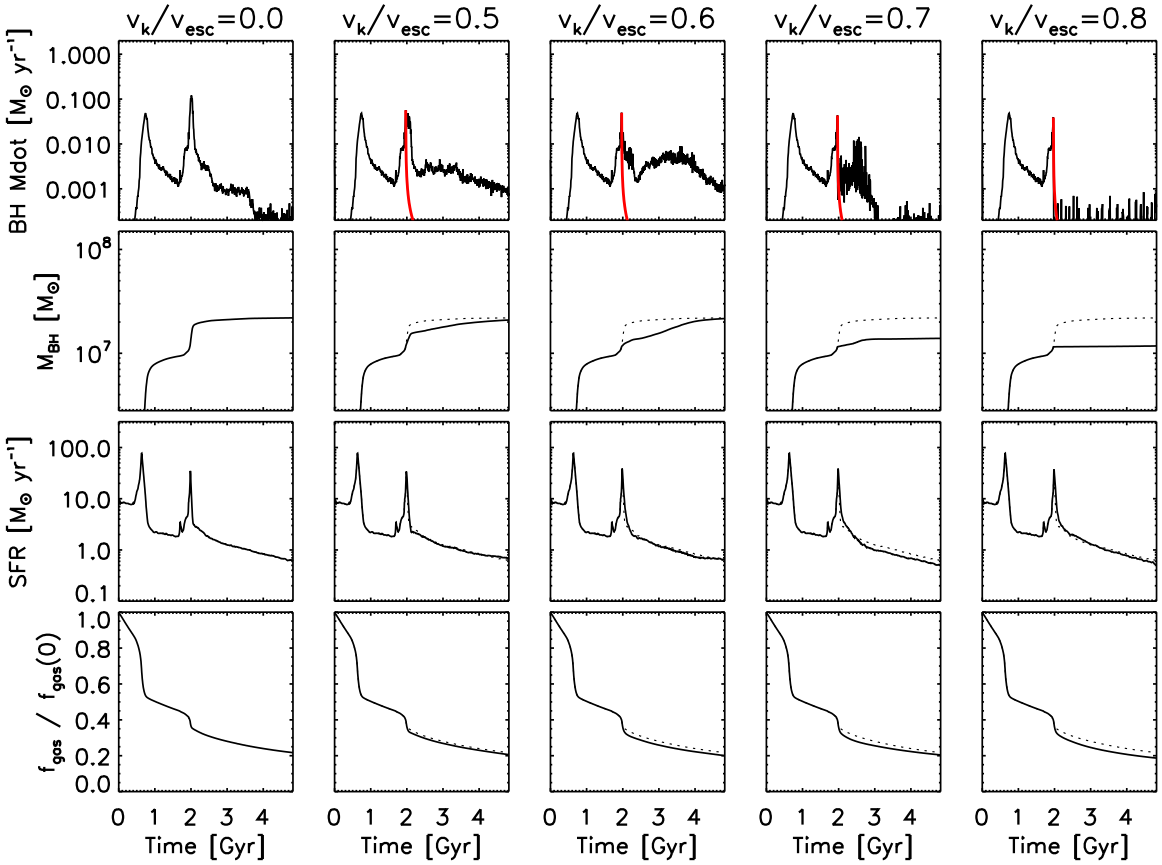

Figure 3.10.—: The same quantities for model q0.5fg0.3a are plotted as in Fig. 3.2, but here they are shown for simulations with $v_{\rm k}/v_{\rm esc} = 0.5 - 0.8$ in addition to the $v_{\rm k} = 0$ case. The red lines in the $\dot{M}_{\rm BH}$ plots (top row) correspond to the accretion rate calculated from our ejected-disk model as described in § 3.5.2. In the $v_{\rm k} \neq 0$ plots, the $v_{\rm k} = 0$ curves are drawn again with dashed lines, except for the $\dot{M}_{\rm BH}$ plots where the dashed lines are omitted for clarity.

Unlike the BHs with lower-velocity recoils, this BH attains a noticeably lower final mass than its zero-kick counterpart.

For recoil kicks $\gtrsim 0.8\ v_{\rm esc}$, the BH accretion cuts off sharply at $t_{\rm mrg}$, and the BH subsequently accretes very little gas as it travels on large, long-period orbits that extend well into the halo. These high-velocity recoil events therefore reduce the AGN lifetime. Additionally, the BH mass is essentially frozen at its value at $t_{\rm mrg}$, which is about half that of the stationary BH mass. If the BH does return to the galaxy center after several Gyr, most of the galaxy's gas will have been consumed in star formation, so the BH will remain undermassive. In the galaxy merger models we have used, the BH mass deficits for high-velocity recoils versus no recoil range from a factor of ~ 1 (almost no deficit) to ~ 5. These BH mass deficits and their implications are discussed in § 3.5.4.

To quantify the amount of enhancement or reduction in AGN activity owing to GW recoil, we calculate AGN lifetimes ($t_{\rm AGN}$) for both stationary and recoiling BHs in six different galaxy models for which we have varied $v_{\rm k}$. Fig. 3.11 shows the results, with colored lines indicating $t_{\rm AGN}$ for recoiling BHs as a function of $v_{\rm k}$ and black horizontal lines indicating $t_{\rm AGN}$ for a stationary BH in the corresponding merger model. In order to differentiate between bright AGN and low-luminosity AGN, we calculate $t_{\rm AGN}$ assuming three different definitions of an "active" BH. The thick solid lines in the figure are calculated assuming the BH is an AGN when $L_{\rm bol} > 10\%\, L_{\rm Edd}$, and the thin solid lines assume $L_{\rm bol} > 3\%\, L_{\rm Edd}$. Because these quantities depend on the BH mass, we use an absolute luminosity value for our third AGN definition: $L_{\rm bol} > L_{\rm min}$ (denoted by the dashed lines in Fig. 3.11). We choose $L_{\rm min} = 3.3 \times 10^9$ L$_\odot$, which is $0.1\, L_{\rm Edd}$ for a 10^6 M$_\odot$ BH.

In these models, the low-luminosity AGN lifetime is generally enhanced by moderate-velocity recoil events, and the bright AGN lifetime is generally reduced. Although the details depend on the model parameters and kick speed, in all models, $t_{\rm AGN}$ falls off steeply at high $v_{\rm k}/v_{\rm esc}$, when the BH is ejected far enough from the center on large enough orbits that Bondi accretion becomes ineffective. This corresponds to the accretion behavior seen in the last column of Fig. 3.10 ($v_{\rm k}/v_{\rm esc} = 0.8$).

For smaller $v_{\rm k}$, such that the BH is confined to the central few kpc, the dependence of $t_{\rm AGN}$ on the nature of the merger remnant is more complex. We examine first the relatively gas-poor models (those with initial $f_{\rm gas} = 0.1$). In the q1fg0.1a model, $t_{\rm AGN}$ is enhanced only for $v_{\rm k}/v_{\rm esc} \leq 0.5$ and falls precipitously at higher $v_{\rm k}$. In the q0.5fg0.1a model, recoil events always reduce the AGN lifetime. Merger remnants with less gas have smaller central gas reservoirs to fuel the BH during pericentric passages, and their shallower central potentials result in larger BH orbits, which have fewer pericentric passages. Consequently, in gas-poor remnants, $t_{\rm AGN}$ will generally be lower for recoiling BHs than for stationary BHs.

In gas-rich merger remnants, $t_{\rm AGN}$ is more readily enhanced by GW recoil. Stationary BHs in gas-rich mergers typically experience a bright AGN phase due to the rapid inflow of cold gas to the central region, which is terminated when the AGN feedback energy heats the surrounding gas enough to quench the BH fueling. Fig. 3.11 shows that although GW recoil shortens this bright AGN phase, the low-luminosity $t_{\rm AGN}$ is enhanced for recoil kicks as high as $v_{\rm k}/v_{\rm esc} = 0.7$. In these cases, the recoiling BHs are on tightly-bound orbits and can accrete gas during their numerous passages through the central dense region. Because they remain in motion, however, their feedback energy is spread over a much greater volume than for stationary BHs. As a result, the gas

encountered by the recoiling BHs never heats up enough to completely cut off the BH fuel supply, and the BH has a longer lifetime as a low-luminosity AGN. In contrast to the traditional "feast or famine" model of merger-triggered AGN fueling, these short-period recoiling BHs are more inclined to "nibble".

We can see evidence of this displaced AGN feedback through its effect on star formation. The bottom row of Fig. 3.10 shows the depletion of gas throughout each simulation, and the dotted lines show the $v_{\rm k} = 0$ curve in each of the other plots. It is evident that slightly less gas remains at the end of each higher-$v_{\rm k}$ simulation. In the merger with a stationary BH, this gas is accreted or expelled from the galactic center via feedback, but when the central BH is removed, the gas continues be consumed by star formation. Although in this example the star formation rate enhancement is small and difficult to discern from examining the SFR evolution alone, the effect can be much larger in higher-q, $f_{\rm gas}$ mergers. We explore in § 3.5.5 the implications of enhanced SFRs for our equal-mass, gas-rich mergers.

Although we have found that $t_{\rm AGN}$ may be enhanced by GW recoil for low-luminosity AGN, we emphasize that the bright AGN phase ($L > 10\% L_{\rm Edd}$) is always shorter for recoiling BHs than for stationary BHs, or at best roughly equal. This is a direct result of the peak accretion episode being disrupted at the time of the recoil kick. The important consequence of this is that the total accreted BH *mass* is never enhanced by GW recoil in our simulations. For moderate recoil speeds, the BH mass deficit relative to a stationary BH is generally slight, but we find that the effect of recoil is *always* to decrease the final BH mass. The implications of this finding are discussed in § 3.5.4.

Figure 3.11.—: (Following page.) AGN lifetimes ($t_{\rm AGN}$) of recoiling BHs with $v_{\rm k}/v_{\rm esc} = 0.4 - 0.9$, compared to $t_{\rm AGN}$ for $v_{\rm k} = 0$ in six different galaxy models. In each plot, the black (colored) lines indicate the stationary (recoiling) AGN lifetimes at each value of $v_{\rm k}/v_{\rm esc}$. The models shown are (from top left): q1fg0.6a (red), q1fg0.3a (blue), q1fg0.1a (green), q0.5fg0.6a (magenta), q0.5fg0.3a (cyan), and q0.5fg0.1a (gold). The line types denote $t_{\rm AGN}$ according to three definitions of an "active" BH. For the thin (thick) solid lines, $t_{\rm AGN}$ is the time for which the BH luminosity $L_{\rm bol} > 3\%$ (10%) $L_{\rm Edd}$. The dashed lines show $t_{\rm AGN}$ for $L_{\rm bol} > L_{\rm min}$, $L_{\rm min} = 3.3{\times}10^9$ $L_\odot$. In all cases $L_{\rm bol}$ is calculated from the Bondi-Hoyle accretion rate as described in the text. No cuts were applied to $t_{\rm AGN}$ based on the BH settling time, so $t_{\rm AGN}$ may include accretion that occurs after the BH settles back to the galactic center.

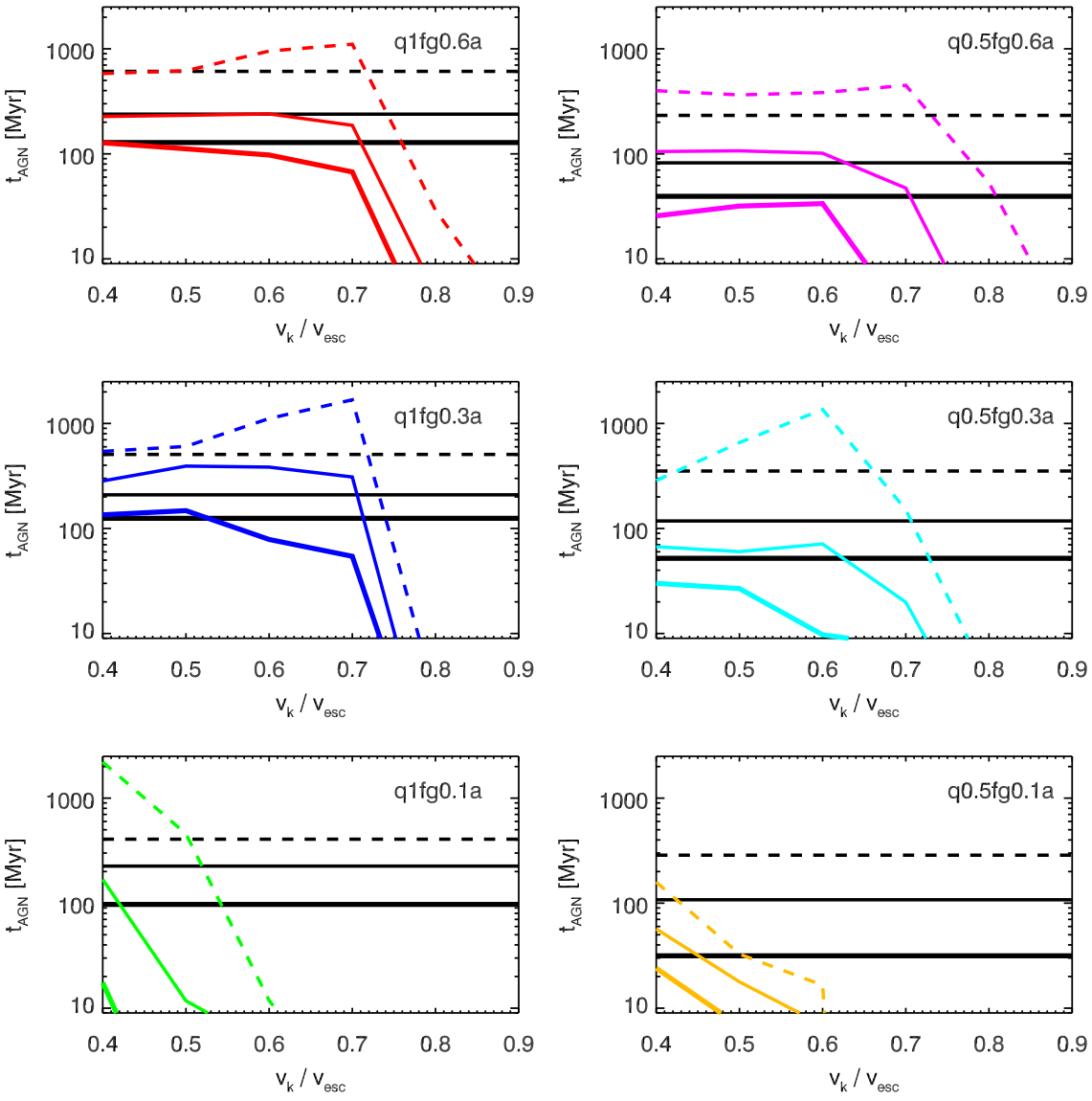

Figure 3.11.—: (Continued)

Finally, we note a possible observational consequence of longer AGN lifetimes. Fig. 3.10 clearly shows that when $v_{\rm k} = 0$, the two main accretion episodes are associated with the periods of rapid star formation. This means that the AGN luminosity may be difficult to distinguish from the starburst luminosity, and the AGN may also be dust-obscured for at least part of its active phase. If GW recoil allows the AGN to remain active long after the starburst is complete, such an AGN might be more readily observable, because it would no longer be competing with the starburst luminosity and may also be less dust-obscured.

3.5.2 Ejected Gas Disk

We have seen that moderate-velocity recoils in gas-rich remnants may allow efficient accretion from ambient gas. However, a BH moving rapidly or in a low-gas-density region is unlikely to sweep up much gas from its surroundings, and we would expect the probability of observing this type of active BH to be low. Indeed, in our simulations, the Bondi accretion rate of the BH rapidly declines following a large recoil kick (see Fig. 3.10). The possibility not accounted for in our simulations is that, if the BH is surrounded by an accretion disk at the time of recoil, some amount of this gas may remain bound to the recoiling BH. We therefore implement an analytic model to calculate the BH accretion rate from this ejected gas disk, based on the BH mass and accretion rate at the moment of recoil.

The BH carries with it the part of the accretion disk where $v_{\rm orb} \gtrsim v_{\rm k}$; i.e., it will carry a disk with radius approximately $R_{\rm ej} \sim GM_{\rm BH}/{v_{\rm k}}^2$. This is a reasonable approximation if the BH is kicked directly out of the orbital plane of the disk, as is the

case when $v_{\rm k} \gtrsim 500$ km s^{-1} and the BH orbital plane is aligned with that of the disk. If the accretion rate from this ejected disk is high enough, such a system could potentially be seen as an offset AGN via either resolved spatial offsets or offset spectral lines. BL08 predicted accretion timescales of $\lesssim 1 - 10$ Myr for the type of recoiling BHs we consider here ($M_{\rm BH} \sim 10^6 - 10^8$ M$_\odot$; $v_{\rm k} \sim 400 - 1000$ km s^{-1}), assuming a constant-$\dot{M}$ model. Here, we improve on these estimates by calculating a time-dependent accretion rate for the ejected disk.

We assume the innermost region of the gas disk is well-modeled by a viscous, Keplerian, thin disk (specifically, an α-disk, Shakura & Sunyaev (1973)). The evolution of the disk surface density, Σ, can be described by a diffusion equation:

$$\frac{\partial}{\partial t}\Sigma(R,t) = \frac{3}{R}\frac{\partial}{\partial R}\left[R^{1/2}\frac{\partial}{\partial R}\left(\nu\Sigma R^{1/2}\right)\right], \tag{3.1}$$

where ν is the kinematic viscosity (see, e.g., Lynden-Bell & Pringle 1974; Pringle 1981). The steady-state solution is recovered when the left-hand side of the equation vanishes, but this is not the case for our ejected disk, which is no longer fed at its outer radius. Exact analytic solutions to Eq. (3.1) can be found when ν scales only with radius (Lynden-Bell & Pringle 1974), but in the α-disk model, ν is a function of both R and Σ. Pringle (1991) has derived self-similar solutions to this equation for viscosity scaling as $\nu \propto \Sigma^m R^n$. These solutions assume a disk with no inner radius, so for our case we must neglect the finite inner disk radius at the innermost stable circular orbit of the BH ($R_{\rm ISCO}$), as well as the possibility of a circumbinary gap in the disk that persists after the BH merger. This should not affect our results, however, as the ejected disk will be much larger than the ISCO ($R_{\rm ej}/R_{\rm ISCO} > 10^3$), and the gap is expected to refill on a timescale of years (Milosavljević & Phinney 2005; Tanaka & Menou 2010). For an

α-disk in which viscosity is assumed to scale with gas pressure and the opacity equals the electron-scattering value ($\kappa_{\rm es} \approx 0.4$ cm^2 g^{-1}), the viscosity is given by

$$\nu = C\,R\,\Sigma^{2/3}\,,\;\; C \equiv \left(\frac{k_B\,\alpha}{\mu\,m_{\rm p}}\right)^{4/3}\left(\frac{\kappa_{\rm es}}{48\,\sigma_{\rm SB}\,G\,M_{\rm BH}}\right)^{1/3}. \tag{3.2}$$

In this equation $k_{\rm B}$ is Boltzmann's constant, α is the thin-disk viscosity parameter, μ is the mean molecular weight, $m_{\rm p}$ is the proton mass, and $\sigma_{\rm SB}$ is the Stefan-Boltzmann constant. This corresponds to the self-similar solution of Pringle (1991) with $m = 2/3, n = 1$ (see also Cannizzo et al. 1990):

$$\frac{\Sigma(R,t)}{\Sigma_0} = \left(\frac{t}{t_0}\right)^{-15/16} f\left[\left(\frac{R}{R_0}\right)\left(\frac{t}{t_0}\right)^{-3/8}\right], \tag{3.3}$$
$$f[u] \equiv (28)^{-3/2}\,u^{-3/5}\,(1-u^{7/5})^{3/2}.$$

The arbitrary constants Σ_0, t_0, and R_0 satisfy

$$t_0^{-1} = \frac{C\,\Sigma_0}{R_0}. \tag{3.4}$$

Integrating Eq. (3.3) yields a time-dependent expression for disk mass:

$$M_{\rm d}(t) = (28)^{3/2}\,\frac{4\pi}{7}\,R_0^2\,\Sigma_0\,\left(\frac{t}{t_0}\right)^{-3/16}. \tag{3.5}$$

From this we obtain the time-dependent accretion rate:

$$\dot{M}_{\rm d}(t) = -\frac{3}{16}\,(28)^{3/2}\,\frac{4\pi}{7}\,\frac{R_0^2\,\Sigma_0}{t_0}\,\left(\frac{t}{t_0}\right)^{-19/16}. \tag{3.6}$$

We determine Σ_0, t_0, and R_0 using Eq. (3.4) along with the conditions that $M_{\rm d}(t') = M_{\rm ej}$ and $\dot{M}_{\rm d}(t') = \dot{M}_{\rm mrg}$, where $t' = t_0 + t_{\rm sim} - t_{\rm mrg}$, $t_{\rm sim}$ is the time in the simulation, $M_{\rm ej}$ is the ejected disk mass, and $\dot{M}_{\rm mrg}$ is the Bondi accretion rate calculated in the simulation

at the time of merger. The mass evolution of the disk is therefore given by:

$$M_{\rm d}(t') = M_{\rm ej}\left(\frac{t'}{t_0}\right)^{-3/16}, \tag{3.7}$$

$$\dot{M}_{\rm d}(t') = \dot{M}_{\rm mrg}\left(\frac{t'}{t_0}\right)^{-19/16}, \tag{3.8}$$

$$t_0 = \frac{3}{16}\frac{M_{\rm ej}}{\dot{M}_{\rm mrg}}. \tag{3.9}$$

We can calculate the initial radius and mass of the ejected disk using the multi-component, self-gravitating disk model of BL08. The calculation takes as input the kick velocity, BH accretion rate, and BH mass at the time of the merger. We refer the reader to BL08 for the details of this model, but we note that for the BH masses and accretion rates considered here, $R_{\rm ej}$ lies in the region of the disk that is self-gravitating but still strongly dominated by the BH potential (i.e., Zone II of the BL08 model). Quantitatively, $R_{\rm ej}$ for our fiducial-mass simulations is between $10^{3.9-5.7}$ Schwarzschild radii, or $\sim 0.02 - 0.6$ pc. The corresponding mass of the ejected disk, $M_{\rm ej}$, is $10^{3.5-7.5}$ $\rm M_\odot$ ($10^{4.6-6.3}$ $\rm M_\odot$ for our fiducial-mass models).

We use these quantities as initial conditions for the ejected disk model outlined above. The timescale for the accretion rate (and mass) decay, t_0, ranges between $10^{5.6-7.6}$ yr. t_0 depends on $M_{\rm ej}$ and $\dot{M}_{\rm mrg}$, which in turn depend $v_{\rm k}$ and the galaxy model parameters. Specifically, t_0 decreases with increasing $v_{\rm k}$, $f_{\rm gas}$, and q. After a time t_0, the accretion rate has dropped by a factor of $2^{-19/16} \approx 0.44$ (note that the time in Eqns. 3.9 is defined such that $t' = t_0$ at $t_{\rm mrg}$). By the end of our simulations, about $55 - 80\%$ of the disk mass has been consumed. This corresponds to an increase in the BH mass of $\Delta M = 0.3 - 6\%$ ($0.3 - 3\%$ for $v_{\rm k}/v_{\rm esc} = 0.9$ simulations only). As expected, these values of ΔM are somewhat lower than the result of BL08, $\Delta M \approx 10\%\, M_{\rm BH}$. BL08 considered kick speeds as low as 100 km $\rm s^{-1}$; their result also assumed that the entire disk mass was

accreted and that the accretion was Eddington-limited at the time of BH merger.

Fig. 3.10 demonstrates that except in high-$v_{\rm k}$ simulations where the average orbital timescale is long ($v_{\rm k} \gtrsim 0.8\ v_{\rm esc}$), the ejected-disk accretion is typically insignificant compared to the Bondi accretion of the oscillating BH. Of course, the BH may still carry an accretion disk during this phase, but the accretion will be more accurately characterized by the highly-variable Bondi rate calculated from the local density and sound speed than by an isolated-disk model. Therefore, our analytic ejected-disk model becomes important only for high-velocity recoils in which the Bondi accretion rate drops sharply after the kick. Below, we discuss the AGN lifetimes resulting from the combined accretion models, as well as the feasibility of observing offset AGN.

3.5.3 Offset AGN

In Fig. 3.12, we show 2 examples of the ΔR, Δv phase space occupied by recoiling BHs. The left and right panels show simulations of the q0.5fg0.3a model with $v_{\rm k}/v_{\rm esc} = 0.6$ & 0.9, respectively. ΔR is the binned spatial offset of the BH from the stellar center of mass, and Δv is the binned kinematic offset from the stellar center-of-mass velocity. The contour shading shows, for each ΔR, Δv bin, the amount of time spent at that location (Δt, top windows), the total AGN energy output ($\Delta E_{\rm bol}$, middle windows), and the average bolometric luminosity $\langle L_{\rm bol} \rangle$ (bottom windows). $L_{\rm bol}$ is determined at each timestep from the relation $L_{\rm bol} = \epsilon_{\rm rad}\, \dot{M}_{\rm BH}\, c^2$, where the radiative efficiency $\epsilon_{\rm rad}$ is 0.1 unless $\dot{M}_{\rm BH} < 0.01 \dot{M}_{\rm Edd}$, in which case the system is considered radiatively inefficient, and $\epsilon_{\rm rad} = 0.1\, \dot{M}_{\rm BH}/(0.01 \dot{M}_{\rm Edd})$ (Narayan & McClintock 2008).

The $v_{\rm k}/v_{\rm esc} = 0.6$ recoiling BH, which settles back to the galaxy center in ~ 400

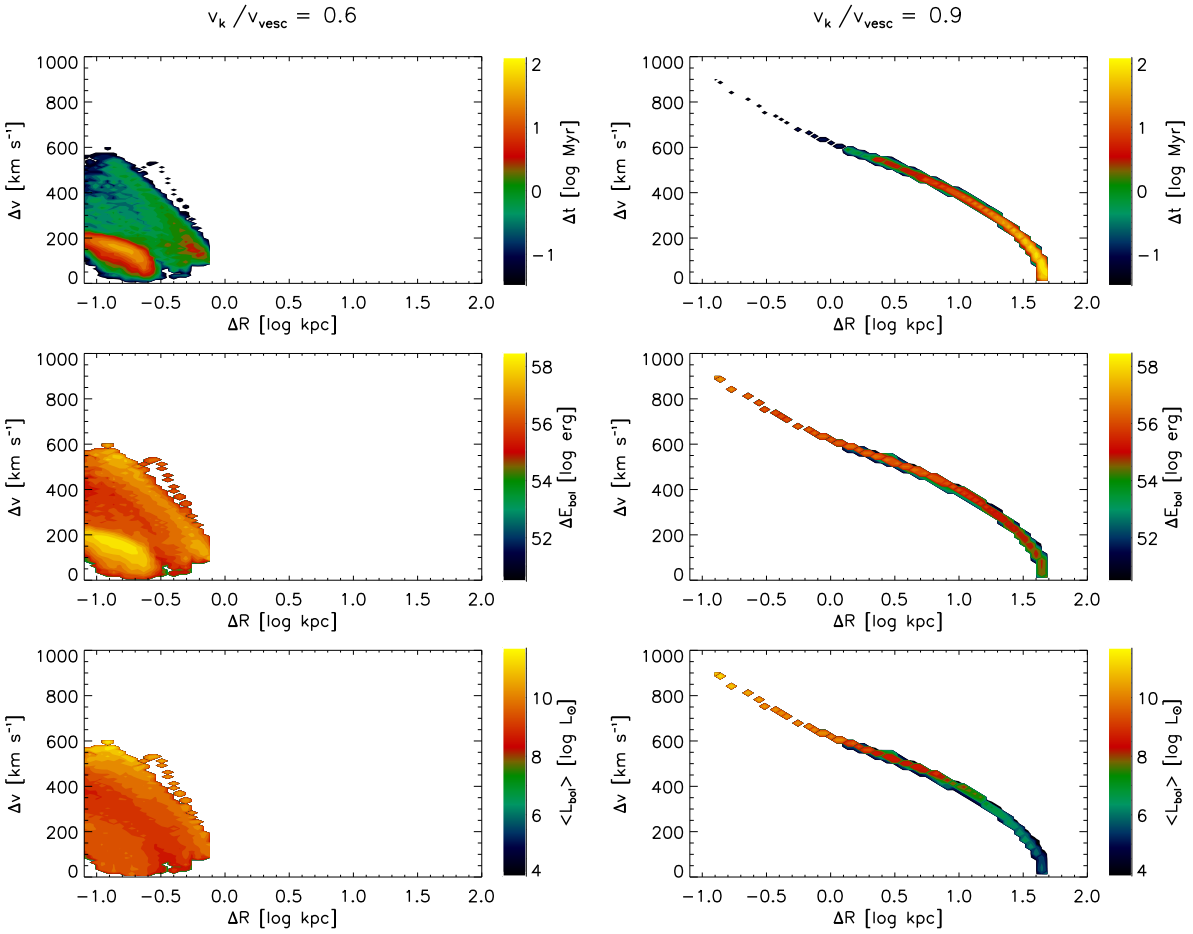

Figure 3.12.—: Contour plot of recoiling BH quantities Δt (top panels), $\Delta E_{\rm bol}$ (middle panels), and $\langle L_{\rm bol} \rangle$ (bottom panels) in ΔR, Δv space. $\langle L_{\rm bol} \rangle$ is the average bolometric BH luminosity per bin. The left panels are calculated from the q0.5fg0.3a merger simulation with $v_{\rm k}/v_{\rm esc} = 0.6$, and the right panels are for the same merger model but with $v_{\rm k}/v_{\rm esc} = 0.9$.

Myr, fills a corner of the phase space. The Δt contours peak at low velocities, as these represent apocentric passages where the BH spends the most time. $\langle L_{\rm bol} \rangle$ is above $10^8 L_\odot$ throughout the simulation, with peak values $> 10^{11} L_\odot$. Unlike the Δt contours, $\langle L_{\rm bol} \rangle$ peaks at high velocities, because the BH has the highest accretion rates immediately after the kick and during pericentric passages. The total bolometric energy output per ΔR, Δv bin, which is the product of these two distributions, accordingly peaks at both high ΔR, Δv and low ΔR, Δv. Instead of emitting all of its AGN feedback energy from a single central point in the galaxy, the BH distributes this energy throughout the central kpc, as discussed in § 3.5.1. Consequently, this BH has a longer AGN lifetime than the $v_{\rm k} = 0$ BH in the same merger model (see Fig. 3.11).

In contrast to this example, the $v_{\rm k}/v_{\rm esc} = 0.9$ recoiling BH occupies a narrow track in the phase space, as it completes only a few orbits and does not experience much drag. The Δt and $\langle L_{\rm bol} \rangle$ contours in this example illustrate an inherent difficulty in observing rapidly-recoiling BHs: the brightest luminosities occur just after the kick, when the BH velocities are highest, but this is also where the BH spends the least amount of time. Still, the BH has luminosities $\gtrsim 10^8 L_\odot$ for ΔR up to 10 kpc. Further analysis is required to determine the observability of the recoiling BHs in both of these examples, as well as those in our other simulations.

Figure 3.13.—: (Following page.) Active lifetimes of recoiling BHs as a function of $v_{\rm k}$. Results are shown for the same six galaxy models shown in Fig. 3.11, separated by mass ratio for clarity ($q = 1$ on the left, $q = 0.5$ on the right). On the left: q1fg0.6a (red), q1fg0.3a (blue), q1fg0.1a (green); on the right: q0.5fg0.6a (magenta), q0.5fg0.3a (cyan), and q0.5fg0.1a (gold). For each model, simulations were run for $v_{\rm k}/v_{\rm esc} = 0.4 - 1.2$. In all plots, the solid and dashed lines denote the three different definitions of $t_{\rm AGN}$ discussed in the text, and the shaded regions denote the range of values between these bounds. The upper and lower solid lines denote $t_{\rm AGN}$ for $L_{\rm bol} > 3\%$ and $10\%\, L_{\rm Edd}$, respectively. The dashed lines show $t_{\rm AGN}$ for $L_{\rm bol} > L_{\rm min}$, where $L_{\rm min} = 3.3 \times 10^9$ L$_\odot$. Unlike Fig. 3.11, here we have applied cuts to $t_{\rm AGN}$ such that only the active time $t_{\rm AGN} < t_{\rm settle}$ is shown. In the top two windows, $L_{\rm bol}$ is calculated from the Bondi accretion rate only, while the bottom two windows show $t_{\rm AGN}$ with the ejected-disk accretion model included as well.

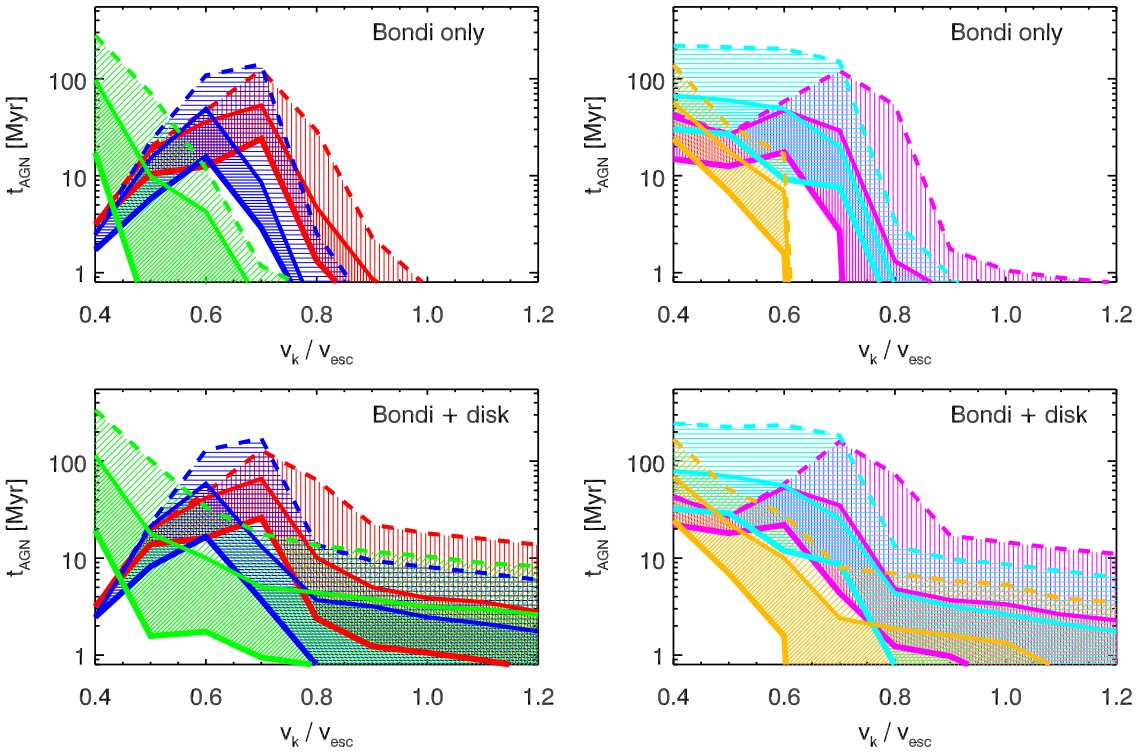

Figure 3.13.—: (Continued)

Fig. 3.13 shows the AGN lifetimes, $t_{\rm AGN}$, in six merger models for which we have varied $v_{\rm k}$. AGN lifetimes in the two windows include only the Bondi accretion rate, while $t_{\rm AGN}$ in the bottom two windows includes the accretion from our ejected-disk model as well. Unlike the lifetimes in Fig. 3.11, here we also apply a cut to the AGN lifetime such that only activity that occurs while the BH is recoiling is shown: $t_{\rm AGN} < t_{\rm settle}$. We calculate $t_{\rm AGN}$ using each of the three AGN definitions described previously. The solid lines in the figure correspond to AGN defined as $L_{\rm bol} > (3\%, 10\%)L_{\rm Edd}$, and the dashed lines correspond to $L_{\rm bol} > L_{\rm min}$. The shaded regions of the plot show the range of values between these definitions. As before, we choose $L_{\rm min} = 3.3 \times 10^9$ L$_\odot$ $= 1.3 \times 10^{43}$ erg s^{-1}.

A notable feature in Fig. 3.13 is that the peak AGN lifetimes for recoiling BHs are quite long, $>$ 100 Myr, even for kick speeds near 1000 km s^{-1}in some cases. Note also that in the lower-$f_{\rm gas}$ mergers, $t_{\rm AGN}$ peaks at the lowest $v_{\rm k}/v_{\rm esc}$, but in the gas-rich mergers the peak value is $v_{\rm k}/v_{\rm esc} = 0.7 - 0.8$. This reflects the fact that we have defined $t_{\rm AGN} < t_{\rm settle}$ in these plots. In the gas-rich mergers, gas drag quickly damps out the low-$v_{\rm k}$ trajectories, and $t_{\rm AGN}$ is limited by $t_{\rm settle}$. For higher $v_{\rm k}/v_{\rm esc}$, gas drag is less efficient and $t_{\rm AGN}$ is instead limited by the gas supply available to the BH.

In all cases, the AGN lifetimes that include only Bondi accretion (Fig. 3.13, top windows) fall sharply to $<$ 1 Myr for large $v_{\rm k}/v_{\rm esc}$. This demonstrates that Bondi accretion is inefficient when the BH is kicked far from the dense central region. However, when we also allow for BH accretion from its ejected disk (Fig. 3.13, bottom windows), the ejected-disk accretion enhances the active lifetime for high $v_{\rm k}/v_{\rm esc}$ recoils by more than an order of magnitude. In the examples shown, $t_{\rm AGN}$ for low-luminosity AGN is 3 - 14 Myr even for kicks as high as 1.2 $v_{\rm esc}$. For even higher kick speeds, $t_{\rm AGN}$ will slowly decay as the trend in the plot indicates, owing to the decreasing ejected disk mass.

The relatively slow decay of $t_{\rm AGN}$ with increasing $v_{\rm k}$ occurs partly because, as opposed to a constant-$\dot{M}$ accretion model, here $t_{\rm AGN}$ depends on the fraction of disk accreted before the BH luminosity falls below the "AGN" limit. In addition, the disk mass in the self-gravitating regime has a fairly weak ($r^{1/2}$) dependence on radius, so $M_{\rm ej} \propto 1/v_{\rm k}$. Recall, however, that the probability of recoil events with kick velocities $\gg 1000$ km s^{-1} is quite small (Schnittman & Buonanno 2007; Campanelli et al. 2007a; Baker et al. 2008; Lousto et al. 2010b; van Meter et al. 2010); this more than the BH's fuel supply limits the chances of observing a recoil event with $v_{\rm k} \gg v_{\rm esc}$.

These findings illustrate the importance of BH accretion from the ejected disk for the lifetimes of rapidly-recoiling AGN. Also crucial, however, is the time-dependent nature of this accretion. If we were to assume a simple constant-$\dot{M}$ model for the ejected-disk accretion, we would greatly overpredict the lifetime of the bright AGN phase, and in some cases we would underpredict the lifetime of the low-luminosity phase. We can calculate the discrepancies between $t_{\rm AGN}$ for a constant-$\dot{M}$ model and the lifetimes shown in Fig. 3.13, restricting the comparison to $v_{\rm k}/v_{\rm esc} \geq 0.9$ to capture only the simulations in which ejected-disk accretion is the dominant mode. $\dot{M}_{\rm BH}(t_{\rm mrg}) \approx 10\% - 50\% \dot{M}_{\rm Edd}$ for all the models shown in Fig. 3.13 except q0.5fg0.1a. If we assumed the accretion continues at this rate for a time $M_{\rm ej}/\dot{M}_{\rm BH}(t_{\rm mrg})$ in these models, we would overpredict $t_{\rm AGN}$ for bright ($L > 10\% L_{\rm Edd}$) AGN by a factor of $\sim 4 - 40$. Conversely, $t_{\rm AGN}$ for $L > L_{\rm min}$ would be *underpredicted* by a factor up to ~ 7. In the q0.5fg0.1a model, $\dot{M}_{\rm BH}(t_{\rm mrg}) \approx 5\% \dot{M}_{\rm Edd}$. In this case, $t_{\rm AGN}$ for $L > 3\% L_{\rm Edd}$ would be overpredicted by a factor of $\sim 10 - 40$, depending on kick speed, and $t_{\rm AGN}$ for $L > L_{\rm min}$ would *also* be overpredicted by a factor of $\sim 2 - 4$. Therefore, it is clear that inclusion of more realistic, time-dependent model for ejected-disk accretion, such as the one presented here, is important for calculating the

lifetimes and luminosities of rapidly recoiling AGN. Similarly, for lower-velocity recoils, the BH + ejected-disk system clearly cannot be treated as isolated, because accretion from ambient gas is the dominant mode of AGN fueling.

To determine whether these recoiling AGN could be distinguished from their stationary counterparts, we need more information than simply the active lifetimes. Recoiling AGN could be identified as such if during their active phase they are either kinematically or spatially offset from their host galaxies; we will consider both possibilities.

The gas carried along with the recoiling BH is expected to include at least part of the BH's broad-line (BL) region, because BL clouds reside deep within the potential well of the BH. The narrow-line (NL) region lies much further from the BH, so in general this gas will not be bound to the recoiling BH and will remain at the redshift of the host galaxy. A kinematically offset AGN could therefore be seen in a spectrum as a broad-line (BL) feature offset from a narrow-line (NL) feature, if the recoiling AGN is able to illuminate NL clouds as it leaves the center of the galaxy. Otherwise, such a system might have a spectrum with no NLs and BLs that are offset from the redshift of the host galaxy's stellar light. Because the physics of the NL region are not included in our analysis, we consider the velocity offset between the recoiling BH and the the stellar center of mass. We calculate the AGN lifetime as before, based on the BH luminosity at each timestep, but in this case we are only interested in the lifetime of *offset* AGN; that is, we calculate the time for which the BH is active *and* exceeds a minimum velocity offset $\Delta v_{\rm min}$. We note that the limit $\Delta v_{\rm min}$ is imposed on the physical velocity difference between the BH and the host galaxy. The line-of-sight velocity seen by a typical observer will be lower, so the velocity-limited AGN lifetimes shown here are upper limits.

Figure 3.14.—: (Following page.) The BH active lifetime is plotted in the same manner as in Fig. 3.13 and for the same galaxy models, but after minimum-velocity or minimum-separation cuts have been imposed. In all cases, both the Bondi accretion and the ejected-disk model are included in calculating $L_{\rm bol}$. The top two windows show the timescale for which the BHs are active and also have a velocity greater than 500 km s^{-1} relative to the host galaxy's stellar center of mass. The middle two windows show $t_{\rm AGN}$ for a minimum velocity of 800 km s^{-1}. The bottom two windows show $t_{\rm AGN}$ for when the BH is spatially offset from the stellar center of mass by > 1 kpc.

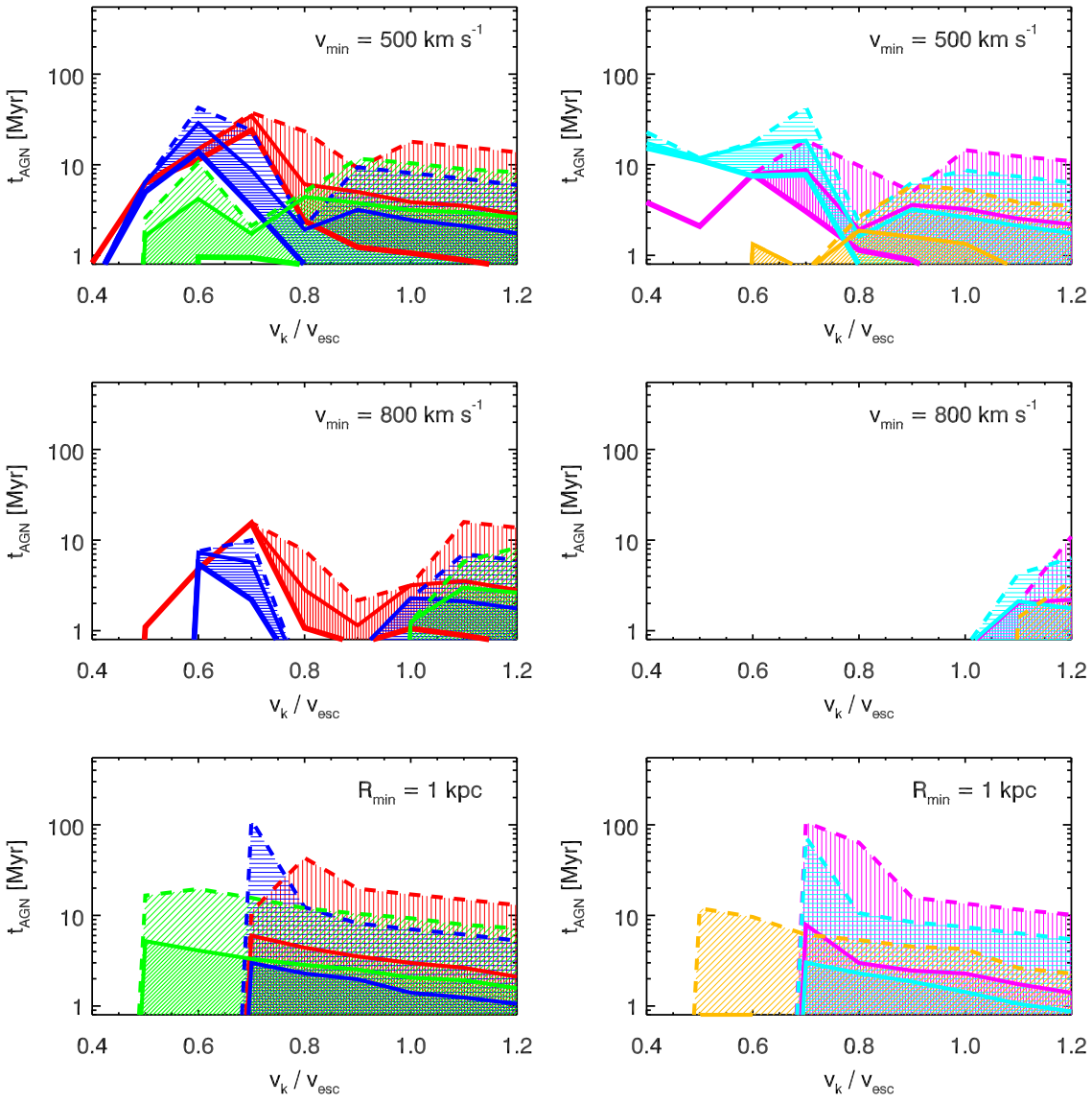

Figure 3.14.—: (Continued)

Fig. 3.14 shows the results of our analysis for $\Delta v_{\rm min} = 500$ km s^{-1} (top windows) and 800 km s^{-1} (middle windows). For $\Delta v_{\rm min} = 500$ km s^{-1}, the offset AGN lifetime for low-$f_{\rm gas}$, low-$v_{\rm k}$ mergers is much smaller than the total AGN lifetime in Fig. 3.13. $v_{\rm esc}$ is relatively low in these models, so kick speeds are also lower for fixed $v_{\rm k}/v_{\rm esc}$. In the q0.5fg0.1a merger, for example, $v_{\rm esc}$= 777 km s^{-1}, so the BH never exceeds the 500 km s^{-1}limit for $v_{\rm k}/v_{\rm esc} \leq 0.6$. The offset AGN lifetimes for low $v_{\rm k}/v_{\rm esc}$ in gas-rich models are a factor of 5-10 lower than the total AGN lifetimes, but the peak lifetimes are still $\sim 10 - 50$ Myr. At high $v_{\rm k}/v_{\rm esc}$ (≥ 0.8), there is little difference between $t_{\rm AGN}$ with or without the velocity cut. In these cases, the ejected disk dominates the BH accretion, and the BH speed is above 500 km s^{-1} for nearly all of the AGN phase.

When $\Delta v_{\rm min}$ is increased to 800 km s^{-1}, the AGN lifetimes drop sharply for most merger models and kick speeds (see the middle windows in Fig. 3.14). Only in the equal-mass, gas-rich models shown here (q1fg0.6a & q1fg0.3a) do the BHs appear as bright offset AGN, and for only a narrow range of kick speeds. These two models have $v_{\rm esc} > 1100$, such that BHs kicked with ~ 800 km s^{-1} may have tightly-bound orbits. In these cases the BHs make many rapid pericentric passages through the dense central region, where they encounter an ample gas supply from which to accrete. Interestingly, in the q1fg0.6a and q1fg0.3a models, kicks < 800 km s^{-1}(≤ 0.6 $v_{\rm esc}$) have nonzero lifetimes in this plot. These are examples of the phenomenon discussed in § 3.4.2, in which the BHs are kicked before $v_{\rm esc}$ reaches its maximum, so the BHs receive mild velocity boosts on subsequent passages through the increasingly deep central potential well.

In the other (lower-q, $f_{\rm gas}$) models, the central region is less dense, such that bound BHs have lower kick speeds and lower accretion rates during pericentric passages. In these models, only ejected-disk accretion is efficient at producing an offset AGN with

$\Delta v > 800$ km s^{-1}, which occurs only when the BHs are ejected entirely from the host galaxy. These ejected AGN have lifetimes < 10 Myr and low luminosities ($t_{\rm AGN} < 1$ Myr for $L > 10\%\, L_{\rm Edd}$).

To be observed as a spatially-offset recoiling AGN, a recoiling BH must travel far enough from the galactic center to be resolved as distinct point source before exhausting its fuel supply. As with the velocity offsets, we define the spatial offsets relative to the stellar center of mass. The maximum galactocentric distance achieved by a recoiling AGN in any of our fiducial-mass simulations is ~ 15 kpc by our lowest-luminosity AGN definition and only ~ 1 kpc by the strictest definition. In our high-mass simulations, which have larger ejected disks, offsets $\gtrsim 50 - 100$ kpc may be achieved while $L > L_{\rm min}$, but the maximum offset while $L > 3 - 10\%\, L_{\rm Edd}$ is still only a few kpc. Offsets of ~ 1 kpc correspond to an angular separation of ~ 0.55" at $z = 0.1$; these could be resolved with *HST/JWST* as long as they are not observed edge-on. Offsets $\gtrsim 3 - 4$ kpc could be resolved at this redshift with *SDSS* and *Chandra*. To determine the lifetimes of the spatially-offset AGN in our simulations, we impose a minimum-distance cut of $\Delta R_{\rm min} = 1$ kpc from the stellar center-of-mass, and we identify an offset AGN as one that simultaneously has $\Delta R > \Delta R_{\rm min}$ and meets our AGN-luminosity criteria. The bottom windows of Fig. 3.14 show the results of this analysis. We find that above $v_{\rm k}/v_{\rm esc} = 0.5 - 0.7$ (physically, the kick speed above which $R_{\rm max}$ exceeds 1 kpc), the offset AGN lifetimes can be long, but only for low-luminosity AGN. In these models, $t_{\rm AGN}$ ranges from $2 - 110$ Myr for $L > L_{\rm min}$, and $0.3 - 8$ Myr for $L > 3\%\, L_{\rm Edd}$. In none of our simulations does the offset exceed $R_{\rm min}$ for more than 1 Myr while its luminosity is $> 10\%\, L_{\rm Edd}$. The reason that spatially-offset AGN are only seen at low luminosities is as follows. For recoiling BHs with short-period oscillations, Bondi

accretion is dominant, and most of the bright AGN activity occurs during pericentric passages with small ΔR. For BHs on long-period orbits or escaping BHs, the ejected disk accretion dominates. In this case the brightest AGN phase occurs as the BH leaves of the central dense region, and once the BH passes $\Delta R_{\rm min}$, its luminosity has already begun a monotonic decay.

We can conclude from Fig. 3.14 that in most of our models, low-luminosity recoiling AGN may be distinguishable via spatial offsets > 1 kpc for kick speeds $\gtrsim 0.5 - 0.7\ v_{\rm esc}$, but as kinematically-offset AGN with $\Delta v_{\rm min} = 800$ km s^{-1}, they may be distinguishable only for kick speeds $\gtrsim v_{\rm esc}$. These offset AGN generally have luminosities $\lesssim 3\% L_{\rm Edd}$, and their luminosity owes mainly to accretion from the disk ejected with the BH. The exceptions are equal-mass, gas-rich mergers (here, q1fg0.6a & q1fg0.3a), in which recoiling BHs on bound trajectories may experience multiple phases as bright ($L > 10\% L_{\rm Edd}$), kinematically-offset AGN accreting from ambient gas during pericentric passages. This scenario can only occur in merger remnants with large central escape speeds ($\gtrsim 1100 - 1300$ km s^{-1}), such that BHs may receive kicks $\gtrsim 800$ km s^{-1}and still undergo short-period oscillations. In lower-q, lower-$f_{\rm gas}$ mergers, the central gas density is lower, and the kick speeds for bound trajectories are smaller, so this bright, velocity-offset phase does not occur. If kinematic offsets can be observed with a resolution of 500 km s^{-1} instead of 800 km s^{-1}, velocity-offset-AGN lifetimes increase significantly, and measurable velocity offsets can be attained for a much wider range of kick speeds.

In the lowest q, $f_{\rm gas}$ merger for which we have varied $v_{\rm k}$ (the q0.5fg0.1a model), the offset AGN lifetimes are always < 10 Myr for $L > L_{\rm lim}$ and < 2 Myr for $L > 3\% L_{\rm Edd}$. Our q0.5fg0.1a model has 10% gas initially, but by the time of the recoil kick only $\sim 4\%$

of the baryonic mass is in gas. We can conclude that merger remnants with gas fractions lower than this and with $q \lesssim 0.5$ are unlikely to fuel bright offset AGN according to our criteria, at least for recoiling BHs with $M_{\rm BH} \sim 10^7$ M$_\odot$. Larger BHs will have larger gas reservoirs and longer AGN lifetimes, and the reverse will be true of smaller BHs. For example, in the q0.5fg0.1a model, a BH with $v_{\rm k}/v_{\rm esc} = 0.9$ has a velocity-offset ($\Delta v_{\rm min} = 800$ km s^{-1}) AGN lifetime < 1 Myr by all AGN criteria, while in the 10$\times$ more massive q0.5fg0.1M10x model, the velocity-offset $t_{\rm AGN}$ is 27 Myr (for $L > L_{\rm min}$). In general, larger BHs will have longer offset-AGN lifetimes for fixed $v_{\rm k}/v_{\rm esc}$. However, larger BHs are found in larger galaxies, where a higher kick speed is required to reach an appreciable fraction of the escape speed, and such kicks have a lower probability of occurring. We discuss recoil kick probabilities further in § 3.6.1.

As a final caveat, we note that when Bondi accretion is dominant, the offset-AGN lifetimes are subject to the assumption that no significant delay occurs between when material becomes bound to the BH and when it is actually accreted. The brightest AGN phases of this type occur during pericentric passages, when the velocity is high and the BH is subsequently traveling away from the galactic center. Therefore, substantial delays in gas accretion would likely decrease lifetimes of velocity-offset AGN and increase lifetimes of spatially-offset AGN.

3.5.4 $\mathbf{M_{BH}}$ - σ_* Relation

Several authors have suggested that GW recoil may contribute to scatter in the observed black hole - host galaxy bulge relations due to ejected BHs (Volonteri 2007) or bound recoiling BHs that leave the central galactic region (Blecha & Loeb 2008; Sijacki et al.

2010). Volonteri (2007) used semi-analytic models to estimate the effect of ejected BHs at high redshifts on the BH mass - bulge stellar velocity dispersion relation at $z = 0$. In this work, we have already demonstrated that, even when they remain bound to the host galaxy, recoiling BHs can undergo substantially different accretion histories than their stationary counterparts, and that the resulting AGN lightcurves may also vary significantly as a function of kick speed (see Figs. 3.10, 3.13, 3.14). Here, we attempt to quantify the effect of individual GW recoil events on the $\mathrm{M_{BH}} - \sigma_*$ relation. Because we have simulated all of our merger models with both with no recoil kick and with $v_\mathrm{k} = 0.9\ v_\mathrm{esc}$, we are able to compare the $\mathrm{M_{BH}} - \sigma_*$ relations that result from each of these samples. The final BH masses and LOS-averaged stellar velocity dispersions from both sets of simulations are plotted in Fig. 3.15; the right window also shows simulations with $v_\mathrm{k}/v_\mathrm{esc}$ $0.4 - 0.8$. We include only models with the fiducial merger orientation angles (orbits a & w - z) in this plot to avoid heavily weighting the fit toward the (q, f_gas) combinations for which we have varied the orbit.

Figure 3.15.—: (Following page.) Top panel: $M_{\rm BH} - \sigma_*$ relation for BHs with no recoil kicks (black circles) and with $v_{\rm k}/v_{\rm esc} = 0.9$ (red triangles). $M_{\rm BH}$ is in all cases the BH mass at the end of the simulation ($t_{\rm mrg} + 2.9$ Gyr) and σ_* is the stellar velocity dispersion averaged over 100 random sight lines, where error bars give the range of sampled values. All merger models with orbits a & w - z are shown. The solid black line is a least-square fit to the no-recoil data and the red dashed line is fit to the high-recoil data; the fit parameters are indicated on the plot. Bottom panel: same data as left panel, but also including data for the six merger models in which we have varied $v_{\rm k}/v_{\rm esc}$. The blue diamonds show these results for $v_{\rm k}/v_{\rm esc} = 0.4 - 0.8$, and the blue dot-dashed line is a fit to these data. The green triple-dot-dashed line is a fit to all data shown.

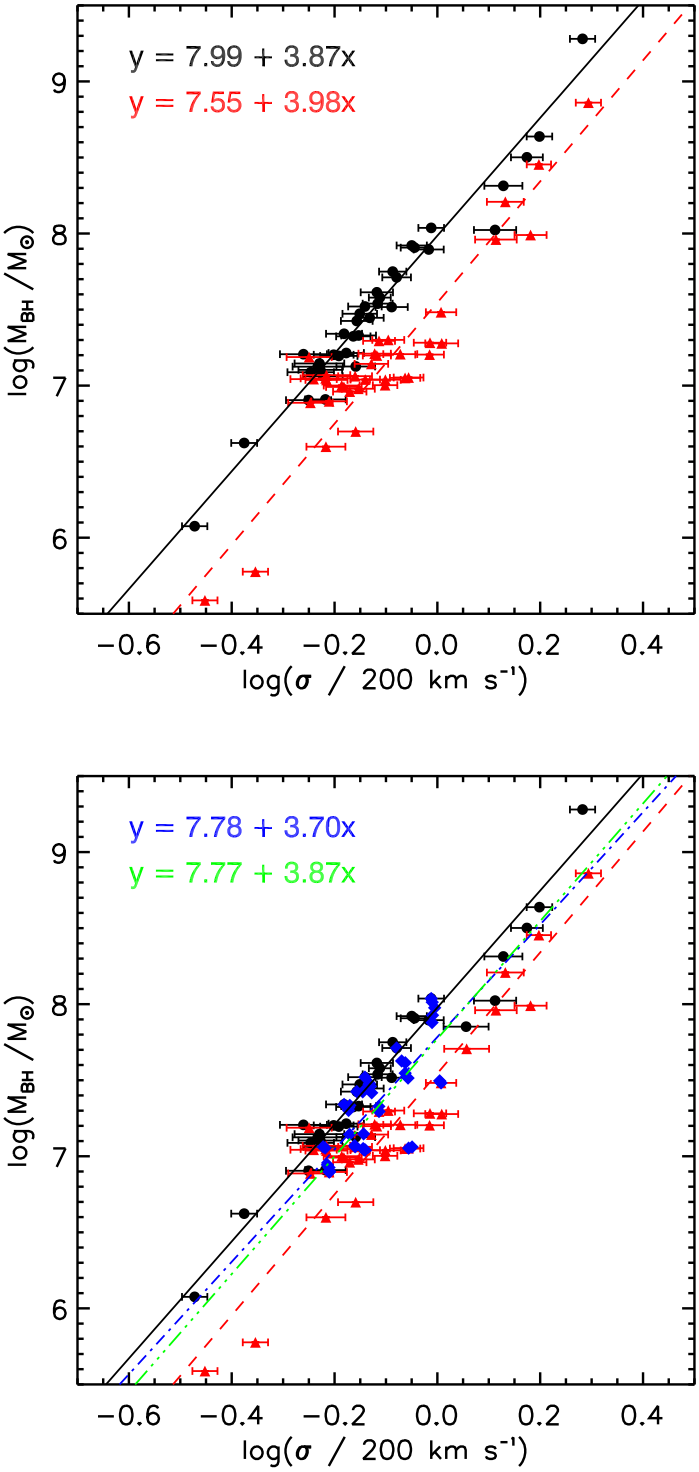

Figure 3.15.—: (Continued)

Note that in many cases, the $v_{\rm k} = 0.9\ v_{\rm esc}$ simulations result in BH wandering times of at least several Gyr, so in reality these BHs will be lost to the galaxy and never contribute to the $\rm M_{BH} - \sigma_*$ relation. However, because these BHs do not grow significantly after the kick, their mass deficits relative to the stationary BHs provide a sound upper limit on the BH mass deficits that can occur via single GW recoil events. We also stress that the data plotted here are *not* meant to represent a random sample, as we have varied parameters in a systematic way. Accordingly, the relations shown are not expected to reproduce the observed $\rm M_{BH} - \sigma_*$ relation. In particular, the scatter in the $v_{\rm k} = 0$ relation (0.13 dex) is smaller than the observed scatter ($\sim 0.25 - 0.3$ dex, e.g., Tremaine et al. 2002a; Aller & Richstone 2007; Hopkins et al. 2007b), owing to a number of factors such as the single merger orbital configuration used in this plot, the constant feedback efficiency assumed for all simulations, and small range of total galaxy mass spanned by the majority of our models. Furthermore, although scaling each kick to $0.9\ v_{\rm esc}$ essentially allows us to capture the maximum effect of a single recoil event, this does not reflect the fact that in galaxies with lower escape speeds, large $v_{\rm k}/v_{\rm esc}$ recoil events will occur more frequently than in massive galaxies. Such a trend with galaxy mass would steepen the slope of the $\rm M_{BH} - \sigma_*$ relation, though this would also depend on the distribution of other merger parameters, such as q and $f_{\rm gas}$, with varying galaxy mass. Despite these caveats, the relative differences in Fig. 3.15 between the simulations with and without recoil are robust and can easily be understood in physical terms.

It can be seen by visual inspection of Fig. 3.15 that the effect of high-velocity recoils is an overall downward offset in normalization and an increase in scatter. Because the LOS-averaged values of σ_* do not change significantly in the presence of a recoil kick, we focus our discussion on variation in the final BH mass.

The downward shift in Fig. 3.15 reflects the fact that GW recoil always reduces the final mass of a merged BH. We quantify the "mass deficit" of recoiling BHs relative to stationary BHs by calculating the fractional mass difference for each recoil simulation relative to its $v_{\rm k} = 0$ counterpart, ($M_{\rm fin}(0)$ - $M_{\rm fin}(v_{\rm k})$) / $M_{\rm fin}(0)$, where $M_{\rm fin}$ is the final BH mass in each case. Fig. 3.16 shows the mass deficit plotted versus $v_{\rm k}$ for the six merger models discussed previously. The deficits generally increase with $v_{\rm k}$, though the details vary substantially between models. In the q0.5fg0.1a model, recoiling BHs with $v_{\rm k} = v_{\rm esc}$ have $\sim 1/3$ lower final mass than do stationary BHs, while in the q1fg0.3a model, a $v_{\rm k} = v_{\rm esc}$ recoil results in a BH almost five times smaller than its stationary counterpart. Note also that the curves in Fig. 3.16 all level out at $v_{\rm k}/v_{\rm esc} = 0.7 - 0.9$; this marks the kick speed in each model above which recoiling BHs are unable to accrete more gas after their ejected disk has been exhausted. The models with lower $f_{\rm gas}$ achieve this limiting value at lower $v_{\rm k}/v_{\rm esc}$, owing to the lower gas drag and shallower potentials in these remnants. The blue diamonds in Fig. 3.15 mark the positions of these varying-$v_{\rm k}$ simulations on the $M_{\rm BH} - \sigma_*$ relation. The points corresponding to lower $v_{\rm k}/v_{\rm esc}$ lie close to the no-recoil (black) line; those with higher $v_{\rm k}$ have lower BH masses.

In Fig. 3.15, the normalization offset between the $v_{\rm k} = 0$ BH population and the $v_{\rm k}/v_{\rm esc} = 0.9$ population is 0.44 dex, and the offset between $v_{\rm k} = 0$ and the total population is 0.22 dex. However, we note that Hopkins et al. (2007a) have demonstrated that the normalization of the black hole - galaxy bulge correlations depends on the efficiency of AGN feedback. In our simulations, we assume a constant fraction (5%) of the BH's bolometric luminosity couples to the surrounding gas as thermal energy. Stationary accreting BHs with lower feedback efficiencies would grow larger before heating the surrounding gas enough to slow or halt accretion. Depending on how much

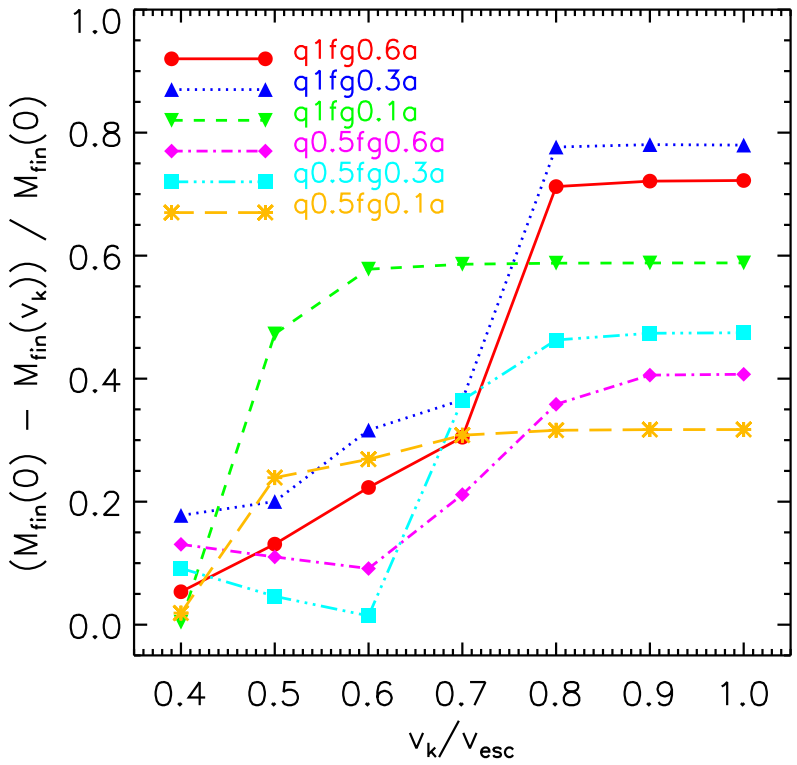

Figure 3.16.—: Fractional mass deficit of recoiling BHs versus stationary BHs as a function of $v_{\rm k}/v_{\rm esc}$. $M_{\rm fin}(0)$ and $M_{\rm fin}(v_{\rm k})$ are the final BH masses (at $t_{\rm mrg}+2.9$ Gyr) for stationary and recoiling BHs, respectively. The plot legend lists the models shown.

accretion occurs prior to versus after the BH merger, higher feedback efficiencies could reduce the normalization offset between our recoiling and stationary BH populations. In general, however, stationary BHs will accrete more after the BH merger than recoiling BHs, so there is likely to be a non-zero downward shift in $M_{\rm BH}-\sigma_*$ normalization caused by GW recoil.

As previously stated, the disproportionate effect of recoil events on galaxies with small $v_{\rm esc}$ could have some effect on the $M_{\rm BH}-\sigma_*$ slope. In our simulations, where we

have scaled kick speeds to $v_{\rm esc}$, there is no significant difference between the $M_{\rm BH} - \sigma_*$ slope for recoiling versus stationary BHs. This is to be expected, because the depth of the central potential well scales more or less self-similarly with total galaxy mass. We do, however, see a trend toward larger BH mass deficits for higher-q mergers, which arises because gas is driven more efficiently to the galaxy centers during coalescence, and recoiling BHs "miss" a larger accretion phase when they are kicked out of this central dense region.

The variation in BH mass deficits between merger models results in larger intrinsic $M_{\rm BH} - \sigma_*$ scatter for BH populations that have undergone recoils. The correlation for the no-recoil sample has a scatter of 0.13 dex, and the $v_{\rm k}/v_{\rm esc} = 0.9$ correlation has a scatter of 0.24 dex. In other words, the high-recoil sample has almost twice as much intrinsic scatter as the no-recoil sample. This increase in scatter is a universal consequence of GW recoil; recoil events essentially add an extra variable to the determination of final BH masses. As opposed to stationary BHs, the final mass of recoiling BHs depends not just on how much gas is available to be accreted, but also *when* this accretion occurs relative to the time of the kick. In mergers with no recoil, $M_{\rm BH}$ is a strong function of the amount of gas driven into the central region (i.e., the depth of the central potential well). The details and timing of the cold gas flow in galaxy mergers depend nontrivially on factors such as q, $f_{\rm gas}$, the galaxy orbits, and the star formation rate, so it is natural that larger intrinsic scatter is found in the final masses of recoiling BHs. If the kick speed is lower, such that the BH can settle back to the center while an ample gas supply is still present, the BH mass deficit will be reduced, but the details of this late-phase accretion add yet another element of unpredictability to the final value of the BH mass.

In addition to the larger intrinsic $M_{\rm BH} - \sigma_*$ scatter for a BH population with

fixed $v_{\rm k}/v_{\rm esc}$, we also anticipate an increase in overall scatter caused by the range of kick speeds that would occur in a realistic population of BHs and by BHs that have undergone multiple recoils through their formation history. The contribution of GW recoil to the total $M_{\rm BH}-\sigma_*$ scatter is difficult to predict from our simulations; quantitative predictions would require following detailed BH formation histories in a cosmological framework, which is beyond the scope of this paper. However, we at least gain a sense of how a range of kick speeds affects the $M_{\rm BH}-\sigma_*$ relation by plotting our varied-$v_{\rm k}$ simulations along with the $v_{\rm k}=0$ and $v_{\rm k}/v_{\rm esc}=0.9$ populations. The right panel in Fig. 3.15 shows the same data as the left panel but also includes data for the simulations in which we have varied $v_{\rm k}/v_{\rm esc}$ (blue diamonds). The blue line is a fit to these points, and the green line is a fit to all data shown. The fit to all the data has a scatter of 0.25 dex, which as expected is larger than the scatter for the $v_{\rm k}=0$ population.

The most robust of our conclusions from this analysis is the increase in intrinsic $M_{\rm BH}-\sigma_*$ scatter for BHs that have undergone a single recoil event, by a factor of ~ 2 in our simulations. This finding suggests that GW recoil events may be a non-negligible contribution to the scatter in the observed $M_{\rm BH}-\sigma_*$ relation, especially because BHs at $z=0$ may have undergone multiple recoil events throughout their formation history.

3.5.5 Evolution of Central Galactic Region

Fig. 3.17 compares the SFRs for simulations with no GW recoil (black dashed curve), with $v_{\rm k}/v_{\rm esc}=0.9$ (red solid curve), and with no BHs (blue dotted curve) in a gas-rich, equal-mass merger model (q1fg0.4a). It is clear that after the merger, the simulation with a large recoil kick has a higher SFR than the simulation with $v_{\rm k}=0$. The post-merger

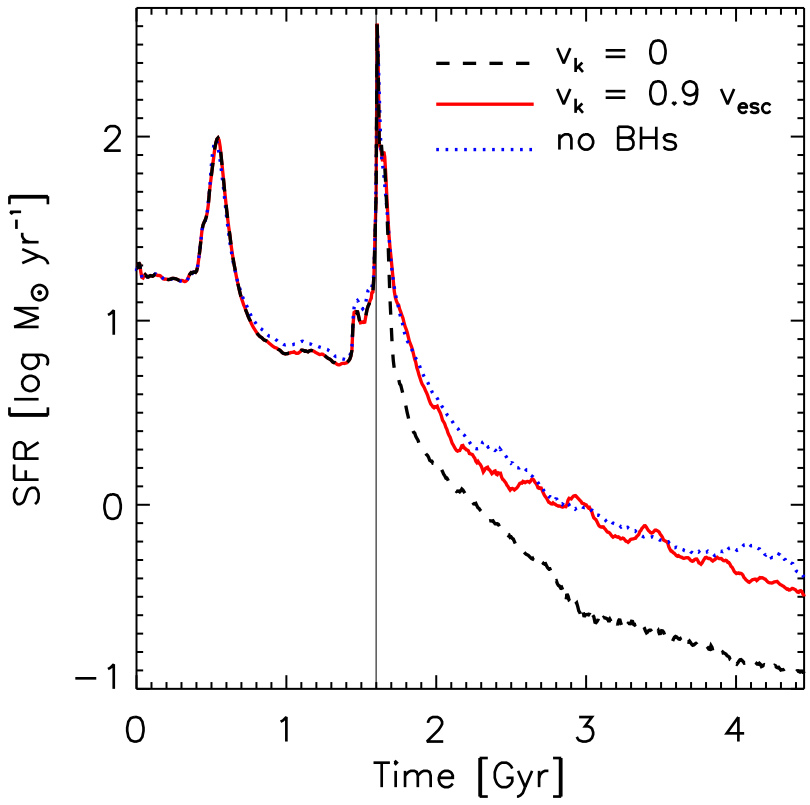

Figure 3.17.—: Total star formation rate (SFR) vs. time for the q1fg0.4a merger model. The black dashed line represents the $v_{\rm k} = 0$ simulation, the red solid line represents the $v_{\rm k}/v_{\rm esc} = 0.9$ simulation, and the blue dotted line represents a simulation with no BHs. The vertical line marks the time of BH merger in the simulations with BHs.

SFRs are similar in the high-recoil case and in the simulation with no BH at all. This same behavior can be seen in the high-recoil simulations of model q0.5fg0.3a shown in Fig. 3.10, though to a lesser degree. These enhanced SFRs occur because when the BH is removed from the center of the merger remnant, the AGN feedback is also displaced. The lack of central energy input allows star formation to continue unhindered in this region for a longer time. We can actually see the effect of the recoiling AGN feedback on the instantaneous SFR in Fig. 3.17. The SFR curve for the $v_{\rm k}/v_{\rm esc} = 0.9$ simulation has a vaguely periodic shape; in fact, each small trough in the SFR coincides with a pericentric passage of the BH through the galactic center, which imparts a small amount of feedback energy to the dense region. This supports the connection between the recoiling BH dynamics and the galactic SFR, but the main consequence of the recoil event is that star formation is never as strongly quenched as when the BH does not recoil. In the example shown in Fig. 3.17, the merger remnant with a stationary BH has almost twice the amount of gas at the end of the simulation as the merger with $v_{\rm k}/v_{\rm esc} = 0.9$. This corresponds to an increase in total star formation of $3.4 \times 10^9 M_\odot$ in the recoil simulation, or $\sim 3\%$ increase in total stellar mass, solely due to the displacement of the BH and its feedback.

In Fig. 3.18, we can clearly see the effect of this enhanced star formation on the remnant stellar density profile. The figure shows the remnant stellar density profiles for the same three simulations shown in Fig. 3.17, with $v_{\rm k} = 0$ (black curves), $v_{\rm k}/v_{\rm esc} = 0.9$ (red curves), and without BHs (blue curves). The results are further broken down into the contribution from stars formed prior to the galaxy merger ("old" stars, thin curves) and those formed during merger-driven starbursts ("new" stars, thick curves). In all cases, the "new" stellar population dominates in the central kpc, but in the remnant

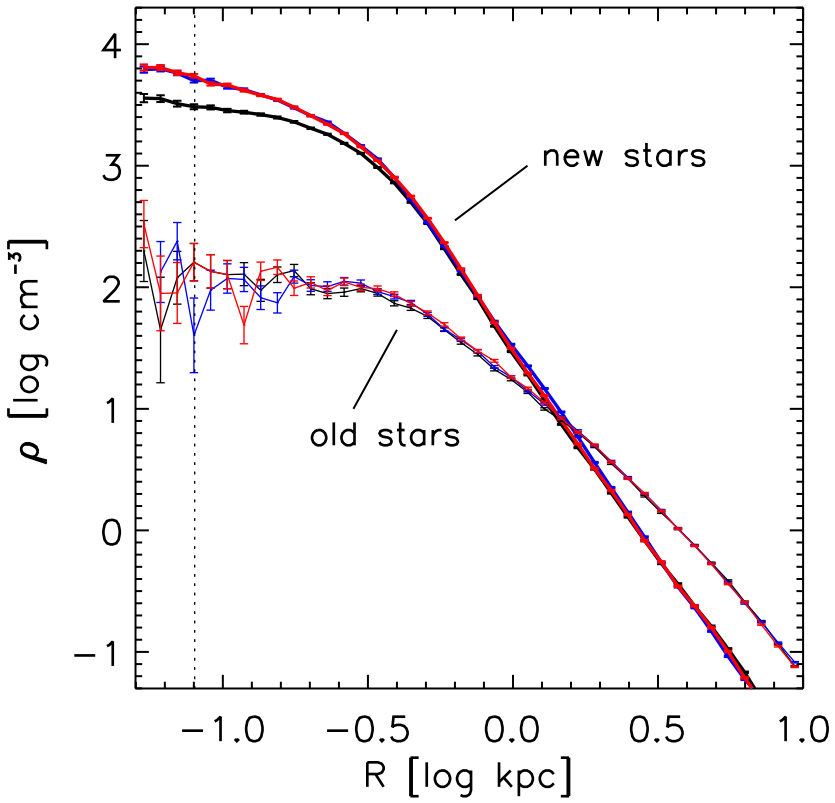

Figure 3.18.—: Final stellar density profiles (2.9 Gyr after $t_{\rm mrg}$) for the same three simulations shown in Fig. 3.17, with the same color coding. The thick curves are the "new" stellar populations that formed during the merger and that dominate within the central $\sim$ kpc, and the thin curves are the "old" stellar populations from the initial stellar disks of the progenitor galaxies. In each case, the black curves are the profiles for the $v_{\rm k} = 0$ simulation, the red curves represent the $v_{\rm k}/v_{\rm esc} = 0.9$ simulation, and the blue curves represent the simulation with no BHs. Poisson error bars are shown on the densities in each radius bin. The vertical dotted line denotes the gravitational softening length (80 pc) in these simulations.

with a recoiling BH the central stellar density is almost twice that of the remnant with a stationary BH. In fact, this stellar profile very closely resembles that of a remnant without a BH. Therefore, recoil events in gas-rich mergers can prolong starburst phases, creating denser and more massive stellar cusps. In § 3.6.5, we discuss the implications of these findings for observable properties of ultraluminous infrared galaxies (ULIRGs) and elliptical galaxies.

We note that this is the *opposite* effect of one that has been proposed for gas-poor mergers, where repeated BH oscillations through the central region of the merger remnant may scour out a stellar core (Boylan-Kolchin et al. 2004; Gualandris & Merritt 2008). Such core-scouring is expected to occur on scales of $\lesssim$ 10s of pc, which are below our resolution limit. However, we do comment that when even a small amount of gas is present in our merger simulations, it is efficiently driven to the center of the merger remnant.

3.6 Discussion

Using the SPH/N-body code GADGET-3, we have generated a suite of galaxy merger simulations both with and without a recoil kick applied to the central SMBH at the time of BH merger. Owing to the large range of parameters sampled, we were able to analyze systematic trends in recoiling BH behavior with variation in galaxy mass ratio, total galaxy mass, initial gas fraction, orbital configuration, and BH merger time. In addition, we have used a range of recoil kick velocities, which are scaled to the galactic central escape speed in each case. We followed the trajectories and accretion history of the recoiling BHs, as well as evolution of host galaxy properties such as the star formation

rate and depth of the central potential well. For the BH accretion, the Bondi-Hoyle accretion rates were used, but we also included a time-dependent model for accretion from a gas disk carried along with the recoiling BH.

3.6.1 Recoil Trajectories & Kick Probabilities

The recoiling BH trajectories in our simulations are characterized by low-angular-momentum orbits (i.e., "oscillations" about the galactic center) that are also highly three-dimensional. In other words, the baryonic component of the merger remnant dominates the BH orbits even if they extend well into the halo, but the unrelaxed nature of this remnant creates complicated BH trajectories. We find that the amplitude and duration of these oscillations varies widely between different galaxy models and kick velocities; some BHs settle back to equilibrium at the galactic center within a few Myr, while others may remain on large orbits through the halo for a Hubble time.

The amplitude and duration of BH oscillations in a given recoil event clearly depend on the central escape speed, i.e., the depth of the central potential well. However, by normalizing kick speeds in our simulations to $v_{\rm esc}$ at the time of the kick, we are able to compare different galaxy models regardless of their escape speed. We find substantial variation in recoil trajectories between models even for fixed $v_{\rm k}/v_{\rm esc}$. Recoil oscillations are more readily suppressed in mergers with higher q and $f_{\rm gas}$. Such merger remnants are more centrally concentrated and gas-rich, resulting in steeper central potential wells and increased gas drag and dynamical friction.

In the models for which we have varied $v_{\rm k}/v_{\rm esc}$, we find that, with the exception of our collisionless simulations, recoiling BHs with $v_{\rm k}/v_{\rm esc} = 0.4 - 0.7$ reach galactocentric

distances $\lesssim 1$ kpc and settle back to the center in < 0.5 Gyr. The corresponding range of kick speeds is 310-880 km s^{-1}.

For large recoil velocities, GW recoil events can produce BH oscillations that persist through the end of our simulations, 2.9 Gyr after the kick. The largest orbits can extend well into the galactic halo, with galactocentric distances up to ~ 100 kpc. In our models these long-lived oscillations occur for kicks $\gtrsim 0.6 - 0.9\ v_{\rm esc}$, again depending on the mass ratio and gas content of the merger.

Furthermore, as illustrated in § 3.4.2, in gas-rich mergers with $q \sim 1$, the central escape speed may increase rapidly around the time of BH binary coalescence. In this case, the trajectory of the recoiling BH may also depend on the *time* of the BH merger relative to the formation time of the central density cusp. Of all the factors influencing the BH trajectories, this is the most unpredictable, as it depends on the relative timing of two short-timescale processes. This adds an element of uncertainty to any attempt, including the current study, to model populations of recoiling BHs in gas-rich galaxies. Our assumption of rapid BH mergers ($t_{\rm mrg} = t_{\rm coal}$) means that our BH oscillation amplitudes may be upper limits in mergers with strong $v_{\rm esc}$ evolution. However, the effect of this uncertainty on the results presented here is limited, due to the relatively small number of merger models affected and our use of the normalization $v_{\rm k}/v_{\rm esc}$.

We have also tested whether recoil trajectories are affected by the direction of the kick. Our generic merger remnants (those that are not formed from highly-aligned galaxy orbits) are highly disturbed at the time of the BH recoil and therefore do not have disk-like structures, i.e., there is no "special" direction in which a recoiling BH would clearly experience much greater drag. Even with the clumpy, irregular density

profiles of our merger remnants, we find that the trajectories of recoiling BHs have little dependence on the kick direction. Much more important in determining the amplitude and duration of recoiling BH oscillations is the *magnitude* of the kick velocity relative to the escape speed, along with the aforementioned global galaxy properties such as the initial gas fraction and mass ratio. We note that there should indeed be a dependence of the recoil trajectory on the kick direction with respect to the plane of the accretion disk; recoils directed into the disk plane likely experience more gas drag and have shorter oscillation timescales. In addition, (Rossi et al. 2010) have shown that the ejected disk mass and AGN luminosity may depend strongly on the direction of the recoil kick with respect to the accretion disk plane. We do not resolve this small-scale region in our simulations; however, recoil kicks $\gtrsim 500$ km s^{-1}will *always* be nearly perpendicular to the orbital plane of the binary (Campanelli et al. 2007a,b; Lousto & Zlochower 2009), which is unlikely to be perpendicular to the orbital plane of the accretion disk. Therefore, for the recoil velocities we consider ($\gtrsim 300$ km s^{-1}), we can assume that the BH is unlikely to be kicked directly into the accretion disk plane.

We mention in § 3.2 that according to the results of NR simulations, the recoil kick speeds in our fiducial-mass merger models, which we have scaled to the escape speeds of $\sim 700 - 1250$ km s^{-1}, should occur with fairly high probabilities. Even if the BH spin magnitudes are randomly distributed between 0 and 1, 41.6% of major mergers should have kicks above 500 km s^{-1}, and 13.5% should be above 1000 km s^{-1}. Furthermore, Lousto et al. (2010b) have conducted statistical analysis of GW recoil spins and kick speeds using post-Newtonian approximations calibrated to numerical relativity results. They provide kick probability distributions for several mass ratio bins, which we can use to estimate the relative probability of "high" ($v_{\rm k} \sim v_{\rm esc}$) or "moderate" ($v_{\rm k} \sim 0.6\ v_{\rm esc}$)

kick speeds in various merger models. Coincidentally, for mass ratios $0.3 \leq q \leq 1.0$ and $300 \lesssim v_{\rm k} \lesssim 1000$ km s^{-1}, which represent a large fraction of our fiducial-mass simulations, the kick probability distribution is quite flat. For these models, the relative probability of a given kick speed between models, as well as the relative probability of high versus moderate $v_{\rm k}$ in a given model, is roughly unity. In our highest-mass (q1fg0.3M20x) simulation, the probability of a kick near $v_{\rm esc} = 2500$ km s^{-1} is about 10 times smaller than the probability of a kick with 0.6 $v_{\rm esc}$ and is also ~ 10 times smaller than the kick probability for $v_{\rm k} \sim v_{\rm esc}$ in the q1fg0.3a model. For mergers with $q \lesssim 0.25$, which we do not model in our study, the kick distribution becomes heavily skewed toward velocities < 500 km s^{-1}.

An important caveat to the interpretation of recoil kick probabilities is that the relevant velocity for observations is the line-of-sight (LOS) velocity, not the actual velocity. For random lines of sight, the probability of observing a given kick $v_{\rm k}$ as a kinematic offset $> \Delta v_{\rm min}$ is therefore reduced by a factor $P(\Delta v_{\rm LOS} > \Delta v_{\rm min}) = 1 - \Delta v_{\rm min}/v_{\rm k}$. For example, about 20% of recoils with $v_{\rm k} = 1000$ km s^{-1} will have $\Delta v_{\rm LOS} > 800$ km s^{-1}. Lousto et al. (2010b) find that the overall probability distribution for $\Delta v_{\rm LOS}$ is lower than the $v_{\rm k}$ distribution by a factor of between ~ 2 (for kicks > 500 km s^{-1}) and ~ 20 (for kicks > 2500 km s^{-1}). Similarly, the probability of observing a recoiling BH with spatial offset $\Delta R_{\rm LOS} > \Delta R_{\rm min}$ is $\sqrt{1 - \Delta R_{\rm min}^2/\Delta R^2}$; i.e., a majority of spatial offsets $\gtrsim 1.2\, R_{\rm min}$ will have LOS offsets exceeding the minimum observable offset.

3.6.2 Recoiling AGN Lightcurves

The final coalescence of two merging, gas-rich galaxies typically triggers both a burst of star formation and a phase of rapid BH accretion. Assuming the BHs themselves coalesce on a short timescale, the resulting recoil event coincides with a period of high activity in the central region of the merger remnant. Thus, we expect recoiling BHs in gas-rich mergers to have substantially different accretion histories than their stationary counterparts. This is indeed the behavior seen in our simulations, with greater disruption to the BH accretion history for higher kick velocities.

Recoil events that produce short-period BH oscillations ($v_{\rm k}/v_{\rm esc} \sim 0.4 - 0.8$, depending on the merger model) cause the BH accretion rate to drop at the time of the kick, thereby reducing the peak luminosity of the BH. However, the BH remains in the central few kpc of the merger remnant where gas densities are large enough that Bondi-Hoyle accretion is efficient. Because the BH's feedback energy is deposited in a much larger volume than for stationary BHs, it is unable to heat the gas sufficiently to completely terminate the AGN phase. The recoiling BH may therefore experience a longer active phase by a factor of a few than its stationary counterpart, although at lower luminosities. This phase continues in some cases until the end of the simulation, 2.9 Gyr after the BH merger. Owing to the lower luminosities of these extended AGN phases, we find that they do not increase the final BH mass relative to stationary AGN. However, this type of accretion episode is distinct from other merger-triggered AGN phases in that it is not accompanied by a simultaneous starburst. The copious amounts of dust produced by starbursts can easily obscure an active central source, and the starburst luminosity may overwhelm the AGN luminosity. Recoiling AGN that continue accreting

long after the starburst is complete therefore may be more easily observable.

When recoil kicks are large enough to produce long-period ($\gtrsim$ 100 Myr) BH oscillations ($v_{\rm k}/v_{\rm esc} \gtrsim 0.6 - 0.9$ depending on the merger model), the Bondi-Hoyle accretion rate drops precipitously as the BH is rapidly ejected to a lower-density region. Even though the BH remains on a low-angular-momentum orbit and returns several times to the dense central region, its velocity is generally too high during these pericentric passages to allow for substantial gas accretion, and the gas is depleted by star formation between subsequent passages.

In such high-velocity recoil events, a portion of the inner accretion disk may remain bound to the BH. We account for this by assigning to each recoiling BH a time-dependent, isolated accretion disk with a mass and initial accretion rate based on the BH mass, recoil velocity and the accretion rate at the time of the kick. The mass of these ejected disks is only a few percent of the BH mass, so they do not contribute significantly to the final BH mass. However, the accretion from these disks does greatly extend the active lifetime of rapidly-recoiling BHs in the regime where Bondi-Hoyle accretion is inefficient. We find that the AGN lifetime in our models may increase from $\ll 1$ Myr to ~ 20 Myr when ejected-disk accretion is included, though these are generally low-luminosity AGN. The peak lifetimes in the Bondi-Hoyle regime are generally longer and correspond to brighter AGN, but for a fairly narrow range of kick speeds. $t_{\rm AGN}$ in the Bondi-Hoyle regime may be up to ~ 300 Myr for low-luminosity AGN and between $\sim 10 - 100$ Myr for AGN accreting at $3 - 10\% L_{\rm Edd}$.

3.6.3 Offset AGN Lifetimes

From an observational standpoint, our primary interest is not the total active lifetime, but rather the time for which the BH is active *and* can be distinguished as a recoiling BH. We find that kinematically-offset AGN – those that are luminous enough to be detected *and* have velocity offsets large enough to be spectrally resolved – occur in two distinct physical scenarios. In the first scenario, the recoiling AGN travel far from the galactic center and are powered by accretion from the ejected disk. This occurs for recoil velocities near or above the central escape speed. In our simulations, AGN with velocity offsets > 800 km s^{-1} have lifetimes $\lesssim 10$ Myr in most cases. In most of our galaxy models, recoiling AGN can only meet this velocity criterion for $v_{\rm k} > v_{\rm esc}$. For reference, the SDSS quasar study conducted by Bonning et al. (2007), which yielded a null result, had a spectral offset limit of 800 km s^{-1}.

The other physical mechanism for producing kinematically-offset recoiling AGN is via multiple pericentric passages through a central dense region. Note that marginally-bound recoiling BHs may also experience close passages, but these will be rapid and few in number; the cumulative probability of observing such an event is low. If a recoiling BH is able to settle back to the galaxy center within $\sim 0.5 - 1$ Gyr, it will undergo many short-period oscillations through the central region. In this case, the BH may be able to accrete efficiently from the ambient gas during high-velocity close passages, producing a kinematically-offset AGN. This scenario favors massive, gas-rich galaxies with high central densities: the larger the central escape speed and the steeper the potential well, the higher the velocity with which a BH can be kicked and still remain tightly bound to the galaxy. In our $q = 1$, gas-rich mergers, offset AGN with $\Delta v > 800$ km s^{-1}can

have lifetimes up to 100 Myr, and may have lifetimes $\gtrsim 10$ Myr at bright ($> 10\% L_{\rm Edd}$) luminosities. Especially for these AGN, an increase of spectral resolution to achieve a limit of 500 km s^{-1} could make a substantial difference; in our models, the lifetimes increase by a factor of $\sim 5-10$ with this lower value of $\Delta v_{\rm min}$.

The maximum spatial offset achieved by a recoiling AGN in our high-mass simulations is $\Delta R = 112$ kpc by our most generous AGN definition ($L > 1.3 \times 10^{43}$ erg s^{-1}) and 3.2 kpc by our strictest definition ($> 10\% L_{\rm Edd}$), but for our fiducial-mass simulations these maximum offsets are only 15 and 1.3 kpc, respectively. To calculate spatially-offset AGN lifetimes, we require a minimum offset $\Delta R_{\rm min} = 1$ kpc. Such an offset could be resolved by *HST* or *JWST* at $z \lesssim 0.1$, or by *SDSS* or *Chandra* at $z \lesssim 0.03$. In our simulations, recoiling BHs achieve $R_{\rm max} > 1$ kpc for $v_{\rm k}/v_{\rm esc} \gtrsim 0.5-0.7$. AGN lifetimes may be quite long near this threshold kick speed (~ 100 Myr), though only at low luminosities. At higher kick speeds, lifetimes are generally $\sim 1-10$ Myr and slowly decrease with higher $v_{\rm k}$, as less gas bound to the recoiling BHs.

Based on our calculated AGN lifetimes, we conclude that for escaping BHs ($v_{\rm k} > v_{\rm esc}$), probabilities for observing recoils via spatial offsets and kinematic offsets are similar. For recoiling BHs on bound trajectories, velocity-offset AGN with high luminosities are favored for massive, gas-rich galaxies ($q = 1$, $f_{\rm gas} = 0.3-0.6$ in our models). Spatially-offset AGN with lower luminosities have similar lifetimes for all models. Recoiling BHs in merger remnants that are both gas poor ($f_{\rm gas} \lesssim 0.1$ initially) and result from lower-q mergers ($q \lesssim 1/3$) are not expected to produce long-lived offset AGN.

3.6.4 $M_{\rm BH} - \sigma_*$ Scatter & Offset

We have demonstrated that recoiling BHs have lower final masses than their stationary counterparts, though the mass deficit varies considerably with kick speed and merger remnant properties. This may affect the formation of the observed correlations between SMBHs and the bulges of their host galaxies. In particular, we consider the possible effects of these mass deficits on the observed $M_{\rm BH}-\sigma_*$ relation by comparing the $M_{\rm BH}-\sigma_*$ correlations of our sets of $v_{\rm k} = 0$ and $v_{\rm k} = 0.9\ v_{\rm esc}$ simulations, as well as our simulations with varying $v_{\rm k}$. We do not find any evidence for a change in $M_{\rm BH} - \sigma_*$ slope caused by recoils with fixed $v_{\rm k}/v_{\rm esc}$, but in a realistic population of galaxy mergers, galaxies with smaller $v_{\rm esc}$ would be disproportionately affected by recoils with $v_{\rm k}$ near or above $v_{\rm esc}$. This could contribute to some steepening of the $M_{\rm BH} - \sigma_*$ slope. In our simulations, we find that GW recoil events may contribute to a downward shift in normalization, an increase in overall scatter, and an increase in intrinsic scatter of the $M_{\rm BH} - \sigma_*$ relation (see Fig. 3.15). The magnitude of these effects, particularly the normalization offset and total scatter, are sensitive to the galaxy population considered and the detailed merger and recoil histories of the central BHs. Therefore, we cannot make quantitative predictions about the contribution of GW recoil to the observed normalization and scatter of the $M_{\rm BH} - \sigma_*$ relation; this would in fact be difficult to predict with any method. A more realistic approach involving BH and galaxy populations derived from a cosmological framework would still be plagued with uncertainties in the recoiling BH masses. We have shown that these masses are sensitive to numerous factors that do not lend themselves to semi-analytical modeling, including the (possibly evolving) central potential depth, the BH merger timescale, and the detailed BH accretion history.

Despite these uncertainties, the existence of a recoiling-BH contribution to the $M_{\rm BH} - \sigma_*$ correlation and its scatter is a necessary consequence of GW recoil events. In particular, we demonstrate that a universal effect of GW recoil is to increase the intrinsic scatter in BH masses. The disruption to BH accretion caused by a recoil event introduces an extra variable into the determination of the final BH mass, namely, the timing of the recoil kick relative to the merger-induced burst of BH accretion (i.e. quasar phase). In our recoil simulations, the intrinsic $M_{\rm BH} - \sigma_*$ scatter of our rapidly-recoiling BH population ($v_{\rm k}/v_{\rm esc} = 0.9$) is almost $2\times$ the scatter in our stationary-BH population. Because these high-velocity recoils do not allow the BH to grow significantly after the kick, this represents the maximal increase in scatter due to GW recoil for our simulated sample. While a more realistic population of BHs will have smaller average mass deficits resulting from a range of kick speeds, the BHs are also likely to have undergone numerous mergers and recoil events in the past, which would increase the contribution of GW recoil to the observed $M_{\rm BH} - \sigma_*$ scatter. The relatively small scatter of the empirical relation, 0.25 - 0.3 dex, places constraints on this contribution and, hence, on the frequency of large $v_{\rm k}/v_{\rm esc}$ recoil events. Similarly, a non-zero contribution of GW recoil to the observed scatter places constraints on the contribution from other sources, such as redshift evolution of the $M_{\rm BH} - \sigma_*$ relation (e.g., Haehnelt & Kauffmann 2000; Shields et al. 2003; Robertson et al. 2006b).

3.6.5 Broader Implications: Starbursts, ULIRGs, and Elliptical Galaxies

Previously, a model for galaxy evolution has been outlined in which mergers play a central role (e.g., Hopkins et al. 2006a, 2008b; Somerville et al. 2008). In this picture, galaxies form originally as disks, and the population of ellipticals is built up through time from mergers. Gas-rich mergers pass through intermediate phases in which they host significant star formation and black hole activity, first as ULIRGs, then as quasars, and finally as dormant elliptical galaxies.

There is a great deal of observational support for this scenario. Nearby ULIRGs are invariably associated with gas-rich mergers (Sanders et al. 1988a; Sanders & Mirabel 1996) and contain large quantities of molecular gas in their centers (Sanders et al. 1991), driving nuclear starbursts. Many display evidence for central AGN through their "warm" spectra (Sanders et al. 1988b), leading to the interpretation that quasars are the descendants of ULIRGs. As the starbursts and quasar activity fade, the merger remnant evolves into a passive elliptical (Toomre & Toomre 1972; Toomre 1977), making the transition from blue to red. The relics of this process can be seen in the central light concentrations in elliptical galaxies that were put into place during the starburst phase of their creation (e.g., Mihos & Hernquist 1994a; Hopkins et al. 2008c), and correlations between supermassive black holes and e.g. the central potentials of their hosts (Hopkins et al. 2007b; Aller & Richstone 2007).

These fossil signatures, and the timing of the events that led to their formation, are sensitive to the interplay between star formation and black hole growth and the feedback processes that accompany each of these. In principle, black hole recoil could impact all

of these phenomena to varying degrees, providing constraints on the modeling we have presented here as well on the interpretation of the observations more generally.

For example, some ULIRGs display evidence for significant AGN activity in the central starburst region. This is strong evidence that the BHs in these systems did not undergo rapid recoil events, and that any recoil motion was quickly damped out. However, merger-triggered central AGN, particularly those in ULIRGs, may be dust-obscured or dwarfed by the luminous starburst. AGN that are instead kicked out of the central region by a large recoil may be more easily detected, provided a large enough region of the galaxy is observed. Additionally, we have shown that in some cases, bound recoiling AGN may have longer lifetimes than stationary AGN. Such AGN may continue shining after the starburst is complete, which may also make them easier to observe.

Moreover, in the simulations, at least, feedback from black hole growth plays a significant role in quenching star formation (Di Matteo et al. 2005; Springel et al. 2005a), allowing the remnant to evolve from a blue, actively star-forming galaxy, to a red, quiescent object. During this transition, the remnant can, for some period of time, be classified as a K+A or E+A galaxy (Snyder 2010). If the central BH were ejected, star formation would linger at higher rates than for a stationary BH, extending the duration of the blue to red transition, modifying the stellar populations, and ultimately yielding an elliptical with denser, more massive central stellar cusps. If the BH did not eventually return to the nucleus, subsequent gas-poor mergers would be less strongly affected by BH scouring, obscuring the relationship between core and cusp ellipticals of the same mass (Hopkins & Hernquist 2010b).

Fig. 3.18 shows that if the BHs recoil at sufficiently high speed, the remnant relaxes

to a state similar to what would have happened had the galaxies not had black holes. Compared to the case of no BH recoil, the remnants with recoiling BHs (or no BHs) have more massive central stellar cusps. These more massive stellar cusps reflect a more extended period of active star formation following final coalescence of the progenitor galaxies, lengthening the period of time to make the blue to red transition. Furthermore, the reduced efficiency of AGN feedback means that the central regions would remain more heavily dust-obscured than if there were no BH recoil, making the remnant less likely to be visible as a K+A galaxy (Snyder 2010) and potentially significantly reducing the number of K+A galaxies expected to be observable as merger remnants.

Using our suite of merger models, we can make some qualitative predictions about the morphologies of recoiling BH hosts. Fig. 3.3 shows that our merger remnants have some common morphological features. In general, at the time of BH merger (and recoil) the merging galaxies have undergone final coalescence (i.e., they no longer have two distinct cores), but are still highly disturbed and have prominent tidal features. This is true even when the progenitor galaxies have low initial gas fractions (4%) or relatively small ratios (0.25). For minor mergers with $q < 0.25$, the disruption to the primary galaxy would be less pronounced, but such mergers would also yield small GW recoil kicks. Highly-aligned (i.e. coplanar) galaxy merger orbits may result in remnants with regular disk structures (see Fig. 3.3), but these orbits should comprise only a small fraction of major galaxy mergers. Therefore, we conclude that the majority of galaxy merger remnants that produce large GW recoil events have single cores but are still tidally disturbed at the time of the recoil kick. Furthermore, we have shown that the offset-AGN lifetimes for recoiling BHs in our simulations are < 100 Myr and are in most cases $\sim 1 - 10$ Myr. Tidal structures in these major merger remnants generally persist

for at least a few hundred Myr, so it follows that most observable recoiling AGN should be found in unrelaxed remnants that may still have visible rings or tidal tails.

3.6.6 Comparison to Recent Work

Shortly before this paper was completed, Guedes et al. (2010) and Sijacki et al. (2010) completed independent studies of recoiling BHs in gaseous mergers. However, both of these papers are exploratory in nature, in that only a few examples of galaxy mergers are studied. While there is agreement between these studies on some fundamental conclusions, our large parameter study allows us to expand upon these findings, connect them into a more coherent picture, and present some entirely new results. Here we give a brief comparison of this work to the work of Guedes et al. (2010) & Sijacki et al. (2010).

Guedes et al. (2010) use one equal-mass and two minor merger remnants as initial conditions for their simulations. The mass and spatial resolution used are comparable to ours, though in their equal-mass merger, higher resolution is obtained at late stages via particle splitting. The merger orbits were coplanar and prograde, a configuration that results in highly disk-like remnants (see our Fig. 3.3). Recoils with a range of kick speeds were applied to the BH, and after a brief initial phase, the BH trajectories were followed semi-analytically. We note that they use $v_{\rm k}/v_{\rm esc}$ as low as 0.14, while we use only $v_{\rm k} > 0.4\ v_{\rm esc}$, such that the BHs do not spend most of their time at radii $\sim R_{\rm soft}$.

Sijacki et al. (2010) use isolated galaxy models as well as one galaxy merger model for their recoiling BH simulations. Like our simulations, theirs were performed using GADGET-3, with similar spatial resolution. However, they use only one merger model, which is massive and gas-rich, resulting in a remnant with a very high central escape

speed (3500 km s^{-1}) and steep central potential. This model is therefore fairly extreme, in that recoils with $v_k \sim v_{esc}$ are required to eject the BH beyond the central few kpc.

Despite the substantially different approaches of these two studies and our own, a common finding is that gas inflow during galaxy mergers can create centrally-dense remnants that impart significant gas drag to recoiling BHs, thereby reducing the amplitude and return time of their trajectories. That this effect remains important even for modest gas fractions ($\lesssim 0.1$) illustrates the limitations of modeling GW recoil dynamics in purely collisionless systems.

Guedes et al. (2010) find that in their minor mergers, recoiling BHs exceed 600 km s^{-1} only for $v_k > v_{esc}$, and they do not calculate AGN lifetimes for escaping BHs. Kinematically-offset AGN have lifetimes up to a few Myr in their $q = 1$ merger. Sijacki et al. (2010) note that velocity offsets up to 500 km s^{-1} may occur during the bright AGN phase in their isolated disk model, but do not discuss offset AGN in their merger model.

Although they use similar values of L_{min} and ΔR_{min}, Guedes et al. (2010) calculate longer spatially-offset AGN lifetimes than we find in our models. The disparity in offset AGN lifetimes may arise partly from the different dynamical treatments; Guedes et al. (2010) calculate the recoil trajectories semi-analytically, as opposed to our N-body approach. Further, they assume $\dot{M}_{BH} = \dot{M}_{Edd}$ for the ejected-disk accretion rather than a time-dependent, isolated-disk model. They argue that spatially-offset AGN are naturally longer-lived than kinematically-offset AGN because the former occur near apocenter and the latter near pericenter. However, we show that in some cases, kinematically-offset AGN may have longer lifetimes, because the BH is much more likely to be actively

accreting during passages though the central dense region.

As we have found in our recoil simulations, Sijacki et al. (2010) show that recoil events interrupt a phase of rapid BH accretion in their gas-rich merger, causing a BH mass deficit relative to a stationary BH. They note that BH mass deficits may introduce scatter into BH mass - host galaxy relationships, which we demonstrate robustly in § 3.5.4.

Furthermore, both our results and those of Sijacki et al. (2010) show that the central SFR is higher after a large recoil, due to the displacement of AGN feedback. Sijacki et al. (2010) note that this further depletes the gas supply available to the BH once it returns to the center. We demonstrate that SFR enhancement due to recoil is strongest in gas-rich, nearly-equal-mass mergers, though it is present in all of our simulations to some degree, and we have outlined several possible observational consequences in § 3.6.5.

In addition to connecting and expanding upon the results of Guedes et al. (2010) and Sijacki et al. (2010), many of our results are entirely new to this work. As we have discussed these previously, we list them here only briefly. First, because we allow the BH merger time to be a free parameter, we are able to demonstrate that recoil trajectories may depend quite sensitively on the BH merger time in $q \sim 1$, gas-rich mergers. We eliminate much of this uncertainty in our simulations by scaling $v_{\rm k}$ to $v_{\rm esc}(t_{\rm mrg})$. This approach also enables a much clearer comparison between models. Also unique to our work is that we test a range of recoil kick directions in generic merger remnants, demonstrating that in general, the kick direction is less important for recoil trajectories than the kick magnitude.

Another novel feature of our models is the inclusion of a time-dependent accretion

disk around the recoiling BH. We also calculate recoiling AGN lifetimes using three different luminosity limits, which allows us to differentiate between bright and faint AGN. We learn from this analysis that some recoiling BHs may actually have longer AGN lifetimes than stationary BHs, though at low luminosities. We also show that kinematically-offset AGN occur via two different mechanisms: repeated pericentric passages in massive, gas-rich remnants, and ejected-disk accretion in high-velocity recoils ($v_{\rm k} > v_{\rm esc}$ in our models). We demonstrate that spatially-offset AGN can occur for a wide range of kick speeds and merger models.

Finally, we use our suite of simulations construct $M_{\rm BH} - \sigma_*$ relations for stationary and rapidly-recoiling BH populations. We find that GW recoil introduces a normalization offset and larger overall and intrinsic scatter into this correlation.

We have shown that recoiling BHs may be observable as offset AGN; discoveries of these objects would both inform models of hierarchical galaxy formation and constrain event rates for future gravitational-wave observatories. In the meantime, the richly varied effects of GW recoil on SMBHs and their host galaxies are not to be discounted as important components of merger-driven galaxy evolution.

Chapter 4

Double-peaked Narrow-Line Signatures of Dual Supermassive Black Holes in Galaxy Merger Simulations

L. Blecha, A. Loeb, & R. Narayan

Abstract

We present a first attempt to model the narrow-line (NL) region of active galactic nuclei (AGN) in hydrodynamic simulations of galaxy mergers, using a novel physical prescription. This model is used to explore the origin of double-peaked NL AGN

in merging galaxies and their connection to supermassive black hole (SMBH) pairs, motivated by recent observations of such objects. We find that double-peaked NLs induced by the relative motion of dual SMBHs are a generic but short-lived feature of gaseous major mergers. Double-peaked NL AGN are most likely to be observed in late-stage galaxy mergers, during the kiloparsec-scale phase of SMBH inspiral or soon after the nuclear coalescence and subsequent SMBH merger. However, even within the kiloparsec-scale phase, only a *minority* of double-peaked NLs are directly induced by the relative motion of binary SMBHs; their lifetimes are typically a few Myr. The majority of double-peaked NLs result from gas kinematics near the SMBH, although prior to the SMBH merger up to $\sim 80\%$ of all double-peaked NL profiles may be *influenced* by SMBH motion via altered peak ratios or overall velocity offsets. The total lifetimes of double-peaked NL AGN depend strongly on viewing angle and on properties of the merging galaxies; gas-rich, nearly-equal-mass mergers have more NL AGN activity but may also be more obscured. Furthermore, in a typical merger, at least 10 to 40% of the double-peaked NLs induced by SMBH motion have small projected separations, $\sim$ 0.1–1 kpc, making it difficult to clearly identify dual peaks of stellar surface brightness. Diffuse tidal features can indicate a late-stage merger, although they do not distinguish an SMBH pair from a merged SMBH. We demonstrate that double-peaked NL AGN spectra with large peak velocity splittings ($\gtrsim 500$ km s^{-1}) or with discernible overall velocity shifts are often associated with inspiraling SMBH pairs. Our results support the notion that selection of double-peaked NL AGN is a promising method for identifying dual SMBH candidates, but demonstrate the critical importance of high-resolution, multi-wavelength follow-up observations, and the use of multiple lines of evidence, for confirming the dual nature of candidate SMBH pairs.

4.1 Introduction

Although supermassive black hole (SMBH) pairs are a natural result of major galaxy mergers, until recently, evidence for their existence has been scarce. On large scales, some constraints are obtained from quasar clustering surveys. About 0.1% of quasars are observed to be in pairs on scales of $\lesssim 1$ Mpc, and evidence for excess quasar clustering on small scales suggests that some of these are induced by galaxy interactions (Hennawi et al. 2006).

In later stages of galaxy merging, at SMBH separations of $\sim$ 1–10 kpc, dynamical friction drives the evolution of the SMBH pair toward the center of the merger remnant. This "kiloparsec-scale" phase has seen by far the most recent observational progress. A few spatially-resolved pairs of active galactic nuclei (AGN) on these scales have been found serendipitously (Komossa et al. 2003; Bianchi et al. 2008; Green et al. 2010; Koss et al. 2011b), and notably, a candidate SMBH pair with $\sim$ 150 pc separation was recently discovered (Fabbiano et al. 2011). However, *spectroscopic* surveys of AGN have found that about 1% of all AGN have double-peaked narrow [O III] lines, a possible signature of SMBH orbital motion on approximately kiloparsec scales (Comerford et al. 2009b; Smith et al. 2010; Liu et al. 2010b). This finding has increased the number of candidate SMBH pairs from a small handful to several hundred.

While only a fraction of these double-peaked narrow-line (dNL) AGN are expected to actually contain SMBH pairs, follow-up observations have already revealed strong evidence that some of these are in fact dual SMBHs. Observations of dNL AGN that combine ground-based, high-resolution optical and near-infrared imaging with long-slit spectroscopy (Liu et al. 2010a; Shen et al. 2011) or integral field unit (IFU) data (Fu et al.

2011b; McGurk et al. 2011) have revealed numerous systems with two resolved stellar components in images that are spatially coincident with the two emission components in their spectra. These are among the most compelling dual SMBH candidates. Shen et al. (2011) estimate that $\sim$ 10–50% of dNL AGN host dual SMBHs, and that, when corrected for sample completeness, up to 2.5% of Type 2 AGN at $z < 0.3$ are active, kpc-scale SMBH pairs.

Additionally, Fu et al. (2011a) and Rosario et al. (2011) have used adaptive optics (AO) imaging to constrain the environment and host galaxy morphology of some dNL AGN; their estimates of the dual SMBH fraction are in broad agreement with those of Shen et al. (2011). Comerford et al. (2011b) have conducted analysis of 81 slit spectra obtained for dNL AGN; they find that *all* of these systems show spatially-separated emission components on approximately kpc scales, and they identify 14 of these as strong dual SMBH candidates. Still more compelling evidence for SMBH pairs comes from the detection of dual compact X-ray (Comerford et al. 2011a) and radio (Fu et al. 2011c) sources, respectively, in two dNL AGN. In contrast, Rosario et al. (2010) combined slit spectroscopy with VLA imaging to demonstrate that the dual SMBH scenario is disfavored in two systems where radio jets are likely responsible for the double-peaked spectral features. Thus, follow-up observations of dNL AGN have already shown great promise for confirming the nature of these candidate dual SMBHs.

On smaller scales ($\lesssim$ 10 pc), SMBH pairs evolve to form a tightly bound binary SMBH. These present a formidable challenge for observers, partly because they are difficult if not impossible to resolve with current telescopes. Only one confirmed example of a tightly bound SMBH binary is known, with a separation of 7.3 parsec (Rodriguez et al. 2006). On scales $\ll$ 1 pc, numerous spectroscopic binary candidates have been

identified, but confirming their binary nature will likely require a better understanding of broad line physics (Dotti et al. 2008; Bogdanović et al. 2009; Boroson & Lauer 2009; Tsalmantza et al. 2011; Eracleous et al. 2011). Therefore, the kiloparsec-scale phase of SMBH pair evolution currently appears to be the most promising avenue for studying dual SMBHs.

Theoretical studies of SMBH mergers face their own challenges, largely owing to the vast range of physical scales involved. Significant progress has been made on the smallest scales; simulations of BH mergers using full general relativity are now possible and can calculate precise waveforms of GW emission as well as the remnant BH properties (e.g., Pretorius 2005; Campanelli et al. 2006; Baker et al. 2006). However, there is still much uncertainty in the timescale on which the binary evolves from parsec scales down to milliparsec scales, where gravitational-wave (GW) emission dominates the orbital decay. In highly symmetric, spheroidal galaxies with little to no gas, SMBH binaries may "stall" at ~ 1 parsec for more than a Hubble time (e.g., Begelman et al. 1980; Milosavljević & Merritt 2001; Yu 2002). If the galaxy is gas-rich or non-axisymmetric, however, the SMBHs may merge on a much shorter timescale ($\sim 10^6$–10^7 yr from the hard binary stage; e.g., Gerhard & Binney 1985; Yu 2002; Armitage & Natarajan 2002; Berczik et al. 2006; Escala et al. 2004; Gould & Miralda-Escude 1997).

Galaxy mergers and SMBH pair formation have been studied extensively with hydrodynamic simulations (e.g., Di Matteo et al. 2005; Robertson et al. 2006a; Hopkins et al. 2006a; Callegari et al. 2009; Colpi & Dotti 2009). Van Wassenhove et al. (2011) have studied the triggering of AGN pairs in merging galaxies, finding that luminous dual AGN occur most frequently in the late phases of merging, when pair separations are $\lesssim 10$ kpc, and that much of the activity in the two nuclei is not simultaneous.

However, despite the current observational focus on NL signatures of dual SMBHs, galaxy merger simulations have not considered the NL region (NLR), and detailed photoionization models have not been applied to the rapidly-varying environment of a late-stage merger. Here, we make a first attempt to model the NLR during galaxy mergers using hydrodynamic simulations, with special attention to the kiloparsec-scale phase that may produce double-peaked NL AGN.

This chapter is organized as follows. In § 4.2.1 & 4.2.2, we describe our simulations and galaxy merger models. Our semianalytic prescription for the NL gas is detailed in § 4.2.3 - § 4.2.4. Our results are presented in § 4.3. In § 4.3.1, we describe the evolution of the NLR throughout a major merger and discuss dependence on merger parameters. We describe the morphological properties of the NLRs in § 4.3.2, and in § 4.3.3 we explore the observable signatures of kiloparsec-scale double-NL AGN. The lifetimes of double-NL AGN are discussed in § 4.3.4. Finally, we summarize and discuss our results in § 4.4. Throughout the chapter, we assume a flat ΛCDM cosmology with $H_0 = 71$ km s^{-1} Mpc^{-1}, $\Omega_m = 0.27$, and $\Omega_\Lambda = 0.73$.

4.2 Methods

4.2.1 Simulations

For our simulations of SMBH pairs in galaxy mergers, we use GADGET, a smoothed-particle hydrodynamics (SPH) and N-body code that conserves both energy and entropy (Springel et al. 2001; Springel 2005). The version we use (GADGET-3) includes radiative cooling as well as a sub-resolution model for a multi-phase interstellar medium (ISM,

Springel & Hernquist 2003) that accounts for star formation and supernova feedback. In addition, the code models SMBHs as gravitational "sink" particles that contain a SMBH seed and a gas reservoir. The reservoir is replenished by stochastic accretion of neighboring gas particles, but the actual accretion rate onto the SMBH is calculated smoothly using the Bondi-Hoyle formula (Bondi & Hoyle 1944) with locally-averaged values for the density and sound speed. The accretion rate is modified by a multiplicative factor to account for the increase in density and sound speed that should occur on sub-resolution scales near the SMBH accretion disk; we adopt a standard value of 100.

We include a model for thermal feedback from the SMBH by assuming that 5% of the luminous output from the SMBH is coupled to the surrounding gas particle as thermal energy. We note that this model does not allow for the possibility of AGN outflows, and thus we are unable to model this possible mechanism for producing some double-peaked spectral features in AGN. Angular momentum is conserved during accretion of gas particles, but because this is a stochastic process we also introduce an accretion drag force calculated from the Bondi accretion rate. These prescriptions are described in more detail in Springel et al. (2005b).

4.2.2 Galaxy and SMBH Merger Models

The progenitor galaxies for our merger simulations consist of a dark matter halo, a disk of gas and stars, and a central SMBH sink particle as described above. We also include a stellar bulge component in some simulations, which we model as a Hernquist (1990) profile. In each case the total mass of the primary galaxy is 1.36×10^{12} $M_{\odot}$, and 4.1% of this mass is in baryons. We simulate major galaxy mergers with mass ratios of q =1, 0.5,

& 0.333, and the initial gas fraction by mass of the disk is varied between 4 and 30%. Galaxies with stellar bulges have bulge-to-disk ratios (by mass) of 10–20%. We use fairly high mass and spatial resolution in order to resolve as best as possible the NLR around each SMBH. The gravitational softening length adopted is $r_{\rm soft} = 37$ pc for baryons and $r_{\rm soft,DM} = 111$ pc for dark matter, and the particle masses for each particle type are $m_{\rm star} = 4.2 \times 10^4$ M$_\odot$, $m_{\rm gas} = 2.8 \times 10^4$ M$_\odot$, and $m_{\rm DM} = 5.4 \times 10^5$ M$_\odot$.

Each galaxy is given a single SMBH with a seed mass of 1.4×10^5 M$_\odot$. The small value chosen reflects the fact that our galaxies are initially bulgeless or disk-dominated, but the SMBH masses grow rapidly after the first close encounter of the galaxies. By the time the SMBHs merge, their masses are a few $\times 10^6$–10^7 M$_\odot$. We use the same SMBH merger prescription as in Blecha et al. (2011), in that the SMBH merger time ($t_{\rm mrg}$) is determined based on the SMBH separation ($a_{\rm sep}$) and relative velocity ($v_{\rm rel}$), and then the simulation is restarted at an earlier point to merge the SMBHs at that exact time. We define $t_{\rm mrg}$ as the time at which $a_{\rm sep} < r_{\rm soft}$ and $v_{\rm rel} < 0.5\, c_{\rm sound}$. Restarting the simulations is particularly important for our present study, because a detailed analysis of the short-lived kpc-scale phase of SMBH evolution requires good time resolution. In order to provide this resolution where needed without generating excessive data in the early merger phase, we run the initial simulations with a time resolution (snapshot output frequency) of 10 Myr, and restart the simulation 100 Myr before the kpc-scale phase (as defined below) with a time resolution of 1 Myr. The galaxies are set on an inclined, parabolic orbit with an initial separation and impact parameter of 143 kpc and 7.1 kpc, respectively.

4.2.3 NLR Identification

Here we outline a basic procedure for determining the location, kinematics, and (Hβ) luminosity of the narrow-line region around one or more AGN in a gaseous galaxy merger simulation with GADGET-3. All of the calculations described here are done in post-processing, that is, after the GADGET simulation has finished.

BH accretion & luminosity

We use the Bondi-Hoyle formula (Bondi & Hoyle 1944), capped at the Eddington limit, to calculate the accretion rate on to the SMBHs:

$$\dot{M} = \min(\dot{M}_{\rm Bondi}, \dot{M}_{\rm Edd}), \tag{4.1}$$

$$\dot{M}_{\rm Bondi} = \frac{4\pi (G M_{\rm BH})^2 \rho_{\rm g,\infty}}{(v_{\rm rel}^2 + c_{\rm s,\infty}^2)^{3/2}} \tag{4.2}$$

$$\dot{M}_{\rm Edd} = \frac{4\pi G M_{\rm BH}}{\eta\, \kappa_{\rm es}\, c} \tag{4.3}$$

where $v_{\rm rel}$, $c_{\rm s,\infty}$, and $\rho_{\rm g,\infty}$ are all computed as averages over the gas particles neighboring the SMBH, and $\eta = 0.1$ is the radiative efficiency. Using this accretion rate, we can calculate the bolometric luminosity

$$L_{\rm bol} = \eta \dot{M}\, c^2. \tag{4.4}$$

Here, $\eta = 0.1$ unless $\dot{M} \ll \dot{M}_{\rm Edd}$, in which case the SMBH is assumed to be radiatively inefficient, with the following scaling for η (Narayan & McClintock 2008):

$$\eta = 0.1 \left(\frac{\dot{M}}{0.01 \dot{M}_{\rm Edd}} \right), \;\; \dot{M} < 0.01 \dot{M}_{\rm Edd}. \tag{4.5}$$

Ionizing photon production rate

To calculate properties of the NL region, we need to know the number of ionizing photons produced by the accreting SMBHs. We begin by applying a reverse bolometric correction to $L_{\rm bol}$ to obtain the B-band luminosity, and then we assume a broken power-law form for the optical - UV spectrum. Following the method of Marconi et al (2004), the bolometric correction is:

$$\log\left(\frac{L_{\rm bol}}{\nu_{\rm B}L_{\nu_{\rm B}}}\right) = 0.8 - 0.067\mathcal{L} + 0.017\mathcal{L}^2 - 0.0023\mathcal{L}^3, \tag{4.6}$$

where $\mathcal{L} = \log L_{\rm bol} - 12$ and $L_{\rm bol}$ is in units of $L_\odot$. For the broken power-law, we use the following spectral indices from the AGN SED fits of Marconi et al. (2004):

$$\alpha_{\rm opt} = -0.44,\ \ 1\,\mu{\rm m} > \lambda > 1300\text{Å} \tag{4.7}$$

$$\alpha_{\rm UV} = -1.76,\ \ 1200\text{Å} > \lambda > 500\text{Å}. \tag{4.8}$$

Then we can get the normalization factor $A_{\rm opt}$ from the bolometric correction by taking $\nu_{\rm B}L_{\nu_{\rm B}} = A_{\rm opt}\nu_{\rm B}^{\alpha_{\rm opt}+1}$. To get the normalization for the UV range we can take $\nu L_\nu(1300\text{Å}) = \nu L_\nu(1200\text{Å})$, which gives

$$\frac{A_{\rm UV}}{A_{\rm opt}} = 2.02 \times 10^{20}. \tag{4.9}$$

The normalization $A_{\rm UV}$ allows us to calculate the number of ionizing photons emitted per unit time by the source:

$$Q = \int_{\nu_0}^{\infty} \frac{L_\nu}{h\nu} d\nu, \tag{4.10}$$

where $\nu_0 = 13.6$ eV.

Selection criterion for cold-phase gas

In order to determine which gas will be ionized by the AGN and produce narrow-line emission, we must impose several criteria on the SPH particles. The multi-phase model for the ISM in GADGET assumes that the gas is comprised of "cold" and "hot" phases that can exchange mass via star formation, cooling, and cloud evaporation by supernovae. First, we select only those gas particles that have a nonzero fraction of mass $f_{\rm cold}$ in the "cold" phase. We assume that the cold-phase gas has fragmented into discrete clouds on sub-resolution scales. The NL clouds are heated by photoionization and should be warmer than the cold clouds in the multiphase ISM ($\sim 10^4$ K versus $\sim 10^3$ K) and thus less dense (assuming pressure equilibrium between phases). Therefore, we use the parameters of the multiphase model only for selection of SPH particles that contain cold gas, and we instead calculate a "cloud density" for each of these particles: $\rho_{\rm cl} = \rho_{\rm SPH}(T_{\rm SPH}/10^4 \text{ K})$. (Here, the subscript "SPH" denotes a mass-weighted average between the hot and cold phases, and the subscript "cl" denotes the quantities for our NL cloud model.)

Selection criterion for gas particle covering fraction

We also impose a criterion on the SPH particles such that the solid angle subtended by NL clouds does not exceed 4π. We cannot determine exactly which clouds will have unobscured sight lines to the AGN, as their size is below our resolution limit and our simulations do not include radiative transfer. However, we account for the problem of particle self-shielding in an average sense, as follows. An SPH particle that subtends a

solid angle $\Omega_{\rm SPH}$ has a covering fraction

$$f_{\Omega_{\rm SPH}} = \frac{\Omega_{\rm SPH}}{4\pi} = \frac{r_{\rm SPH}^2}{4\, r_{\rm BH}^2}, \tag{4.11}$$

$$r_{\rm SPH} = \left(\frac{m_{\rm SPH}}{\frac{4\pi}{3}\,\langle\rho\rangle} \right)^{1/3}, \tag{4.12}$$

where $m_{\rm SPH}$ is the mass of the SPH particle, $r_{\rm SPH}$ is the effective size of the particle and $r_{\rm BH}$ is the distance to the SMBH. The "area filling factor" ($\epsilon_{\rm A}$) and volume filling factor ($\epsilon_{\rm V}$) are the fractions of the SPH particle's area and volume covered by the cold clouds, respectively:

$$\epsilon_{\rm A} = \epsilon_{\rm V}^{2/3}\, N_{\rm cl}^{1/3}, \tag{4.13}$$

$$\epsilon_{\rm V} = f_{\rm cold}\, \frac{\rho_{\rm SPH}}{\rho_{\rm cl}}, \tag{4.14}$$

where $N_{\rm cl} = f_{\rm cold}\, m_{\rm SPH}/m_{\rm cl}$ is the number of clouds within the particle. In this formulation, $m_{\rm cl}$ is a free parameter that serves mainly to set the surface area to volume ratio of the NL clouds. For a typical area covering fraction of order unity on NLR scales of $\sim 0.1 - 1$ kpc (as inferred observationally), we are led to adopt $m_{\rm cl} = 200 M_\odot$.

The covering fraction of the clouds in each particle is then

$$f_\Omega = \frac{\epsilon_{\rm A}\, \Omega_{\rm SPH}}{4\pi}. \tag{4.15}$$

In order to avoid allowing a photon to be absorbed by multiple clouds, we truncate the NLR beyond the radius where the total covering fraction of clouds reaches unity. While this method is not exact, it does allow for the correct rate of photoionization in an average sense.

Selection criteria for ionization parameter & density

For the selected gas particles, we calculate the ionization parameter for the cold clouds in a given SPH particle when ionized by a single SMBH:

$$U = \frac{Q}{4\pi r_{\rm BH}^2 c\, n_{\rm H,cl}}, \tag{4.16}$$

where $n_{\rm H,cl} = \rho_{\rm cl}/\mu m_{\rm H}$ is the number density of the NL clouds and $r_{\rm BH}$ is the distance from the SMBH to the cloud. The ionization parameter quantifies the ratio of the ionizing photon density to the electron density at each cloud. In the case of a galaxy merger where two active SMBHs may be present, the ionization parameter becomes

$$U = \frac{1}{4\pi c\, n_{\rm H,cl}} \left(\frac{Q_1}{r_{\rm BH1}^2} + \frac{Q_2}{r_{\rm BH2}^2} \right), \tag{4.17}$$

where the subscripts "1" and "2" refer to the primary and secondary SMBHs. We impose an additional cut on the NL gas particles by selecting only those with U in the range $10^{-4.5} - 10^{-1.5}$, under the assumption that the gas is transparent to ionizing radiation for AGN luminosities.

Finally, to ensure that the cloud densities are reasonable, we impose a final cut on the SPH particles such that only those with $n_{\rm H,cl}$ in the range $10^2 - 10^6$ cm^{-3} are included. The maximum of this range is typically the more limiting criterion, and is chosen to be roughly equal to the critical density for [O III] emission. Above this density, collisional de-excitation begins to dominate over the forbidden-line emission. While we do not consider forbidden lines in our model, we know they are present in real NLRs, and further that NL AGN typically have [O III]/H$\beta \gtrsim 3$. Thus, gas above the maximum density will not contribute to the NL AGN profile in a conventional manner, and we exclude these particles from our NL model. We consider a NLR to be "active" if at

least 10 SPH particles meet the above criteria, although in practice the NLRs in our simulations typically contain hundreds to thousands of SPH particles.

Identification of gas particles with each SMBH

After the galaxies have undergone a close passage, and especially during their final coalescence, particles are easily exchanged between galaxies, and the initial identifications of which particles are in which galaxy are no longer relevant. Nonetheless, we wish to know which NL particles are associated with each SMBH; this is helpful for understanding the NLR kinematics even when the SMBHs are near coalescence. Accordingly, we assign particles to each SMBH based on their proximity to and degree of photoionization from each SMBH. Specifically, we switch gas particles from their initial galaxy identification if (a) they are closer to the SMBH in the other galaxy and (b) the quantity $Q/r_{\rm BH}^2$ is substantially larger for the SMBH in the other galaxy (we use $U_{1,2}/U_{2,1} > 4$).

4.2.4 Hβ Luminosity and Velocity Profiles

Hβ luminosity

Once we have selected the NL particles according to the above procedure, we may estimate the Hβ luminosity of each cloud, $L_{\rm H\beta}$. While [O III] is generally the strongest narrow emission line, and thus has been the focus of most searches for dNL AGN, for our models the Hβ line offers the advantage that its recombination coefficient depends only weakly on temperature, and thus the line strength is much less sensitive to the exact conditions in the ISM. Because AGN typically have [O III]/H$\beta \gtrsim 3$, our results for the

lifetime of observable NL emission, calculated from $L_{\mathrm{H}\beta}$, may be considered lower limits in this sense. However, in AGN spectra with double-peaked [O III] lines, Hβ also appears double-peaked when the spectrum has a sufficient signal-to-noise, indicating that this simplifying assumption is not unfounded. $L_{\mathrm{H}\beta}$ may be written as

$$L_{\mathrm{H}\beta} = h\,\nu_{\mathrm{H}\beta}\,\frac{\alpha^{\mathrm{eff}}_{\mathrm{H}\beta}(T)}{\alpha^{\mathrm{eff}}_{\mathrm{B}}(T)}\,f_{\Omega}\,Q\,, \tag{4.18}$$

where Q is the rate of ionizing photon production as before, f_Ω is the cloud covering fraction discussed above, and $\alpha^{\mathrm{eff}}_{\mathrm{H}\beta}(T)/\alpha^{\mathrm{eff}}_{\mathrm{B}}(T) \approx 1/8.5$ is the number of Hβ photons produced per hydrogen recombination for $T = 10^4$ K (Osterbrock & Ferland 2006). Thus, when two ionizing sources (two SMBHs) are present, the total Hβ luminosity is

$$L_{\mathrm{H}\beta} = \frac{h\,\nu_{\mathrm{H}\beta}}{8.5}\frac{\epsilon_{\mathrm{A}}}{4\pi}\left(\Omega_{1,\mathrm{SPH}}\,Q_1 + \Omega_{2,\mathrm{SPH}}\,Q_2\right). \tag{4.19}$$

Hβ velocity profiles

In order to understand the kinematics of the NLR, we construct and analyze velocity profiles for each NLR. From the simulations we have the 3-D velocities for each NL-emitting SPH particle, measured with respect to the stellar center of mass. After projecting these along a given sight line, we assume that within each particle, the NL clouds have a Gaussian internal velocity dispersion with a full-width at half maximum (FWHM) equal to 0.5 c_{sound}. The resulting total velocity profile is then convolved with another Gaussian to degrade it to the desired resolution, chosen to correspond to the spectral resolution of SDSS or DEIMOS at typical redshifts for dNL AGN (we use a fiducial value of 65 km s^{-1}).

For most of our analysis, we calculate the 1-D velocity profiles for 40 random sight lines in order to account for this source of intrinsic variation in the observed spectra.

When individual examples are shown, we present the kinematics for three orthogonal sight lines corresponding to the x, y, & z axes that define the initial orbits of the merging galaxies.

4.3 Results

4.3.1 Evolution of Narrow-Line AGN in Major Mergers

General Properties

The maximum angular SMBH separation for which double-peaks resulting from distinct, orbiting NLRs could be seen on the same spectrum is set by the size of the spectral slit or fiber of the instrument used. The size of the spectral slit on the DEIMOS spectrograph is 0.75", corresponding to 5.36 kpc at $z = 0.7$. Thus, only a dual SMBH with separation $a_{\rm max} \lesssim 5.36$ kpc could be observed in a single DEIMOS spectrum. The diameter of the SDSS spectroscopic fiber is 3", which projects to 5.47 kpc and 21.4 kpc at $z = 0.1$ & 0.7, respectively. Thus, for the mean redshifts of the AGN samples studied by Comerford et al. (2009b); Smith et al. (2010); Liu et al. (2010b), the dNL AGN diagnostic is sensitive to dual SMBHs with projected separation $\lesssim 5.5$ kpc. Most of our results assume $a_{\rm max} = 5.5$ kpc, but we also consider $a_{\rm max} = 21$ kpc, corresponding to higher-redshift systems observed with SDSS.

For our analysis of NLRs in galaxy merger simulations, we divide the merger evolution into phases based on these limits for observing double NLs. We refer to the early merger stage as Phase I, when the NLRs are well-separated and could not be

observed in a single spectrum ($a_{\rm sep} > a_{\rm max}$). Phase II refers to the "kiloparsec-scale phase", which occurs when the following criteria are met: (i) $a_{\rm sep} < a_{\rm max}$, (ii) at least one SMBH has an active NLR, and (iii) the SMBHs have not yet merged. We define the post-BH-merger phase as Phase III. If for any time between Phases I & III the criteria (i) & (ii) are not met, we define this period as Phase IIb.

In Fig. 4.1, we show the evolution of AGN and NL activity throughout a major merger. The Hβ luminosity traces the bolometric luminosity; both curves have peaks after the first close passage of the two galaxies and a larger peak during the final coalescence. Note that the NLR is not active at all for the first 600 Myr of the merger simulation, owing to the low SMBH luminosity. Only after the galaxies undergo a close pericentric passage, and significant SMBH growth occurs, do the gas particles meet our minimum criteria for an active NLR, after which they remain active for the rest of the simulation. The Hβ luminosities of the two NLRs are within a factor of ten throughout most, but not all, of the simulation.

Figure 4.1 also demonstrates a key feature of AGN triggered by major, gaseous mergers: the peak AGN and NL activity typically occurs during the final coalescence of the two galaxies. Assuming the SMBHs merge efficiently, this means that peak activity also occurs near the time of the SMBH merger. Thus, merger-triggered AGN are typically brightest between the kiloparsec-scale phase of SMBH inspiral and the post-BH-merger phase. This simple fact enhances the probability of observing dNL AGN in the kpc-scale phase versus earlier stages in the merger, as is discussed further in § 4.3.4.

Figure 4.1.—: (Following page.) Time evolution of relevant quantities for an equal-mass merger containing 10% gas initially. In each panel, the gray-shaded regions denote Phase II, i.e., the kpc-scale phase. The dark-gray shade denotes (3-D) SMBH separations of < 5.5 kpc, corresponding to the size of the SDSS spectroscopic fiber for objects at $z \sim 0.1$, or the size of the DEIMOS spectral slit for objects at $z \sim 0.7$. The light-gray shade denotes SMBH separations of < 21 kpc, corresponding to the SDSS fiber size for objects at $z \sim 0.7$. Top plot: bolometric luminosity ($L_{\rm bol}$) versus time. Blue and red curves denote each SMBH's luminosity prior to the SMBH merger, and the green curve denotes $L_{\rm bol}$ after the merger. The thick solid and dashed lines (uppermost) denote the Eddington limit for each SMBH, and the thin solid and dotted lines denote three different definitions of an AGN (3% & 10% $L_{\rm Edd}$ for each SMBH, and a constant luminosity of 3×10^9 $L_\odot$). Upper-middle plot: Hβ luminosity, L(Hβ). Same color scheme as in top plot. Lower-middle plot: Ratio of $L_{\rm H\beta}$ for each SMBH. Points where $L_{\rm H\beta 2} > L_{\rm H\beta 1}$ are shown in blue, and those where $L_{\rm H\beta 1} > L_{\rm H\beta 2}$ are shown in red. Bottom plot: SMBH separation vs time. The magenta points denote the snapshots in which both NLRs are simultaneously active.

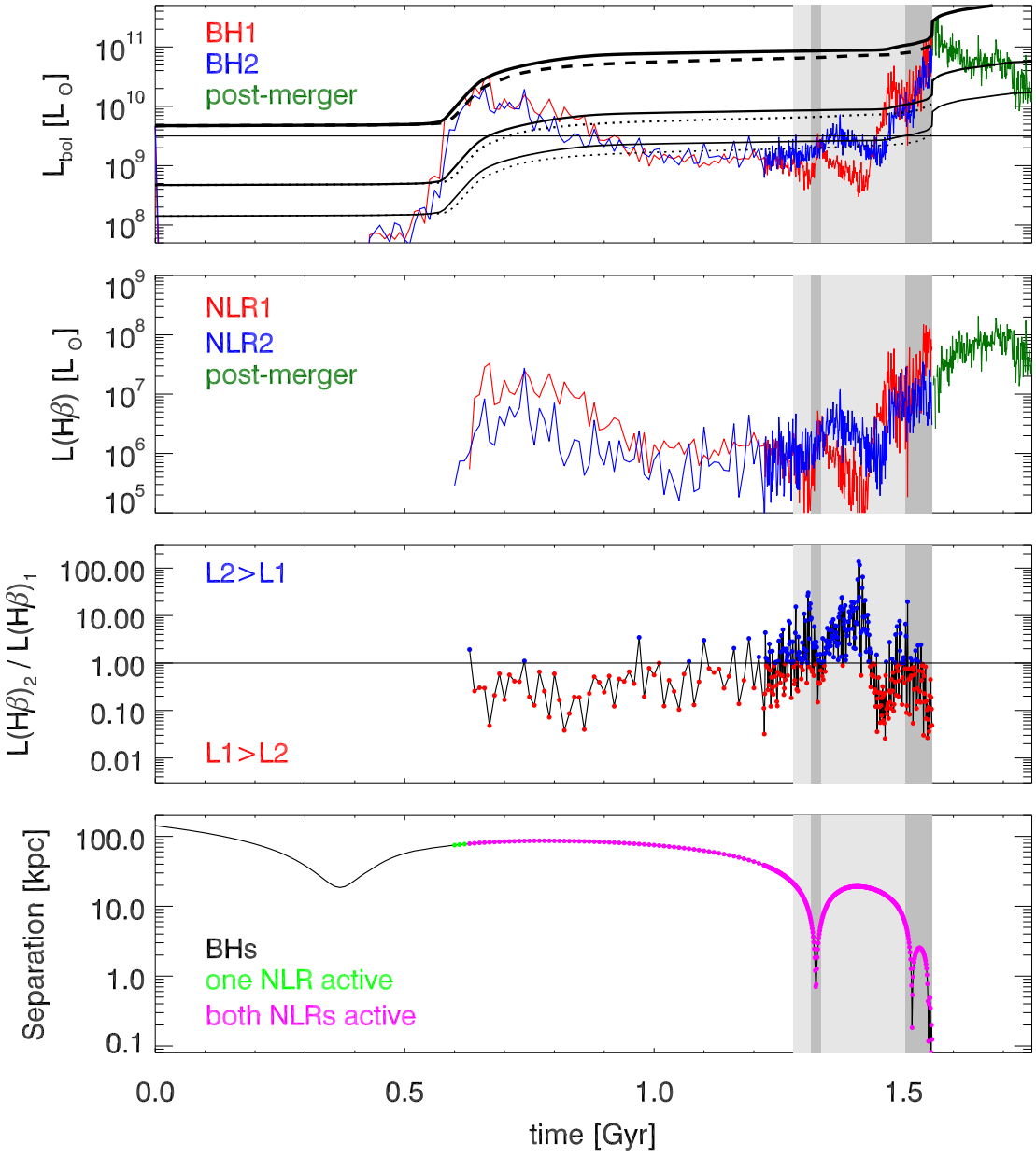

Figure 4.1.—: (Continued)

Another interesting feature in Fig. 4.1 is a slight dip in $L_{\mathrm{H}\beta}$ that occurs near the time of SMBH merger and peak L_{bol} (note the much sharper peak in L_{bol} versus $L_{\mathrm{H}\beta}$). This occurs when the central gas density in the merger remnant reaches its peak and briefly exceeds our maximum density criterion for NLRs. As described in § 4.2.3, in such conditions the emission from collisional de-excitation begins to outweigh forbidden-line emission, so this gas cannot be considered part of the narrow-line region as it is typically defined for an AGN (with, e.g., [O III]/H$\beta \gtrsim 3$). This dip in NL emission occurs only in the mergers that attain the highest peak densities, i.e., those with nearly equal mass and moderate-to-high gas fractions, but it is nonetheless an interesting feature of NL emission in a dense, rapidly-varying environment. We note that because these dips in emission are brief, they do not affect our results qualitatively and have only a small effect on our quantitative results. Specifically, the dNL AGN lifetimes increase by $< 50\%$ for n_{max} as high as 10^8 cm^{-3}, which is much less than the variation in these lifetimes for different viewing angles.

The total merger time from the start of the simulation to the time of SMBH merger is 1.6 Gyr, but Phase II, shaded in dark (light) gray for $a_{\mathrm{max}} = 5.5$ (21) kpc, has a duration of 72 (278) Myr. In general, efficient dynamical friction and gas drag in the dense merger remnant potential ensure that Phase II is always a small fraction of the total merger timescale.

Our progenitor galaxies initially have 4 - 30% of their baryonic mass in gas. This gas is depleted substantially via star formation during the course of the merger; at the onset of Phase II, the gas content is typically about half of its initial value. However, major mergers are efficient at rapidly fueling gas to the central regions of galaxies, such that by Phase II the remaining gas and newly-formed stars dominate the central region

of each merging galaxy.

Dependence on Merging Galaxy Parameters

We find that the amount of NL activity in galaxy mergers is strongly influenced by the conditions in the host galaxies. Figure 4.2 shows the same quantities as Fig. 4.1, but for an unequal-mass merger ($q = 0.5$) with a low initial gas fraction of $f_{\rm gas} = 0.04$. The SMBH in the primary galaxy has an Eddington-limited burst of accretion following the first close passage, triggering strong feedback that heats the surrounding gas and limits further accretion until final coalescence. The secondary SMBH never reaches its Eddington limit but maintains a fairly constant $L_{\rm bol}$ following the pericentric passage until final coalescence. While at least one of the NLRs is active for most of the simulation, they are simultaneously active virtually only during the kpc-scale phase, and even then the $L_{\rm H\beta}$ ratio fluctuates significantly.

Unlike the example in Fig. 4.1, in this example the peak of AGN and NL activity occurs several tens of Myr prior to the SMBH merger, and thus most of the NL activity coincides with the kpc-scale phase. Nonetheless, we see that substantially less NL activity occurs in this low-$f_{\rm gas}$, unequal-mass merger than in the previous example. This holds true of our merger models in general; mergers with lower mass ratios and gas fractions have less AGN and NL activity, and thus are less likely to produce observable dNL AGN. (See § 4.3.4 for a comparison of dNL lifetimes.) This is as expected, because equal-mass mergers induce the strongest perturbations in the merging galaxies, causing more gas to lose angular momentum and flow rapidly to the galaxy centers. Galaxies with substantial gas reservoirs will likewise provide more fuel to the central SMBHs than

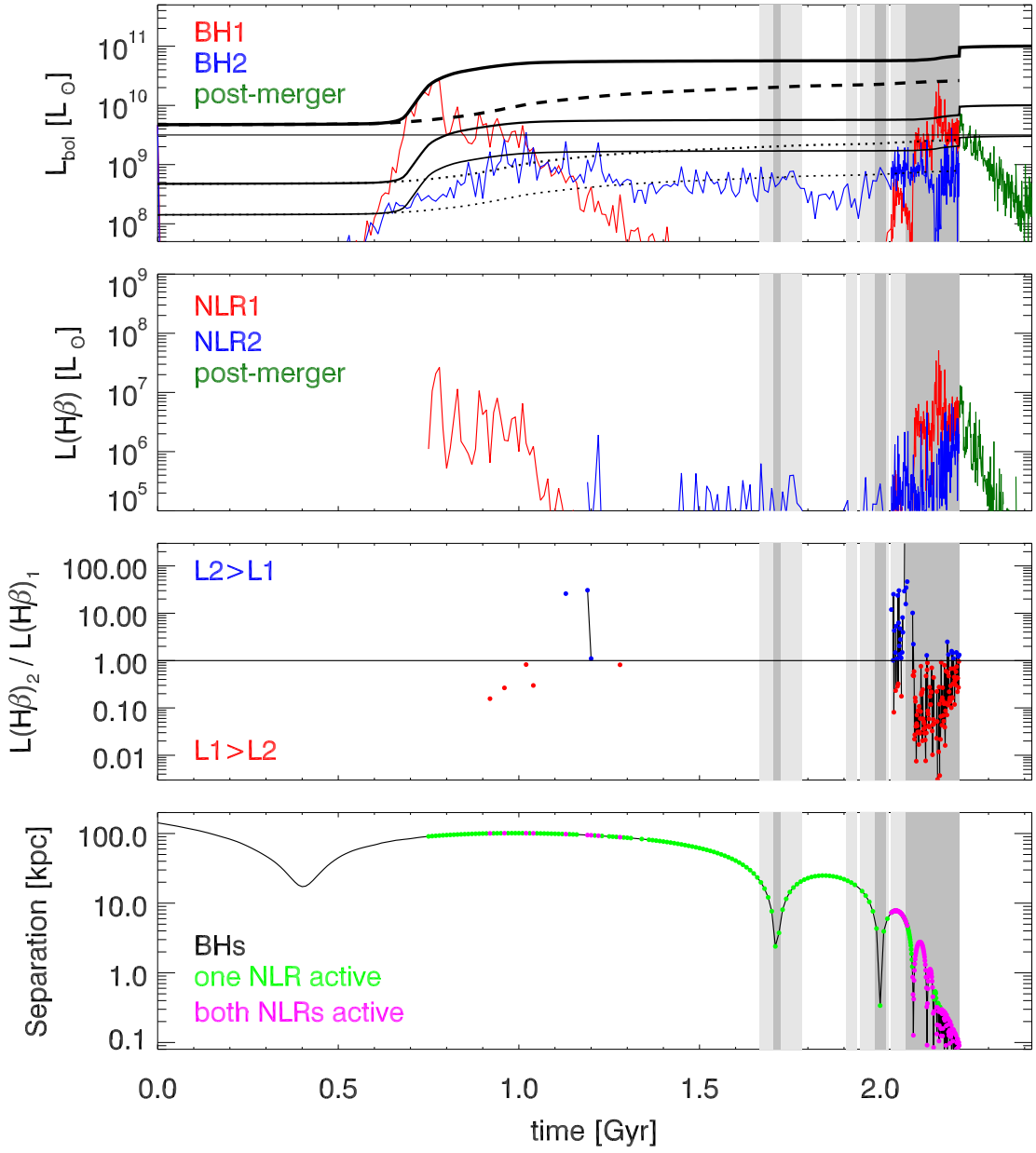

Figure 4.2.—: Same quantities as in Fig. 4.1, but for an unequal-mass merger (mass ratio $q = 0.5$) with a lower initial gas fraction ($f_{\rm gas} = 0.04$).

those that are gas-poor. However, two additional effects, described below, cause the NL activity in Phases II and III to be especially sensitive to the merging galaxy parameters.

As mentioned in § 4.3.1, the peak SMBH accretion rates for major, gaseous mergers are generally higher during final coalescence than following the first close passage. This owes in large part to the fact that the SMBH masses and Eddington limits are typically 1 - 2 orders of magnitude larger at coalescence than at the first passage. However, in mergers with lower q and $f_{\rm gas}$, the peak accretion rates may not reach the Eddington limit, or accretion and feedback early in the merger may deplete the central gas reservoir. Fig. 4.2 illustrates that in such cases, the AGN luminosity may actually be *lower* during coalescence than after the first passage. Such mergers should contribute little to the population of dNL AGN. This is consistent with the assertion in § 4.3.1 that most merger-triggered dNL AGN that are *observable* should occur in the late stages of merging.

A related effect is that in nearly-equal-mass, gaseous mergers, the inflow of gas that fuels SMBH accretion can also cause rapid changes to the central potential of the merger remnant. Specifically, the central escape speed ($v_{\rm esc}$) may increase substantially during final coalescence. This is the same effect noted by Blecha et al. (2011) in the context of its importance for the timing of GW recoil kicks. As the central potential deepens, the SMBH and central gas velocities increase. This causes longer-lived and more-pronounced double-peaked NLs via SMBH motion and via rotating gas disks. We find that this effect generally leads to a larger fraction of dNL AGN in Phase III (see § 4.3.3 & 4.3.4). However, this increase in $v_{\rm esc}$ occurs only for nearly-equal-mass, relatively gas-rich mergers. For the merger models presented here, only those with $f_{\rm gas} = 0.3$ show a rapid $v_{\rm esc}$ increase at coalescence, and only in the $q = 1$, $f_{\rm gas} = 0.3$ model does $v_{\rm esc}$ increase by

more than ~ 200 km s^{-1}.

The same processes that fuel AGN can also trigger rapid star formation, which may produce large amounts of obscuring dust. The problem is especially complex for the NLR, which exists at large enough radii to be intermingled with the newly-forming central cusp of stars. Because the present work, as a first attempt to model the NLR in galaxy mergers, does not account for the potential effects of obscuration or reprocessing of emission by dust, we must consider this an important caveat to interpretations of our simulated NLRs as "observable".

In order to avoid as much as possible a strong-starburst regime, we do not consider initial gas fractions above 30%, and much of the analysis presented here concerns galaxies with $f_{\rm gas} \leq 0.1$ initially. Thus, our simulations produce low- to moderate-luminosity AGN, rather than luminous quasars. Furthermore, while the peak star formation rate (SFR) following the first pericentric passage can be in excess of 100 M$_\odot$ yr^{-1} for our higher-q and $f_{\rm gas}$ simulations, the peak SFR during final coalescence (i.e., during Phase II) is typically much lower, $\lesssim 1 - 10$ M$_\odot$ yr^{-1} for these same simulations. For lower-q, $f_{\rm gas}$ mergers, the peak SFR is much lower than this; the example in Fig. 4.2 has a peak SFR at coalescence of only 0.4 M$_\odot$ yr^{-1}. At these SFRs, the cumulative UV emission from massive stars should be much weaker than the AGN emission, such that we may neglect its contribution to photoionization of circumnuclear gas.

We also consider the addition of a stellar bulge component to our progenitor galaxies, which are nominally pure disks in these simulations. It is well-known that the presence of a bulge can act to stabilize a galactic disk to perturbations during encounters, thereby delaying catastrophic loss of gas angular momentum until the final

coalescence of the galaxies (e.g., Mihos & Hernquist 1996). Much of the star formation and SMBH growth triggered by gas inflow is thereby similarly delayed. We use Hernquist bulge profiles containing 10 - 20% of the total stellar mass, and find that the SFRs and SMBH accretion rates are lower following the first passage and are slightly higher during coalescence. For mergers with higher $f_{\rm gas}$, the peak SFR can change by a factor of several in each direction when a bulge s added. However, because AGN activity is generally highest during coalescence for the mergers that produce the most AGN activity overall, the presence of a bulge only serves to modestly enhance this effect.

Although we do not consider bulge-dominated or elliptical galaxy models in the present study, it is possible that the central gas kinematics could differ during mergers between such progenitors. For example, the gas may have less angular momentum, reducing the importance of rotation-induced double-peaked spectral features in NL AGN. If so, this would increase the fraction of dNL AGN induced by dual SMBH motion. We discuss the frequency of dNLs induced by gas kinematics versus SMBH motion in § 4.3.3.

The multiphase ISM model of Springel & Hernquist (2003) includes a parameter, $q_{\rm EOS}$, that determines the degree of "softening" of the gas equation of state (EOS). When this parameter is set to zero, the EOS is purely isothermal, and when it is set to one, the full multiphase ISM model is used. Intermediate values of $q_{\rm EOS}$ interpolate between these two. We adopt a fiducial value of $q_{\rm EOS} = 0.25$, as in Springel & Hernquist (2003), but because of the potential for the choice of EOS to affect our results, we also test values of 0.5 and 0.05 for select merger models.

In general, the gas disk is more stable with the softer EOS ($q_{\rm EOS} = 0.5$), while for $q_{\rm EOS} = 0.05$ the gas is much more prone to fragmentation and has a very clumpy

distribution. Higher SMBH accretion rates result in the latter case, including sustained higher accretion rates following the first close passage of the two galaxies. The final SMBH masses may be up to an order of magnitude higher for $q_{\rm EOS} = 0.05$ versus 0.5, and the dNL AGN lifetimes may be larger by a similar factor in Phases II & III. (See § 4.3.4 for more discussion of dNL lifetimes.) The simulations with $q_{\rm EOS} = 0.5$ have less NL AGN activity, especially in Phase I, but in general are more similar to the fiducial simulations than are those with $q_{\rm EOS} = 0.05$. We consider the nearly-isothermal EOS ($q_{\rm EOS} = 0.05$) to be a fairly extreme model, but regardless, it is clear that the SMBH activity in these galaxy mergers does depend to some degree on the gas EOS. Specifically, gas distributions that are clumpier and closer to isothermal should result in more AGN and NL activity.

Finally, we have examined the dependence of our results on the mass and spatial resolution of the simulations, using a set of simulations with the $q = 0.5$, $f_{\rm gas} = 0.1$ merger model. We test baryonic mass resolutions of a factor of two higher and lower than our fiducial value, and we test DM mass resolutions up to a factor of five higher than our fiducial value. The gravitational softening lengths are scaled as $r_{\rm soft} \propto M^{1/3}$.

Broadly speaking, our results are quite similar for simulations with different resolutions. There is a trend toward somewhat higher central densities for higher resolutions; this essentially reflects the need for the multiplicative factor for the accretion rate, described in § 4.2.1, which accounts for the higher densities not captured on sub-resolution scales. Owing to the approximate nature of the sub-resolution SMBH accretion model, it is impossible to know the "true" value to which the accretion rates should converge, and this must be considered a source of uncertainty in any numerical study utilizing semi-analytic SMBH models. However, the dependence of central density

and corresponding accretion rate on resolution is weak. In our resolution study the peak bolometric and Hβ luminosities vary by at most a factor of a few over the resolutions sampled, and the *integrated* SMBH accretion rates (i.e., the final SMBH masses) are very nearly identical.

4.3.2 NLR Morphology and Kinematics

Here we examine in detail the structure, kinematics, and luminosity of the NLRs in our simulations. Figure 4.3 shows velocity maps of the NLRs at various stages of a single merger simulation, along with corresponding $L_{\mathrm{H}\beta}$ maps. Figure 4.3a shows a snapshot about 150 Myr after the onset of NL activity, following the first close passage of the galaxies. We see that each NLR is $\gtrsim 500$ pc across, has a disky structure as seen in the xz projection, and is rotating. Additionally, in the first galaxy (left panels in each plot), a gap in the NLR is seen in the disk midplane. Because the gas density is highest along the midplane, the gas here may at times exceed our maximum-density criterion.

Figure 4.3b shows a later snapshot when L_{bol}, $L_{\mathrm{H}\beta}$, and the gas density are near their minima between the first passage and final coalescence of the galaxies. Accordingly, the NLRs are fainter and more diffuse. In the following snapshot (Fig. 4.3c), the NLRs are shown just after a pericentric passage, ~ 200 Myr prior to SMBH merger. The SMBH separation here is only 0.76 kpc, and a large relative line-of-sight (LOS) velocity is apparent in the xz projection. The NLRs are still quite diffuse and faint here, with $L_{\mathrm{H}\beta} \sim$ few $\times 10^6$ $\mathrm{L}_\odot$.

Soon thereafter, the central gas density increases as the galaxies near their final coalescence, and the NLRs become brighter and more compact (Fig. 4.3d). Their shape

becomes more spherical, as their size is now limited mostly by the self-shielding criterion described in § 4.2.3, but a velocity gradient and a preferred axis for the brightest Hβ emission can still be seen.

The next snapshot (Fig. 4.3e) occurs just before a close passage of the SMBHs. The red- and blueshifted NLRs are apparent as in Fig. 4.3c, but here $L_{\rm bol}$ and $L_{\rm H\beta}$ are about 10 times higher. This is in fact an example of a double-peaked NL AGN induced by SMBH motion, as will be discussed in the next section. Finally, Fig. 4.3f shows the last snapshot of the simulation, 200 Myr after the SMBH merger. (Accordingly, only one set of panels is shown, centered on the single SMBH.) The gas density, $L_{\rm bol}$ and $L_{\rm H\beta}$ have all declined, causing the NLR to become somewhat more diffuse.

The persistence of flattened, rotating NLR morphologies throughout the merger is critical for the resulting velocity profiles; many double-peaked profiles simply arise from the disk rotation, rather than from the relative SMBH motion. As such, these features merit closer examination. If we define the SMBH radius of influence as the radius at which the baryonic mass surrounding the SMBH equals twice its mass, $r_{\rm infl} \equiv r(M_{\rm b} = 2M_{\rm BH})$, then $r_{\rm infl}$ ranges from $\gtrsim 100$ pc early in the merger, when the gas density is low, to only a few pc at late stages when the gas density is much higher. Thus, at all times, $r_{\rm NLR} \gg r_{\rm infl}$, so the gravitational potential of the SMBH alone is not responsible for keeping the NL clouds bound in coherent rotation. However, following the first close passage of the galaxies, a dense cusp of new stars forms and dominates the central region of each galaxy. Figure 4.4a illustrates that the NL gas kinematics match that of the central gas distribution, which itself traces the kinematics of the stellar cusp. Thus, it is indeed the angular momentum of the central gas and newly-formed stars that underlies the flattened rotation features in the NLRs seen in Fig. 4.3.

Figure 4.3.—: (Following three pages.) Line-of-sight (LOS) velocity maps and $L_{\mathrm{H}\beta}$ maps of NLRs at six different snapshots throughout a single galaxy merger. In each subfigure **(a) - (f)**, the left plot is the velocity map and the right plot is the $L_{\mathrm{H}\beta}$ map. Within each 6-panel plot, the left column of shows three orthogonal projections centered on SMBH2, and the right column shows the same three projections centered on SMBH1. All panels are 800 pc across. Fig. 4.3 is a post-BH-merger snapshot, so only one column of panels is shown. In the velocity maps, the magnitude of the colored arrows denotes the projected SMBH velocity, and their hue denotes the LOS SMBH velocity. Each panel is 800 pc on a side, and the velocity scale spans from -400 km s^{-1} (blue) to +400 km s^{-1} (red). This sign convention for LOS velocity is used throughout the chapter. The $L_{\mathrm{H}\beta}$ maps use the same spatial scale.

(a) t_{mrg} – 707 Myr

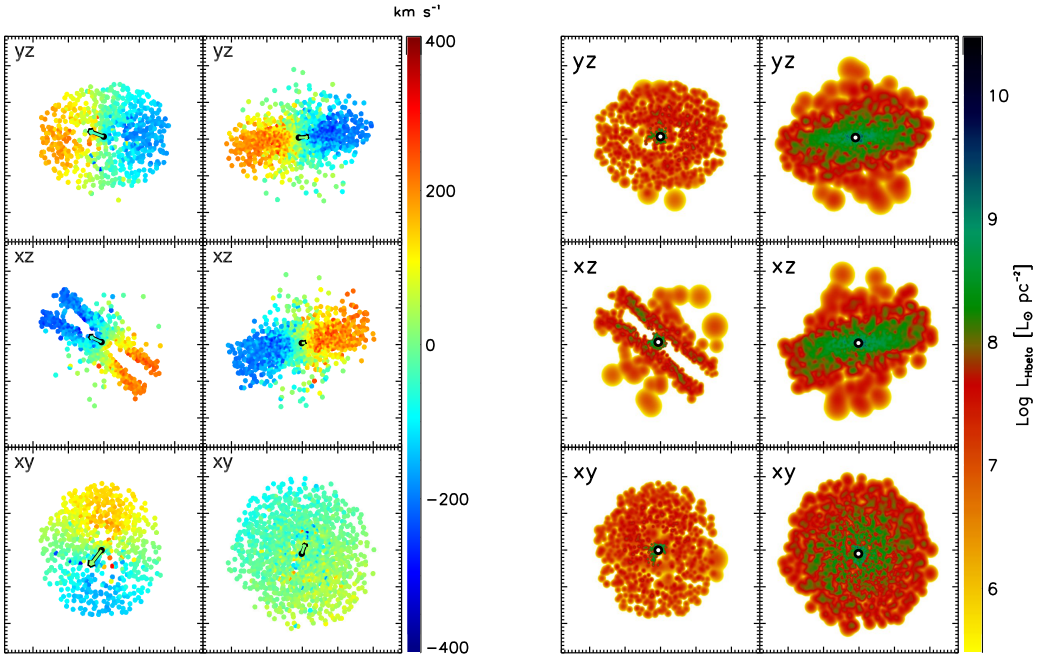

(b) t_{mrg} – 397 Myr

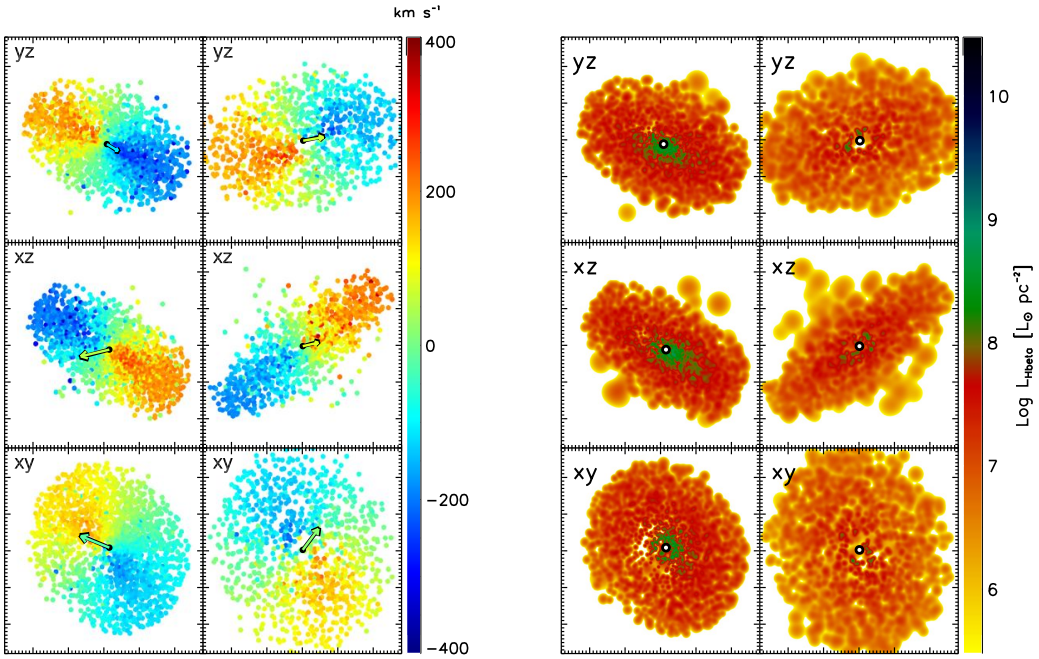

Figure 4.3.—: (Continued)

(c) t_{mrg} – 232 Myr

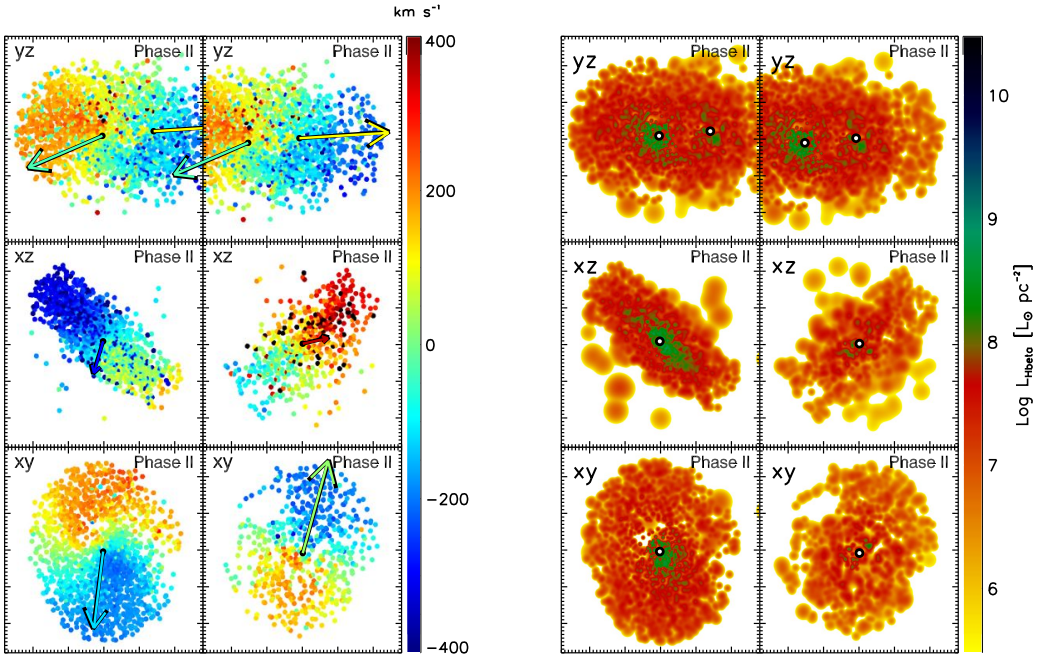

(d) t_{mrg} – 81 Myr

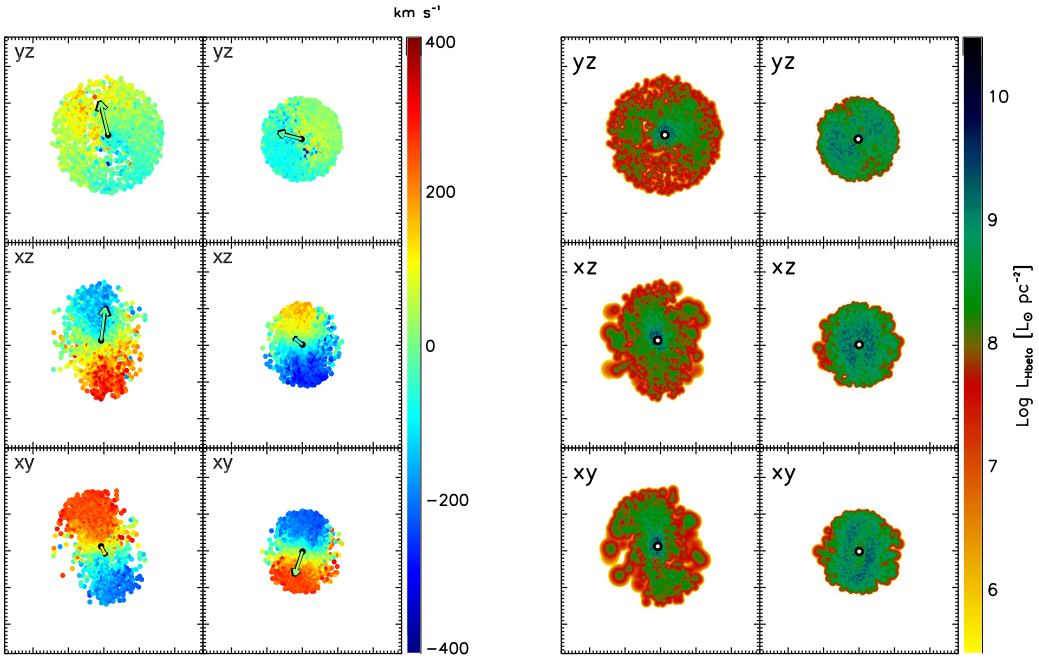

Figure 4.3.—: (Continued)

(e) $t_{mrg} - 41$ Myr

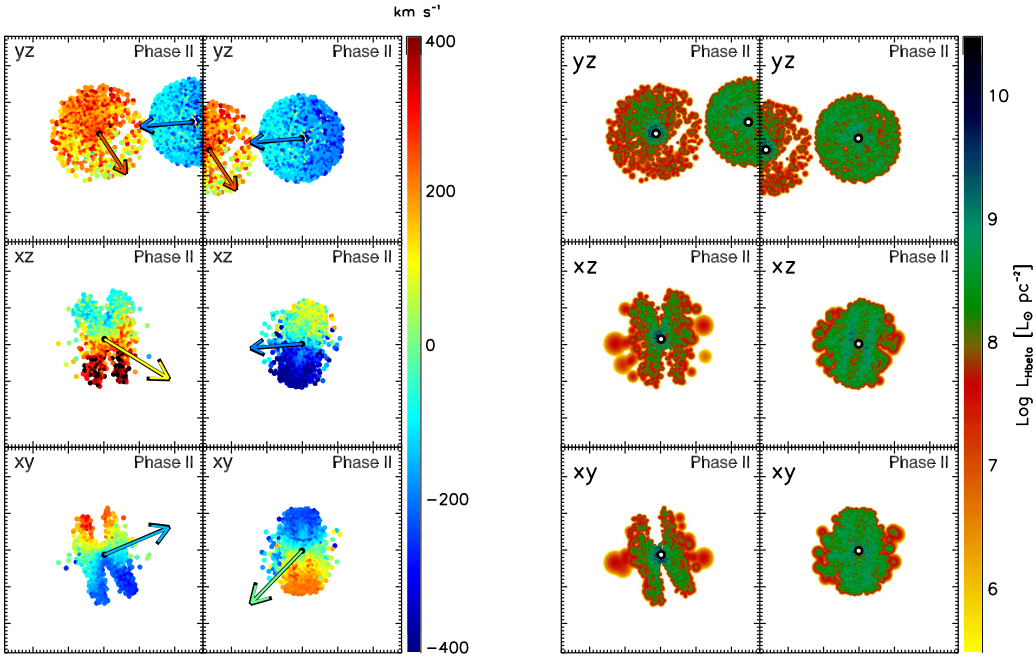

(f) $t_{mrg} + 200$ Myr

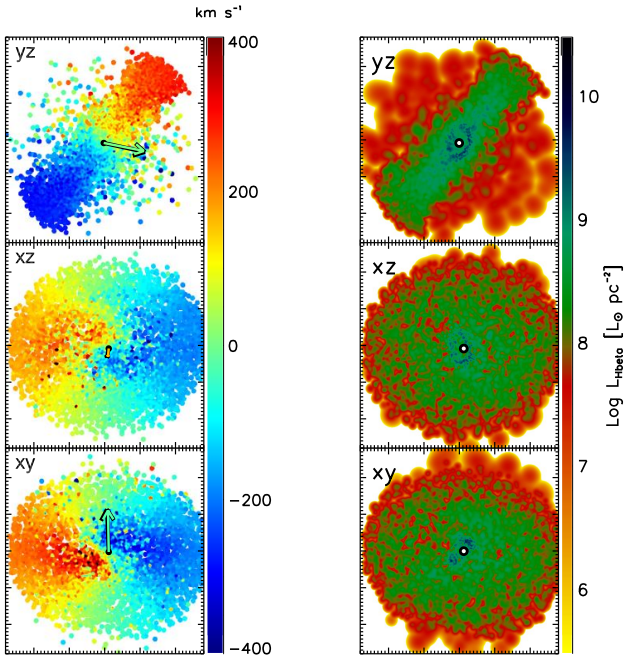

Figure 4.3.—: (Continued)

A remaining question is whether the softened gravitational potential used in our simulations has a nonnegligible effect on the kinematic structure of the central region. The gravitational softening length used in our simulations is $r_{\rm soft} = 37$ pc, which is smaller than the size of our NLRs, but because of the softening kernel used, the gravitational forces are not strictly Newtonian until $2.8r_{\rm soft}$, i.e., 104 pc. When the galaxies are near coalescence and the NLRs are most compact, their size can indeed be comparable to this value. We have drawn these two radii, $r_{\rm soft}$ and $2.8r_{\rm soft}$, on the panels in Fig. 4.4.

In the first example (Fig. 4.4a), the central stellar rotation feature is comparable in size to the extent of the softening kernel. However, we have resimulated part of this merger with a softening length five times smaller, and we show the result for the same snapshot in Fig. 4.4b. Here, the circle drawn at $2.8r_{\rm soft}$ is barely larger than the size of the dot that denotes the SMBH position, yet the kinematic stellar structure has the same spatial extent. In fact, the smaller softening length seems to allow the stellar rotation to persist down to smaller scales around the SMBH. This is evidence that if anything, the gravitational softening "washes out" rotation features on scales of < 10 pc, and it is certainly not artificially inducing or supporting rotation on larger scales. In both cases the motion of the gas traces that of the stars, so we can have similar confidence in the rotation observed in our NLRs.

Figure 4.4.—: (Following page.) (a, left plot): Hβ velocity map centered on one SMBH, in three projections, in a similar manner as in Fig. 4.3. The simulation shown has $q = 1$ and initial $f_{\rm gas} = 0.1$. (a, right plot): For the same simulation, the velocity map is shown for the *total* gas distribution (rather than only the NL gas) in the left panels, and for the total *stellar* distribution in the right panels. The solid circle drawn around the SMBH denotes the gravitational softening radius ($r_{\rm soft}$), and the dashed circle denotes $2.8r_{\rm soft}$, the point at which the gravitational force becomes Newtonian. (b): Gas and stellar velocity maps are shown as in the previous plot, but here the merger has been partially re-simulated with $r_{\rm soft}$ 5 times smaller. The same circles are drawn here, but their size barely exceeds that of the dot that marks the SMBH position. (c): Gas and stellar velocity maps are shown for a different merger model with $q = 1$ and $f_{\rm gas} = 0.3$. The larger gas supply causes enhanced central star formation and a kinematic feature extending well beyond $r_{\rm soft}$.

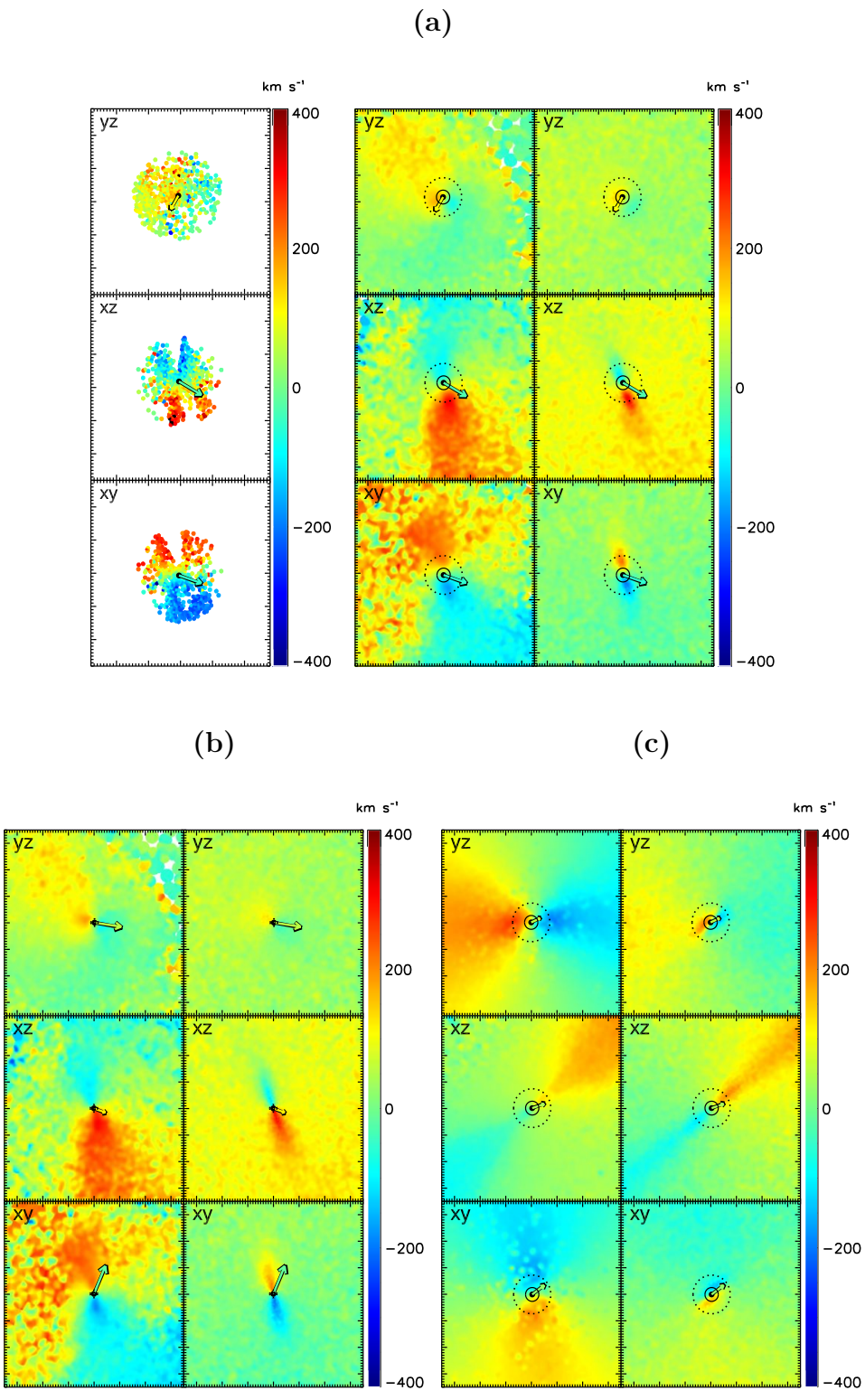

Figure 4.4.—: (Continued)

Additionally, we find that the central, rotating cusp of stars does not appear until after the first burst of star formation following the close passage of the galaxies. This argues against a numerical origin for the gas rotation features, as the gravitational softening remains constant throughout the simulation. Further evidence along these lines comes from Fig. 4.4c, which shows a snapshot from an equal-mass merger with a higher gas fraction ($f_{\rm gas} = 0.3$). In this simulation, the higher central SFR creates a more extended, rotating, disk-like stellar feature that can be seen in the xz velocity map, well beyond the influence of the softened gravitational potential.

4.3.3 Observable Signatures of kpc-scale Double-peaked NL AGN

Double-Peaked NL Velocity Profiles

In Figs. 4.5 - 4.7, we illustrate some examples of kiloparsec-scale dual AGN with double-peaked NLs. Foremost, these examples demonstrate that a variety of velocity structures can give rise to dNL AGN during the kiloparsec-scale phase. Figure 4.5 (the xy projection) is an example of the "standard" picture that motivates the association of dNL AGN with dual SMBHs. In Fig. 4.5a, we see two distinct NLRs with LOS velocities corresponding to the SMBH velocities. The velocity profile in Fig. 4.5c (v_z; last column) shows a peak with virtually no offset arising from the NLR associated with "galaxy 1", and a blueshifted peak arising from the other NLR. (Note that the asymmetry of the latter owes to the asymmetric distribution of the NLR gas, as seen in Fig. 4.5b.) The combined profile, which is what an observer would see, is double peaked with a velocity splitting of ~ 300 km s^{-1}. This is an example of a dNL AGN resulting directly from

SMBH motion when the NLRs are non-overlapping (the SMBH separation is 2.3 kpc).

Figure 4.6 also shows a dNL AGN that results directly from SMBH motion, but in a very different regime. Here, the SMBH separation is comparable to the size of the NLR, so we would not expect two brightness peaks to be resolvable with imaging. The SMBH luminosities are quite different; the middle panels of Fig. 4.6c show that the NLR emission arises mostly from the AGN in "galaxy 1". However, it is obvious from the velocity map (Fig. 4.6a) that the second SMBH influences the NLR kinematics as it plows through the edge of the NLR. Recall that each SMBH is bound within a dense stellar cusp, such that the dynamics of its inspiral may impact a region much larger than the SMBH radius of influence. The resulting double-peaked velocity profile is apparent in all three orthogonal projections. Thus, the dNL AGN results directly from SMBH motion even though the SMBHs do not have comparable luminosities and their separation is less than the size of the NLR. Such features will be very short-lived, but should be hard to avoid once the SMBH separation falls below the size of the NLR.

In addition to dNL AGN produced directly by SMBH motion, we find many examples where double-peaked profiles are produced by gas kinematics but are still *influenced* by the SMBH motion. In Figure 4.7, the combined velocity profile is a redshifted, uneven double peak that arises from NLR1 but is influenced by the blueshifted peak in NLR2. Thus, the SMBH motion is not responsible for the double peak but affects both the centroid and the peak ratio of the combined NLR profile.

In many other cases we find that the double-peaked features arising from gas kinematics are simply coincident with the kpc-scale phase. We note that examples of this scenario have been found in real systems (Fu et al. 2011b).

Figure 4.5.—: (Following two pages.) The NLR velocity maps, NL luminosity, and 1-D velocity profiles, as well as the stellar density maps, are shown for three orthogonal projections of a single snapshot during the kpc-scale phase (Phase II). The merger has $q = 1$ and $f_{\rm gas}$= 0.1 initially, and the snapshot occurs at $t_{\rm mrg}$ −20 Myr. The SMBH separation is 2.3 kpc. **(a):** LOS velocity maps for NLR particles, in the same manner as in Fig. 4.3. The left column of this plot is centered on SMBH2, the right column is centered on SMBH1, and the arrows denote the SMBH velocity. **(b):** maps of Hβ surface brightness, on the same scale. The SMBH positions are denoted by the black open circle. **(c):** NLR velocity profiles. The three columns show v_x, v_y, & v_z, corresponding to the yz, xz, and xy projections, respectively. The top row shows the NLR profiles associated with galaxy 1 (and SMBH1), and the middle row shows those associated with galaxy 2 (SMBH2). The bottom row shows the combined profile. In this Phase II snapshot, the combined profile is by definition what would be seen by observers. The projected BH separation for each LOS is indicated on these panels. In all panels, the black curve shows the profile from our NL model, and the red curve is a double-Gaussian fit. The horizontal black dotted line marks the minimum observability threshold we have set for the Hβ line: $L_{\rm H\beta} = 5 \times 10^4$ M$_\odot$. This corresponds approximately to the sensitivity of SDSS for an AGN at $z = 0.1$. The vertical black line is the rest frame of the host galaxy (stellar center-of-mass velocity), and the blue dashed vertical lines denote the SMBH velocities corresponding to each NLR; both are shown in the combined profile. The velocity profiles assume a Gaussian internal velocity dispersion with FWHM = $0.5\,c_{\rm sound}$ and are degraded to a resolution of 65 km s^{-1}. **(d) & (e):** Projected stellar density shown from the same three orientations, but with different spatial scales; the panels are 15 and 43 kpc on a side, respectively.

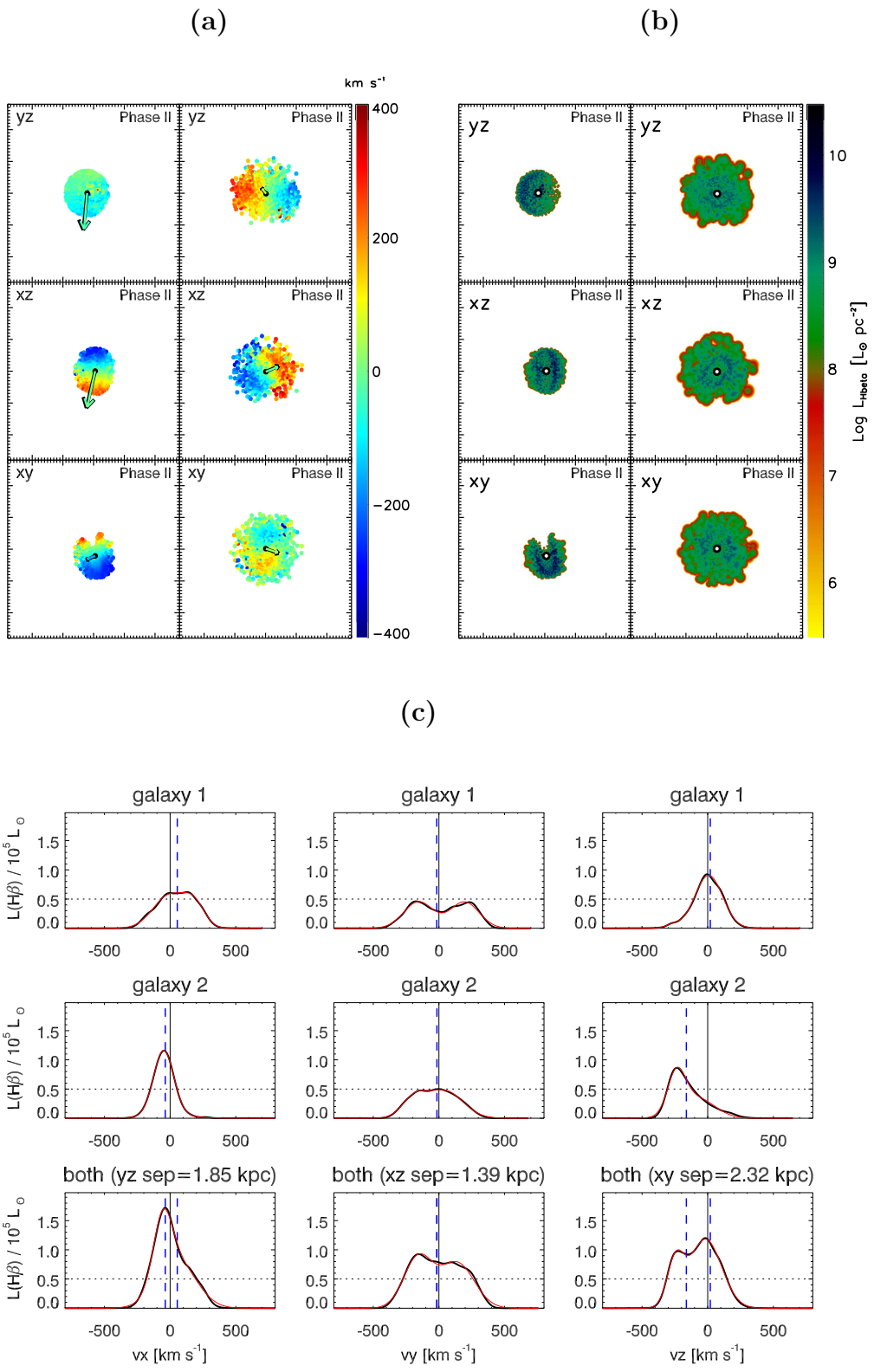

Figure 4.5.—: (Continued)

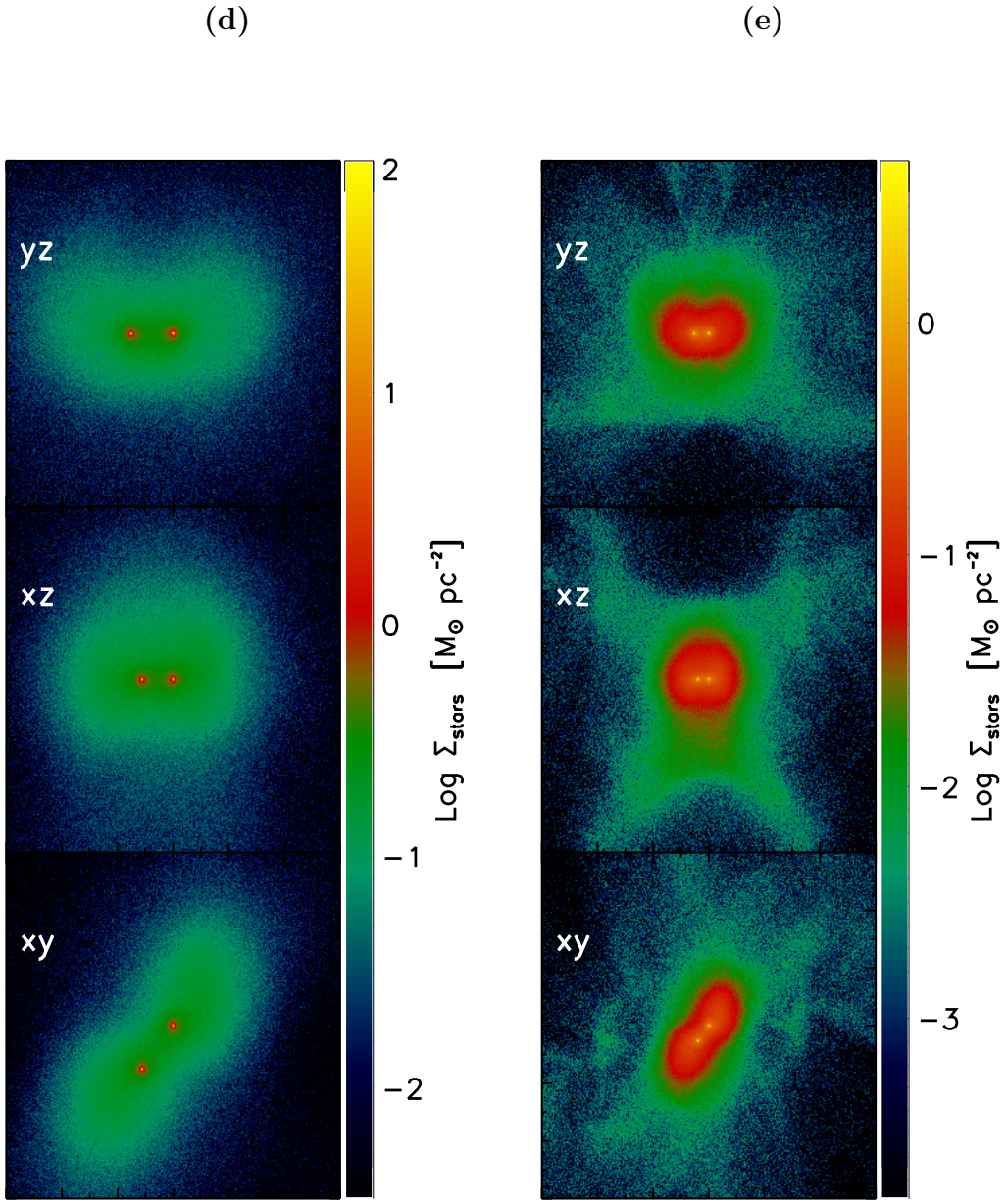

Figure 4.5.—: (Continued)

Figure 4.6.—: (Following two pages.) NLR velocity maps, Hβ luminosity maps, and 1-D velocity profiles, as well as stellar density maps, are shown in the same manner as Fig. 4.5 for a Phase II snapshot in a simulation with $q = 1$ and $f_{\rm gas}$= 0.1 initially. This snapshot occurs 8 Myr prior to SMBH merger, when the SMBH separation is only 0.17 kpc.

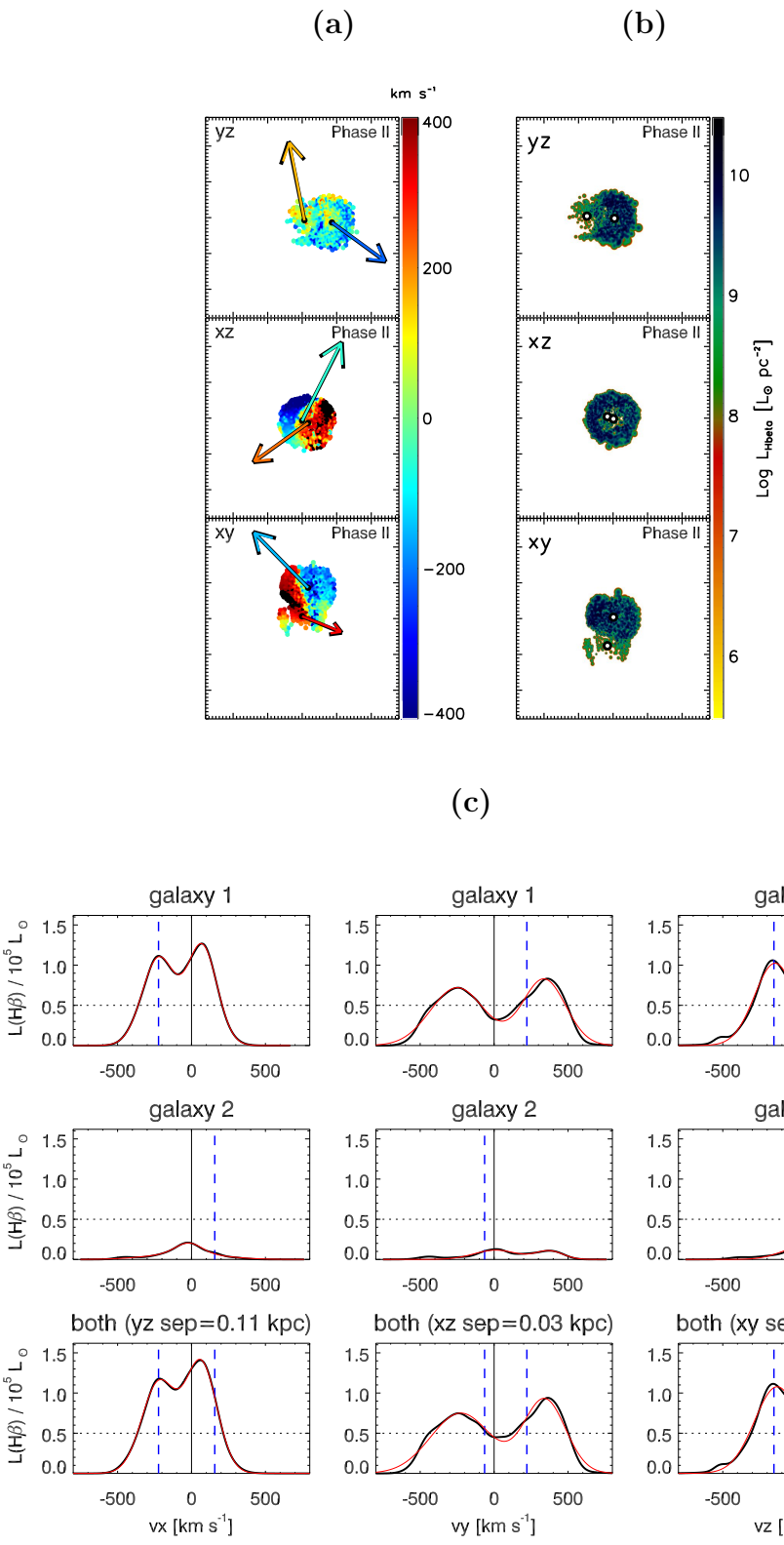

Figure 4.6.—: (Continued)

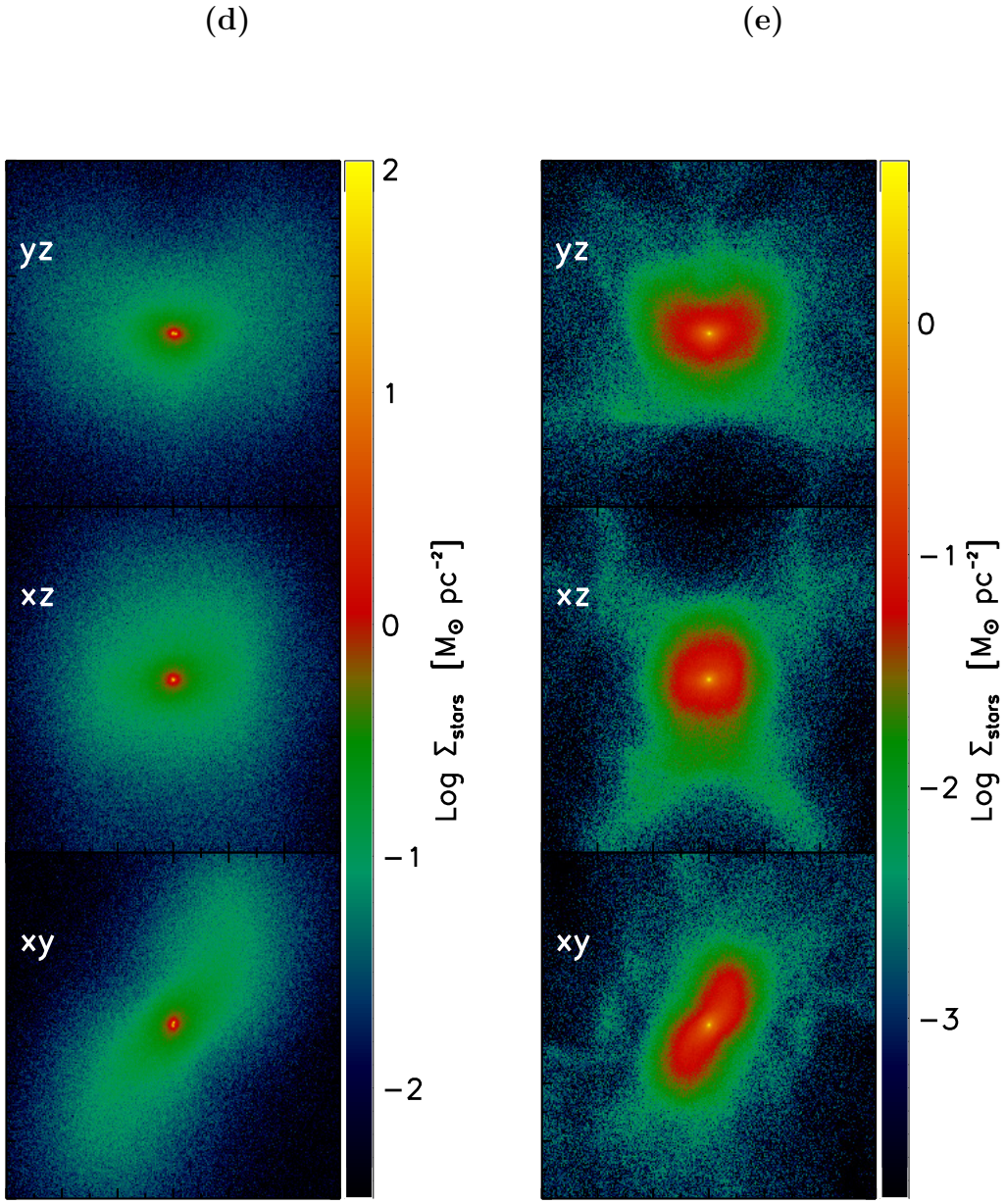

Figure 4.6.—: (Continued)

Figure 4.7.—: (Following two pages.) NLR velocity maps, Hβ luminosity maps, and 1-D velocity profiles, as well as stellar density maps, are shown in the same manner as Fig. 4.5 for a Phase II snapshot in a $q = 0.5$, $f_{\rm gas} = 0.3$ simulation. This snapshot occurs 20 Myr prior to SMBH merger, when the SMBH separation is 1.1 kpc.

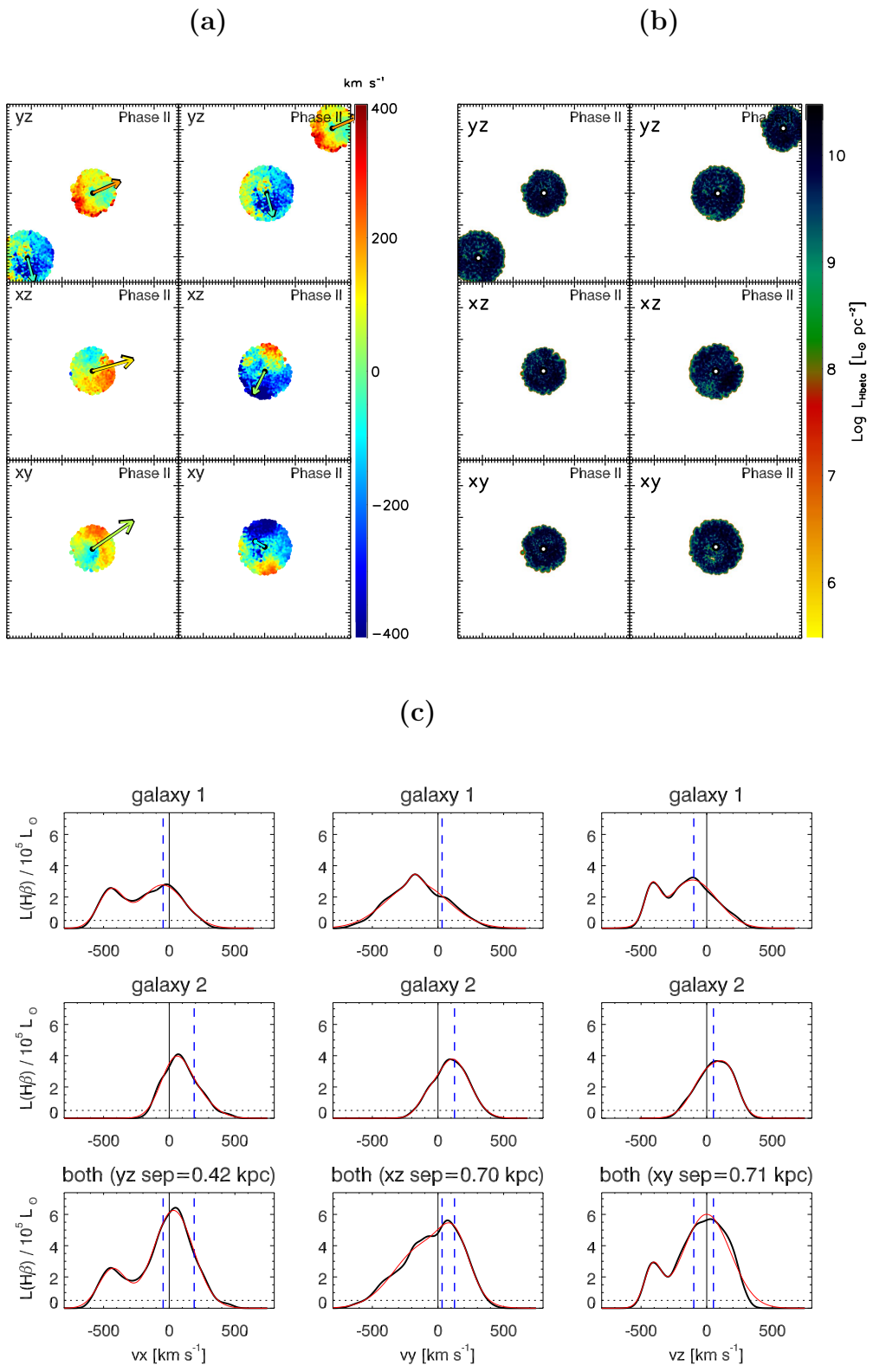

Figure 4.7.—: (Continued)

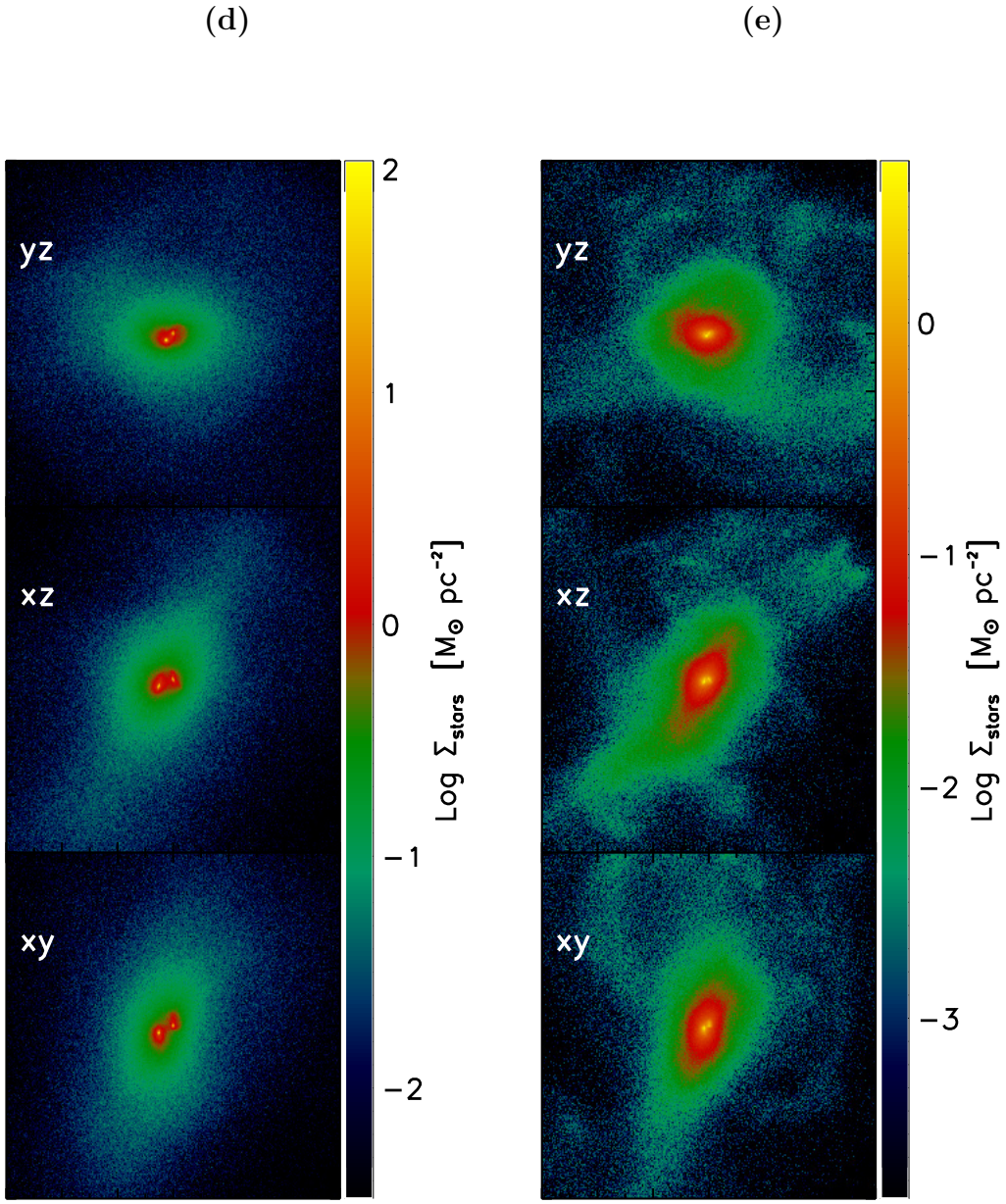

Figure 4.7.—: (Continued)

In order to estimate the fraction of Phase II dNL AGN that are affected either directly or indirectly by the SMBH motion. We have undertaken a visual analysis of the velocity profiles at each Phase II snapshot, from three orthogonal viewing angles, in two of our simulations (mergers with $q = 1$, $f_{\rm gas} = 0.1$ and with $q = 0.5$, $f_{\rm gas} = 0.3$). We have visually classified each observable double-peaked profile in Phase II (for both $a_{\rm max} = 5.5$ & 21 kpc) as **(i)** directly induced by SMBH motion, **(ii)** indirectly influenced by SMBH motion, **(iii)** merely coincident with Phase II, or **(iv)** a complex or highly asymmetric profile.

The fraction of snapshots in each category varies substantially between the three sight lines and two simulations, owing to small number statistics and to intrinsic variability with viewing angle and galaxy merger model. Nevertheless, we can draw some general conclusions from this analysis. The directly-induced dNLs occur in only a few snapshots, corresponding to lifetimes of 3–6 Myr. These primarily occur for SMBH separations < 5.5 kpc, and thus they account for up to 60% (33%) of the Phase II dNL lifetime for $a_{\rm max} = 5.5$ (21) kpc. The total fraction of Phase II for which the SMBH motion has *some* influence on the velocity profiles, directly or indirectly, is between 30 and 80% depending on $a_{\rm max}$ and the merger model. Most of the remaining double-peaked profiles arise from gas rotation in a single, disk-like NLR. However, between 0 and 30% of the Phase II profiles classified as double peaks are actually complex (multi-peaked) or highly asymmetric profiles. These are important signatures as well, because they are often associated with relative SMBH motion. The complex profiles, in particular, typically arise either from a highly-disturbed NLR gas distribution following a close passage or from the superposition of two double-peaked profiles with different velocity centroids.

Stellar Structure

In addition to the NLR kinematics, subfigures (d) & (e) in Figs. 4.5–4.7 show stellar density maps for each of these examples. In both Fig. 4.5 and Fig. 4.7, two density peaks are present in all projections, but in the latter, very high resolution imaging would be required to resolve the two peaks. The yz projection in particular has the smallest projected separation but the largest relative LOS SMBH motion. This is not uncommon for kpc-scale SMBH pairs; owing to their rapid inspiral on these scales, their orbits are evolving and are generally *not* circular. Thus, the largest LOS velocity separation may occur when the LOS is oriented along the major axis of the eccentric orbit, corresponding to smaller projected spatial separations. This creates an added challenge for attempts to confirm dual SMBH candidates via spatially-resolved stellar cusps, but it also means that some apparently single-core galaxies with dNL AGN may in fact be hiding dual SMBHs at small projected separations.

In such cases, other clues may hint at the object's true nature. For example, some but not all of the the projections in Figures 4.5d–4.7d show disturbed or double-lobed morphology that indicates an ongoing merger. In contrast, the subfigures (e), which have a larger field of view and a lower minimum density by a factor of 20, show diffuse tidal features for all sight lines. Thus, sufficiently deep imaging of dNL AGN hosts, for example with *HST*, could reveal the disturbed nature of late-stage mergers that might otherwise appear as normal, isolated ellipticals. While disturbed morphology in a dNL AGN host galaxy does not not necessarily indicate a SMBH pair, as the SMBHs may have already merged, this signature would establish the system as a late-stage merger, thus removing the possibility of an isolated galaxy or a galaxy with a close, but still

widely separated companion.

Comerford et al. (2011b) note that the objects in their dNL AGN sample are preferentially aligned with the major axis of the host galaxy and propose this as an additional diagnostic for the presence of a SMBH pair. In Figure 4.5d we see that there is indeed a strong alignment between the orientation of the SMBH pair and the apparent ellipticity of the merger remnant. In this case, when the SMBHs are separated by > 2 kpc, this "ellipticity" of the remnant results directly from the superposition of unmerged galaxy cores. The fainter tidal features shown in Fig. 4.5e make clear that the overall morphology is highly disturbed rather than ellipsoidal. In Fig. 4.7, however, the SMBHs have a separation of ~ 1 kpc, and the progenitor galaxy cores have essentially merged. In this case the SMBH pair is less closely aligned with the apparent ellipticity of the remnant, as the BH orbits are now decoupled from their progenitor host galaxies. We therefore predict an inverse correlation between projected SMBH pair separation and the degree of alignment with the apparent major axis of the merger remnant, though with large scatter owing to variation in the SMBH orbits, the viewing angle, and the structure of the unrelaxed merger remnant.

Figure 4.8.—: (Following page.) LOS-averaged properties of narrow-Hβ velocity profiles. For clarity, only the merger phases II and III are shown. Phase II snapshots are shaded for $a_{\rm max} = 5.5$ kpc (light gray) and 21 kpc (dark gray). The simulation has $q = 1$ and initial $f_{\rm gas} = 0.1$. The top panel shows, as a function of time, the fraction of the 40 random sight lines sampled from which the combined velocity profile (NLR1 + NLR2) has an observable double peak. Only snapshots in which these criteria are met for at least one viewing angle are plotted. In the other panels, various quantities from the profile fits are shown, averaged over *only* the sight lines for which the profile is double-peaked. The mean (extremal) values are shown in red (blue) and connected with solid (dotted) lines. Starting with the second panel from the top, the panels show: the luminosity ratio of the double peaks, the offset of the entire profile, and the velocity splitting of the two peaks ($\Delta_{\rm cen}$).

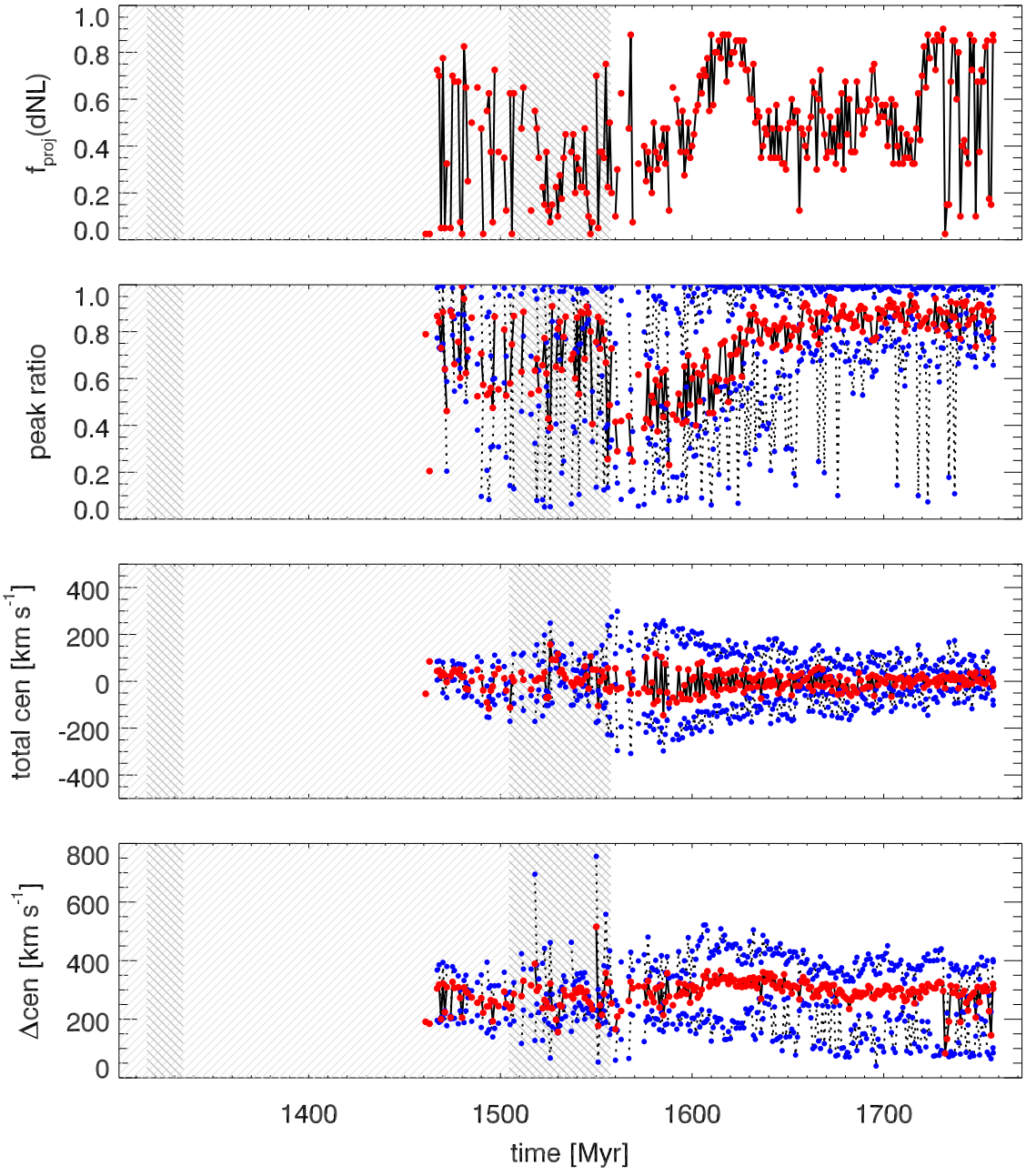

Figure 4.8.—: (Continued)

Our results indicate that the absence of two resolvable stellar components does not rule out the presence of a dual AGN, even for spatial resolutions of ~ 1 kpc. Although a candidate dual AGN has recently been found with a separation of 150 pc (Fabbiano et al. 2011), the recent work by Comerford et al. (2011b)—in which all 81 objects observed with slit spectroscopy showed spatially-distinct emission components with separations of at least 200 pc—suggests that sub-kpc-scale dual AGN may be relatively rare. If so, this likely owes to their short lifetimes, which are typically a few Myr, or 1–2% of Phase II. Thus, for most of our simulations, $\sim 10 - 40\%$ of of the dNL AGN in Phase II contain sub-kpc SMBH pairs. However, for gas-poor mergers ($f_{\rm gas} = 0.04$ initially), we find that $\gtrsim 90\%$ of the Phase II dNL AGN may be associated with sub-kpc SMBH pairs. Because these mergers are less dissipative, the SMBH inspiral is more gradual, and the SMBHs spend more time at small separations prior to merger. Also, the low-level AGN activity in gas-poor mergers means that the NL AGN may be under-luminous until the peak of SMBH accretion, near the time of SMBH merger. Therefore, we argue that some systems with a single stellar component but with disturbed morphology may contain dual AGN with separations of a few hundred parsec (see Fig. 4.6); these may be good candidates for high-resolution *Chandra* (c.f. Fabbiano et al. 2011) or EVLA (c.f. Fu et al. 2011c) observations.

NL Velocity Profile Diagnostics

Figure 4.8 shows the evolution of several LOS-averaged quantities for the Hβ velocity profiles in the late-merger stage of an example simulation. For each snapshot, the values shown are averages of profiles for 40 random sight lines, and the definitions of merger phases are based on the projected SMBH separation for each sight line. This equal-mass

merger with initial $f_{\rm gas} = 0.1$ was chosen for illustration because it has sufficient NLR activity to demonstrate all the salient features of the Hβ profiles, but still has a moderate gas content and thus should not be strongly affected by a rapid post-merger increase in $v_{\rm esc}$ or by a strong starburst. For each snapshot, the data shown are averaged over the sight lines for which the profile has an observable double peak. "Observable" double peaks are defined as those with a velocity splitting larger than FWHM$_{\rm a}$ (corresponding to the brightest peak), a peak ratio larger than 0.05, and a peak $L_{\rm H\beta} > 5 \times 10^4$ L$_\odot$.

Several trends are apparent in Fig. 4.8. The top panel shows the fraction of sight lines from which the profile appears double-peaked, and the second panel shows the luminosity ratio of the two peaks. Both quantities are generally lower and more variable during Phase II than during Phase III. This is because double peaks arising from a single NLR are generally caused by rotating gas disks in our simulations, whereas some of the double peaks in Phase II are caused or influenced by SMBH motion. In principle, the 1-D velocity profile for two NL AGN in a circular orbit could appear quite similar to that of a rotating disk of the same size. However, as the dual SMBHs in our simulations generally have non-circular orbits, they appear as double-peaked for a smaller fraction of viewing angles than do the rotating disks.

We also see a tendency for double peaks in Phase III (those caused exclusively by gas kinematics) to have peak ratios closer to unity than those in Phase II. This is the diagnostic proposed by Smith et al. (2011) to differentiate between dNL AGN arising from rotating disks versus dual SMBHs. While we see that this distinction does exist in an average sense, the peak ratios in Phase III still have substantial variation with viewing angle. In the best cases, the peak ratios for a single snapshot range from $\sim 0.6 - 1.0$ depending on the sight line, while at other times the *mean* peak ratios are

$\lesssim 0.5$. Furthermore, in almost every snapshot with an observable double peak, including those in Phase II, the maximum peak ratio is $> 0.8 - 0.9$; i.e., there is usually at least one viewing angle from which the profile has nearly even peaks. We therefore conclude that for individual systems, an uneven-peaked dNL AGN has at most a modestly higher probability of containing a dual SMBH than one with an even-peaked profile, even for peak ratios as low as $\sim 0.1 - 0.2$.

The velocity splitting of the double peaks ($\Delta_{\rm cen}$, bottom panel of Fig. 4.8) also shows distinct behavior in different merger phases. The spikes in $\Delta_{\rm cen}$ during Phase II correspond to pericentric passages of the SMBHs shortly before their merger, revealing a brief but direct effect of the SMBH motion on the Hβ velocity profiles. Generally, we find that values of $\Delta_{\rm cen} \gtrsim 500$ km s^{-1} occur only during pericentric passages in Phase II, and only for SMBH pair separations < 1 kpc. They are also short lived, with a cumulative lifetime of at most a few Myr in a given merger. In our unequal-mass, gas-poor simulations with shallower central potentials, NL velocity splittings > 500 km s^{-1} are never achieved. Nonetheless, the association between large $\Delta_{\rm cen}$ and sub-kpc SMBH pairs suggests that spatially-unresolved dNL AGN with large $\Delta_{\rm cen}$ may be good follow-up candidates for high-resolution imaging studies.

Excluding these brief, large spikes in $\Delta_{\rm cen}$, we note that the maximum $\Delta_{\rm cen}$ for each snapshot is typically a bit larger in Phase III than in Phase II, owing to the higher gas velocities that reflect a (modest) increase in the depth of the central potential during this time. In the $q = 1$, $f_{\rm gas} = 0.3$ merger model (the most extreme model used in terms of central gas density), the maximal $\Delta_{\rm cen}$ may be as high as 800 km s^{-1} in Phase III, but obscuration is likely important in such an environment and may reduce the probability of observing such large velocity splitting in a single NLR.

We also calculate the velocity centroid of the entire double-peaked profile (the median velocity of the two peak centroids) and examine phases in which it differs from zero (second panel from bottom in Fig. 4.8). In principle, a double-peaked profile with an offset centroid could arise from one orbiting SMBH in a pair, as in Fig. 4.7. The total offsets are generally less than 150 km s^{-1}, but can briefly reach values of $\sim 300 - 400$ km s^{-1}. Again, there is a correspondence between larger offsets and pericentric passages of the SMBHs, but such offsets also occur in Phase III owing to some "sloshing" of the recently-merged SMBH in the steepening central potential. It is important to note that even in this case, offset profiles are still indicators of SMBHs in motion, and that in real systems, comparable-mass BH mergers may have a non-negligible probability of resulting in a GW recoil kick of at least 100–200 km s^{-1} (e.g., van Meter et al. 2010; Lousto & Zlochower 2011b). At such kick speeds, the SMBH could retain much of its central cusp and NLR, such that a double-peaked NL profile with an overall offset could result. Finally, in our "extreme", $q = 1$, $f_{\rm gas} = 0.3$ merger, the total offsets during Phase III owing to SMBH sloshing are < 300 km s^{-1} despite the significantly deeper central potential, indicating that this signature is less sensitive to the underlying density profile than is the velocity splitting.

Figure 4.9.—: (Following page.) The total time during the merger, separated by merger phase, for which the NL AGN have an observable double-peaked profile ($t_{\rm dNL}$). Data are shown for eight simulations with different galaxy models, with q and $f_{\rm gas}$ values as indicated on the plots. The top panel in each plot shows the lifetimes for a kpc-scale phase definition of $a_{\rm max} = 5.5$ kpc, and the bottom panel in each plot is for $a_{\rm max} = 21$ kpc. Within each panel, Phase I is shown in the first two gray bars, separated into NLR1 and NLR2 as during these phases the NLR from each galaxy would not be observable in the same spectrum, followed by Phase II (the kpc-scale phase, as defined in the text), then Phase IIb (g1 & g2) and Phase III. The height of each gray bar represents the mean total duration of each phase averaged over 40 random sight lines (as the phase definitions depend on *projected* SMBH separation). The error bars give the range of values sampled. Within each phase, the green bars denote the mean lifetime for which the system has an observable double-peaked NL profile *and* $L_{\rm bol} > 3\% L_{\rm Edd}$ for one BH. Similarly, in Phase II, the cyan bar denotes the double-peaked NL AGN lifetime for which *both* BHs have $L_{\rm bol} > 3\% L_{\rm Edd}$.

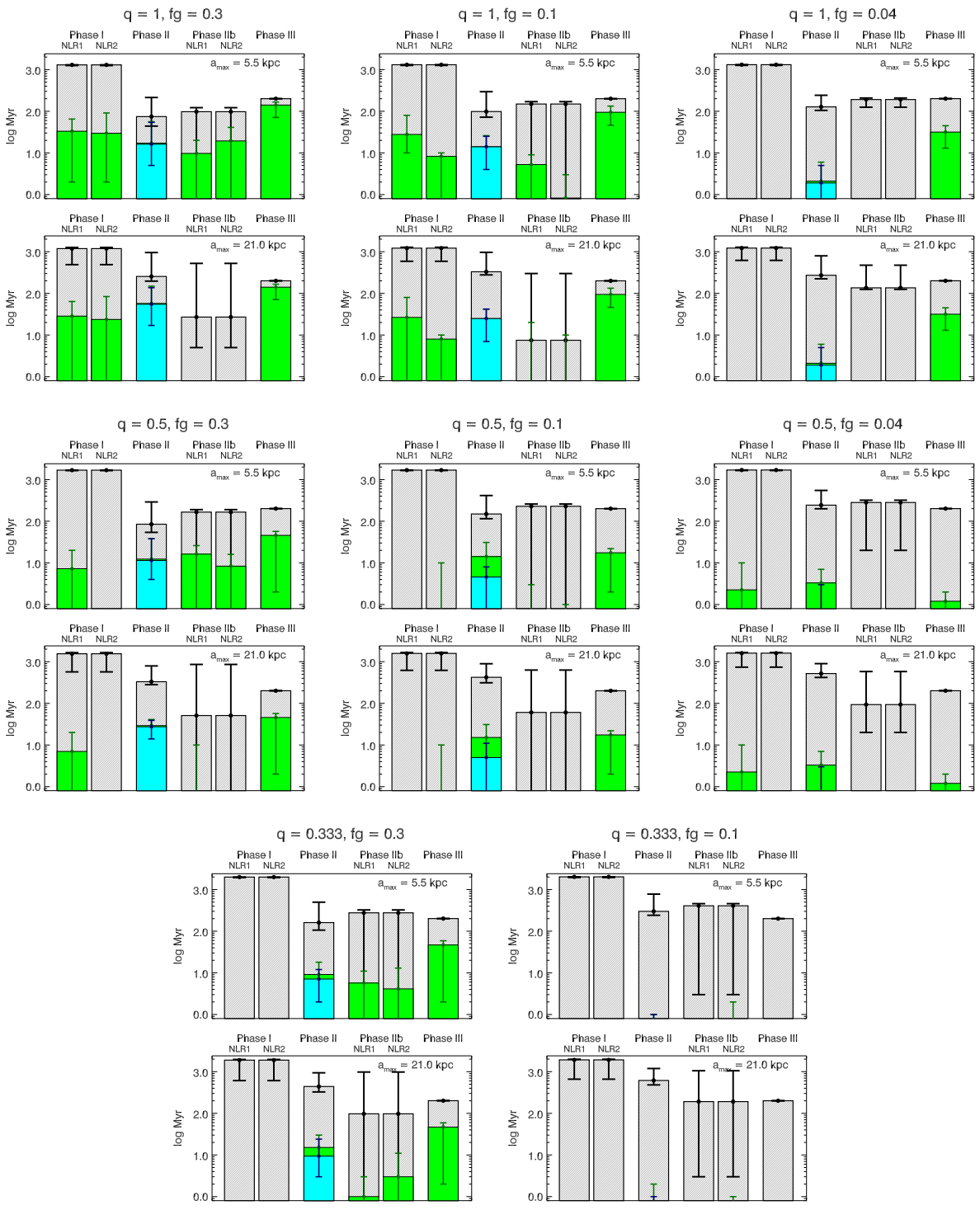

Figure 4.9.—: (Continued)

4.3.4 Lifetimes of Double-NL AGN

Figure 4.9 shows the time for which the NLRs have an observable double-peaked profile ($t_{\rm dNL}$) and are active as AGN ($L_{\rm bol} > 3\%\ L_{\rm Edd}$) in each merger phase, for eight different galaxy models and for two definitions of Phase II ($a_{\rm max} = 5.5$ and 21 kpc). As in Fig. 4.8, the values shown are averaged over 40 random sight lines. When the Hβ line flux is above the minimum observable criterion, the continuum luminosity is almost always $> 3\%\ L_{\rm Edd}$; thus, we do not make a distinction between these observability criteria in Fig. 4.9. In Phase II, lifetimes are shown for when one (green) or both (cyan) SMBHs meet the AGN criterion. In the equal-mass mergers, the SMBHs have similar Eddington ratios during Phases II and III, as both SMBHs are near their peak luminosities.

We see that the definition of Phase II does not affect our results qualitatively, aside from Phase IIb, which depends strongly on $a_{\rm max}$ and the LOS. More importantly, the variation in merger phase duration and in $t_{\rm dNL}$ for different values of $a_{\rm max}$ is much less than the variation for different sight lines.

Comparing $t_{\rm dNL}$ in each phase, we see that in nearly all simulations, Phase III (the post-BH-merger phase) has the longest average $t_{\rm dNL}$. These lifetimes are typically tens of Myr, but range from zero to nearly 200 Myr (the post-merger time at which we stop the simulation) for the merger models and sight lines shown. Phase II has somewhat shorter dNL lifetimes, typically a few Myr to a few tens of Myr, but ranging from 0 - 110 Myr.

As discussed in § 4.2.3, we use the narrow Hβ line for our calculations instead of the more luminous [O III] line because the former is less sensitive to the exact conditions in the ISM. Accordingly, we note that these lifetimes can be considered lower limits on the lifetime of NL emission above the observability threshold, because at times when $L_{\rm H\beta}$ is

slightly below this threshold, the stronger [O III] line may easily be detectable.

$t_{\rm dNL}$ for Phase I is somewhat variable but typically shorter than $t_{\rm dNL}$ for Phase II or III. Although Phase I is quite long (> 1 Gyr), and $L_{\rm bol}$ is often Eddington-limited for a brief time after the first close passage, the Eddington limit is nearly ten times higher during coalescence, owing to the SMBH growth in the meantime. Accordingly, the NLRs are generally less luminous during Phase I and the lifetime of observable double-peaked NLs is shorter, despite the fact that the *total* duration of Phase I is much greater than the combined duration of Phase II and Phase III.

As discussed in § 4.3.1, mergers with lower q and $f_{\rm gas}$ have less AGN and NL activity overall, and we see the consequences of the strong dependence of dNL AGN lifetimes on q and $f_{\rm gas}$ in Fig. 4.9. The merger with $q = 0.333$ and initial $f_{\rm gas} = 0.1$, which is still a major merger, has almost no double NL AGN in any merger phase. A large parameter study, which is outside the scope of this work, would be required to determine which galaxies and merger remnants are most likely to host dNL AGN overall. However, these initial results demonstrate that the mass ratio and gas content of merging galaxies (and by extension, the efficiency of gas inflow during the merger event) are crucial factors.

4.4 Discussion

Motivated by recent identifications of candidate SMBH pairs via double-peaked narrow emission line signatures, we have developed the first model for NL emission from AGN in hydrodynamic simulations of evolving, interacting galaxies. Specifically, our model was applied to SPH/N-body (GADGET-3) galaxy merger simulations with central, accreting

SMBHs, allowing us to calculate NL velocity profiles for arbitrary sight lines throughout the galaxy merger. While this work represents only a first attempt to understand the complex dynamical and radiative processes in the centers of merging galaxies, our approach highlights several general properties of the kinematics and luminosity of photoionized gas around AGN in mergers. Combined with information about the underlying stellar distribution and the AGN continuum luminosity, these results inform the prospects for confirming candidate dual SMBHs via future follow-up observations of double-peaked NL AGN.

4.4.1 Evolution and Kinematics of Double-Peaked Narrow-Line AGN

The kpc-scale phase of SMBH pair evolution (Phase II in the above discussion) lasts up to a few hundred Myr, while the merger itself lasts a few Gyr from first infall to final coalescence. The SMBHs in our simulations have observable double-peaked NL AGN profiles for only a fraction of Phase II, with lifetimes ranging from less than 1 Myr to a few tens of Myr. Thus, we find that dNL AGN are a generic but relatively short-lived feature of major, gaseous mergers.

We find that NL AGN have lower luminosities during the early merger phase (Phase I in the above discussion). Therefore, the brightest NL emission triggered by mergers should occur in the late stages of merging. This is consistent with a recent study by Van Wassenhove et al. (2011), which also found that merger-triggered AGN pairs are most active in the late merger phase. Owing to this coincidence in timing, dNL AGN triggered by major mergers are most likely to be associated with kpc- or sub-kpc-scale

SMBH pairs (Phase II), or with recent SMBH mergers (Phases III).

Follow-up observations of dNL AGN indicate that a minority of these objects show evidence for dual SMBHs; the rest of the double-peaked features are either ambiguous or are presumed to result from gas kinematics. If a substantial fraction of dNL AGN were *directly* associated with kpc-scale SMBH pairs, our results might be in tension with this finding. However, we find that only a minority of dNL AGN result directly from SMBH motion, *even within the kpc-scale phase of SMBH evolution*. Thus, the canonical picture of two distinct NLRs orbiting about a common central potential is only one of several possible mechanisms for producing double peaks, and it is not the most common.

As the example in Fig. 4.6 shows, if the SMBH separation is comparable to the size of the NLRs, then double peaks may arise from the direct interaction of the SMBHs with the NL gas. In other cases, a double-peaked feature may arise from gas kinematics in a single NLR, but still may be *influenced* by the relative SMBH motion. For example, the SMBH motion may alter the peak ratio or impart an overall velocity shift to the observed dNL profile. The fraction of double-peaked profiles in Phase II that are influenced by SMBH motion either directly or indirectly can be up to $\sim 80\%$, depending on the merger model and the definition of Phase II.

We also find many NL profiles in which the dNL AGN arising from gas kinematics are not significantly affected by the SMBH motion and are simply *coincident* with the kpc-scale phase. This is consistent with the empirical finding that a minority of dNL AGN show clear association with dual SMBHs. It also indicates that "serendipitous" discoveries of dual AGN with double-peaked profiles in which the double peak results from gas kinematics (cf. Fu et al. 2011b) may in fact be a relatively common occurrence.

The remainder of double-peaked NLs mostly arise from rotating gas disks, though in some cases almost 30% of profiles classified as double peaks in Phase II have complex (multi-peaked) or highly-asymmetric profiles. These generally also indicate relative SMBH motion via disturbed or superimposed NL emission regions.

We note that our thermal feedback model for AGN does not allow for AGN outflows or jets, which may be additional mechanisms for producing double-peaked NLs. This could mean that the prevalence of dNLs induced by gas rotation is lower in reality than in our simulations. However, dNL AGN produced by outflows or jets may be distinguishable from dNLs produced by dual SMBHs. Rosario et al. (2010) demonstrate that jets in some dNL AGN may be resolved via radio imaging, and Comerford et al. (2011b) suggest that spatially-extended NL emission components may be caused by outflows, though the possibility of a dual AGN with outflows cannot be excluded.

Another important consideration is that the observed kinematic features of NL AGN are strongly dependent on viewing angle. To account for this, we fit velocity profiles and calculate dNL AGN lifetimes for many lines of sight. The LOS variation in dNL AGN lifetimes is typically at least an order of magnitude; this constitutes an intrinsic uncertainty in the statistics of dNL AGN.

The amount of merger-triggered dNL AGN activity also depends strongly on the conditions in the merging galaxies, owing largely to variation in the SMBH accretion rates. Specifically, more AGN and NL activity occurs in mergers with higher mass ratio (closer to equal mass) and gas content, i.e. those that drive the strongest inflow of gas to the central galactic regions. Second-order effects steepen this trend somewhat, as discussed in § 4.3.1. We also consider the addition of a stellar bulge in the progenitor

disk galaxies and find that this has little effect on our qualitative results. We do not include bulge-*dominated* or elliptical galaxies in this initial study, though we note that such progenitors could have different central gas kinematics during mergers. However, a key result of this study is that dNL AGN induced by SMBH motion are generic to gaseous major mergers; variations in the gas kinematics alter only the importance of dNL AGN induced by dual SMBH motion relative to those produced by other means.

4.4.2 Additional Signatures of Dual AGN

The dNL AGN that have been identified as strong dual SMBH candidates are those with with two resolved surface brightness peaks that coincide spatially with the dual NL components in spatially-resolved spectra. In our simulations, we find that after the burst of star formtion triggered by the first close passage of the galaxies, each SMBH is surrounded by a dense cusp of stars and gas. These cusps should appear as two brightness peaks with sufficient spatial resolution. However, in most of our simulations, $\sim$ 10–40% of dNL AGN induced by SMBH motion have projected SMBH separations of less than a kpc and may be difficult to resolve. Gas-poor mergers have an even higher fraction of dNL AGN associated with sub-kpc-scale SMBH pairs, more than 90% in some cases. This is further evidence that a significant population of dNL AGN may not show clear association with SMBH pairs, even when a pair is present. Other means must be employed to confirm the presence of a dual SMBH in such systems.

Some additional information may be obtained from sensitive, high-resolution (i.e., *HST*) imaging that can capture diffuse tidal features in the merger remnant. If the galaxy appears undisturbed, or if it shows obvious signs of being in an early-merger phase

(for example, two widely-separated galaxies, perhaps with characteristic tidal bridge and tail features), a kpc-scale dual AGN would be disfavored. If a kpc-scale SMBH pair is present, the galaxy should appear as a late-stage merger remnant—a single galaxy, possibly with a double core, that is morphologically disturbed. However, because the morphology should appear much the same after the SMBHs have merged, this diagnostic cannot rule out a post-BH-merger (Phase III) dNL AGN.

We also consider the degree of alignment between the projected SMBH orbital plane and the apparent ellipticity of the host galaxy, as suggested by Comerford et al. (2011b). When the merging galaxies are physically overlapping (in projection) but their cores have not quite merged, the system may appear to have a significant ellipticity that is strongly aligned with the SMBH orbit (as in Fig. 4.5). However, in this stage the disturbed merger remnant is not a true ellipsoid, and deeper imaging could reveal fainter tidal features. Once the cores of the progenitor galaxies have merged, the SMBHs begin to decouple from this orbital plane as they continue their inspiral. Thus, SMBH pairs with projected separations $\lesssim 1$ kpc should be more weakly correlated with the ellipticity of the host galaxy.

Smith et al. (2011) have suggested that dNL AGN with similar peak luminosities are less likely to be dNL AGN, on the grounds that rotating gas disks may have double-peaked profiles with roughly even peaks, and that dual AGN are unlikely to have nearly equal luminosities. We do see a trend toward higher peak luminosity ratios (closer to unity) for dNLs arising from rotating gas disks than for those resulting from SMBH pairs. However, in the single-NLR case, the peak ratios still vary substantially, and in the dual-BH case there is almost always at least one viewing angle for which the double-peaked profile has nearly even peaks. Thus, dNL AGN with uneven peak ratios

($\lesssim 0.5$) should have a slightly higher probability of containing a dual SMBH, but this appears to be a fairly weak correlation.

In addition, we find that large velocity splittings in double-peaked profiles ($\Delta_{\rm cen} \gtrsim 500$ km s^{-1}) are often associated with relative motion of sub-kpc SMBH pairs, because $\Delta_{\rm cen}$ increases during close passages of the SMBHs. Large dNL velocity splittings may also occur in AGN with high-velocity outflows, though these may be more easily distinguished via spatially-extended emission components. Thus, dNL AGN with spatially-compact emission components separated by $\gtrsim 500$ km s^{-1} may be good candidates for high-resolution imaging.

Finally, double-peaked profiles with overall velocity offsets may indicate the presence of an inspiraling SMBH pair. Again, this signature could also arise from a recently-merged SMBH if it sloshes though the central region before settling down, especially if the SMBH experiences a non-negligible GW recoil kick. In any event, double-peaked profiles with discernible velocity offsets should be associated with SMBH motion of some kind, and some of these systems should contain dual SMBHs.

If, indeed, many dNL AGN not associated with dual SMBHs are instead associated with recent SMBH mergers, then this result is interesting in its own right. If binary SMBH spins do not align efficiently prior to merger in all cases, many SMBH mergers may result in GW recoil kicks above $\gtrsim 100 - 200$ km s^{-1} (e.g., van Meter et al. 2010; Lousto et al. 2012). As mentioned above, at these velocities the SMBH could retain much of its cusp of gas and stars, such that the SMBH motion might be detectable for a short while as a *narrow-line* offset in the AGN spectrum. At larger velocities that could displace the SMBH significantly from the center of the galaxy ($\gtrsim 500 - 1000$ km

s^{-1}), only the inner region would be remain bound to the SMBH. This would result in the offset *broad line* signature that is more commonly considered for recoiling SMBHs (e.g., Loeb 2007; Blecha et al. 2011), and in such cases the post-BH-merger phase clearly would not contribute to the dNL AGN lifetime.

4.4.3 Model Assumptions and Prospects for Future Work

The qualitative picture outlined in this initial study of NL AGN in merging galaxies is insensitive to our choice of parameters for the simulations and NL model. However, the quantitative results do have some dependence on these model parameters. The variation in our results with these parameters is in general smaller than the intrinsic variability of NL activity with viewing angle, and we have chosen parameters such that our simulated NLRs broadly reproduce the size and luminosity of observed NL AGN. Here we discuss this model dependence in more detail, as well as possibly relevant physics to be included in future work.

As discussed in § 4.3.1, our results have some quantitative dependence on the gas EOS used; softer EOS models result in more stable gas disks, and thus less gas inflow to fuel AGN and NL activity. Conversely, a nearly-isothermal EOS (softened EOS parameter $q_{\rm EOS} = 0.05$) results in higher sustained accretion rates following the initial close passage of the galaxies and significantly more NL activity in the early merger phase.

Our results are generally independent of the choice of mass and spatial resolution, though we do require that the NLRs be at least marginally resolved in order to impart physical meaning to the results. By conducting a small resolution study we do find a weak trend toward higher central densities and accretion rates for higher resolution, but

this has little effect on our results. In particular, despite small variations in the AGN lightcurves and peak luminosities, the *total* amount of SMBH accretion remains constant regardless of resolution.

Without arbitrarily high resolution, we cannot exclude the possibility that gas kinematics on sub-resolution scales could shape the resulting velocity profiles in an unpredictable manner. However, this will only affect double-peaked profiles arising from gas kinematics, and it is possible that turbulent motion in single NLRs would smear out some of these double peaks, thereby increasing the fraction of dNL AGN caused by SMBH motion. Most importantly, we can robustly predict that for at least a small fraction of the kpc-scale (and sub-kpc scale) phase, the NL gas kinematics will be dominated by the SMBH motion.

A related issue is the extent to which our NL models are limited by the multi-phase ISM treatment used in the simulations (Springel & Hernquist 2003). While this model has shown success in reproducing the global properties of merging galaxies (e.g., Cox et al. 2006; Hopkins et al. 2006a), its treatment of gas physics on small scales is necessarily highly simplified. For example, if star formation feedback drives strong turbulence in the ISM, then the assumed pressure equilibrium between hot and cold gas phases would be violated. Future work that relies on a turbulent-pressure-driven ISM model will produce more realistic distributions of gas density and temperature, allowing a more accurate identification of the NL-emitting gas.

Perhaps the most important caveat to the work presented here is the lack of obscuring dust in our models. While we do account for self-shielding of NL clouds in an average sense, such that AGN continuum photons are not double-counted, our

models do not include radiative transfer and thus are unable to account for the effects of obscuration and reprocessing of emission by dust. We accordingly restrict our analysis to galaxies with relatively low initial gas fractions, as higher gas fractions generally drive stronger starbursts and produce much more dust. Starbursts can additionally produce substantial NL emission from stellar photoionization, which is also not accounted for in our model. The results from models with initial gas fractions of 30%, the highest included in this study, may be considered less robust in this sense. However, we note that in cases where the central galactic region is only partially obscured, it is possible that double-peaked features arising from kinematics in a single NLR would be preferentially smeared out by dust reprocessing, thus strengthening the correlation between dNL AGN and dual SMBHs. The incorporation of full radiative transfer calculations in future work, including models for dust and stellar photoionization, will allow a more direct comparison of our simulated results to observed AGN.

Because this work represents an initial study of NL AGN in merging galaxies using a novel method, we have analyzed a relatively small number of high-resolution simulations that illustrate numerous key aspects of the relationship between dNL AGN and SMBH pairs. As such, many of our results are largely qualitative, and because we have left a full parameter study of dNL AGN in merging galaxies for future work, we cannot comment directly on the statistics of the observable dNL AGN population. It is also important to note that while we have focused on AGN triggered by major galaxy mergers, AGN triggered by minor mergers or secular processes may also contribute to the population of double-peaked NL objects. A strong consensus on the fraction of merger-triggered AGN does not currently exist, as surveys with different selection criteria have obtained widely disparate results (e.g., Cisternas et al. 2011; Ellison et al. 2011; Koss et al. 2011a).

We have shown that the scenario conceived to motivate searches for dual SMBHs in double-peaked NL AGN—i.e. two well-separated, observable NLRs in relative motion—occurs for only a small fraction of the kpc-scale phase. Instead, SMBH orbital motion and gas kinematics may be combined in a variety of ways to produce the observed double-peaked profiles, such that the population of dNL AGN is quite heterogeneous. Observations indicate that a minority of dNL AGN show clear evidence of association with dual brightness peaks in imaging. Therefore, we may ask the question of whether double-peaked NL signatures are a good tool for identifying dual SMBHs. In relative terms, studies of dNL AGN have certainly proved to be an *effective* means of finding good dual SMBH candidates; the number of strong candidates has greatly increased via follow-up observations. Less obvious is whether observing dNL AGN is an *efficient* means of identifying dual SMBHs.

Certainly our results demonstrate that the population of dNL AGN as dual SMBH candidates should contain many false positives and negatives. However, no alternative feature of SMBH pairs emerges from the simulations as a clear, unambiguous signature of their dual nature. Because SMBH pairs may be associated with dNL AGN even on sub-kpc scales or in apparently undisturbed galaxies, we expect some of the currently ambiguous dNL AGN candidates to contain dual SMBHs. A dedicated effort will be required, however, with multi-wavelength follow-up and the use of multiple lines of evidence, including the signatures discussed in this work, in order to Identify the true SMBH pairs.

Chapter 5

Constraints on the Nature of CID-42: Recoil Kick or Supermassive Black Hole Pair?

L. Blecha, F. Civano, M. Elvis, & A. Loeb

Abstract

The galaxy COSMOS J100043.15+020637.2, also known as CID-42, is a highly unusual object. An apparent galaxy merger remnant, it displays signatures of both an inspiraling, kiloparsec-scale active galactic nucleus (AGN) pair and of a recoiling AGN with a kick velocity $\gtrsim$ 1300 km s^{-1}. Among recoiling AGN candidates, CID-42 alone has both spatial *and* spectroscopic offsets. In order to constrain the relative likelihood of both scenarios, we develop models using hydrodynamic galaxy merger simulations coupled

with radiative transfer calculations. Our gas-rich, major merger models are generally well matched to the galactic morphology and to the inferred stellar mass and star formation rate. We show that a recoiling supermassive black hole (SMBH) in CID-42 should still be observable as at least a low-luminosity AGN at the time of observation. However, in order for the recoiling AGN to produce narrow-line emission, it must be observed shortly after the kick while it still inhabits a dense gaseous region, implying a large total kick velocity ($\sim$ 2000 km s^{-1}). For the dual AGN scenario, an unusually large broad line offset is required, and the best match to the observed morphology requires a galaxy and AGN that are somewhat less luminous than CID-42. Further, the lack of X-ray emission from one of the two optical nuclei is likely not due to an intrinsically quiescent SMBH or a Compton-thick galactic environment, though obscuring material close to the SMBH cannot be ruled out. While the current data do not allow either the recoiling or the dual AGN scenario for CID-42 to be excluded, our models highlight the most relevant parameters of the system for distinguishing these possibilities with future observations. In particular, high-quality, spatially-resolved spectra that can pinpoint the origin of the broad and narrow line features will be critical for determining the nature of this unique source.

5.1 Introduction

Recent breakthroughs in numerical relativity have allowed for fully general-relativistic simulations of black hole (BH) mergers, including calculations of gravitational waveforms and kick velocities from gravitational-wave (GW) recoil (e.g., Pretorius 2005; Campanelli et al. 2007a; Baker et al. 2008). Surprisingly, these simulations have found that GW

recoil kicks may be quite large, up to ~ 5000 km s^{-1} (Campanelli et al. 2007b; Lousto & Zlochower 2011a). Thus, the merged supermassive black hole (SMBH) may be ejected from its host galaxy in some cases, and kick velocities of even a few percent of this maximum could be of astrophysical relevance. This discovery has prompted many studies of the possible electromagnetic (EM) signatures from recoiling SMBHs as well as observational searches for such objects.

While prompt EM signatures from SMBH mergers are of great interest for identifying counterparts to eventual GW detections, long-lived signatures such as offset AGN provide the best chance of finding recoiling SMBHs using purely EM observations. An accreting SMBH ejected from the center of a galaxy can carry along its accretion disk as well as the broad-line region, which could produce an AGN spatially offset from its host galaxy or an AGN with offset broad emission lines (Madau & Quataert 2004; Loeb 2007; Blecha & Loeb 2008; Komossa & Merritt 2008a). In either case the offset AGN lifetimes may be up to tens of Myr for a fairly wide range in kick speeds (Blecha et al. 2011). To date, several candidate recoiling SMBHs have been found with either spatial offsets (Batcheldor et al. 2010; Jonker et al. 2010) or kinematic offsets (Komossa et al. 2008; Shields et al. 2009b; Robinson et al. 2010), though none have been confirmed (see Komossa (2012) for a review).

Recent years have also seen renewed energy in the search for inspiraling pairs of SMBHs. Systematic searches revealed that about 1% of AGN have double-peaked narrow [OIII] lines, which could be a signature of SMBH orbital motion on kiloparsec scales (Comerford et al. 2009b; Liu et al. 2010b; Smith et al. 2010). Follow-up observations using higher-resolution imaging and slit or integral field unit (IFU) spectra have identified many strong dual AGN candidates (Liu et al. 2010a; Shen et al. 2011; Fu et al. 2011a,b;

McGurk et al. 2011; Rosario et al. 2011; Comerford et al. 2011b), and in two cases, evidence for dual compact X-ray (Comerford et al. 2011a) and radio (Fu et al. 2011c) sources, respectively, has been found. Shen et al. (2011) estimate that at least 10% of double-peaked NL AGN may actually contain dual SMBHs.

Among these new data and interpretations of SMBHs in merging galaxies, the galaxy COSMOS J100043.15+020637.2 (also known as CID-42; $z = 0.359$) is a fascinating case. Discovered serendipitously by Comerford et al. (2009a, hereafter JC09) based on the striking morphology evident in its COSMOS *HST*/ACS image, it is an apparent face-on spiral with a prominent tidal tail and two well-resolved brightness peaks in its center, separated by 2.46 kpc (Figure 5.1a). The disturbed morphology strongly indicates a recent galaxy merger. DEIMOS slit spectroscopy revealed dual emission components in three different narrow lines (NLs) with a velocity separation of ~ 150 km s^{-1} and a spatial offset roughly consistent with the separation of the two brightness peaks in the image, albeit with low signal-to-noise (S/N, JC09). No evidence for broad lines (BLs) is apparent in this spectrum. Thus, JC09 conclude that CID-42 is a good candidate for a kpc-scale, Type 2 AGN pair.

Around the same time, CID-42 was also identified as an unusual object during visual inspection of the optical counterparts to *Chandra*-COSMOS sources (Elvis et al. 2009). Civano et al. (2010, hereafter FC10) also found that optical spectra from IMACS/Magellan (Trump et al. 2007, 2009) and VIMOS/VLT (zCOSMOS; Lilly et al. 2007) show a prominent broad Hβ line that was not detected in the DEIMOS spectrum. More interestingly, the broad and narrow Hβ components are *offset* by ~ 1360 km s^{-1}. The double-peaked narrow lines seen in the DEIMOS spectrum would be unresolved in these spectra, which have higher S/N but lower spectral resolution. There is also no

measurable spatial offset between the broad and narrow emission components, though this may be attributable to seeing conditions (FC10).

A BL/NL offset of 1360 km s^{-1} is much too large to be explained by orbital motion of dual AGN on kiloparsec scales. As this is in fact a signature expected from a recoiling AGN, FC10 proposed that CID-42 may contain a single, rapidly-recoiling SMBH rather than two inspiraling SMBHs. In this scenario, one of the brightness peaks in the *HST* image corresponds to the recoiling AGN, and the other corresponds to the stellar cusp left behind in the galactic center. A surface brightness decomposition performed by FC10 is consistent with this picture, in that the SE source (the purported recoiling AGN) is best fit as a point source, while the NW source (the purported empty stellar cusp) is best fit as an extended Sersic component (see Figure 5.1a).

Still more intriguing evidence comes from High-Resolution Chandra observations (Civano et al. 2012, , hereafter FC12), which reveal that the X-ray emission detected in CID-42 arises from only the SE source, with an upper limit of 4% of the observed X-ray flux from the NW source. This finding supports the recoil scenario for CID-42, in which only one of the optical brightness peaks contains an AGN, but does not rule out the possibility of a quiescent or Compton-thick AGN.

Another possibility discussed by FC10 is a gravitational *slingshot* recoil resulting from a triple-SMBH interaction. This may occur if the binary SMBH inspiral time is long enough that the host galaxy undergoes a subsequent merger in the meantime, bringing a third SMBH into the system. We focus on GW recoil in our modeling, on the grounds that a triple-SMBH interaction is most likely in a gas-poor merger remnant, unlike CID-42. Nonetheless, a slingshot recoil cannot be ruled out by the observations.

Much of our analysis for the GW recoil and the inspiraling SMBH pair scenarios can be applied to a slingshot recoil, as this corresponds to the case in which the NW source contains an AGN (or a close binary AGN) *and* the SE source contains a rapidly-recoiling SMBH. This is discussed further in § 5.3.1.

As CID-42 displays signatures of both dual and recoiling AGN, and because it is the only recoil candidate with evidence for both spatial and kinematic offsets, this object is an ideal case study for theoretical models. Blecha et al. (2011) have conducted a large parameter study of recoiling SMBHs in hydrodynamic simulations of galaxy mergers, which allowed them to estimate observable lifetimes of spatially- and kinematically-offset recoiling AGN for a wide range of kick velocities and merging galaxy parameters. Here, we use hydrodynamic simulations to constrain the possible parameters of a recoiling or binary AGN in CID-42 and to gain insight about the relative plausibility of these scenarios. We provide models for both a GW-recoiling AGN and for an AGN pair, based on the methods of Blecha et al. (2011) and Blecha et al. (2012).

The details of our simulations are outlined in § 5.2.1. We describe the properties of our best-fit recoiling SMBH simulations in § 5.2.2, and those of our best-fit dual SMBH simulation in § 5.2.3. In § 5.3.1-5.3.3, we discuss the plausibility of the recoiling and dual AGN scenarios, and we briefly summarize in § 5.3.4.

5.2 Models

5.2.1 Initial Conditions and Merger Simulations

To model the possible origins of CID-42, we begin by simulating a major galaxy merger using the smoothed-particle-hydrodynamics (SPH) code GADGET-3 (Springel 2005). Each progenitor galaxy contains dark matter, star, and gas particles, as well as an accreting, central massive SMBH. GADGET-3 also contains sub-resolution models for star formation and for supernova and AGN feedback.

We have designed simulations for both the GW recoil and dual SMBH scenarios that match as closely as possible the observed properties of CID-42. Specifically, the progenitor galaxies have a mass ratio of $q = 0.5$, and the primary galaxy has a total (baryonic) mass of 4.5×10^{11} $M_\odot$ (1.9×10^{10} $M_\odot$). Because star formation occurs throughout the simulation, the initial baryonic mass is chosen such that by the time the system would be observed, near the time of SMBH merger, the stellar mass matches that inferred for CID-42 ($\sim 2.5 \times 10^{10}$ $M_\odot$, FC10). The galaxies are disk-dominated with 10% of the initial stellar mass in a bulge component. For the recoiling (dual) SMBH model, the initial gas fraction in the disk ($f_{\rm gas}$) is 0.5 (0.4). The slightly lower gas content in the latter results in a more relaxed galaxy morphology prior to the SMBH merger, consistent with observations.

Each SMBH particle has an initial dynamical mass of 10^{-4} the total mass. The initial "seed" mass (onto which accretion is calculated smoothly via the Bondi-Hoyle-Lyttleton formula) is 7×10^5 $M_\odot$ for the recoil model and 10^6 $M_\odot$ for the dual SMBH model. The BH and star formation prescriptions are described in more detail in Springel et al.

(2005b).

In the event of a high-velocity GW recoil kick, the Bondi accretion rate ($\propto \rho_{\rm gas}/v_{\rm BH}^3$) drops precipitously. Accretion onto the recoiling SMBH instead becomes dominated by the gas that remains bound to the SMBH. We adopt the "ejected-disk" model described in Blecha et al. (2011), in which the gas ejected along with the SMBH is modeled as an isolated accretion disk with a monotonically decreasing accretion rate normalized to the Bondi rate at the time of the kick.

Assuming a minimum Eddington ratio, $f_{\rm AGN} = \dot{M}_{\rm AGN}/\dot{M}_{\rm Edd}$ for the recoiling SMBH to be observable as an AGN, then the observable lifetime of the SMBH is given by

$$t_{\rm AGN} = \frac{3}{16}\ \frac{M_{\rm BH}}{\dot{M}_{\rm Edd}}\ \frac{f_{\rm M_{BH},ej}}{f_{\rm Edd,mrg}} \left[\left(\frac{f_{\rm AGN}}{f_{\rm Edd,mrg}} \right)^{-16/19} - 1 \right], \tag{5.1}$$

where $f_{\rm M_{BH},ej}$ is the initial mass of the ejected disk and $f_{\rm Edd,mrg}$ is the Eddington ratio at the time of SMBH merger. ($M_{\rm BH}$ and $\dot{M}_{\rm Edd}$ are time-dependent but change negligibly over the timescales with which we are concerned.)

In order to compare our hydrodynamic models more directly with observations, we have employed the three-dimensional, polychromatic dust radiative transfer code SUNRISE (Jonsson et al. 2010). The *HST*/ACS (F814W) image of CID-42 is shown in Figure 5.1a, along with SUNRISE images in the same band for our GW recoil model (Figure 5.1b) and dual SMBH model (Figure 5.1b). Recall that in the GW recoil scenario, only one (post-merger) SMBH is present in CID-42, as opposed to the two SMBHs present in the latter model. Figures 5.1b & c show the mergers at the time of observation ($t_{\rm obs}$), i.e. when the spatial offset (and for the recoil, the velocity offset) of the SMBH(s) match the observed values. Although the recoiling SMBH position is marked in Figure 5.1b, the ejected-disk luminosity is not accounted for in the image,

Figure 5.1.—: (Following page.) Comparison of 9" × 9" *HST*/ACS image of CID-42 (*a*, Figure 3 from FC10) with simulated broadband (F814W) images of our best-fit recoiling (*b*) and dual (*c*) SMBH models. The orientation of the NW and SE optical brightness peaks is labeled in *(a)*; north is up, east is to the left. The simulated images were generated with the radiative-transfer code SUNRISE and have the same spatial and pixel scale (0.03"/pixel) as the HST image. They are shown at the time of observation ($t_{\rm obs}$), i.e. when the spatial and velocity offsets of the BH match the observed values. The GW recoil model shown has $v_{\rm k} = 1428$ km s^{-1} and $t_{\rm obs} = t_{\rm mrg} + 5.9$ Myr, though the galactic morphology is essentially identical in the model with $v_{\rm k} = 2470$ km s^{-1} and $t_{\rm obs} = t_{\rm mrg} + 1.3$ Myr. The BH is offset from the stellar density peak by 2.5 kpc. In the dual BH model, $t_{\rm obs}$= $t_{\rm mrg} - 50$ Myr and the two BHs are separated by 2.5 kpc.

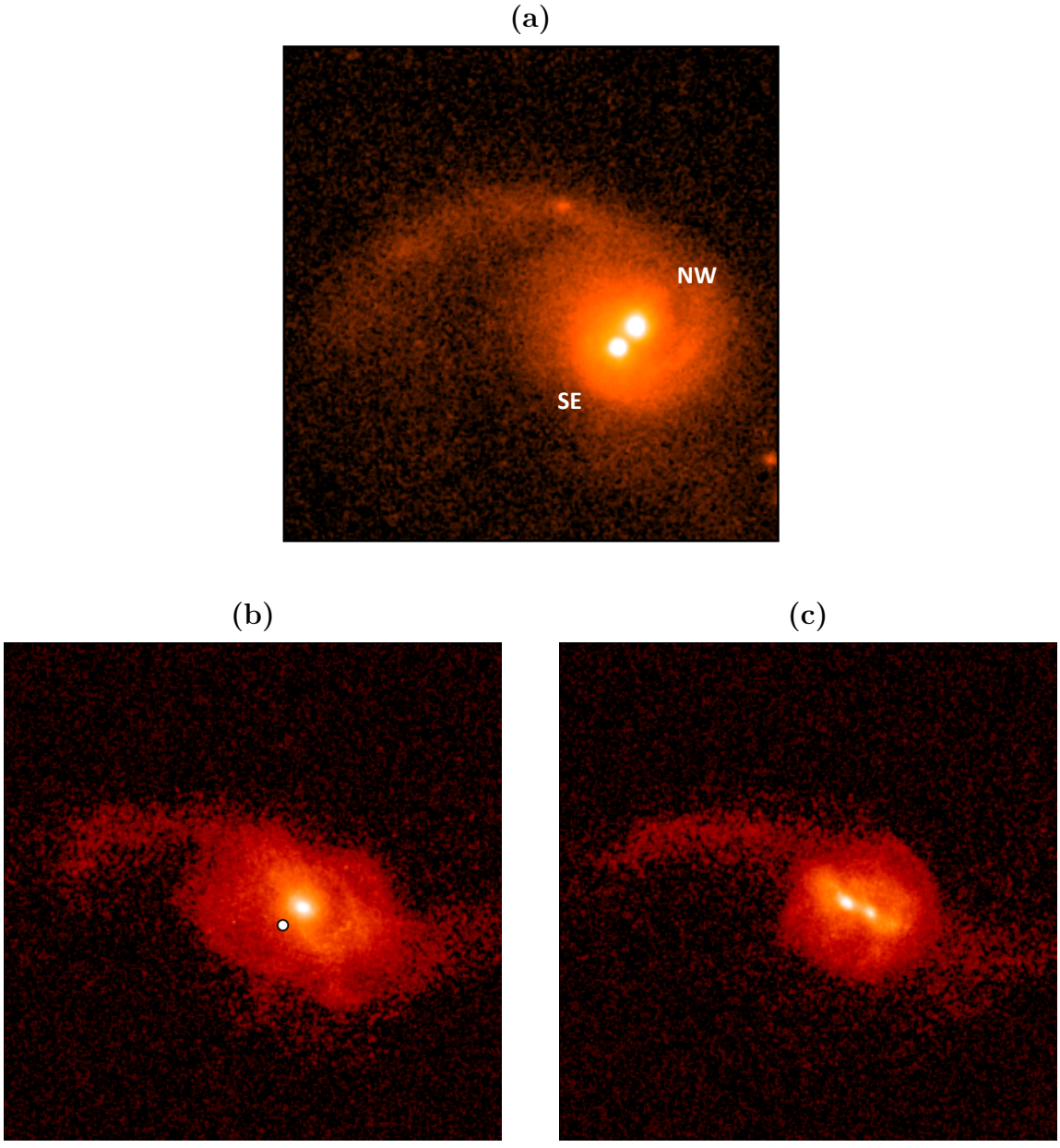

Figure 5.1.—: (Continued)

so there is no observable excess of emission from this point. In the dual SMBH model (Figure 5.1c), the SMBH positions correspond to the two central brightness peaks.

The galactic morphology of each model is broadly similar to the observed morphology. While these models are not unique solutions, they have a few generic properties. For example, the prominent asymmetric tidal feature can arise in the late stages of a major, but unequal-mass merger, such as the $q = 0.5$ mergers shown here. Fainter tidal features can also be seen in the lower-right (SW) edge of both the observed and simulated images. Some differences between the two models can be seen as well. The merger remnant with dual SMBHs has a somewhat "rounder" morphology than does the remnant with a recoiling SMBH. However, the bolometric luminosity of the recoil model ($L_{\rm bol} \sim 2.5 \times 10^{11}$ L$_\odot$) is closer to that inferred for CID-42 from SED fitting ($L_{\rm bol} \sim 2.9 \times 10^{11}$ L$_\odot$). In the dual SMBH model, $L_{\rm bol}$ is only $\sim 6.5 \times 10^{10}$ L$_\odot$. Table 5.1 summarizes the relevant physical parameters of our models in comparison to those inferred from observations of CID-42.

Fig. 5.2 shows the merger evolution of various quantities for both the recoil model (black curves) and the dual SMBH model (red curves). Because the SFR inferred from SED fitting is ~ 25 M$_\odot$ yr^{-1}, the models require a starburst that more or less coincides with $t_{\rm obs}$. Similarly, the estimated bolometric ($L_{24\mu{\rm m}-{\rm UV}}$) luminosity of the SE source, assuming it is a Type 1 AGN, is 7.3×10^{10} L$_\odot$, or $\sim 4\%$ L$_{\rm Edd}$ for an estimated SMBH mass of 6.5×10^7 M$_\odot$ (FC10). Thus, the SMBHs are also near their peak luminosity at the time of the SMBH merger. The presence of a stellar bulge in the progenitor galaxies acts to stabilize the gas and stellar disks against perturbations such that the strongest gas inflow is delayed until the galaxies' final coalescence (e.g., Mihos & Hernquist 1996). The high initial gas content in the progenitor galaxies (40-50% of the disk mass) is also

		Model				
Quantity	**Units**	**high-$v_{\rm k}$**	**low-$v_{\rm k}$**	**dual SMBH**		**CID-42**
$v_{\rm k}$	[km s^{-1}]	2470	1428		–	–
$v_{\rm LOS}/v_{\rm k}$	–	0.58	0.81		–	–
$v_{\rm LOS}(t_{\rm obs})$	[km s^{-1}]	1360	1180		–	–
$t_{\rm obs}-t_{\rm mrg}$	[Myr]	+1.3	+5.9		−50	–
$M_{\rm star}$	[10^{10} M$_\odot$]	2.4	2.4		2.3	2.5
$M_{\rm gas}$	[10^{10} M$_\odot$]	0.43	0.43		0.53	–
SFR	[M$_\odot$ yr^{-1}]	21	21		6.3	25
$L_{\rm bol}$	[10^{10} L$_\odot$]	24.1	25.6		6.5	28.6
$L_{24\mu{\rm m}}$	[10^{10} L$_\odot$]	10.0	11.0		1.4	3.2
				BH1	**BH2**	**SE**
$M_{\rm BH}$	[10^7 M$_\odot$]	0.98	0.97	0.45	0.21	6.5
$L_{\rm bol,BH}$	[10^{10} L$_\odot$]	0.50	0.32	0.12	0.89	7.3

Table 5.1:: Relevant parameters of recoiling and dual SMBH models for CID-42, along with the parameters inferred from observations (from FC10 and FC12). $v_{\rm k}$ denotes the total kick velocity imparted to the merged SMBH for the recoil models; all other quantities are calculated at the time of observation ($t_{\rm obs}$). The galactic $L_{\rm bol}$ and $L_{24\mu{\rm m}}$ for each model are obtained from radiative transfer calculations with SUNRISE. For the dual SMBH model, $M_{\rm BH}$, $L_{\rm bol,BH}$, and the local number density $n_{\rm gas,BH}$ are given for each SMBH. The $M_{\rm BH}$ and $L_{\rm bol,BH}$ estimated for the SE optical source in CID-42 (FC10) are given in the last column.

important for fueling star formation and SMBH growth.

The dual and recoiling SMBH models have very similar evolution, but because $t_{\rm obs}$ in the dual SMBH model necessarily occurs some time prior to the SMBH merger ($t_{\rm mrg}$ -50 Myr in our case), the system is observed before the peak SFR and $\dot{M}_{\rm BH}$. Specifically, the SFR at $t_{\rm obs}$ in the dual SMBH model is ~ 6 M$_\odot$ yr^{-1}, versus ~ 21 M$_\odot$ yr^{-1}for the recoil model. The SMBH accretion rates follow a similar trend, though in the case of GW recoil, $\dot{M}_{\rm BH}$ is dominated by ejected-disk accretion and declines relatively quickly after the kick. At $t_{\rm obs}$, $\sim$ 50 - 70% of the gas has been consumed. The remaining gas mass, ~ 4 – 5×10^9 M$_\odot$, might be detectable, and an estimate of its neutral fraction obtained, via CO or 21cm observations.

Our simulated merger remnants are consistent with being luminous infrared galaxies (LIRGs), as is CID-42. However, our spectra are also more IR-dominated than the observed SED, with $L_{24\mu m}/L_{\rm bol} \sim 0.2$ and 0.4 for the dual and recoiling SMBH models, respectively, compared with $L_{24\mu m}/L_{\rm bol} \sim 0.1$ for the Seyfert 1.8 SED fit to CID-42. As our merger models were designed to fit the remnant stellar mass, morphology, and SFR at the time of observation, this might mean that the SF history or dust model parameters for our simulations differs from reality, such that more obscuring dust was generated earlier in the merger, or it could indicate that the SFR inferred for CID-42 is an overestimate. We discuss the implications of this discrepancy for our interpretations in § 5.2.3.

Figure 5.2.—: (Following page.) Time evolution of relevant quantities throughout the galaxy merger for our best-fit recoiling SMBH (black curves) and dual SMBH (red curves) models. Note that the quantity $t-t_{\rm mrg}$ is plotted on the x-axis; each model has slightly different $t_{\rm mrg}$. From top to bottom, the panels show the total BH accretion rate, the global star formation rate (SFR), the total gas mass, and the BH separation prior to BH merger. In each panel, the dot-dashed red line denotes $t_{\rm obs}$ for the dual SMBH model, the black dashed line denotes $t_{\rm obs}$ for the recoiling SMBH model with $v_{\rm k}$= 1428 km s^{-1}, and the solid blue line denotes $t_{\rm mrg}$.

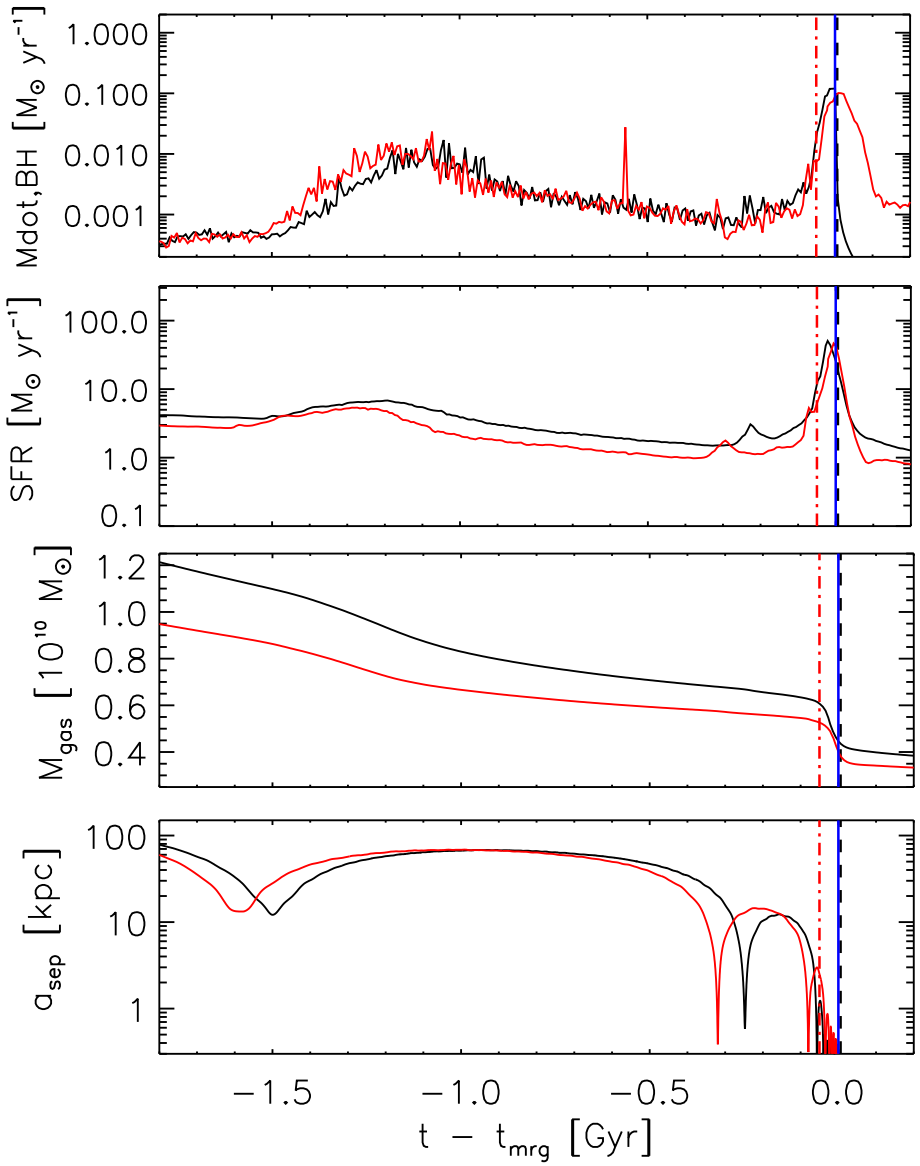

Figure 5.2.—: (Continued)

5.2.2 Recoiling SMBH Model

In our recoil simulations, the central escape speed from the merger remnant at the time of the SMBH merger is 773 km s^{-1}. If the $\sim$ 1300 km s^{-1} offset between the broad and narrow emission lines in CID-42 corresponds to a GW recoil velocity, then $v_{\rm k} \gg v_{\rm esc}$. Thus, a recoiling SMBH in CID-42 must have been kicked recently.

The kick velocity has two free parameters: the fraction of the total kick directed in the line of sight, and the amount of the measured 1360 km s^{-1} BL/NL offset that is due to the motion of the SMBH. Specifically, if the NL emission originates from the NW source and the BL emission from the SE, then a spatial-offset correction must be applied to the measured velocity offset, such that the actual BL/NL velocity offset would be 1180 km s^{-1} (FC10).

We consider models for two different kick speeds. The "low" kick, $v_{\rm k}$ = 1428 km s^{-1}, corresponds to $(v_{\rm LOS}/v_{\rm k})^2 = 0.9$ and $v_{\rm LOS}(t_{\rm obs}) = 1180$ km s^{-1}, and the "high" kick, $v_{\rm k}$ = 2470 km s^{-1}, corresponds to $(v_{\rm LOS}/v_{\rm k})^2 = 1/3$ and $v_{\rm LOS}(t_{\rm obs}) = 1360$ km s^{-1} (see Table 5.1). Note that although $v_{\rm k} \gg v_{\rm esc}$, there is a small difference between $v_{\rm LOS}(0)$ and $v_{\rm LOS}(t_{\rm obs})$ in each case owing to deceleration. We choose these values of $v_{\rm k}$ because velocities lower than $\sim$ 1400 km s^{-1} would require the kick to be oriented almost entirely along the LOS, and velocities substantially higher than $\sim$ 2500 km s^{-1} would have a very small probability of occurring. These probabilities are discussed further in § 5.3.1, but we note that both the "low" and "high" kick velocities are quite large in absolute terms.

For the low kick, $t_{\rm obs}$ occurs 5.9 Myr after the recoil. The mass of ejected gas disk is $\sim 1.4\%\ M_{\rm BH}$ according to our model, and $L_{\rm bol,BH} = 0.56 L_{\rm Edd}$ at the time of the kick. At $t_{\rm obs}$, the AGN luminosity has declined to 1% $L_{\rm Edd}$, or 3.2×10^9 L$_\odot$ (assuming a radiative

efficiency of 0.1). For the high kick, a gas mass of only $\sim 0.5\%$ $M_{\rm BH}$ remains bound to the recoiling SMBH. However, because $t_{\rm obs}$ is only 1.3 Myr after the kick, the AGN luminosity is slightly higher at $t_{\rm obs}$ than for the low kick: 5×10^9 $L_\odot$ (1.6% $L_{\rm Edd}$). These values are summarized in Table 5.1. While the AGN luminosities in each case are lower than that estimated for CID-42 via SED fitting (FC10), the inferred Eddington ratios of the order of $\sim 1\%$ are consistent.

The relationships between $t_{\rm obs}$, $t_{\rm AGN}$, and $v_{\rm k}$ are illustrated in Fig. 5.3. For the low-luminosity AGN definition ($L_{\rm bol,BH} > 3 \times 10^9$ $L_\odot$), the AGN lifetimes of the recoiling BHs as defined in Eqn. 5.1 are 2.3 Myr and 6.4 Myr for the low and high kicks, respectively; i.e., both have $t_{\rm AGN} > t_{\rm obs}$. In fact, for the observed parameters of CID-42, virtually *all* allowed values of $v_{\rm k}$ and $t_{\rm obs}$ result in a low-luminosity recoiling AGN with $t_{\rm AGN} > t_{\rm obs}$. Thus, the fuel supply to the SMBH is probably not a limiting factor for the recoiling AGN scenario. Furthermore, because the AGN luminosity and SMBH mass in our recoil models are somewhat lower than the values inferred for the SE source, the AGN lifetimes as defined by a minimum luminosity (rather than a minimum Eddington fraction) should be even longer.

Another key consideration is whether the recoiling AGN is able to ionize gas and produce NL emission as it leaves the galaxy. Based on the current data, it is unclear whether the NL emission is coming from the SE or NW source. However, this will be constrained in the near future via individual *HST* spectra of each source (Civano et al. 2012b, in preparation), so it is important to know whether a recoiling AGN might be capable of producing the observed emission lines.

Figure 5.3.—: (Following page) The time at which the system is observed ($t_{\rm obs}$, solid black line) and the post-recoil AGN lifetime ($t_{\rm AGN}$, colored lines) are plotted for various total and LOS velocities ($v_{\rm k}$ & $v_{\rm LOS}$). $t_{\rm obs}$ is calculated assuming no deceleration, a spatial offset of 2.46 kpc, and a LOS velocity offset at $t_{\rm obs}$, ($v_{\rm LOS}(t_{\rm obs})$), of either 1180 km s^{-1} (*top plot*) or 1360 km s^{-1} (*bottom plot*), corresponding to the possible values discussed in the text. ($v_{\rm LOS}(t_{\rm obs})$) is shown as the dashed horizontal lines in each plot and represents a hard lower limit on the total kick speed. The colored solid lines correspond to $t_{\rm AGN}$ for three definitions of the minimum AGN luminosity, as indicated in the plot legend. The points marked along each solid line indicate different values of $v_{\rm LOS}/v_{\rm k}$ from 0.2-0.9 in intervals of 0.1. The dotted lines show to the upper limit on $t_{\rm AGN}$, which assumes $\dot{M}_{\rm BH} = \dot{M}_{\rm Edd}$ at $t_{\rm mrg}$. Note that while the brighter AGN phases do not last until $t_{\rm obs}$, the low-luminosity AGN lifetimes extend *beyond* $t_{\rm obs}$ for almost all $v_{\rm k}$. The solid red triangle in each plot corresponds to $t_{\rm obs}$ for the kick given in the simulation, assuming no deceleration. Because a small amount of deceleration does occur, we set the actual kicks to be slightly higher, such that with deceleration, the open triangles denoting the actual BH velocity at $t_{\rm obs}$ match the desired values.

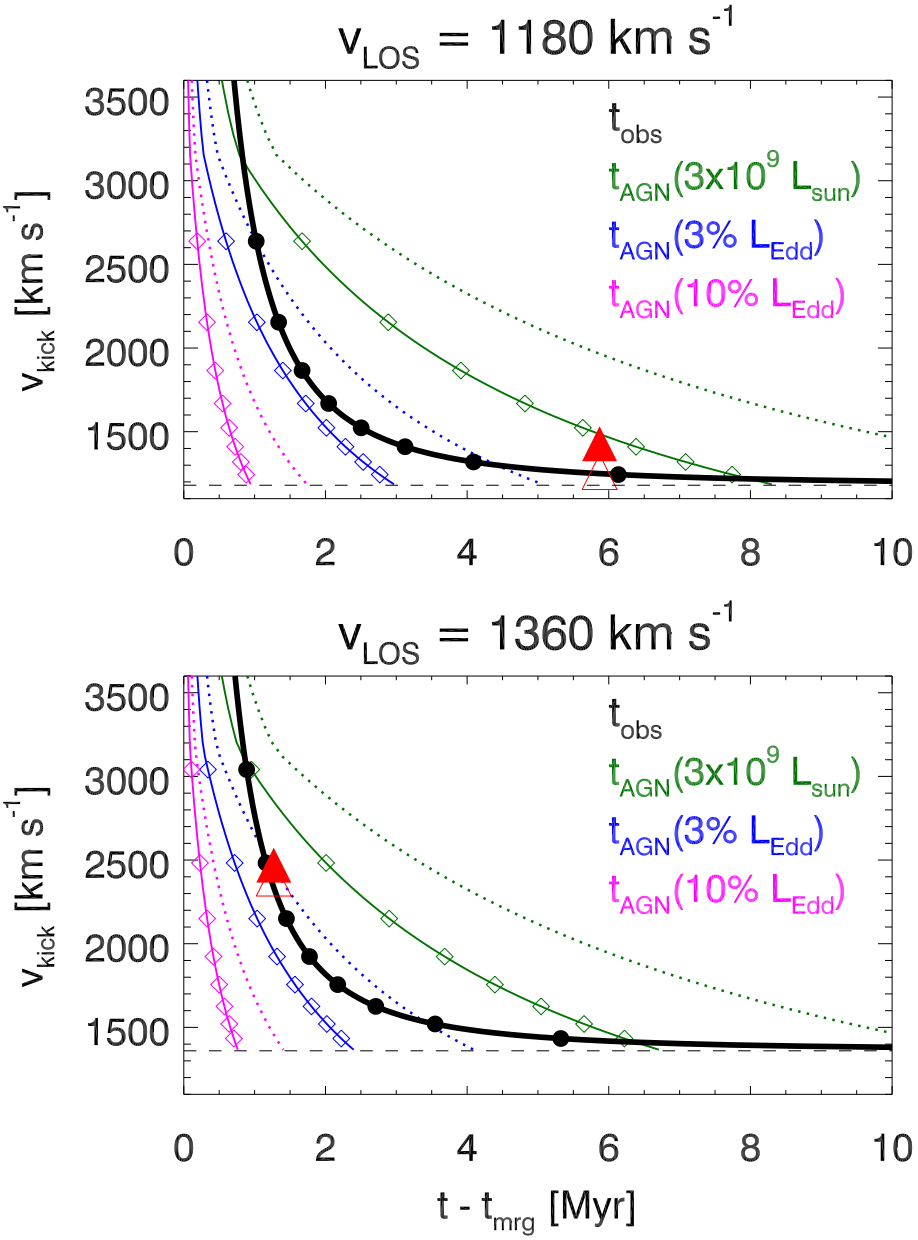

Figure 5.3.—: (Continued)

Figure 5.4.—: (Following page.) Map of gas column density from side view for our best-fit recoiling SMBH models, shown at the time of observation ($t_{\rm obs}$), i.e. when the spatial and velocity offsets of the BH match the observed values. In each case, the black & white dot denotes the position of the BH, and the "eye" symbol denotes the observer's LOS. The color scale shows the gas density in units of cm^{-2}. *Top plot*: best-fit GW recoil model with $v_{\rm k} = 2470$ km s^{-1}and $t_{\rm obs} = t_{\rm mrg} + 1.3$ Myr. *Bottom plot*: best-fit recoil model with $v_{\rm k} = 1428$ km s^{-1}and $t_{\rm obs} = t_{\rm mrg} + 5.9$ Myr.

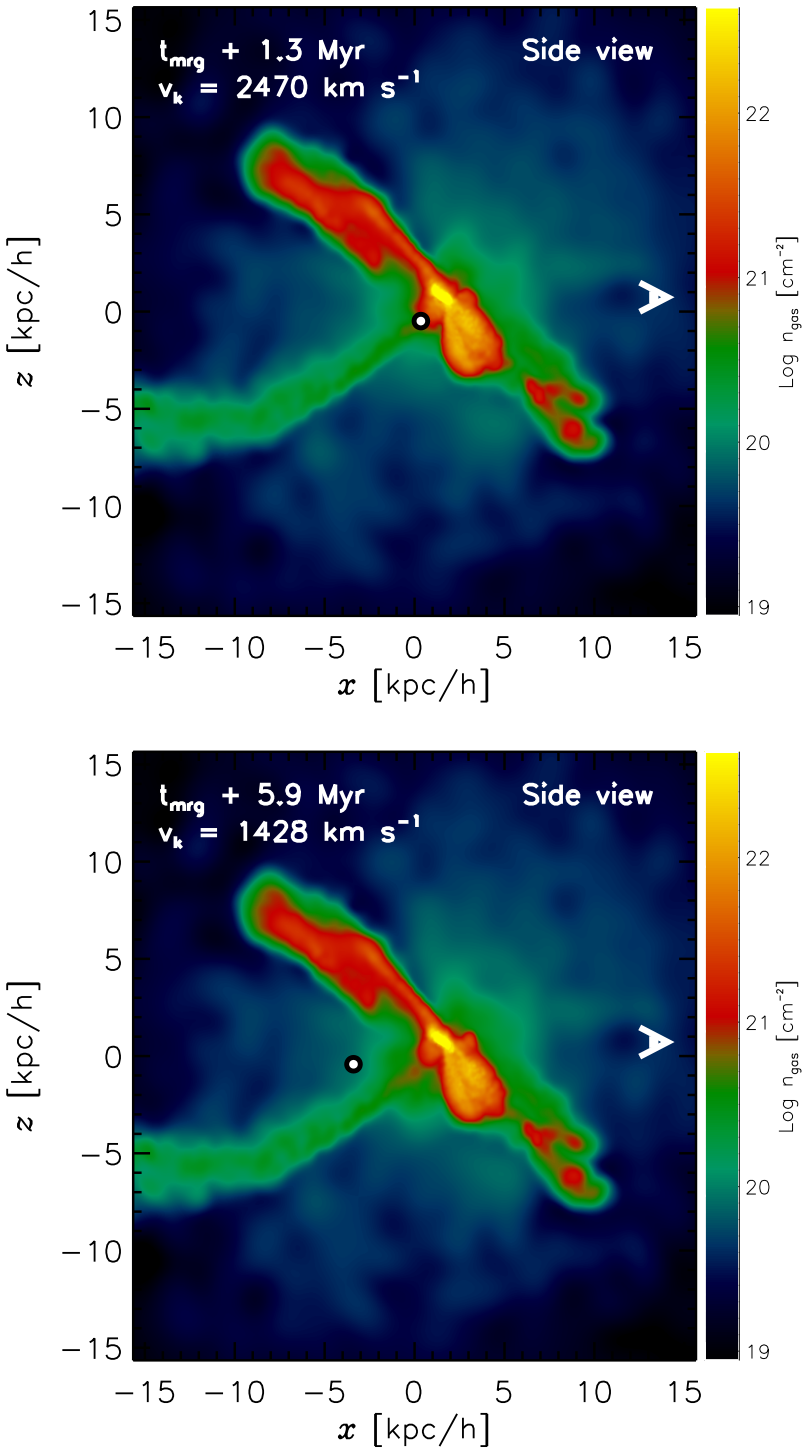

Figure 5.4.—: (Continued)

It is clear from Figure 5.4 that the recoiling SMBH is ejected to a low-gas-density region within at most a few Myr. In both recoil models, all of the gas near the SMBH at $t_{\rm obs}$ is warm and diffuse, with an average temperature of a few $\times 10^5$ K and densities of $10^{-1.5}$ and $10^{-2.5}$ cm^{-3} for the high-kick and low-kick models, respectively. None of this gas is condensed into the "cold" phase of the multiphase model for the interstellar medium (ISM) used in GADGET-3 (Springel & Hernquist 2003). Thus, we would not *a priori* expect any cold clouds to be locally ionized by the recoiling SMBH.

Blecha et al. (2012) have developed a semi-analytic model for estimating the narrow-line emission from the gas around AGN in hydrodynamic simulations of galaxy mergers. We have applied this model to our simulations of recoiling SMBHs in CID-42, including the accretion from the ejected gas disk. In order to estimate the lifetime of observable NL emission, we assume a ratio of the [O III] λ5007 luminosity to the bolometric AGN luminosity of $L_{\rm [OIII]}/L_{\rm bol,BH} = 10^{-3}$. This is the ratio of the total [O III] luminosity to the luminosity of the SE source in CID-42 estimated by FC10. In reality, this ratio may be higher (such that the estimated NL lifetime would be an upper limit), because $L_{\rm [OIII]}$ is measured from the total continuum rather than just the AGN continuum. However, additional uncertainty comes from the fact that $L_{\rm [OIII]}$ is measured from a slit spectrum, whereas $L_{\rm bol,BH}$ is measured in a circular aperture; the direction of this effect is less clear. We therefore consider the ratio 10^{-3} to be a reasonable guess, but not necessarily an upper limit.

The NL model of Blecha et al. (2012) calculates the Hβ rather than the [O III] luminosity, because the former is less sensitive to the conditions in the ISM. Thus, we must also assume an [O III]/Hβ ratio. The ratio estimated from the spectra of CID-42 is ~ 6 (JC09, FC10), so we use a ratio of 10 as a conservative upper limit. This implies a

minimum observable $L_{\mathrm{H}\beta}/L_{bol,BH}$ of 10^{-4}.

In this analysis of the NLR, it is important to account for the $\sim$ order of magnitude difference between the self-consistent AGN luminosities in our simulations and the AGN luminosity of the SE source estimated from its F814W magnitude. Because the recoiling SMBH accretion rate is determined by the fully-analytic ejected disk model after the kick, we may calculate post-recoil AGN luminosities for arbitrary values of $M_{\mathrm{BH}}(t_{\mathrm{mrg}})$, $\dot{M}_{\mathrm{BH}}(t_{\mathrm{mrg}})$, and v_{k}. Taking the values from the simulation, we find that the recoiling AGN can produce NL emission above the estimated minimum value of $3-5\times10^{5}$ $\mathrm{L}_{\odot}$ for only about $1-2$ Myr after the kick, depending on v_{k}. In each case the NL lifetime is shorter than t_{obs}. Note that the recombination time for the photoionized gas is very short, $\lesssim 10^{3}$ yr, such that any observed photoionization of NLRs must be ongoing.

If we instead assume the recoiling AGN has $M_{\mathrm{BH}}(t_{\mathrm{mrg}})= 6.5\times10^{7}$ $\mathrm{M}_{\odot}$ and $L_{\mathrm{bol,BH}} = 7.3\times10^{10}$ $\mathrm{L}_{\odot}$ (the estimates for the SE source in CID-42 assuming it is a Type I AGN, FC10), the NL lifetimes are somewhat longer, despite a stricter minimum Hβ luminosity of 7.3×10^{6} $\mathrm{L}_{\odot}$. Specifically, for the low kick, the NL lifetime is 4.0 Myr—this is still shorter than $t_{\mathrm{obs}} = 5.9$ Myr, so we would not expect the recoiling AGN in this model to produce observable NL emission. In the high-kick model, however, the NL lifetime is 1.6 Myr, compared to $t_{\mathrm{obs}} = 1.3$ Myr. This analysis indicates that a recoiling AGN in CID-42 may be able to produce the observed narrow lines, provided the total kick velocity is sufficiently high ($\sim$ 2000 km s^{-1}).

If the NL emission arises from stellar photoionization in the NW source, the recoiling AGN scenario does not require that the kicked SMBH produce observable NLs. However, the current spectra of CID-42 have AGN-like narrow line flux ratios (JC09). This

suggests that the recoil scenario requires either a large total kick velocity or an unusual star-forming region in the NW source. Alternatively, a recoiling AGN might be able to produce NL emission more locally if the SMBH happened to be ejected along a dense tidal stream or if the galactic line-of-sight gas distribution differs substantially from that of our model.

Finally, we note that the total LOS gas column density to the position of the BHs is low; $\log N_{\rm gas} \approx 20.8 - 20.9$ cm^{-2}. Thus, attenuation is insignificant along the LOS to the recoiling AGN, even though it is recoiling *away* from the observer (as inferred from the redshifted broad Hβ line).

5.2.3 Dual SMBH Model

In our dual SMBH model, $t_{\rm obs}$ occurs 50 Myr prior to the SMBH merger, when the projected SMBH separation is 2.5 kpc. The slightly less dissipative merger in this model is key to reproducing the observed morphology prior to the SMBH merger. If we simply examine the pre-merger snapshot from the recoil model in which the SMBHs have a projected separation of 2.5 kpc, we find that the galaxy is substantially more disturbed, with multiple prominent tidal features and a more compact and asymmetric core.

The SMBH masses at $t_{\rm obs}$ are 4.5×10^6 M$_\odot$ and 2.1×10^6 M$_\odot$. Thus, each SMBH is more than a factor of ten smaller than the estimated mass of the SE source in CID-42. The accretion rates in this snapshot are just beginning to rise to their peak values. The less massive SMBH is actually *more* luminous, with $\dot{M} = 13\% \dot{M}_{\rm Edd}$ and $L_{\rm bol,BH} = 8.9 \times 10^9$ erg s^{-1}. As in the recoil model, this is still lower than the AGN luminosity inferred for the SE source in CID-42 (see Table 5.1). The more massive

SMBH is accreting at only 0.8% $\dot{M}_{\rm Edd}$, which corresponds to a bolometric luminosity $L_{\rm bol,BH} = 1.2 \times 10^9$ erg s^{-1}. Notably, this lower-luminosity AGN is consistent with the upper limit on the X-ray luminosity for the NW source of CID-42 ($L_{\rm X} < 10^{42}$ erg s^{-1}), so this alone does not place constraints on whether it may contain a SMBH.

However, because the more luminous AGN in our model is about eight times fainter than the AGN luminosity inferred for the SE source in CID-42, the AGN luminosity *ratio* in our model may be more informative than the absolute luminosities. In CID-42, the measured F814W luminosity ratio of the NW and SE sources is ~ 2.5, with the NW source being brighter (FC10). Given the uncertainty as to whether an AGN exists at all in the NW source, this tells us little about the limits on the possible *AGN* luminosity ratio. Instead, we may compare the limit on X-ray emission from the NW source with the bolometric luminosity ratio of our simulated AGN. Luminosity ratios greater than 25 correspond to the 4% upper limit on the fraction of hard X-ray flux originating in the NW source (FC12). In the kpc-scale phase of our simulation (defined loosely as SMBH separations < 10 kpc), the AGN luminosity ratio is above 25 for $\lesssim 1\%$ of the time, and not at all for separations < 5 kpc. At $t_{\rm obs}$, the luminosity ratio of the two AGN is 7.5. This suggests that an AGN pair with an *intrinsically* large luminosity ratio is a possible but relatively unlikely explanation for the lack of X-ray emission from the NW optical source of CID-42.

We must also consider that a highly *obscured* AGN could be present in the NW source. Given the lack of detection of hard ($2 - 10$ keV) X-rays from this location, an obscured AGN here would have to be Compton thick ($\log N_{\rm H} > 24$ cm^{-2}). The total LOS gas column densities to the SMBHs in our model are $\log N_{\rm gas} \approx 23.8$ & 22.1 cm^{-2} for the more and less luminous SMBHs, respectively. The column density of the more

luminous AGN is near the Compton-thick limit, though these numbers should not be taken at face value. The Compton-thick limit refers to the equivalent neutral hydrogen column density of the gas, which depends on the ionic fraction of each element, whereas we obtain the total gas column density from our simulations. Our column densities therefore represent an upper limit on $N_{\rm H}$ as thus defined. Further, the fact that the more intrinsically luminous AGN is hosted in the more obscured density cusp works against the need for a large emergent luminosity ratio in the hard X-ray band.

Strong Fe Kα absorption is also expected in heavily obscured X-ray sources, (those with $\log N_{\rm H} \gtrsim 23$ cm^{-2}). A strong absorption feature is indeed observed in both the *Chandra* and *XMM-Newton* data for CID-42, but its energy is highly variable over four years of observations (FC10). It is implausible that such rapid changes in either ionization state or velocity of the absorbing gas could originate in the ISM, far outside the gravitational potential well of a SMBH.

Additionally, we noted in § 5.2.1 that the SEDs calculated from our models with SUNRISE are more IR-dominated than the SED of CID-42; for the dual SMBH model, $L_{24\mu{\rm m}}/L_{\rm bol}$ is larger by a factor of ~ 2. This indicates that attenuation is likely overestimated in our simulation. Conversely, because the galaxy as a whole is a factor of ~ 4 less luminous than CID-42, a more luminous galaxy could have higher gas densities. Owing to these uncertainties, we cannot rule out the possibility of a Compton-thick AGN in the NW source, but we do not find strong evidence for an AGN obscured by the galactic environment of CID-42. However, many AGN are thought to contain dense, obscuring material on small scales, well below the resolution limit of our simulations. If Compton-thick obscuring clouds fell along our line of sight to the AGN, this could, in principle, "hide" an AGN in the NW source with significant attenuation through the

hard X-ray band.

As with the recoil scenario, we have applied the NL model of Blecha et al. (2012) to our dual SMBH simulation. In this case we wish to know whether the system should appear as a NL AGN, and whether the emission lines may be double-peaked, as indicated by the spectra in JC09. We find that at $t_{\rm obs}$, the lower-luminosity AGN has a peak narrow-Hβ luminosity too low to be observable. The more luminous AGN has a higher ionizing photon flux, but as it also resides in a higher-density region than the first AGN, its ionization parameter is marginally too low. The lack of clear evidence for strong NL emission from these AGN reflects their low luminosities relative to the AGN luminosity of CID-42.

Regardless of the NL luminosities from this AGN pair, their relative LOS velocity in this snapshot is only 64 km s^{-1}. Because this is smaller than the typical FWHM of NLs, it is unlikely that double-peaked emission lines would be resolvable in this case. The LOS velocities for projected SMBH separations of 2-3 kpc range from $\sim 0 - 150$ km s^{-1}. Our model for CID-42 is not a unique solution, so we cannot rule out the possibility that a system with the properties of CID-42 could produce dual AGN with double-peaked NLs. Civano et al. (2012b, in preparation) have obtained a new DEIMOS spectrum of CID-42 with much higher S/N, which will reveal definitively whether the NLs are double-peaked.

5.3 Discussion

5.3.1 GW Recoil Scenario

Several observed features of CID-42 support the scenario that this system contains a single, rapidly-recoiling SMBH. The offset between the broad and narrow emission lines is expected to be a characteristic signature of recoiling AGN. The finding of a single X-ray source coincident with the SE optical brightness peak also supports, and is fully consistent with, the GW recoil scenario (FC12). Additionally, the best-fit surface brightness decomposition performed by FC10 consisted of an extended (Sersic) component for the NW source and a point-like component for the SE source, consistent with a stellar cusp and a recoiling AGN, respectively.

Our models of CID-42 demonstrate that, within the uncertainties, the properties of this system are consistent with a recoiling AGN. We are able to reproduce the morphology and inferred stellar mass of CID-42 in the late stages of a gas-rich, major galaxy merger. The peak SFR and $\dot{M}_{\rm BH}$ occur near the time of SMBH merger, and their values at $t_{\rm obs}$ are consistent with estimates from the observations (SFR ~ 25 M$_\odot$ yr^{-1} & $L_{\rm bol,BH}/L_{\rm Edd} \sim$ few percent, FC10).

Less clear is whether a recoiling AGN could produce the observed NL emission in CID-42. The local gas densities around the recoiling SMBH are too low at $t_{\rm obs}$ to produce a NLR *in situ*. If the total kick velocity is large, such that the system is observed soon after the kick, the recoiling AGN may still be close enough to the dense gaseous region to produce observable NL emission. Specifically, we find that the recoiling AGN in our high-kick model ($v_{\rm k} = 2470$ km s^{-1}) could produce the observed NLs in CID-42, but that

it probably could not do so with a lower kick of 1428 km s^{-1}.

If the total kick velocity is not sufficiently high, then special configurations may be required for the recoiling AGN to produce the NL emission, such as ejection of the SMBH along a dense tidal stream. If the observed NLs originate from star formation in the NW source rather than from the recoiling SMBH, then the recoil scenario requires unusual line flux ratios for a star-forming region. The origin of the NL emission is therefore an important consideration in evaluating the likelihood that CID-42 contains a recoiling AGN, and underscores the need for corroborating evidence. Individual spectra of the NW and SE sources will provide important constraints in this regard (Civano et al. 2012b, in preparation), and IFU data could provide useful information as well about the spatial distribution of narrow (and broad) emission lines in CID-42.

IFU spectra, or HST imaging in multiple bands, would also constrain the colors of the NW and SE sources, and of the galaxy as a whole. Specifically, this would indicate whether the galaxy is indeed blue and actively star-forming, as predicted by SED fitting (FC10, FC12) and our simulations. Such observations would also reveal whether the starburst is concentrated within the NW source, and they would provide an independent check on the starburst age of a few Myr estimated from SED fitting (FC12).

Another consideration is that in principle, a merger remnant with a recoiling AGN should contain one central brightness peak (the stellar cusp) and one offset brightness peak (the AGN). An AGN pair, in contrast, should have both brightness peaks offset from the center. However, in practice, the center of stellar light is not well-constrained for CID-42. The surface brightness decomposition of FC10 places the center between the NW and SE sources, but it is consistent with being at the position of the NW source

within the errors. The central stellar cusp could also be intrinsically asymmetric in the unrelaxed merger remnant, and tidal features seen in projection could contribute light to the apparent galactic disk. Therefore, the position of the NW and SE sources is an inconclusive diagnostic for the nature of CID-42.

As noted in § 5.2.2, even the lowest possible recoil velocity for CID-42 is quite large ($\gtrsim$ 1300 km s^{-1}). The intrinsic probability of such a large kick is not clear. Recoil kick probability distributions have been derived from the results of numerical relativity simulations (e.g., Baker et al. 2008; van Meter et al. 2010; Lousto et al. 2012). However, the distributions of progenitor mass ratios, spins, and spin orientations are still quite uncertain. In particular, a circumbinary gas disk can form around the inspiraling SMBHs and may align or partially align their spins (Bogdanović et al. 2007; Dotti et al. 2010). If the BH spins become aligned, the maximum recoil velocity resulting from their merger is only $\sim$ 200 km s^{-1}. Partial alignment may also occur via GR precession effects (Kesden et al. 2010; Berti et al. 2012), though this mechanism can also result in *anti*-alignment of the BH spins, yielding substantially larger kicks. At any rate, it is clear that the GW recoil scenario for CID-42 requires that spin alignment prior to BH merger is inefficient, at least in some cases.

5.3.2 Gravitational Slingshot Recoil Scenario

Aside from GW recoil, the other possible origin of a rapidly-recoiling SMBH is a gravitational slingshot recoil. As described in § 5.1, this requires a long binary SMBH inspiral time, such that a subsequent galaxy merger brings a third SMBH into the system before the initial SMBH binary has coalesced. A three-body encounter may result in the

ejection of the lightest SMBH at high speeds, and may also cause the rapid merger of the remaining SMBHs (Hoffman & Loeb 2007). Thus, in the slingshot-recoil scenario, two *or three* SMBHs would be present in CID-42: the SE source would be the ejected SMBH, and the NW source would contain the SMBH(s) left behind.

While we have not constructed a model for this scenario, much of our analysis for the GW recoil model can be applied here. If the ejected SMBH retains an accretion disk during the three-body encounter (such that it appears as an AGN), the ejected disk will evolve in the same manner described in § 5.2.1. Also, the relationship between $v_{\rm k}$ and $t_{\rm obs}$ would be the same as in Figure 5.3. If the NW source contains an obscured AGN that is also a radio source, this could be detected with very long baseline interferometry (VLBI). If it contains a *binary* AGN that survived the three-body encounter, the binary might be spatially resolvable with VLBI imaging, provided the binary separation were at least a few parsec and the AGN were both radio sources. However, binary radio-detected AGN are intrinsically quite rare, with only one example known (Rodriguez et al. 2006) despite a dedicated search of thousands of archival VLBI images (Burke-Spolaor 2011).

If SMBH binaries do not merge efficiently, the probability of such triple SMBH systems forming is non-negligible, especially at high redshift ($z \gtrsim 2$, Kulkarni & Loeb 2011). In our simulations, efficient merging of the SMBHs is merely an assumption owing to resolution limits. However, smaller-scale simulations of inspiraling SMBHs indicate that gas drag (e.g., Escala et al. 2005; Dotti et al. 2007) or triaxiality of the stellar potential (e.g., Berczik et al. 2006; Khan et al. 2012) can prevent SMBH binaries from "stalling" (the so-called "final parsec problem", e.g., Begelman et al. 1980; Yu 2002). CID-42 is clearly a gas-rich system with an irregular morphology. Thus, while we cannot exclude the possibility of gravitational slingshot recoil, we consider it to be unlikely. Put

another way, if new evidence points toward a slingshot recoil in CID-42 (for example, if compact radio emission were detected in the NW source and consistent velocity offsets were found in multiple broad lines in the SE source), the implications for binary SMBHs would be far-reaching. This would indicate that a substantial population of unmerged SMBH binaries may be lurking below resolution limits even in gas-rich environments, to the detriment of SMBH merger event rates for future gravitational-wave observatories.

5.3.3 Dual SMBH Scenario

The observations of CID-42 are also consistent with an SMBH pair rather than a recoiling SMBH. In this scenario, the NW and SE sources are two inspiraling SMBHs with a 2.5 kpc separation. However, the $\sim$ 1300 km s^{-1} offset of the broad Hβ line is too large to be associated with orbital motion on kiloparsec scales. Although many AGN spectra show offset broad lines that are often attributed to outflows, the offset line in CID-42 is atypically large. Less than 1% of SDSS quasars have broad Hβ lines offset by $>$ 1000 km s^{-1} (Bonning et al. 2007; Eracleous et al. 2011), and CID-42 constitutes 1/323, or 0.003%, of BL AGN in the *Chandra*-COSMOS survey that have spectroscopic redshifts (Elvis et al. 2009).

Theoretically, a projected SMBH separation of 2.5 kpc could also occur during an early close passage of the merging galaxies, or even during a flyby encounter. However, this is an unlikely explanation for CID-42. Its tidal features are indicative of a late-stage merger, and the highest $\dot{M}_{\rm BH}$ and SFR typically occur near coalescence (see Fig. 5.2). An unbound encounter would be required to explain the 1300 km s^{-1} BL offset via relative galactic motion. (In comparison, the maximal relative speeds in our galaxy merger

simulations are $\sim 500 - 600$ km s^{-1}.) In such a flyby, only very specific configurations and timing would allow a projected separation of 2.5 kpc to be observed.

As with our recoiling AGN model, the dual SMBH model has similar morphology and stellar mass to that observed in CID-42. We find that a slightly less dissipative merger (lower $f_{\rm gas}$) is required in order to match the observed morphology prior to the SMBH merger and recoil. The projected SMBH separation of 2.5 kpc also occurs slightly before the peak SFR and SMBH accretion rate. As a consequence, the SFR, $\dot{M}_{\rm BH}$, and luminosity are slightly lower in the dual SMBH model than the estimates for CID-42.

We also investigate whether double-peaked NLs would be produced by the dual AGN in this model. Owing to the aforementioned low AGN luminosities of a few $\times 10^9$ L$_\odot$), their NL emission (as determined from the model of Blecha et al. 2012) may be too faint to be observable, and their relative LOS velocity of only 64 km s^{-1} is unlikely to be spectroscopically resolvable. This is not a conclusive test as to whether CID-42 could host a double-peaked NL AGN, but it is consistent with the supposition that the double-peaked NL structure in the DEIMOS spectrum (JC09) arises from its low S/N rather than from dual SMBH kinematics.

The non-detection of X-ray emission in the NW source (FC12) places some constraints on whether it may host an AGN. The NW source could contain a *quiescent* SMBH with $L_{\rm X} < 10^{42}$ erg s^{-1}, but our models indicate that two SMBHs in a late-stage, gas-rich major merger are unlikely to have a large luminosity ratio. Specifically, an X-ray faint AGN in the NW source requires a luminosity ratio > 25, which occurs for $< 1\%$ of the kpc-scale phase in the dual SMBH simulation.

The NW source could also contain a heavily-obscured, Compton-thick AGN. The

upper limits estimated for the gas column densities to each SMBH (log $N_{\rm gas} \approx 22.1$ & 23.8 cm^{-2}) indicate that these AGN should be absorbed and highly obscured, respectively, but not Compton-thick. The hard X-ray detected AGN pair in NGC 3393, for example, has estimated line-of-sight column densities of a few $\times 10^{23}$ cm^{-2} (Fabbiano et al. 2011). However, it is possible that obscuring material on sub-resolution scales could hide an AGN in the NW source. Finally, we note that while a strong iron emission line can indicate the presence of a heavily obscured AGN, this diagnostic is not informative for CID-42. A fairly strong FeKα emission line is detected (equivalent width $\sim$ 500 eV), but it is impossible to say how much, if any, of this emission is contributed by the NW source, which has a weaker continuum by a factor of at least 25.

The detection of compact radio emission from either or both optical brightness peaks in CID-42 would provide strong evidence for the presence of one or two AGN. As mentioned above, however, radio-detected AGN *pairs* appear to be very rare, with only one radio-loud kpc-scale quasar pair (3C 75; Owen et al. 1985) and one pc-scale AGN pair (Rodriguez et al. 2006) known. However, given the ambiguous nature of the NW optical source and the X-ray non-detection there, the possibility of a radio detection is enticing, as this would provide the clearest evidence for an obscured AGN in the NW source.

5.3.4 Summary

We find that neither the recoiling nor dual SMBH scenarios for CID-42 can be ruled out based on current data. It is clear that whatever its true nature, CID-42 is not a "typical" galaxy even among the rather exotic subsets that host dual or recoiling

AGN. Both scenarios require some extraordinary features, such as a dual AGN with an unusually large broad line offset or a rapidly-recoiling AGN with an atypical narrow line region. Through our analysis we have identified and constrained the requisite properties of CID-42 in either case. These constraints combined with further observations in the coming months and years, such as spatially-resolved and higher-quality optical spectra, radio imaging, and CO or 21 cm observations, should rapidly narrow the possible origins of this intriguing system.

Chapter 6

Conclusions and Future Directions

Supermassive black holes (SMBHs) represent a unique intersection of the physics on small scales near black hole event horizons and the physics of galaxy formation on cosmological scales. While these objects have been the focus of intense research for decades, the study of SMBH *mergers*, and their associated phenomena, has truly come of age in the last several years. When the work for this thesis was begun, full simulations of black hole mergers with numerical relativity were a brand-new result, and the number of SMBH pair candidates could be counted on one hand. Today, black hole merger simulations are carried out routinely, and Advanced LIGO offers hope of achieving the first detections of gravitational waves in just a few years. Observational searches for inspiralling and recoiling SMBHs have developed into an active field of research.

In this context, the work presented here provides a theoretical basis for understanding the phenomenology of SMBH inspiral, merger, and recoil. Specifically, we have modeled the observable signatures of these events and examined their importance in the broader framework of black hole-galaxy co-evolution.

In Chapters 2 and 3, we developed semi-analytical models for the evolution of recoiling SMBHs in galaxies. In Chapter 2 we demonstrated the potential for recoiling SMBHs to spend substantial time in motion and off-center from their host galaxies, as well as their ability to self-regulate their growth. Chapter 3 revealed the critical role of gas dynamics in determining recoil trajectories and the final black hole masses. We also showed that recoiling SMBHs may be observable as offset AGN for tens of Myr, and that recoil events can affect the observed black hole-bulge relations and the central properties of the galaxy merger remnant.

Given the uncertainty as to whether black holes spins align efficiently prior to merger, thus producing only small recoil kicks, it not clear that the probability of observing a recoiling AGN is non-negligible. Our finding that gas dynamics may suppress the motion of some recoiling black holes only exacerbates this problem. Nonetheless, it is encouraging that even in the presence of gas drag, we find offset AGN lifetimes of up to tens of Myr for a wide range of kick speeds. The confirmation of even one recoiling black hole would provide a new validation of general relativity and conclusive evidence that binary SMBHs do in fact merge, among other things. Given this enormous potential scientific payoff, the search for candidate recoiling black holes is certainly worthwhile.

Moreover, despite the setback to gravitational-wave astronomy with the de-funding of the *LISA* mission, pulsar timing arrays will be capable of detecting gravitational waves from merging SMBHs in the near future. In the longer term, of course, a new space-based gravitational-wave mission is still possible, especially if Advanced LIGO is successful in opening the window to gravitational-wave astronomy. Thus, there is strong motivation to continue developing constraints on the rates and observable counterparts of SMBH mergers.

In Chapter 4, we modeled the signatures of dual narrow-line AGN in galaxy mergers, motivated by recent surveys of such objects and their possible connection to SMBH pairs on kiloparsec scales. Our work demonstrated that double-peaked narrow-line AGN are a heterogeneous population. Some arise from dual SMBH motion on kiloparsec scales, but more often they are caused by gas kinematics in the narrow-line region. We have also suggested some possible signatures that could aid in distinguishing dual SMBHs from single SMBHs in the double-peaked narrow-line AGN sample.

The narrow-line models developed here represent an important but preliminary step in modeling the signatures of AGN pairs. Much remains to be be done to develop more realistic models of black holes in merging galaxies. A large source of uncertainty in the current simulations is the simplified nature of the sub-resolution models for the interstellar medium and for black hole accretion and feedback. The implementation of a turbulent-pressure-driven model for the ISM, for example, or AGN models that incorporate momentum feedback and outflows, will greatly improve our ability to model the narrow-line region around AGN. Furthermore, the inclusion of dust radiative transfer calculations will account for the possibly large effects of AGN obscuration, as well as the influence of dust absorption and scattering, on the emergent narrow-line profiles.

The methods developed in Chapters 2–4 were applied directly to a real galaxy (CID-42) in Chapter 5. We have developed realistic models of two possible scenarios for this unusual object: a kiloparsec-scale AGN pair and a recoiling SMBH. We showed that both scenarios are consistent with the current data, and we placed key constraints on the possible parameters of a dual or recoiling AGN in this galaxy. In addition to being an ideal test case for our methods, this system highlights the present difficulties with confirming both pre- and post-merger SMBH candidates. We note that this confusion

with recoil signatures is also an issue for *sub-parsec* binaries, which like recoil candidates are often identified via unusual broad emission lines. This underscores the need for improved modeling of SMBH signatures in mergers, along with dedicated follow-up observations of potential candidates.

Finally, while mergers play a demonstrably important role in galaxy formation and are the origin of SMBH pairs, it is clear that at least for some redshifts and luminosities, major galaxy mergers are not the dominant trigger of AGN fueling. Thus, in order to further our understanding of SMBH evolution, we must explore beyond the realm of major mergers. Possible areas for future study include simulations of the efficiency of *minor* mergers in fueling low-luminosity AGN, as well as simulations of AGN fueling via secular instabilities such as stellar bars in isolated galaxies. Simulations of the narrow-line region in isolated galaxies would also allow a valuable comparison to existing photoionization models and to local observations of narrow-line AGN. Furthermore, it is worth noting that the current *eLISA/NGO* design has a shorter interferometric baseline than the original *LISA* design. As a consequence, the peak sensitivity to SMBH mergers will be at masses $< 10^6$ $M_\odot$. Given our quite limited knowledge of the black hole population in this mass range, this is a strong incentive to explore their contribution to the population of low-luminosity AGN and AGN in minor mergers.

References

Aller, M. C., & Richstone, D. O. 2007, ApJ, 665, 120

Amaro-Seoane, P., et al. 2012, ArXiv e-prints

Anderson, M., Lehner, L., Megevand, M., & Neilsen, D. 2010, Phys. Rev. D, 81, 044004

Armitage, P. J., & Natarajan, P. 2002, ApJ, 567, L9

Baker, J. G., Boggs, W. D., Centrella, J., Kelly, B. J., McWilliams, S. T., Miller, M. C., & van Meter, J. R. 2008, ApJ, 682, L29

Baker, J. G., Centrella, J., Choi, D.-I., Koppitz, M., & van Meter, J. 2006, Phys. Rev. Lett., 96, 111102

Barausse, E. 2012, ArXiv e-prints

Barnes, J. E., & Hernquist, L. 1996, ApJ, 471, 115

Barnes, J. E., & Hernquist, L. E. 1991, ApJ, 370, L65

Batcheldor, D., Robinson, A., Axon, D. J., Perlman, E. S., & Merritt, D. 2010, ApJ, 717, L6

Begelman, M. C., Blandford, R. D., & Rees, M. J. 1980, Nature, 287, 307

Begelman, M. C., & Nath, B. B. 2005, MNRAS, 361, 1387

Bekenstein, J. D. 1973, ApJ, 183, 657

Berczik, P., Merritt, D., Spurzem, R., & Bischof, H.-P. 2006, ApJ, 642, L21

Berentzen, I., Preto, M., Berczik, P., Merritt, D., & Spurzem, R. 2009, ApJ, 695, 455

Berti, E., Kesden, M., & Sperhake, U. 2012, ArXiv e-prints

Berti, E., & Volonteri, M. 2008, ApJ, 684, 822

Bertin, G. 1997, ApJ, 478, L71+

Bertin, G., & Lodato, G. 1999, A&A, 350, 694

Bianchi, S., Chiaberge, M., Piconcelli, E., Guainazzi, M., & Matt, G. 2008, MNRAS, 386, 105

Blanchet, L., Qusailah, M. S. S., & Will, C. M. 2005, ApJ, 635, 508

Blecha, L., Cox, T. J., Loeb, A., & Hernquist, L. 2011, MNRAS, 412, 2154

Blecha, L., & Loeb, A. 2008, MNRAS, 390, 1311

Blecha, L., Loeb, A., & Narayan, R. 2012, ArXiv e-prints

Bode, T., Bogdanović, T., Haas, R., Healy, J., Laguna, P., & Shoemaker, D. 2012, ApJ, 744, 45

Bogdanović, T., Eracleous, M., & Sigurdsson, S. 2009, ApJ, 697, 288

Bogdanović, T., Reynolds, C. S., & Miller, M. C. 2007, ApJ, 661, L147

Bondi, H., & Hoyle, F. 1944, MNRAS, 104, 273

Bonning, E. W., Shields, G. A., & Salviander, S. 2007, ApJ, 666, L13

Boroson, T. A., & Lauer, T. R. 2009, Nature, 458, 53

Boylan-Kolchin, M., Ma, C., & Quataert, E. 2004, ApJ, 613, L37

Bullock, J. S., Kolatt, T. S., Sigad, Y., Somerville, R. S., Kravtsov, A. V., Klypin, A. A., Primack, J. R., & Dekel, A. 2001, MNRAS, 321, 559

Burke-Spolaor, S. 2011, MNRAS, 410, 2113

Callegari, S., Mayer, L., Kazantzidis, S., Colpi, M., Governato, F., Quinn, T., & Wadsley, J. 2009, ApJ, 696, L89

Campanelli, M., Lousto, C., Zlochower, Y., & Merritt, D. 2007a, ApJ, 659, L5

Campanelli, M., Lousto, C. O., Marronetti, P., & Zlochower, Y. 2006, Phys. Rev. Lett., 96, 111101

Campanelli, M., Lousto, C. O., & Zlochower, Y. 2008, Phys. Rev. D, 77, 101501

Campanelli, M., Lousto, C. O., Zlochower, Y., & Merritt, D. 2007b, Physical Review Letters, 98, 231102

Cannizzo, J. K., Lee, H. M., & Goodman, J. 1990, ApJ, 351, 38

Centrella, J., Baker, J. G., Kelly, B. J., & van Meter, J. R. 2010, Reviews of Modern Physics, 82, 3069

Chandrasekhar, S. 1943, ApJ, 97, 255

Cisternas, M., et al. 2011, ApJ, 726, 57

Civano, F., et al. 2010, ApJ, 717, 209

—. 2012, ApJ submitted

Colpi, M., & Dotti, M. 2009, ArXiv e-prints

Comerford, J. M., Griffith, R. L., Gerke, B. F., Cooper, M. C., Newman, J. A., Davis, M., & Stern, D. 2009a, ApJ, 702, L82

Comerford, J. M., Pooley, D., Gerke, B. F., & Madejski, G. M. 2011a, ApJ, 737, L19

Comerford, J. M., et al. 2009b, ApJ, 698, 956

—. 2011b, ArXiv e-prints

Cora, S. A., Muzzio, J. C., & Vergne, M. M. 1997, MNRAS, 289, 253

Cox, T. J., Dutta, S. N., Di Matteo, T., Hernquist, L., Hopkins, P. F., Robertson, B., & Springel, V. 2006, ApJ, 650, 791

Croton, D. J., et al. 2006, MNRAS, 365, 11

da Silva, R. L., Prochaska, J. X., Rosario, D., Tumlinson, J., & Tripp, T. M. 2011, ApJ, 735, 54

Damour, T., & Gopakumar, A. 2006, Phys. Rev. D, 73, 124006

Debuhr, J., Quataert, E., Ma, C.-P., & Hopkins, P. 2010, MNRAS, 406, L55

Decarli, R., Dotti, M., Falomo, R., Treves, A., Colpi, M., Kotilainen, J. K., Montuori, C., & Uslenghi, M. 2009, ApJ, 703, L76

Dehnen, W. 1993, MNRAS, 265, 250

Di Matteo, T., Springel, V., & Hernquist, L. 2005, Nature, 433, 604

Dotti, M., Colpi, M., Haardt, F., & Mayer, L. 2007, MNRAS, 379, 956

Dotti, M., Montuori, C., Decarli, R., Volonteri, M., Colpi, M., & Haardt, F. 2008, ArXiv e-prints

—. 2009, MNRAS, 398, L73

Dotti, M., Sesana, A., & Decarli, R. 2012, Advances in Astronomy, 2012

Dotti, M., Volonteri, M., Perego, A., Colpi, M., Ruszkowski, M., & Haardt, F. 2010, MNRAS, 402, 682

Ellison, S. L., Patton, D. R., Mendel, J. T., & Scudder, J. M. 2011, MNRAS, 418, 2043

Elvis, M., et al. 2009, ApJS, 184, 158

Eracleous, M., Boroson, T. A., Halpern, J. P., & Liu, J. 2011, ArXiv e-prints

Escala, A., Larson, R. B., Coppi, P. S., & Mardones, D. 2004, ApJ, 607, 765

—. 2005, ApJ, 630, 152

Fabbiano, G., Wang, J., Elvis, M., & Risaliti, G. 2011, Nature, 477, 431

Fabian, A. C., Sanders, J. S., Allen, S. W., Crawford, C. S., Iwasawa, K., Johnstone, R. M., Schmidt, R. W., & Taylor, G. B. 2003, MNRAS, 344, L43

Fan, X., et al. 2001, AJ, 122, 2833

—. 2003, AJ, 125, 1649

Farris, B. D., Liu, Y. T., & Shapiro, S. L. 2011, Phys. Rev. D, 84, 024024

Favata, M., Hughes, S. A., & Holz, D. E. 2004, ApJ, 607, L5

Feain, I. J., Papadopoulos, P. P., Ekers, R. D., & Middelberg, E. 2007, ApJ, 662, 872

Ferrarese, L., & Ford, H. 2005, Space Science Reviews, 116, 523

Ferrarese, L., & Merritt, D. 2000, ApJ, 539, L9

Fitchett, M. J. 1983, MNRAS, 203, 1049

Fitchett, M. J., & Detweiler, S. 1984, MNRAS, 211, 933

Fu, H., Myers, A. D., Djorgovski, S. G., & Yan, L. 2010, ArXiv e-prints

—. 2011a, ApJ, 733, 103

Fu, H., Yan, L., Myers, A. D., Stockton, A., Djorgovski, S. G., Aldering, G., & Rich, J. A. 2011b, ArXiv e-prints

Fu, H., et al. 2011c, ArXiv e-prints

Gammie, C. F. 2001, ApJ, 553, 174

Gebhardt, K., et al. 2000, ApJ, 543, L5

Gerhard, O. E., & Binney, J. 1985, MNRAS, 216, 467

Gerke, B. F., et al. 2007, ApJ, 660, L23

González, J. A., Hannam, M., Sperhake, U., Brügmann, B., & Husa, S. 2007a, Physical Review Letters, 98, 231101

González, J. A., Sperhake, U., Brügmann, B., Hannam, M., & Husa, S. 2007b, Physical Review Letters, 98, 091101

Goodman, J. 2003, MNRAS, 339, 937

Goodman, J., & Tan, J. C. 2004, ApJ, 608, 108

Gould, A., & Miralda-Escude, J. 1997, ApJ, 483, L13+

Green, P. J., Myers, A. D., Barkhouse, W. A., Mulchaey, J. S., Bennert, V. N., Cox, T. J., & Aldcroft, T. L. 2010, ApJ, 710, 1578

Gualandris, A., & Merritt, D. 2008, ApJ, 678, 780

Guedes, J., Madau, P., Kuhlen, M., Diemand, J., & Zemp, M. 2009, ApJ, 702, 890

Guedes, J., Madau, P., Mayer, L., & Callegari, S. 2010, ArXiv e-prints

Haehnelt, M. G., Davies, M. B., & Rees, M. J. 2006, MNRAS, 366, L22

Haehnelt, M. G., & Kauffmann, G. 2000, MNRAS, 318, L35

Hayasaki, K., Mineshige, S., & Sudou, H. 2007, PASJ, 59, 427

Heckman, T. M., Krolik, J. H., Moran, S. M., Schnittman, J., & Gezari, S. 2009, ApJ, 695, 363

Heckman, T. M., Miley, G. K., van Breugel, W. J. M., & Butcher, H. R. 1981, ApJ, 247, 403

Hennawi, J. F., et al. 2006, AJ, 131, 1

—. 2010, ApJ, 719, 1672

Hernquist, L. 1990, ApJ, 356, 359

Hobbs, G., et al. 2010, Classical and Quantum Gravity, 27, 084013

Hoffman, L., & Loeb, A. 2006, ApJ, 638, L75

—. 2007, MNRAS, 377, 957

Hohl, F. 1971, ApJ, 168, 343

Hopkins, P. F., Cox, T. J., & Hernquist, L. 2008a, ApJ, 689, 17

Hopkins, P. F., Cox, T. J., Kereš, D., & Hernquist, L. 2008b, ApJS, 175, 390

Hopkins, P. F., & Hernquist, L. 2010a, MNRAS, 402, 985

—. 2010b, MNRAS, 407, 447

Hopkins, P. F., Hernquist, L., Cox, T. J., Di Matteo, T., Robertson, B., & Springel, V. 2006a, ApJS, 163, 1

Hopkins, P. F., Hernquist, L., Cox, T. J., Dutta, S. N., & Rothberg, B. 2008c, ApJ, 679, 156

Hopkins, P. F., Hernquist, L., Cox, T. J., & Kereš, D. 2008d, ApJS, 175, 356

Hopkins, P. F., Hernquist, L., Cox, T. J., Robertson, B., & Krause, E. 2007a, ApJ, 669, 45

—. 2007b, ApJ, 669, 67

Hopkins, P. F., Hernquist, L., Cox, T. J., Robertson, B., & Springel, V. 2006b, ApJS, 163, 50

Hut, P., & Rees, M. J. 1992, MNRAS, 259, 27P

Jing, Y. P., & Suto, Y. 2002, ApJ, 574, 538

Jonker, P. G., Torres, M. A. P., Fabian, A. C., Heida, M., Miniutti, G., & Pooley, D. 2010, MNRAS, 407, 645

Jonsson, P., Groves, B. A., & Cox, T. J. 2010, MNRAS, 403, 17

Karas, V., & Šubr, L. 2001, A&A, 376, 686

Kesden, M., Sperhake, U., & Berti, E. 2010, ApJ, 715, 1006

Khan, F. M., Berentzen, I., Berczik, P., Just, A., Mayer, L., Nitadori, K., & Callegari, S. 2012, ArXiv e-prints

Kim, W.-T., El-Zant, A. A., & Kamionkowski, M. 2005, ApJ, 632, 157

King, A. R., & Dehnen, W. 2005, MNRAS, 357, 275

King, A. R., Pringle, J. E., & Hofmann, J. A. 2008, MNRAS, 385, 1621

Komossa, S. 2012, Advances in Astronomy, 2012

Komossa, S., Burwitz, V., Hasinger, G., Predehl, P., Kaastra, J. S., & Ikebe, Y. 2003, ApJ, 582, L15

Komossa, S., & Merritt, D. 2008a, ApJ, 689, L89

—. 2008b, ApJ, 683, L21

Komossa, S., Zhou, H., & Lu, H. 2008, ApJ, 678, L81

Kormendy, J., & Richstone, D. 1995, ARA&A, 33, 581

Kornreich, D. A., & Lovelace, R. V. E. 2008, ApJ, 681, 104

Koss, M., Mushotzky, R., Veilleux, S., & Winter, L. 2010, ApJ, 716, L125

Koss, M., Mushotzky, R., Veilleux, S., Winter, L. M., Baumgartner, W., Tueller, J., Gehrels, N., & Valencic, L. 2011a, ApJ, 739, 57

Koss, M., et al. 2011b, ApJ, 735, L42

Kulkarni, G., & Loeb, A. 2011, ArXiv e-prints

Lehto, H. J., & Valtonen, M. J. 1996, ApJ, 460, 207

Libeskind, N. I., Cole, S., Frenk, C. S., & Helly, J. C. 2006, MNRAS, 368, 1381

Lilly, S. J., et al. 2007, ApJS, 172, 70

Lin, D. N. C., & Tremaine, S. 1983, ApJ, 264, 364

Lippai, Z., Frei, Z., & Haiman, Z. 2008, ApJ, 676, L5

Liu, F. K., Wu, X.-B., & Cao, S. L. 2003, MNRAS, 340, 411

Liu, X., Greene, J. E., Shen, Y., & Strauss, M. A. 2010a, ApJ, 715, L30

Liu, X., Shen, Y., Strauss, M. A., & Greene, J. E. 2010b, ApJ, 708, 427

Liu, X., Shen, Y., Strauss, M. A., & Hao, L. 2011, ApJ, 737, 101

Lodato, G. 2008, ArXiv e-prints, 801

Lodato, G., & Rice, W. K. M. 2004, MNRAS, 351, 630

Loeb, A. 2007, Physical Review Letters, 99, 041103

Lousto, C. O., Campanelli, M., Zlochower, Y., & Nakano, H. 2010a, Classical and Quantum Gravity, 27, 114006

Lousto, C. O., Nakano, H., Zlochower, Y., & Campanelli, M. 2010b, Phys. Rev. D, 81, 084023

Lousto, C. O., & Zlochower, Y. 2009, Phys. Rev. D, 79, 064018

—. 2011a, Physical Review Letters, 107, 231102

—. 2011b, Physical Review Letters, 107, 231102

Lousto, C. O., Zlochower, Y., Dotti, M., & Volonteri, M. 2012, ArXiv e-prints

Lynden-Bell, D. 1969, Nature, 223, 690

Lynden-Bell, D., & Pringle, J. E. 1974, MNRAS, 168, 603

MacFadyen, A. I., & Milosavljevic, M. 2006, ArXiv Astrophysics e-prints

Madau, P., & Quataert, E. 2004, ApJ, 606, L17

Magain, P., Letawe, G., Courbin, F., Jablonka, P., Jahnke, K., Meylan, G., & Wisotzki, L. 2005, Nature, 437, 381

Magorrian, J., et al. 1998, AJ, 115, 2285

Maio, U., Dotti, M., Petkova, M., Perego, A., & Volonteri, M. 2012, ArXiv e-prints

Marcillac, D., Elbaz, D., Charlot, S., Liang, Y. C., Hammer, F., Flores, H., Cesarsky, C., & Pasquali, A. 2006, A&A, 458, 369

Marconi, A., & Hunt, L. K. 2003, ApJ, 589, L21

Mayer, L., Kazantzidis, S., Madau, P., Colpi, M., Quinn, T., & Wadsley, J. 2007, Science, 316, 1874

McGurk, R. C., Max, C. E., Rosario, D. J., Shields, G. A., Smith, K. L., & Wright, S. A. 2011, ApJ, 738, L2

McNamara, B. R., & Nulsen, P. E. J. 2007, ARA&A, 45, 117

McNamara, B. R., et al. 2000, ApJ, 534, L135

Megevand, M., Anderson, M., Frank, J., Hirschmann, E. W., Lehner, L., Liebling, S. L., Motl, P. M., & Neilsen, D. 2009, Phys. Rev. D, 80, 024012

Merritt, D., & Ferrarese, L. 2001, in Astronomical Society of the Pacific Conference Series, Vol. 249, The Central Kiloparsec of Starbursts and AGN: The La Palma Connection, ed. J. H. Knapen, J. E. Beckman, I. Shlosman, & T. J. Mahoney, 335–+

Merritt, D., Milosavljević, M., Favata, M., Hughes, S. A., & Holz, D. E. 2004, ApJ, 607, L9

Merritt, D., Schnittman, J. D., & Komossa, S. 2009, ApJ, 699, 1690

Merritt, D., Storchi-Bergmann, T., Robinson, A., Batcheldor, D., Axon, D., & Cid Fernandes, R. 2006, MNRAS, 367, 1746

Mestel, L. 1963, MNRAS, 126, 553

Mihos, J. C., & Hernquist, L. 1994a, ApJ, 437, L47

—. 1994b, ApJ, 431, L9

—. 1996, ApJ, 464, 641

Milosavljević, M., & Merritt, D. 2001, ApJ, 563, 34

Milosavljević, M., & Phinney, E. S. 2005, ApJ, 622, L93

Moesta, P., Alic, D., Rezzolla, L., Zanotti, O., & Palenzuela, C. 2011, ArXiv e-prints

Myers, A. D., Richards, G. T., Brunner, R. J., Schneider, D. P., Strand, N. E., Hall, P. B., Blomquist, J. A., & York, D. G. 2008, ApJ, 678, 635

Narayan, R. 2000, ApJ, 536, 663

Narayan, R., & McClintock, J. E. 2008, New Astronomy Review, 51, 733

O'Leary, R. M., & Loeb, A. 2009, MNRAS, 395, 781

—. 2011, ArXiv e-prints

Osterbrock, D. E., & Ferland, G. J. 2006, Astrophysics of gaseous nebulae and active galactic nuclei

Ostriker, E. C. 1999, ApJ, 513, 252

Owen, F. N., O'Dea, C. P., Inoue, M., & Eilek, J. A. 1985, ApJ, 294, L85

Paczynski, B. 1978, Acta Astronomica, 28, 91

Palenzuela, C., Lehner, L., & Liebling, S. L. 2010, Science, 329, 927

Perego, A., Dotti, M., Colpi, M., & Volonteri, M. 2009, MNRAS, 399, 2249

Peres, A. 1962, Physical Review, 128, 2471

Preto, M., Berentzen, I., Berczik, P., & Spurzem, R. 2011, ApJ, 732, L26

Pretorius, F. 2005, Physical Review Letters, 95, 121101

Pringle, J. E. 1981, ARA&A, 19, 137

—. 1991, MNRAS, 248, 754

Richstone, D., et al. 1998, Nature, 395, A14+

Robertson, B., Bullock, J. S., Cox, T. J., Di Matteo, T., Hernquist, L., Springel, V., & Yoshida, N. 2006a, ApJ, 645, 986

Robertson, B., Hernquist, L., Cox, T. J., Di Matteo, T., Hopkins, P. F., Martini, P., & Springel, V. 2006b, ApJ, 641, 90

Robinson, A., Young, S., Axon, D. J., Kharb, P., & Smith, J. E. 2010, ApJ, 717, L122

Rodriguez, C., Taylor, G. B., Zavala, R. T., Peck, A. B., Pollack, L. K., & Romani, R. W. 2006, ApJ, 646, 49

Roedig, C., Sesana, A., Dotti, M., Cuadra, J., Amaro-Seoane, P., & Haardt, F. 2012, ArXiv e-prints

Rosario, D. J., McGurk, R. C., Max, C. E., Shields, G. A., Smith, K. L., & Ammons, S. M. 2011, ApJ, 739, 44

Rosario, D. J., Shields, G. A., Taylor, G. B., Salviander, S., & Smith, K. L. 2010, ApJ, 716, 131

Rossi, E. M., Lodato, G., Armitage, P. J., Pringle, J. E., & King, A. R. 2010, MNRAS, 401, 2021

Sánchez-Salcedo, F. J., & Brandenburg, A. 2001, MNRAS, 322, 67

Sanders, D. B., & Mirabel, I. F. 1996, ARA&A, 34, 749

Sanders, D. B., Scoville, N. Z., & Soifer, B. T. 1991, ApJ, 370, 158

Sanders, D. B., Soifer, B. T., Elias, J. H., Madore, B. F., Matthews, K., Neugebauer, G., & Scoville, N. Z. 1988a, ApJ, 325, 74

Sanders, D. B., Soifer, B. T., Elias, J. H., Neugebauer, G., & Matthews, K. 1988b, ApJ, 328, L35

Schnittman, J. D. 2011, Classical and Quantum Gravity, 28, 094021

Schnittman, J. D., & Buonanno, A. 2007, ApJ, 662, L63

Schnittman, J. D., & Krolik, J. H. 2008, ApJ, 684, 835

Sesana, A., Volonteri, M., & Haardt, F. 2007, MNRAS, 377, 1711

Shakura, N. I., & Sunyaev, R. A. 1973, A&A, 24, 337

Shen, Y., Liu, X., Greene, J. E., & Strauss, M. A. 2011, ApJ, 735, 48

Shields, G. A., & Bonning, E. W. 2008, ApJ, 682, 758

Shields, G. A., Bonning, E. W., & Salviander, S. 2009a, ApJ, 696, 1367

Shields, G. A., Gebhardt, K., Salviander, S., Wills, B. J., Xie, B., Brotherton, M. S., Yuan, J., & Dietrich, M. 2003, ApJ, 583, 124

Shields, G. A., et al. 2009b, ApJ, 707, 936

Sijacki, D., & Springel, V. 2006, MNRAS, 366, 397

Sijacki, D., Springel, V., & Haehnelt, M. 2010, ArXiv e-prints

Sijacki, D., Springel, V., & Haehnelt, M. G. 2009, MNRAS, 400, 100

Silk, J., & Rees, M. J. 1998, A&A, 331, L1

Sillanpaa, A., Haarala, S., Valtonen, M. J., Sundelius, B., & Byrd, G. G. 1988, ApJ, 325, 628

Smith, K. L., Shields, G. A., Bonning, E. W., McMullen, C. C., Rosario, D. J., & Salviander, S. 2010, ApJ, 716, 866

Smith, K. L., Shields, G. A., Salviander, S., Stevens, A. C., & Rosario, D. J. 2011, ArXiv e-prints

Snyder, G. F., e. a. 2010, ApJ submitted

Soltan, A. 1982, MNRAS, 200, 115

Somerville, R. S., Hopkins, P. F., Cox, T. J., Robertson, B. E., & Hernquist, L. 2008, MNRAS, 391, 481

Springel, V. 2005, MNRAS, 364, 1105

Springel, V., Di Matteo, T., & Hernquist, L. 2005a, ApJ, 620, L79

—. 2005b, MNRAS, 361, 776

Springel, V., & Hernquist, L. 2002, MNRAS, 333, 649

—. 2003, MNRAS, 339, 289

Springel, V., Yoshida, N., & White, S. D. M. 2001, New Astronomy, 6, 79

Stone, N., & Loeb, A. 2010, ArXiv e-prints

—. 2011a, MNRAS, 412, 75

—. 2011b, ArXiv e-prints

Tabor, G., & Binney, J. 1993, MNRAS, 263, 323

Tanaka, T., & Menou, K. 2010, ApJ, 714, 404

Tanaka, T., Menou, K., & Haiman, Z. 2011, ArXiv e-prints

Thompson, T. A., Quataert, E., & Murray, N. 2005, ApJ, 630, 167

Toomre, A. 1964, ApJ, 139, 1217

Toomre, A. 1977, in Evolution of Galaxies and Stellar Populations, ed. B. M. Tinsley & R. B. Larson, 401–+

Toomre, A., & Toomre, J. 1972, ApJ, 178, 623

Tremaine, S., et al. 2002a, ApJ, 574, 740

—. 2002b, ApJ, 574, 740

Trump, J. R., et al. 2007, ApJS, 172, 383

—. 2009, ApJ, 696, 1195

Tsalmantza, P., Decarli, R., Dotti, M., & Hogg, D. W. 2011, ApJ, 738, 20

Valtonen, M. J., et al. 2008, Nature, 452, 851

van Meter, J. R., Miller, M. C., Baker, J. G., Boggs, W. D., & Kelly, B. J. 2010, ApJ, 719, 1427

Van Wassenhove, S., Volonteri, M., Mayer, L., Dotti, M., Bellovary, J., & Callegari, S. 2011, ArXiv e-prints

Vicari, A., Capuzzo-Dolcetta, R., & Merritt, D. 2007, ApJ, 662, 797

Vivek, M., Srianand, R., Noterdaeme, P., Mohan, V., & Kuriakosde, V. C. 2009, MNRAS, L321+

Volonteri, M. 2007, ApJ, 663, L5

Volonteri, M., Haardt, F., & Madau, P. 2003, ApJ, 582, 559

Volonteri, M., Madau, P., Quataert, E., & Rees, M. J. 2005, ApJ, 620, 69

Volonteri, M., & Rees, M. J. 2006, ApJ, 650, 669

Wise, M. W., McNamara, B. R., Nulsen, P. E. J., Houck, J. C., & David, L. P. 2007, ApJ, 659, 1153

Wyithe, J. S. B., & Loeb, A. 2003, ApJ, 595, 614

Xu, G., & Ostriker, J. P. 1994, ApJ, 437, 184

Yu, Q. 2002, MNRAS, 331, 935

Zhou, H., Wang, T., Zhang, X., Dong, X., & Li, C. 2004, ApJ, 604, L33